Dissertation
submitted to the
Combined Faculties for the Natural Sciences and for Mathematics
of the Ruperto-Carola University of Heidelberg, Germany
for the degree of
Doctor of Natural Sciences

presented by
Diplom-Phys. Dario Giuseppe Motta
born in Catania
oral examination: May 5 2004

Feasibility Analysis and Prototype Measurements of a Novel Approach for the Real-Time Spectroscopy of Low Energy Solar Neutrinos

Referees:

Prof. Dr. Till Kirsten

Prof. Dr. Karl-Tasso Knöpfle

Abstrakt Ziel des LENS Projekts ist die Echtzeit-Spektroskopie von niederenergetischen Sonnenneutrinos. Der Neutrinonachweis erfolgt durch inverse Elektroneneinfangs-Reaktionen in einen isomeren Zustand. Die Koinzidenz zwischen promptem Elektron und verzögerter Kernabregung gibt eine spezifische Signatur zur Untergrundunterdrückung. ^{176}Yb und ^{115}In sind die aussichtsreichsten Targetisotope. In beiden Fällen wäre der Detektor modular aufgebaut und das Target-Element in Flüssigszintillatoren gelöst.

Der Neutrinonachweis bei ^{176}Yb ist aufgrund der kurzen Verzögerung ($\tau = 50\,ns$) und der niedrigen Energie ($E_\gamma = 72\,keV$) des Koinzidenzereignisses technisch schwierig. Der Untergrund durch statistische Selbstkorrelationen einzelner Ereignisse wurde untersucht. Dies schlieSSt die Messung der Fluoreszenzzeit von metallbeladenen Szintillatoren, die Studie von Reflektionen an Photoelektronen-Vervielfachern und die Entwicklung von photonspurverfolgenden Simulationen ein.

Die Untergrundunterdrückung in einem Indium-Detektor erfordert eine hohe Granularität und gute Energieauflösung. Durch Messungen und Simulationen wurde gezeigt, dass die optischen Eigenschaften des Detektors nicht durch die Segmentierung dominiert würden. Als Ergebnis dieser Untersuchungen, konnte das LENS-Projekt mit dem Aufbau von Detektorprototypen in die Pilotphase übergehen.

Die optischen Eigenschaften von Prototypzellen wurden gemessen, im einzelnen die Lichtabschwächungslänge, Energie- sowie Ortsauflösung. Erste Ergebnisse zum Untergrund des endgültigen LENS Prototypen werden vorgestellt.

Die Folgerungen dieser Untersuchungen für die Machbarkeit der beiden vorgeschlagenen Nachweismethoden werden diskutiert.

Abstract The LENS project aims at the real-time spectroscopy of low energy solar neutrinos. Detection would proceed via inverse-EC to an isomeric state. The coincidence of prompt electron and delayed nuclear de-excitation gives a specific signature for background suppression. The most promising targets are ^{176}Yb and ^{115}In. In both cases the detector would be modular and the target dissolved in liquid scintillators.

The ^{176}Yb tag is difficult, because of the short delay ($\tau = 50\,ns$) and low energy ($E_\gamma = 72\,keV$) of the coincident event. The background due to statistical self-correlations of single events was investigated. This included the measurement of the fluorescence time of metal-loaded scintillators, the study of reflections from photomultipliers and the development of photon-tracing simulations.

In a indium detector the background suppression requires high granularity and good energy resolution. Through measurements and simulations it was shown that the detector optical performances would not be dominated by the segmentation. As a result of these investigations, the project advanced to the pilot phase, with the construction of prototype detectors.

The optical performances of prototype cells were measured, including attenuation length, energy and spatial resolution. First background results of the final LENS prototype are presented.

The implications of these investigations for the feasibility of both proposed approaches is discussed.

Contents

Part I

Introduction

Chapter 1

Neutrinos, Solar Neutrinos and Low Energy Solar Neutrinos

1.1 Neutrinos: Standard Model, Masses, Mixing and Flavor Oscillations

Neutrinos were first postulated in 1930 by W. Pauli to save the principle of conservation of energy and angular momentum which seemed to be violated in the nuclear β-decay. They were given their name by E. Fermi, who developed in 1933 the first theory of weak interactions. Their direct experimental discovery had to await more than 20 years, when in 1956 Reines and Cowan announced the observation of the anti-neutrino induced reaction $p(\bar{\nu}, e^+)n$ in proximity of a nuclear reactor [RC56]. In the classic form of the Standard Model (SM), neutrinos are assumed to be massless Dirac particles, members of a weak left-handed isospin doublet made up of the neutrino and the associated charged lepton. Three lepton families are known (e, μ, τ) and accordingly three neutrino flavors have been experimentally established. Data from the width of the Z boson decay at LEP [Gro00] have demonstrated that three is also the total number of light ($m_\nu < M_Z/2$) neutrinos that couple to the scalar bosons and hence interact via the weak force ("active" neutrinos).

Recent experimental observations have shown that neutrinos undergo flavor conversion, i.e. a neutrino produced by a weak processes in a specific flavor, can be detected at a certain distance in some other flavor. The first experimental evidence of such a phenomenon has come from atmospheric neutrinos, where an asymmetry between "downward-going" and "upward-going" ν_μ has been reported by SuperKamiokande and other experiments, consistent with a transition $\nu_\mu \to \nu_\tau$ of the upward-going neutrinos [SK98]. Also solar neutrinos show compelling evidence for transitions $\nu_e \to \nu_x$, with ν_x being some combination of ν_μ and ν_τ. The reactor experiment KamLAND has recently observed disappearance of $\bar{\nu}_e$ at long distance, which is well consistent with the solar data (a more detailed discussion about solar and reactor data will follow in Sec. 1.4). A controversial evidence for $\bar{\nu}_\mu \to \bar{\nu}_e$ conversion from the LSND short baseline accelerator experiment has also been reported [LSND01].

The SM of electro-weak interactions does not provide for lepton family number non-conserving phenomena, and thus neutrino flavor conversion must be somehow accommodated in an extension of the SM. The most simple and best data-supported explanation is that neutrinos do have a mass and that they mix, i.e. that mass and flavor eigenstates do not coincide (see the historic papers [MNS62] and [GP69] or the textbook [BV92]). Each flavor eigenstate

$\nu_{e,\mu,\tau}$ is thus the superposition of the three mass eigenstates $\nu_{1,2,3}$ with masses $m_{1,2,3}$:

$$\begin{pmatrix} \nu_e \\ \nu_\mu \\ \nu_\tau \end{pmatrix} = \begin{pmatrix} U_{11} & U_{12} & U_{13} \\ U_{21} & U_{22} & U_{23} \\ U_{31} & U_{32} & U_{33} \end{pmatrix} \begin{pmatrix} \nu_1 \\ \nu_2 \\ \nu_3 \end{pmatrix} \tag{1.1}$$

The matrix U is non-diagonal, if mixing does occur. It is the leptonic equivalent of the CKM mixing matrix in the quark sector. Neutrinos are always produced in pure flavor states, which are defined as those coupling to the electro-weak vector bosons. However the propagating states are the mass eigenstates. In vacuum the propagation introduces the phases $e^{-iE_i t}$, where E_i includes the mass eigenvalues m_i. As a consequence of the different masses, an initially pure flavor state undergoes a "rotation" and becomes a superposition of all flavors. This implies that there is a certain probability that the neutrino is revealed in a different flavor than the original one. The U matrix of eq. 1.1 can be expressed as the product of three 2-dimensional rotations, parametrized by three mixing angles[1]: θ_{12}, θ_{23} and θ_{13}. Let us assume that flavor conversion phenomena among the three generations are nearly decoupled in 2ν transitions, so that only one of the above rotations must be considered:

$$\begin{pmatrix} \nu_\alpha \\ \nu_\beta \end{pmatrix} = \begin{pmatrix} \cos\theta & \sin\theta \\ -\sin\theta & \cos\theta \end{pmatrix} \begin{pmatrix} \nu_1 \\ \nu_2 \end{pmatrix} \tag{1.2}$$

where ν_α is the initial flavor and ν_β an other flavor or some combination of the two other flavors. Developing the formalism of time evolution in vacuum leads to the formula for the $\nu_\alpha \to \nu_\beta$ transition probability:

$$P(\nu_\alpha \to \nu_\beta) = P_{\alpha\beta} = \sin^2(2\theta)\sin^2\left(\frac{1.27\Delta m^2(eV^2)L(m)}{E(MeV)}\right) \tag{1.3}$$

where $\Delta m^2 = m_2^2 - m_1^2$, L is the traveled distance and E the neutrino energy. According to eq. 1.2 the flavor content of a ν_α beam oscillates with an oscillation length $L_{osc} = \frac{2.48E}{\Delta m^2}$ and an amplitude given by $\sin^2(2\theta)$. Mass driven flavor conversions are therefore *flavor oscillations*. If the source or detector extension is much bigger than L_{osc}, or in general if the baseline L varies of an amount $\Delta L \gg L_{osc}$ the oscillatory term in eq. 1.2 averages out to $\frac{1}{2}$ and the experimental observable conversion probability becomes:

$$P_{\alpha\beta} = \frac{1}{2}\sin^2(2\theta) \tag{1.4}$$

Ordinary matter is not symmetric with respect to the lepton families, since electrons are present while muons and tauons are not. This implies that the propagation through matter introduces interaction potentials that distinguish ν_e from ν_μ and ν_τ, which in turn generate additional "effective mass" terms in the propagation Hamiltonian. In matter, the mass squared difference Δm^2_m and the mixing angle θ_m are in general different than those in vacuum. Both are a function of the electron density, N_e, and the flavor transition can have a resonant character for a specific value of N_e. In this case, for neutrinos crossing layers of matter of different density, it is also possible to observe an averaged conversion probability $P_{\alpha\beta} > \frac{1}{2}$, which is not allowed in vacuum (cf. eq. 1.4). Neutrino oscillations in matter are named MSW oscillations, from the name of the physicists Mikheyev, Smirnov and Wolfenstein, who

[1] In this simplified discussion complex phases are neglected

developed for the first time the required formalism and applied it to the case of solar neutrinos [Wol78, MS86].

Several independent experimental data give convincing evidence of mass driven neutrino flavor oscillations[2]: atmospheric-ν data point at $\Delta m^2_{atm} \sim 2.5 \times 10^{-3} eV^2$ with nearly maximal mixing; solar ν_e and reactor $\bar{\nu}_e$ experiments have now converged on $\Delta m^2_{sol} \sim 7 \times 10^{-5} eV^2$ and large non-maximal mixing $0.7 \lesssim \sin^2 2\theta_{sol} \lesssim 0.97$, while $\bar{\nu}_e$ oscillations in the range Δm^2_{atm} have not been observed, resulting in an upper limit $\sin^2 2\theta_{13} \lesssim 0.1$[3]. The different scales for Δm^2 and the smallness of the U_{13} parameter, which connects solar and atmospheric oscillations, justifies the simplification of assuming decoupled 2ν oscillations, used to derive eq. 1.3. The LSND positive signal implies ν - oscillations at a third mass squared difference scale $\Delta m^2_{LSND} \sim 1 eV^2$. If this evidence will be confirmed then three different scales for Δm^2 require 4 mass eigenvalues and hence a fourth neutrino. Since this neutrino is not observed in the $Z \to \nu\bar{\nu}$ decay and does not have a charged lepton partner, it have to be a *sterile* neutrino.

In this chapter the part of ν - oscillation evidence relevant to the solar neutrino sector, with the last developments from reactor anti-neutrinos, will be reviewed, with particular emphasis on the role of low energy solar neutrino detection in this context.

1.2 The Standard Solar Model and the Predictions for the Solar Neutrinos Fluxes

1.2.1 Introduction

A solar model is a thermodynamic description of the sun, aiming at understanding and predicting the most significant observables, at any radius and time. A "Standard Solar Model" (SSM) is a solar model that assumes that best available physics and the most accepted hypothesis. The description and information reported in this section are a brief summary based on refs. [Bah89, Cla83, Cas85], with updates from the most recent literature.

The SSM first assumes a perfect spherical symmetry (thus neglecting any effect from rotation and magnetic fields), which reduces the problem from three-dimensional to monodimensional: the free variables are time (measured from the sun's entrance on the *main sequence*) and radius (or, equivalently, fractional mass). The unknown functions are:

1. Mass or Radius: $M(r,t)$ or $R(m,t)$
2. Density: $\rho(r,t)$
3. Pressure: $P(r,t)$
4. Temperature: $T(r,t)$
5. Luminosity: $L(r,t)$
6. Chemical Composition: $X_i(r,t)$ (X_i chemical abundance of the i^{th} element)

[2]Strictly speaking, no unquestionable proof was yet found that the observed phenomena are *oscillations*: so far only neutrino flavor *conversions* have been observed, but no signature of an oscillatory behaviour, neither in energy nor in baseline, has been reported.

[3]The indices are chosen in a such a way that ν_e is predominantly a mixture of ν_1 and ν_2, solar oscillations involve Δm^2_{12} and θ_{12}, while atmospheric oscillations are driven by the mass difference between $m_1 \simeq m_2$ and m_3, with mixing θ_{23}.

The density can be expressed as the volume derivative of the mass function, which provides a first trivial differential equation. It is then assumed that the sun evolves slowly between states of "quasi-equilibrium". "Equilibrium" means that each elementary volume is subject to a nett null force, i.e. the pressure difference and the gravitational force must balance each other at any radius, otherwise the sun would rapidly collapse or expand (hydrostatic equilibrium). Also, the nett energy irradiated by any layer must be compensated by the energy produced in the layer, otherwise the sun would not maintain hydrostatic equilibrium (thermal equilibrium). These two conditions translate to differential equations for the pressure and luminosity gradients. In the latter a new function appears: the rate of energy production per unitary mass, $\epsilon(r,t)$. An additional differential equation expresses the mechanism of radiative energy transport in the star [4] and relates the temperature gradient to the local luminosity and to the *opacity* (see e.g. [Cla83] for a definition). It states that the energy flux is proportional to the temperature gradient and is inversely proportional to the opacity.

Finite equations must be added to solve the system: the pressure is given as $P(\rho, T, X_i)$ by an appropriate equation of state. The wavelength averaged opacity $\bar{\kappa}$ is expressed as $\bar{\kappa}(\rho, T, X_i)$ by adding the contributions of all the absorption, elastic and inelastic scattering processes of the electromagnetic radiation. Fixing the sun surface luminosity to the observed value, the higher the opacity, the higher the temperature gradient and hence the central temperature.

1.2.2 Nuclear Reactions

The condition of thermal equilibrium requires a source of energy able to compensate the radiative energy loss from the sun surface with a time scale consistent with its age. It was soon recognized [Edd20] that nuclear reactions, and in particular the fusion of 4 protons into a helium nucleus, is the only possible source. After preliminary pioneering studies [AH29] and the contribution of many physicists (e.g. [Wei37] and [Gam38]), H.A. Bethe [Bet39] proposed in 1939 the reaction chains leading to the formation of helium, which are still believed to power the sun and all the other *main sequence* stars: the *pp-chain* and the *CNO-cycle* (Fig. 1.1).

In the pp-chain the sequence is initiated by the weak interaction:

$$p + p \rightarrow {}^2H + e^+ + \nu_e \tag{1.5}$$

or, with lower probability (3-body interaction) by:

$$p + e^- + p \rightarrow {}^2H + \nu_e \tag{1.6}$$

In both cases, the deuteron rapidly absorbs a proton and is converted to ^3He. At this point the chain presents a branching: ^3He can either react with another ^3He (PP-I chain):

$${}^3He + {}^3He \rightarrow {}^4He + 2p \tag{1.7}$$

or with ^4He (this isotope was already present in the primordial cloud from which the sun formed and is continuously fed by the fusion chains):

$${}^3He + {}^4He \rightarrow {}^7Be + \gamma \tag{1.8}$$

[4] Energy transport through convection dominates over radiative transport in the outermost regions of the sun, for $R \gtrsim 0.7 R_\odot$

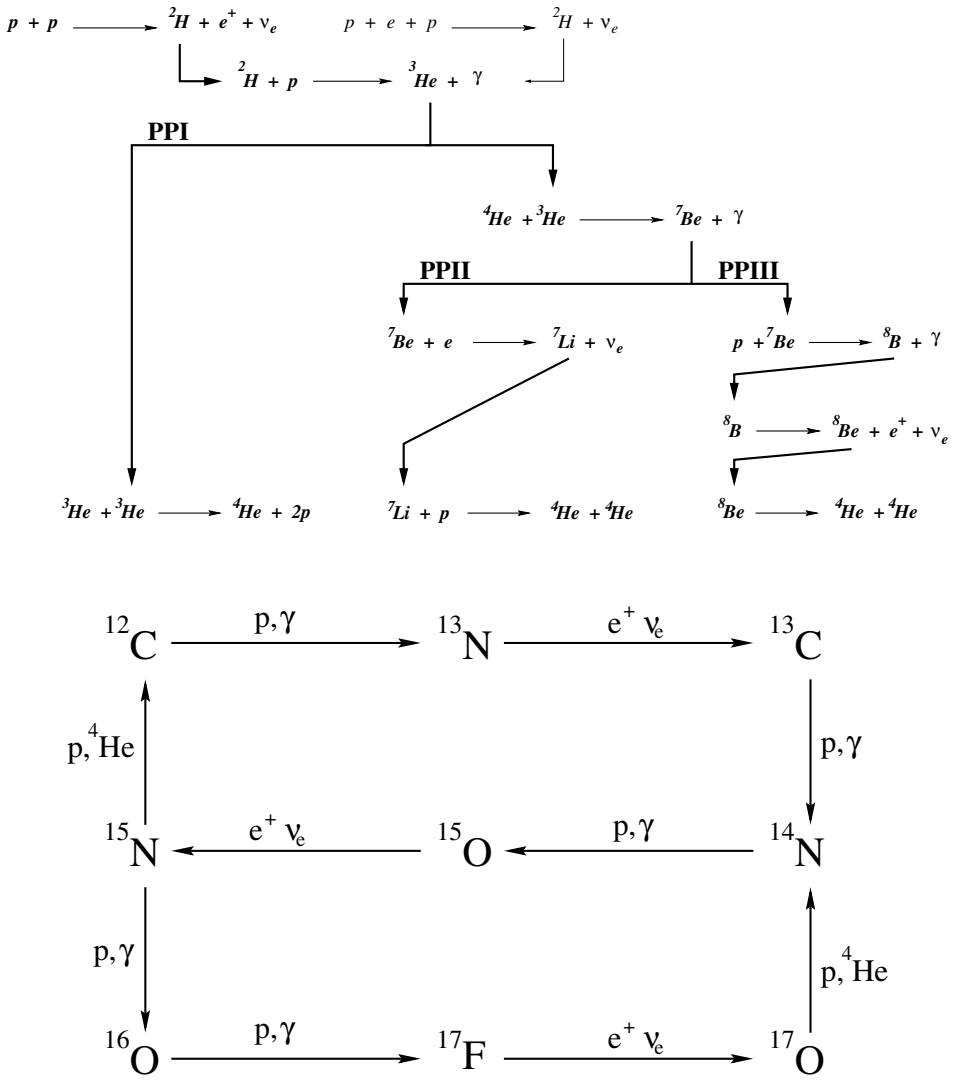

Figure 1.1: *The two nuclear reaction chains leading to the fusion of 4 protons into a helium nucleus: the "pp-chain" (top) and the "CNO-cycle" (bottom). Not shown in the figure is the very rare "hep" branching in the pp-chain (see table 1.2).*

In the latter case, ^7Be can in turn either capture an electron or absorb another proton:

$$^7Be + e^- \rightarrow {}^7Li + \gamma \tag{1.9}$$

$$^7Be + p \rightarrow {}^8B + \gamma \tag{1.10}$$

This second branching leads to the chain terminations PP-II and PP-III shown in Fig. 1.1. Whatever termination, after annihilation of the positrons, any pp-chain has the nett balance:

$$4p + 2e^- \rightarrow {}^4He + 2\nu_e + 26.731\,MeV \tag{1.11}$$

The same result is obtained in the CNO-cycle (Fig. 1.1), where carbon, nitrogen and oxygen simply act as catalysts for eq. 1.11. The energy production function $\epsilon(\rho, T, X_i)$ is calculated by adding the interaction rates of each fusion branching, times the average energy released per chain. This is the Q of equation 1.11 ($26.731\,MeV$) minus the mean kinetic energy carried by neutrinos, which escape the sun. The relative weight of the pp-chain compared to the CNO-cycle and of the terminations PP-I, PP-II and PP-III within the pp-chain is determined by the reaction rates at the branching, which in turn depend on element abundances (X_i) and specific nuclear cross sections. At the typical temperature of the sun core ($T \sim 1.5 \times 10^7 K$), the kinetic energy of the interacting particles are far lower than the Coulomb barrier, therefore the nuclear reactions proceed only due to quantum tunneling. As a consequence, the cross sections energy dependence is dominated by the exponential suppression factor of the tunneling probability. The center of mass energy of two interacting particles is statistically distributed according to the Maxwell-Boltzmann distribution, which is parametrized by T, so that the energy-averaged quantum penetration factor is a function of the temperature. The temperature dependence of the reaction rates is stronger the higher the Coulomb barrier, thus the higher the product of the reagent nuclear charges. This makes the predictions of the rates of the most "Coulomb-suppressed" reactions most uncertain.

1.2.3 Solution of a Solar Model

The time evolution of the sun is driven by the local changes of the chemical composition, which in turn are due to the effects of the nuclear reactions and element diffusion. A solar model is solved numerically by using all the available differential and finite equations for the unknown functions and by imposing proper border conditions for the functions specified by differential equations (table 1.1). The solution is then evolved iteratively in time, by calculating the expected local changes in the chemical composition. The last constraint is then added, i.e. that at a time equal to the solar age the actual sun observables (radius and luminosity) are reproduced. Table 1.1 shows the boundary conditions and the input parameters of the problem.

1.2.4 Predictions of the SSM

The solution of a solar model provides the radial profiles of all the unknown functions at any time, in particular $\rho(r,t)$, $T(r,t)$ and $X_i(r,t)$. Therefore it is possible to predict the present rates of all the nuclear reactions introduced above. It is found [BPB01, Tur01]:

- The pp-chain dominates the solar energy production, while the CNO-cycle is expected to contribute only $\sim 1.5\%$ of the total nuclear energy generation. This happens despite

Table 1.1: *Boundary conditions and input parameters of the SSM. The chemical composition is derived by spectroscopic measurement of the solar atmosphere (it is assumed that the sun entered the main sequence with homogeneous composition) and by chemical analysis of meteorites. The primordial abundance of helium is more difficult to estimate and is normally left as a free parameter of the model.*

Age	$t_\odot = 4.57 \times 10^9\, y$
Total Mass	$M(R_\odot) = M_\odot = 1.99 \times 10^{33}\, g$
Actual Radius	$R(t_\odot) = 6.96 \times 10^{10}\, cm$
Actual Electromagnetic Luminosity	$L(R_\odot, t_\odot) = L_\odot = 3.84 \times 10^{33}\, erg/s$
Effective Surface Temperature	$T_{eff}(R_\odot, t_\odot) = 5.78 \times 10^3\, K$
Border Conditions	$M(0) = 0;\ L(0) = 0;\ P(M_\odot) = 0;$
Primordial Chemical Composition	$X_i(t = 0)$

the fact that the pp-chain is initiated by a weak interaction (eq. 1.5 or 1.6), whereas the proton capture reactions in the CNO-cycle are all due to strong interactions. The higher Coulomb barriers (and, secondarily, the low CNO elemental abundance) more than compensate for the intrinsically lower probabilities of the *pp* and *pep* reactions. The CNO cycle takes over the pp-chain at a higher temperature and hence in more massive stars than the sun.

- The PP-I termination takes place in about 85% of the cases. The remaining $\sim 15\%$ of the chains is almost entirely terminated via the PP-II branch, while the PP-III termination is expected to occur only in about 0.02% of the cases. Again, the Coulomb barrier in eq. 1.10 is the decisive factor in the competition between PP-II and PP-III.

- The probability that ^2H is produced by the *pep* reaction (eq. 1.6) is expected to be $\sim 0.4\%$.

Solar Neutrinos The fusion of 4 protons into a helium nucleus (eq. 1.11) requires the transmutation of two protons into two neutrons, which occurs mediated by the weak interaction, with consequent emission of two electron neutrinos. Table 1.2 summarizes the neutrino-emitting weak processes of the nuclear fusion chains. For each complete pp-chain at least one *pp* (or *pep*) neutrino is emitted, while the second is specific of the termination: another $pp - \nu$ in the PP-I, a $^7Be - \nu$ in the PP-II or a $^8B - \nu$ in the PP-III termination.

Neutrino cross sections with matter at the typical solar energies (sub-MeV up to $\sim 15 MeV$), are so low that the sun is almost "transparent". Neutrinos travel out of the core of the sun, where they are produced, to the Earth without significant absorption or scattering. Therefore they bring direct information about the interior of the sun, otherwise unobservable via any other known form of radiation. The predictions of the SSM for the neutrino fluxes mirror the predictions for the reaction rates of the proton fusion chains: the *pp* neutrinos are the most abundant ($\sim 90.9\%$ of the total flux), followed by ^7Be ($\sim 7.3\%$), CNO (total $\sim 1.6\%$) and *pep* ($\sim 0.2\%$). Only about 0.008% of the predicted solar neutrino flux comes from the ^8B β-decay. In fact, the PP-III termination plays such a marginal role for the sun energetics that "switching off" the reaction 1.10 would not produce observable consequences. The uncertainties of the fluxes are calculated propagating the uncertainties of all the parame-

Table 1.2: *Weak processes in the pp-chain and CNO-cycle producing neutrinos and recent SSM predictions for the corresponding year-averaged ν fluxes [BPB01]. The hep reaction competes with the strong interactions ${}^3He + {}^3He \rightarrow {}^4He + 2p$ (PP-I termination) and ${}^3He + {}^4He \rightarrow {}^7Be + \gamma$ (PP-II and PP-III terminations), therefore the hep branching is very rare. The neutrinos produced in each reaction are named as the symbol of the reaction.*

Fusion Chain	Reaction	Symbol	SSM ν flux: $\Phi(1 \pm \sigma_\Phi/\Phi)(cm^{-2}s^{-1})$
PP	$p + p \rightarrow {}^2He + e^+ + \nu_e$	pp	$5.95 \times 10^{10}\,(1 \pm 0.01)$
PP	$p + e^- + p \rightarrow {}^2H + \nu_e$	pep	$1.40 \times 10^{8}\,(1 \pm 0.015)$
PP-II	${}^7Be + e^- \rightarrow {}^7Li + \nu_e$	${}^7Be$	$4.77 \times 10^{9}\,(1 \pm 0.10)$
PP-III	${}^8B \rightarrow {}^8Be + e^+ + \nu_e$	${}^8B$	$5.05 \times 10^{6}\ \left(1^{+0.20}_{-0.16}\right)$
PP-hep	${}^3He + p \rightarrow {}^4He + e^+ + \nu_e$	hep	9.3×10^{3}
CNO	${}^{13}N \rightarrow {}^{13}C + e^+ + \nu_e$	${}^{13}N$	$5.48 \times 10^{8}\ \left(1^{+0.21}_{-0.17}\right)$
CNO	${}^{15}O \rightarrow {}^{15}N + e^+ + \nu_e$	${}^{15}O$	$4.80 \times 10^{8}\ \left(1^{+0.25}_{-0.19}\right)$
CNO	${}^{17}F \rightarrow {}^{17}O + e^+ + \nu_e$	${}^{17}F$	$5.63 \times 10^{6}\,(1 \pm 0.25)$

ters of the model. Each flux is more sensitive to certain parameters (in particular the nuclear part of the specific reaction cross sections), however the uncertainties are rather dominated by the different degree of dependence of the fusion processes on the solar conditions and in particular on the temperature. The pp reaction is the basis of the solar nuclear power, which is required to be equal to the observed luminosity (thermal equilibrium, or "luminosity constraint"). Consequently, the $pp - \nu$ flux is predicted with a high accuracy ($\sim 1\%$). The ${}^7Be$ and ${}^8B$ fluxes are predicted with less precision (respectively $\sim 10\%$ and $\sim 20\%$), primarily because of the lower contribution to the sun energetics (the luminosity constraint is not effective) and (especially for ${}^8B$) the stronger dependence on T. Table 1.2 reports all of the SSM-predicted solar neutrino fluxes and their relevant uncertainties.

In Fig. 1.2 the solar neutrino spectrum is shown, decomposed in the single fluxes of table 1.2. The spectra are continuous in the energy interval $\left[0,\, Q - 2m_e c^2\right]$ (m_e rest mass of the electron) for the weak processes with three bodies in the final state; discrete lines for the electron-capture reactions, having two bodies in the final state. The two lines of the ${}^7Be$ spectrum correspond to the decay to the ground state of ${}^7Li$ ($\sim 90\%$ branching) and to the first excited state ($\sim 10\%$). It is important to note that the fundamental pp component of the solar neutrino flux has the lowest energy spectrum, and more than 99.99% of the total flux has energy below $2\,MeV$.

1.2.5 Helioseismology and the Robustness of the SSM

Sec. 1.4 will explain why solar neutrino detection did not provide directly the confirmation of the theoretical model of the sun. In fact, a thorough test of the SSM based on neutrino observations still need to be accomplished. Nevertheless, important progress has been made in the study of the solar seismic waves (*helioseismology*), observable on the solar surface as radial velocity oscillations. Only stationary waves can be detected, which are decomposed into spherical harmonics and compared with the predictions of the SSM. The result is that the SSM predicted sound speeds differ from the measured one of an average of 0.1%

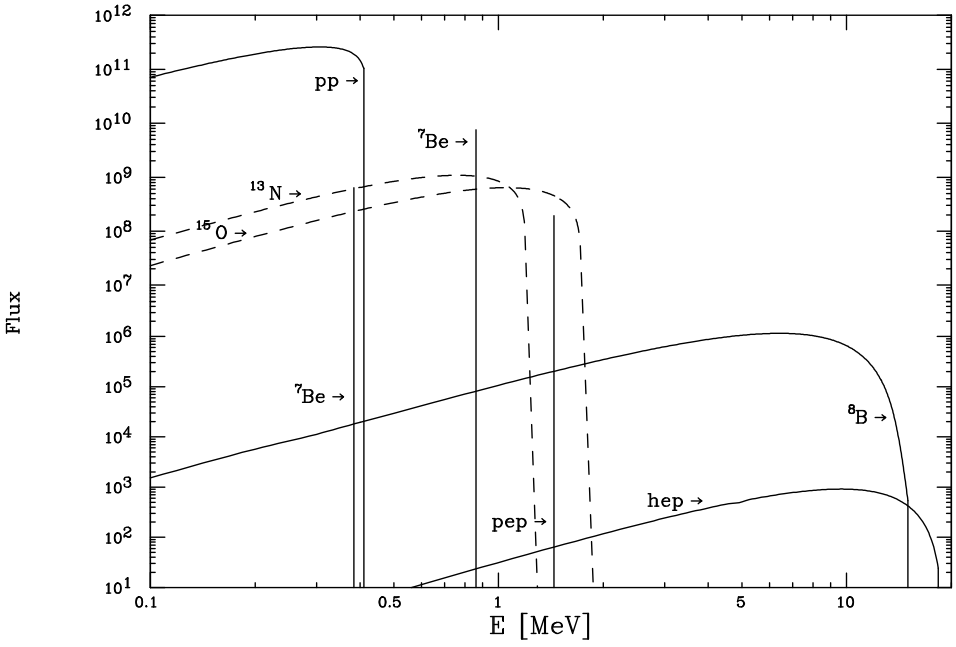

Figure 1.2: *Energy spectra of the solar neutrinos fluxes (from [Cas97]). The unit for the continuous sources is* $cm^{-2}\,s^{-1}\,MeV^{-1}$*, for the lines it is* $cm^{-2}\,s^{-1}$*. The end-point of the* $pp-\nu$ *spectrum is at* $\sim 420\,keV$*, the two* $^7Be-\nu$ *lines at* $384\,keV$ *and* $862\,keV$*.*

for all solar radii between $0.05R_\odot$ and $0.95\,R$, with a maximum difference of $\sim 0.35\%$ at $R \sim 0.7R_\odot$(corresponding to the transition from the radiative to the convective zone). In the internal region $[0.05R_\odot,\, 0.25R_\odot]$, where 95% of the nuclear energy and neutrino flux is produced, the departure of the model from the observations is $\lesssim 0.1\%$ and the rms is of the same order of magnitude of the experimental uncertainties of the helioseismologic data [BPB01]. The sound speed relative uncertainty is the sum of the relative uncertainties of temperature and mean molecular weight. Assuming no fine tuning cancellations, it follows that the SSM relative error for the latter two quantities (in particular the uncertainty of T) is of the same order of the relative error of the sound speed. It has been pointed out that such uncertainties imply errors on the solar neutrino fluxes of several percent or less [Bah97].

1.3 Solar Neutrino Detection

Solar neutrino detection is a challenging task, due to the very low interaction rates. Irrespective of the exploited detection technique, all experiments share some essential characteristics:

- **Large Masses**: due to the low neutrino cross sections at solar energies, large exposed target masses are required to obtain interaction rates of at least ~ 1 event per day. Solar neutrino experiments range from the multi-ton to the several kiloton scale.
- **Background Suppression**: because of the large detector masses and the small neutrino interaction probabilities, events from other natural sources producing signals not distinguishable from the neutrino signals have typically several order of magnitude higher

rates. The background is first reduced by choosing an underground location for the experiment, so that a substantial fraction of the cosmic rays is shielded. Cosmic rays originate background events by direct interaction in the detector, but also through secondary particles, spallations, etc. The "external background" due to the natural radioactivity of the surrounding rocks and to the remaining cosmic rays is suppressed by shielding the sensitive volume with active veto systems and/or passive high-density shielding. In large volume targets with spatial reconstruction capability, the external background can be further decreased by imposing a "fiducial volume cut", i.e. rejecting events originating from the outermost fraction of the sensitive volume (self-shielding). The "internal background" due to radioactive trace impurities in the target mass, such as the primordial ^{238}U, ^{232}Th (including for both the progenies),^{40}K, the cosmogenic ^{39}Ar and ^{14}C, or the man-made ^{85}Kr, can still overwhelm the low neutrino signal. Before construction, all components of the detectors must be screened for their specific concentrations of radioactive contaminants and carefully selected. The development of on-line and off-line purification techniques is also part of the experimental concept of most solar neutrino detectors. A review about low-background techniques can be found in [Heu95] and for further specific applications see [Bor98]. The spectrum of the residual background is higher the lower the energy. For this reason the detection of low energy neutrinos is particularly challenging, especially in case the neutrino events have no distinctive signatures.

The measurement of solar neutrinos has been pursued following three main detection principles:

1. Inverse Electron-Capture
2. Electron-Scattering
3. Disintegration of Deuterium

These are discussed in the three following subsections, where all the past and running experiments that have implemented those detection principles are briefly described. The results of these experiments and their implications will be discussed next, in Sec. 1.4, while Sec. 1.5.2 is devoted to a review of the proposed future experiments for the detection of low energy solar neutrinos.

1.3.1 Inverse Electron-Capture

As first proposed in 1946 by B. Pontecorvo [Pon46], electron neutrinos can interact with a suitable target nucleus via a charge current process, which is the inverse of the nuclear EC reaction:

$$\nu_e + {}^{A}_{Z}X \rightarrow {}^{A}_{Z+1}Y + e^- \tag{1.12}$$

Depending on the lifetime and decay-mode of the neutrino-produced ${}^{A}_{Z+1}Y$ nucleus, the reaction can be exploited through two experimental techniques: radiochemical and real-time.

Radiochemical Experiments

In radiochemical experiments a large target mass is "exposed" to solar neutrinos for a sufficiently long time that the products of eq. 1.12 can accumulate in the detector in measurable quantity. The key issue is that the change of one unit in the atomic number leads to different chemical properties, so that the few ν-produced atoms can be extracted from the target with high efficiency in a reasonably short time and subsequently counted by observing their β or EC decay. Important technical requirements for a radiochemical target are:

1. Lifetime of the product nucleus long enough that only a small fraction decays during the chemical extraction and counter filling ($\tau \gtrsim 1\,d$), but sufficiently short that the ν-induced exponential activity can be statistically separated from the constant background ($\tau \lesssim 1\,y$)

2. High isotopic abundance, to minimize the detector mass and hence costs and backgrounds

3. Low interaction threshold, so that a large part of the solar neutrino spectrum can be probed

4. Interaction cross section known with adequate precision

Two such target isotopes have been successfully used for neutrino detection in three experiments: ^{37}Cl in the pioneer Homestake experiment, ^{71}Ga in the SAGE and GALLEX-GNO experiments.

Homestake The chlorine experiment [Dav68] (1970-1994) was located at the Homestake Gold Mine (Lead, South Dakota, USA) in an underground facility at a depth of $1478\,m$, 4200 m.w.e. (m.w.e. = "meters of water equivalent"). It consisted of a steel tank filled with 615 tons of tetrachloroethylene (C_2Cl_4), corresponding to 133 tons of the target isotope ^{37}Cl. Neutrino detection is based on the reaction $^{37}Cl(\nu_e,\, e^-)\,^{37}Ar$, which has an energy threshold of $814\,keV$. The signal is expected to be dominated by the ^8B flux, with good sensitivity to ^7Be and some sensitivity to CNO and *pep* neutrinos (table 1.3). ^{37}Ar has a lifetime of 50.5 days and decays by EC, giving as a measurable signal a $2.82\,keV$ Auger electron from the ^{37}Cl atomic de-excitation. After $\sim 100\,d$ exposure time, the tank is flushed with helium, which sweeps along ^{37}Ar and a macroscopic amount of stable Ar isotope, added to serve as a carrier and to determine, at the end of the process, the overall extraction efficiency. Argon is then mixed with a counting gas and introduced in miniaturized proportional counters. These are measured for several months, to allow the complete decay of ^{37}Ar and a precise estimation of the background. Finally, the neutrino interaction rate is determined by fitting the data with an exponential activity plus a constant background. The procedure described is repeated cyclically to improve the statistical accuracy of the results and to study the time dependence of the neutrino rate.

SAGE and GALLEX-GNO SAGE (1990 -) [SAG99b] and GALLEX-GNO (1991 -) [GAL92] use the reaction $^{71}Ga(\nu_e,\, e^-)\,^{71}Ge$. The former utilizes $\sim 50\,t$ of natural gallium (39.9% ^{71}Ga i.a.) in pure metallic form (liquid above $30°C$), the latter $30.3\,t$ in $100.9\,t$ of a $GaCl_3 - HCl$ solution. The threshold for ν - capture in ^{71}Ga in only $233\,keV$, hence gallium

Table 1.3: *SSM predicted neutrino capture rates in ^{37}Cl and ^{71}Ga, decomposed in the contributions of the single neutrino fluxes (ref. [BPB01]). The signals are given in SNU (Solar Neutrino Units), where 1 SNU is defined as one neutrino capture per second in 10^{36} target atoms.*

Source	S_{Cl} (SNU)	S_{Ga}(SNU)
pp	-	69.7
pep	0.22	2.8
hep	0.04	0.1
^{7}Be	1.15	34.2
^{8}B	5.76	12.1
^{13}N	0.09	3.4
^{15}O	0.33	5.5
^{17}F	0.0	0.1
Total	$7.6^{+1.3}_{-1.1}$	128^{+9}_{-7}

gives sensitivity to the $pp-\nu$ flux. In fact, the SSM predicts that more than the half of the signal is due to pp neutrinos, and the second most important contribution comes from ^{7}Be (table 1.3). GALLEX-GNO and SAGE are still the only experiments which have measured the most abundant and fundamental solar neutrino flux.

SAGE (Soviet-American Gallium Experiment) is located in the Baksan underground laboratory, Caucasus, Russia (depth $\sim 2000\,m$, 4700 m.w.e.); GALLEX (GALLium EXperiment) and its successor GNO (Gallium Neutrino Observatory) in the Gran Sasso underground laboratory, Italy (depth $\sim 1400\,m$, 3300 m.w.e.).

After an exposure time of 3 to 6 weeks the radioactive ^{71}Ge and a stable carrier are extracted from the target, synthesized as GeH_4. The GeH_4 is mixed with Xe and introduced in miniaturized low-background proportional counters [Win93]. In SAGE the extraction of germanium from the metallic gallium involves several chemical steps, while in GALLEX-GNO germanium is directly available in the form of $GeCl_4$. This is highly volatile in an acidic environment and is swept along by flushing the target solution with N_2. ^{71}Ge has a lifetime of 16.49 days and decays by EC. The subsequent atomic de-excitation of ^{71}Ga leads predominantly to an energy deposition of $\sim 10\,keV$ ("K peak") or $\sim 1\,keV$ ("L peak"). Each proportional counter is measured continuously for ~ 6 months and regularly calibrated with external sources. Energy selection and pulse shape discrimination are employed to improve the signal-to-background ratio.

Real-Time Experiments

In the radiochemical experiments the neutrino interaction is not detected in real time, but only through the subsequent decay of the radioactive product nuclei. As a consequence, no information is available on the energy of the interacting neutrino and only the integral rate above the threshold of eq. 1.12 can be measured. However, the inverse-EC process offers also the potential for a spectroscopic and real-time measurement of the solar neutrino flux, with the on-line detection of the prompt electron in eq. 1.12. Due to kinematics, the energy carried by the electron is nearly equal to the incoming neutrino energy minus the Q of the reaction, so that the spectroscopy of the inverse-EC electron relates directly to the spectroscopy of

the solar neutrino flux. This technique is considered only for very low Q-values, such that the CNO, *pep*, ^7Be and possibly *pp* fluxes are observable, since the real-time and energy resolved measurement of the ^8B flux has been successfully accomplished via the use of other techniques (see next sections and Sec. 1.4). In this case the background from natural-occurring radio-isotopes and cosmic-rays-induced events is very challenging. Backgrounds are however suppressed if it is required that ν interactions either produce a nucleus that β-decays with a short lifetime, or populate an isomeric state that subsequently decays with the emission of one or more gammas [Rag76]:

$$\begin{aligned} \nu_e + {}^{A}_{Z}X &\rightarrow {}^{A}_{Z+1}Y^* + e^- \\ {}^{A}_{Z+1}Y^* &\rightarrow {}^{A}_{Z+1}Y + \gamma s \end{aligned} \tag{1.13}$$

The coincidence of prompt electron and delayed gammas provides a "tag" that can reduce the background of several orders of magnitude. Target nuclei suitable for interactions of the kind of eq. 1.13 have been experimentally investigated within the LENS project (Chapter 2).

A common feature of the experiments based on neutrino capture on nuclei is that they are all based on a charge current interaction and are thus flavor specific, since only electron neutrinos can be detected. Another common aspect is that the expected interaction rates are estimated by combining the SSM-predicted ν spectra with the theoretical calculation of the interaction cross sections, $\sigma(E)$. Ground-to-ground state ν-induced transitions benefit from the measurement of the inverse decay, which provides the nuclear matrix element of the transition. In this case the accuracy of the theoretical calculation of the cross section is typically a few percent. If the transition to excited states are important or even dominant, as in the case of the real-time targets of eq. 1.13, the nuclear matrix element is inferred through (p, n) or $\left({}^3He, t\right)$ reactions. Such determinations lead to a systematic uncertainty of the order of 10% - 20% in the expected ν interaction rate. In this case, dedicated experiments for the measurement of the cross section with intense artificial ν sources are often considered.

1.3.2 Elastic Scattering off Electrons

Neutrinos can be detected via elastic scattering off an electron:

$$\nu_x + e^- \rightarrow \nu_x + e^- \tag{1.14}$$

where ν_x is a neutrino belonging to any of the three active lepton families. In fact, the elastic-scattering process (ES) can be mediated by the exchange of either a $W^{\pm}$ or a Z_0 boson. The former case is prerogative of the ν_e, whereas neutral current scattering occurs with equal amplitudes for ν_e, ν_μ and ν_τ. At solar neutrino energies, the electron-scattering cross section for $\nu_{\mu,\tau}$ is a factor of ~ 6 smaller than for ν_e, nevertheless the weak sensitivity of this process to $\nu_{\mu,\tau}$ is important in the context of neutrino flavor-oscillations. Compared to the inverse-EC interaction, the total cross section for ES is very well known, because it can be calculated with high precision in the frame of the the electro-weak theory. Another advantage of the ES is its directionality: the angular distribution of the recoil electron is "forward" peaked relative to the direction of the incoming neutrinos, hence radially away from the sun. If the detector has tracking capabilities, signal and isotropic background can be separated on a statistical basis. Eq. 1.14 has no physical threshold, but since the neutrino signal has no distinctive signatures, except for the directionality, the high background at low energies imposes an analysis threshold

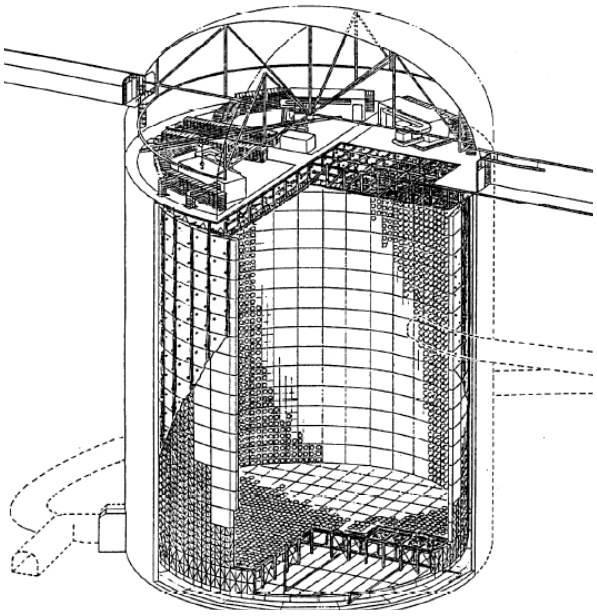

Figure 1.3: *Drawing of the SuperKamiokande detector.*

on the energy of the recoil electron. So far, ES detection has been implemented only in water Cherenkov detectors: Kamiokande, SuperKamiokande and SNO. In the next paragraphs the two Japanese detectors are briefly described. SNO will be treated separately in Sec. 1.3.3.

Kamiokande and SuperKamiokande Kamiokande [Kam96] (1987 - 1995) was located in the Kamioka mine ($200\,km$ west of Tokyo, Japan), at a depth of $\sim 1000\,m$ (2700 m.w.e.) and consisted of a cylindrical pool with $3000\,t$ of ultra-pure water exposed to 948 PMTs. Charge particles were revealed in real time through the detection of their Cherenkov light. The detector was originally designed to investigate nucleon decay and only in a later phase modified for solar neutrino observations, after an upgrade that involved careful water purification from natural radioactive contaminants, and the introduction of an external anti-coincidence detector. For the neutrino measurement only a fiducial volume of $680\,t$ was used, and the threshold on the recoil electron was set at $7\,MeV$, corresponding to a threshold of $\sim 7.5\,MeV$ for neutrinos. Thus only a portion of the ^8B neutrino flux was accessible, with additional sensitivity to the rare, high energy $hep - \nu$. The reconstruction of the Cherenkov light cone from the recoil electron gave an angular resolution of $\pm 28°$for the direction of the incoming neutrino.

The great success of Kamiokande promoted the construction of a larger and improved detector. SuperKamiokande [SK99] (1996 -) is also located in the Kamioka mine. The detector (see Fig. 1.3) is a cylinder $41.4\,m$ high with a diameter of $39.3\,m$, divided in two coaxial volumes. It is filled with $50\,kton$ of pure water, $32\,kton$ in the inner detector, $18\,kton$ in the outer detector, which serves as an active muon-veto. The fiducial volume is defined as the innermost $22.5\,kton$. The inner volume was watched by 11146 $50 - cm$ PMTs[5] . The

[5]An accident in November 2001 during water refilling after a maintenance period has destroyed about 8000 PMTs. The detector has been promptly rebuilt and restarted in 2002 with about 47% of the initial PMT coverage.

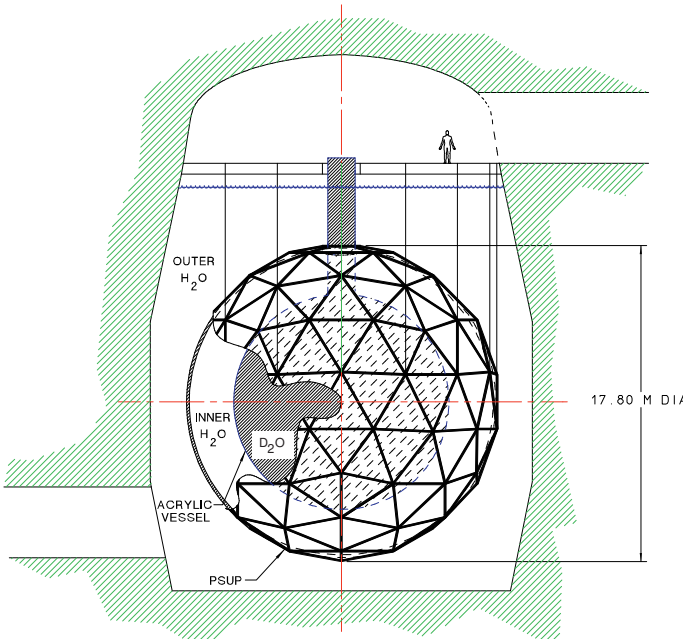

Figure 1.4: *Schematic view of the SNO detector.*

detection principle is the same as in Kamiokande, with 33 times larger fiducial volume and a neutrino energy threshold decreased to $\sim 5 MeV$.

1.3.3 Disintegration of Deuterium

Deuterium is a very attractive target for solar neutrino detection, because it offers two independent reaction channels:

$$\nu_e + D \rightarrow p + p + e^- \; E_\nu > 1.4\, MeV \tag{1.15}$$

$$\nu_x + D \rightarrow \nu_x + p + n \; E_\nu > 2.2\, MeV \tag{1.16}$$

eq. 1.15 is essentially the inverse-EC interaction studied in Sec. 1.3.1, which here leads to the unbound pp system. This reaction is due to a charge current process (CC), thus it is only sensitive to electron neutrinos. Eq. 1.16 is inelastic neutrino scattering which breaks up the deuterium nucleus. It is a neutral current interaction (NC), with a flavor-independent cross section. Therefore this reaction measures the total solar neutrino flux above threshold, irrespective of the the flavor content (provided active). Neutrino detection by deuterium disintegration has been implemented in the SNO experiment.

SNO SNO [SNO00] (Subdury Neutrino Observatory) is a heavy water Cherenkov detector located in the Creighton mine, near Subdury, Ontario, Canada ($2073\, m$ underground, 6010 m.w.e.). The core of the detector is a $12\, m$ spherical acrylic vessel filled with $1\, kton$ of D_2O (Fig. 1.4). This is surrounded by a geodesic structure, to which 9456 $20 - cm$ PMTs are mounted. The volume outside the vessel is filled with $1.7\, kton$ of ultra-pure light water. SNO detects neutrinos with reaction 1.15 by measuring the Cherenkov light emitted by the electron,

with an analysis threshold of $5\,MeV$ for the electron energy. As pointed out in Sec. 1.3.1, the neutrino energy spectrum (in this case for the ^8B component) is also measured. The NC interactions (eq. 1.16) are revealed by detecting the neutron from the deuterium disintegration. In the first phase of SNO pure heavy water was used and neutrons were detected via the $6.25\,MeV$ gamma cascade following the capture in deuterium. In the second phase, about $2.7\,t$ of salt ($NaCl$) was added to enhance the neutron detection efficiency through capture on ^{35}Cl, which has a higher absorption cross section for thermal neutrons and gives rise to a higher energy gamma cascade ($\sim 8.6\,MeV$). In the last phase, the salt was removed and ^3He proportional counters are being deployed, so that the NC detection is completely independent of the other ν signals and performed on a event-by-event basis rather than statistically. SNO detects neutrinos also through ES (eq. 1.14), with similar technique as Kamiokande and SK. The ES channel provides lower statistics than the CC and NC reactions, nevertheless the strong directionality of the recoil electrons allows a clear extraction of this signal, which provides an important consistency check for the other two reaction channels.

1.4 Solar neutrinos: an Historical Retrospective

The original motivation of the pioneers of the solar neutrino research was to look into the interior of the sun to test directly the theory of solar energy generation. Nevertheless the field turned out to be even more interesting than this. After a long phase of serious and controversial disagreement between experimental results and theoretical predictions it was finally understood that it was not the "source", but rather the "messengers" that behave unexpectedly. Solar neutrino observations have eventually revealed new properties of neutrinos that deeply impact our understanding of the elementary particles and their interactions and have important implications for cosmology. In this section the history of solar neutrino detection and its implications are reviewed.

1.4.1 The Pioneer Homestake Experiment and the Birth of the "Solar Neutrino Problem"

In 1946 B. Pontecorvo suggested the possibility of using ^{35}Cl to detect solar neutrinos [Pon46], but only in 1964, after the first calculation of the expected detection rate was carried out and an experimental concept established, R. Davis and J. Bahcall published a proposal [BD64]. The Homestake chlorine experiment started data-taking in its final configuration in 1970 and measured the ν interaction rate for 26 years. It was soon clear that the observed rate was much lower than the SSM expectation, about 1/3. The Homestake final result is [Hom98]: $R_{Cl}^{exp} = 2.56 \pm 0.16(sys) \pm 0.16(stat)\,SNU$, compared to the SSM prediction [BPB01]: $R_{Cl}^{SSM} = 7.6^{+1.3}_{-1.1}\,SNU$. This conflict was named the *Solar Neutrino Problem* (SNP).

Since more than 3/4 of the chlorine signal is expected to come from the ^8B flux (see table 1.3), most of the observed deficit had to be attributed to this component, while only upper limits could be given for the $^7Be - \nu$ and CNO fluxes. Already in 1968 Gribov and Pontecorvo suggested that the interaction rate observed in Homestake could be reduced due to neutrino flavor transitions [GP69], but at that time there was no great trust in the SSM calculations and the neutrino deficit was rather given astrophysical explanations: the ^8B was not predicted with great accuracy and its dependence on the solar core temperature is extremely strong. Several alternative "non standard" solar models were developed (see [Bah89]), all trying to reduce the sun core temperature, thus reproducing the Homestake results.

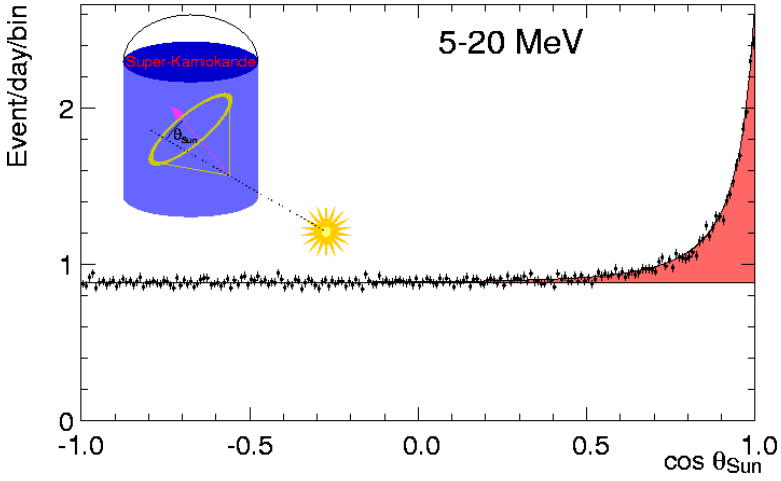

Figure 1.5: *Distribution of the reconstructed electron direction for the full SK statistics (1496 days). The points with error bars represent the measured rates, the gray histogram is the best fit solar signal plus background. The abscissa is given in* $cos\theta_{sun}$*, where* θ_{sun} *is the angle with respect to the vector sun-to-SK. The first evidence of the solar origin of the neutrino signal was given by Kamiokande.*

1.4.2 Kamiokande and the Second Solar Neutrino Problem

Kamiokande was the first real time neutrino detector and, because of the directionality of the ES reaction and the Cherenkov light, was also the first to confirm that the detected neutrinos did come from the sun (see Fig. 1.5 with the last update of the SK data). Kamiokande data were easier to interpret, since the high threshold allowed only the detection of $^8B - \nu$, plus a negligible contribution of the $hep - \nu$. Kamiokande's result, $\Phi_{Kam}^{^8B-\nu} = (2.82^{+0.25}_{-0.24} \pm 0.27) \times 10^6\, cm^{-2}s^{-1}$ [Kam96], showed that the observed ^8B flux was about 50% of the SSM expectation. On one hand this reinforced the Homestake evidence of a solar neutrino deficit, on the other hand raised new questions: the ^8B flux measured by Kamiokande would have produced in Homestake, alone, a higher signal than observed. There was no room for $\sim 1.8\, SNU$ from ^7Be and the other contributions, thus Homestake and Kamiokande appeared in conflict not only with the SSM, but also with each other.

1.4.3 GALLEX: First Observation of *pp*-Neutrinos and Indirect Evidence of Neutrino Flavor Conversion

The experimental solar neutrino data available until 1992 were mostly based on the observation of the ^8B flux, which is totally insignificant for the solar energy balance (see Sec. 1.2.4) and very much model-dependent. It was essential to test the theoretical understanding of the sun with the most abundant, fundamental, and robustly predicted $pp - \nu$ flux. This task was accomplished by GALLEX and SAGE.

GALLEX has provided the first observation of *pp* neutrinos[6] [GAL92]. The first published interaction rate was $R = (83 \pm 11)\, SNU$. This result was more than 3σ away from the SSM

[6]SAGE released data before GALLEX, however the first published results were consistent with the non-observation of a solar neutrino signal [SAG91].

prediction, however it gave the first experimental evidence that the sun primary source of energy is the *pp* nuclear chain.

The last update of the combined GALLEX-GNO result is: $R = [69.3 \pm 4.1(stat) \pm 3.6(syst)]\, SNU$ [GNO03]. SAGE finds $R = \left[69.2^{+4.3}_{-4.2}(stat)^{+3.8}_{-3.4}(syst)\right]\, SNU$ [SAG02], which is in good agreement with GALLEX. Both gallium experiments are not consistent with the SSM predictions: $R^{SSM}_{Ga} = 128^{+9}_{-7}$ [BPB01].

The measured interaction rate is about equal to the expected $pp-\nu$ contribution. The ^8B flux measured by Kamiokande should add $\sim 6\, SNU$ (Table 1.3), and there is no room for the other components, especially for the ^7Be flux. The gallium results ruled out any astrophysical explanation of the SNP, since:

1. no alternative solar models could explain the data
2. it was shown that chlorine, water-Cherenkov and gallium experiments were inconsistent with each other on a solar-model-independent basis, with the unique assumption of the luminosity constraint (see e.g. [BKS99])

Speculations on the reliability of the radiochemical technique were refuted by a two-fold test performed by GALLEX [GAL98]: the detector was exposed twice to an intense artificial ^{51}Cr ν-source and underwent a ^{71}As test at the end of data-taking[7]. The combined result of the two ^{51}Cr irradiations was $R = 0.93 \pm 0.08$ (where R is the ratio between measured and predicted signal), showing that GALLEX response to neutrinos is consistent with the expectations[8]. The ^{71}As test gave $R = 1.00 \pm 0.01$ and thus demonstrated that the ν-produced ^{71}Ge is recovered as expected.

The GALLEX results, combined with those of the other experiments and with the excellent agreement of the SSM with helioseismology (Sec. 1.2.5) provided a strong evidence, though indirect, that the SNP must be explained by postulating new neutrino physics (see [Kir99] for a review). The simplest solution was that neutrinos undergo mass-driven flavor-oscillations, as described in Sec. 1.1. If neutrinos oscillate between the three known active families on the path from the core of the sun to the Earth, the electronic content will be depleted in favor of the other two. Neutrino oscillations can explain simultaneously all the observed deficits because: 1) the ν_e surviving probability is in general energy dependent; 2) $\nu_{\mu,\tau}$ contribute no signal in the CC experiments and a weaker signal in the ES experiments.

The global fit of all the measured solar neutrino rates with the model of flavor oscillations (either in vacuum and in matter) left distinct regions in the oscillation parameter space emerge (Fig. 1.6). They were called SMA (Small Mixing Angle), LMA (Large Mixing Angle), LOW (low mass square difference) and VAC (vacuum oscillations). For the SMA, LMA and LOW solutions, the MSW effect is dominant.

1.4.4 SuperKamiokande: the Era of High Statistics

With SuperKamiokande the solar neutrino physics entered a new era of high statistics and precision measurements. SK provided an unprecedented amount of data on the high energy solar neutrinos, which have strongly constrained the oscillation scenarios. The measured integral interaction rate is: $\Phi^{8B-\nu}_{SK} = (2.348 \pm 0.025^{+0.075}_{-0.066}) \times 10^6\, cm^{-2} s^{-1}$, corresponding to

[7] ^{71}As decays by EC/β^+ to $^{71}Ge (t_{1/2} = 2.72\, d)$, with a kinematic that mimics the $^{71}Ga(\nu_e, e^-)^{71}Ge$ process.
[8] SAGE was irradiated with a ^{51}Cr source, too. The result is $R = 0.95^{+0.11\,+0.06}_{-0.10\,-0.05}$ [SAG99a].

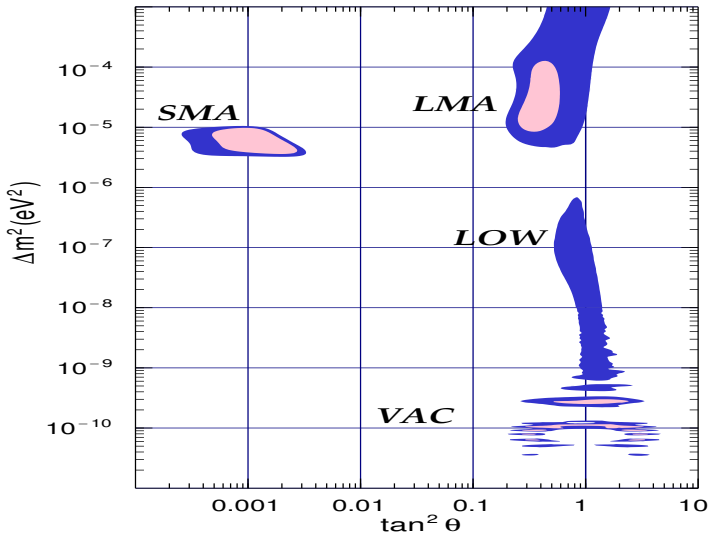

Figure 1.6: *The oscillation solutions consistent with the gallium, chlorine and water-Cherenkov interaction rates (from ref. [GFM00]). The light-shaded regions correspond to* 2σ *confidence, the dark-shaded to* 3σ.

22400 ± 800 observed neutrinos, about 46% of SSM [SK02]. Beside integral information, SK data have been used to produce several "differential" distributions, which have excluded or strongly disfavored large regions of the oscillation parameter space shown in Fig. 1.6. The different solutions have distinctive signatures, many at reach of the SK sensitivity:

- **Spectral Distortions**: the ν_e survival probability is a function of the energy. Most of the VAC and SMA solutions predict distortions of the ^8B energy spectrum compared to the predicted shape above the SK threshold.

- **Earth Regeneration Effects**: in the MSW scenario, neutrinos flavor-converted inside the sun can be "regenerated" as ν_e in the interior of the Earth [CHRV86]. The efficiency of Earth flavor regeneration depends on oscillation parameters and ν energy. At SK energies, the SMA solution predicts a higher ν_e flux when neutrinos have to cross the Earth core (MSW resonance at high density). The low-LMA and high-LOW regions predict a measurable night rate enhancement with no zenith-angle dependence (low density resonance).

The SK energy spectrum shows no distortions, no significant day-night rate asymmetry and no zenith-angle dependence at night. These results exclude (or strongly disfavor) the VAC (spectral distortions) and SMA (spectral distortions and zenith-angle modulation) scenarios and shrink the allowed parameter space for the LMA and LOW solutions [SK02].

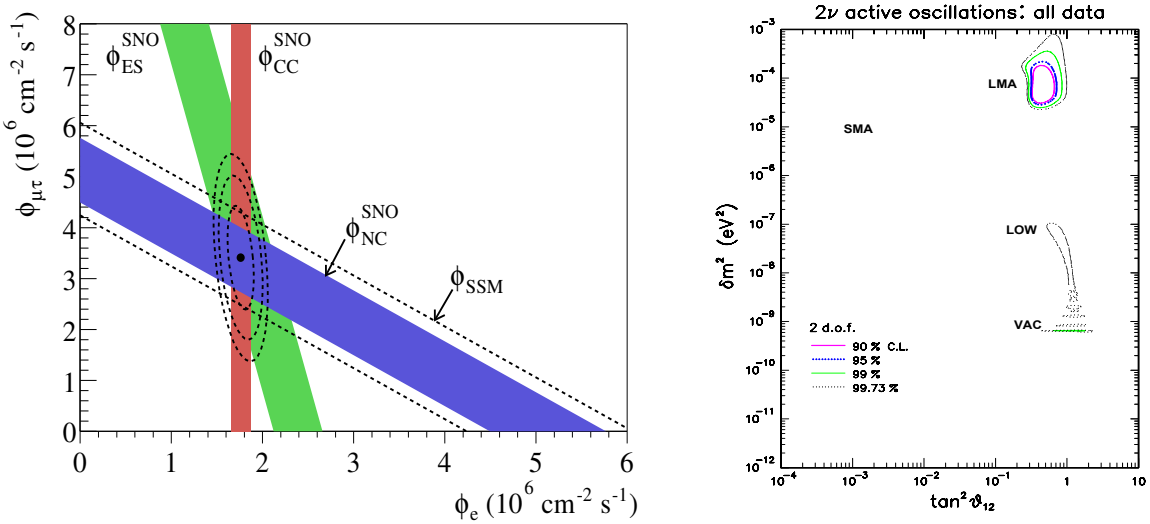

Figure 1.7: *Left: flux of ν_e vs. $\nu_{\mu,\tau}$ for the ^8B energy range deduced from the SNO results in eq. 1.17. Each solid band represents one of the SNO measurements, after a change of variable from CC, NC, ES rates to ν fluxes. The diagonal bands show the total B^8 flux as predicted by the SSM (dashed lines) and that measured with the NC reaction in SNO (solid band). The intercepts of all the bands with the axes represent the $\pm 1\sigma$ errors. The fact that all the bands intersect in a small region indicate that the three measurements are consistent with each other and with the hypothesis of $\nu_e \to \nu_{\mu,\tau}$ conversion.*
Right: global fit to all solar neutrino data after SNO (2ν oscillation to active flavors, figure from [Fog02]). The SMA solution has disappeared, while solutions other than the LMA appear only at very low confidence level.

1.4.5 SNO: First Direct Evidence of Solar Neutrino Flavor Conversion

The published final result of the SNO pure heavy water phase, given in units of $10^6 cm^{-2} s^{-1}$ ν_e equivalent flux is [SNO02]:

$$\begin{aligned}
\phi_{CC}^{SNO} &= 1.76^{+0.06}_{-0.05}(stat.)^{+0.09}_{-0.09}(syst.) \\
\phi_{ES}^{SNO} &= 2.39^{+0.24}_{-0.23}(stat.) \pm 0.12(syst.) \\
\phi_{NC}^{SNO} &= 5.09^{+0.44}_{-0.43}(stat.)^{+0.46}_{-0.43}(syst.)
\end{aligned} \tag{1.17}$$

The above fluxes are extracted by a global likelihood fit of the energy, direction and radial position distributions for all the events above threshold. Eq. 1.17 is the first direct, solar-model independent proof that solar ν_e undergo flavor conversion to the other active species $\nu_{\mu,\tau}$. The comparison of CC, and NC gives evidence for the presence of flavors other than electron in the solar neutrino flux (the no-conversion scenario is rejected at $> 5\sigma$). The ES rate is in good agreement with SK (statistics is limited due to the low target mass) and is consistent with the CC and NC rates (Fig. 1.7). The results in eq. 1.17 have also important astrophysical implications: the NC reaction gives the first unambiguous determination of one of the solar neutrino fluxes (assuming that ν_e converts exclusively to $\nu_{\mu,\tau}$) and the measurement is in good

agreement with the SSM prediction. In Sept. 2003 the SNO collaboration has released the first data of the salt-phase [SNO03]:

$$\begin{aligned}
\phi_{CC}^{SNO} &= 1.59^{+0.08}_{-0.07}(stat.)^{+0.06}_{-0.08}(syst.) \\
\phi_{ES}^{SNO} &= 2.21^{+0.31}_{-0.26}(stat.) \pm 0.12(syst.) \\
\phi_{NC}^{SNO} &= 5.21 \pm 0.27(stat.) \pm 0.38(syst.)
\end{aligned} \tag{1.18}$$

Eqs. 1.17 and 1.18, together with the data on the energy spectrum and day-night asymmetries [SNO02], set further constraints for the global oscillation analysis: at 3σ level only the LMA, LOW and a small part of the VAC solutions are allowed and the LMA is strongly favored (Fig 1.7).

1.4.6 KamLAND and the LMA Solution

Nuclear reactors are an intense source of $\bar{\nu}_e$ from the β-decays of the fission products, with typical energies of up to several MeV. The detection of $\bar{\nu}_e$ is based on the inverse - β reaction on protons:

$$\bar{\nu}_e + p \rightarrow n + e^+ \ (E_{\bar{\nu}_e} > 1.8\, MeV) \tag{1.19}$$

The signal is given by the prompt e^+ in coincidence with the γ emission following the subsequent neutron capture. The delayed tag is a good experimental tool for "low-background" $\bar{\nu}_e$ detection. Folding the calculated $\bar{\nu}_e$ spectrum with the interaction cross section, it is found that the expected $\bar{\nu}_e$ detected spectrum has a broad peak around $\sim 3\, MeV$. Given this range of energy and considering the 2ν oscillation scenario, eq. 1.3 fixes the relationship between Δm^2 and the vacuum oscillation length, L_{osc}. If $L_{osc} \sim L_{det}$ (L_{det} distance reactor to detector), then $\bar{\nu}_e$ oscillations to $\bar{\nu}_{\mu,\tau}$ are observable. In the past, several experiments at short ($\lesssim 100m$) and middle ($\sim 1km$) baseline have searched for $\bar{\nu}_e$ disappearance, in all cases reporting rates and spectra consistent with a null effect, thus setting only limits on $\bar{\nu}_e \rightarrow \bar{\nu}_x$ conversion. Of particular importance is the CHOOZ result [CHO99]. CHOOZ, with a baseline of $\sim 1km$, was sensitive to oscillations for $\Delta m^2 \gtrsim 10^{-3}$ and large mixing, the same parameter region where SK has established $\nu_\mu \rightarrow \nu_\tau$ conversion for atmospheric neutrinos. The observation of a number of $\bar{\nu}_e$ events consistent with the expectations and of an undistorted spectrum implies that the admixture of the electron neutrino flavor eigenstate with the "atmospheric" mass eigenstate (in jargon θ_{13}, see Sec. 1.1) is small. Moreover, CHOOZ put an upper bound to the solar oscillation analysis, constraining the LMA solution. With KamLAND for the first time the sensitivity of a reactor $\bar{\nu}_e$ experiment entered the solar oscillation parameter region.

KamLAND (Kamioka Liquid Anti-Neutrino Detector) [Shi03] was built in the same enlarged cavern of the earlier Kamiokande. The core of the detector is $1\, kton$ of ultra-pure liquid scintillator (Fig. 1.8). Most of the Japanese nuclear power plants are distributed around the detector site, with a distance distribution strongly peaked at $175 \pm 35\, km$ from Kamioka. KamLAND primary objective is to probe the LMA oscillation solution, by detecting $\bar{\nu}_e$ disappearance and spectral distortions. KamLAND first results have been reported in Dec. 2002 to be [Kam03]:

Expected $\bar{\nu}_e$events:	86.8 ± 5.6
Expected background events:	0.95 ± 0.99
Observed $\bar{\nu}_e$events:	54

(1.20)

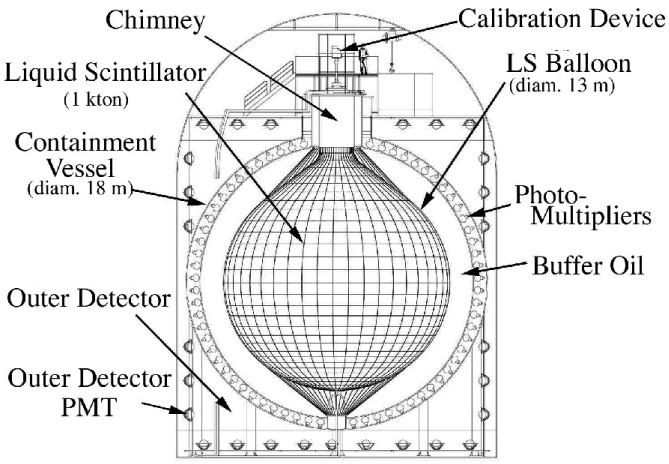

Figure 1.8: *Schematic view of the KamLAND detector. The inner nylon balloon contains* $1\,kton$ *of ultra-pure liquid scintillator. The mineral oil buffer provides hydrostatic support for the scintillator and shielding from external backgrounds. Nylon vessel and buffer are contained in a stainless-steel sphere, which supports 1879 inward-watching PMTs. The outer water-Cherenkov detector absorbs the radiation from the rocks and tags cosmic-ray muons. The detector concept is similar to Borexino (cf. Fig. 1.10).*

The energy-binned statistics for the 54 $\bar{\nu}_e$ events has not yet determined the presence of distortions in the energy spectrum.

If it is assumed that the mass pattern is the same for neutrinos as it is for anti-neutrinos - an implication of the CPT invariance - then KamLAND evidence of $\bar{\nu}_e$ disappearance selects unambiguously the LMA solution of the solar neutrino problem. The global fit of solar plus reactor data is shown in Fig. 1.9. Two separate sub-solutions emerge: LMA-I at $\Delta m^2_{sol} \sim 7 \times 10^{-5}\, eV^2$ and LMA-II at $\sim 1.5 \times 10^{-4}\, eV^2$, with LMA-I favored. If the solution realized in nature is LMA-I, then in the future KamLAND will be able to pin down with high precision the Δm^2_{sol} by analyzing the $\bar{\nu}_e$ energy spectrum. In case the LMA-II is the real solution, KamLAND would be at the limit of its sensitivity for the spectral shape analysis and a follow-up experiment at $\sim 20\,km$ baseline should be considered [SLO03].

1.5 Low Energy Solar Neutrinos

1.5.1 Physical and Astrophysical Relevance

The recent direct observation of ν_e flavor conversion with SNO and the selection of the LMA oscillation solution with KamLAND have likely given the ultimate solution to the long standing solar neutrino problem and closed an epoch. Upcoming experiments must now address simultaneously a serious of basic questions, which can be summarized in 4 items:

1. Independent confirmation of the most likely post SNO-KamLAND scenario
2. High precision parameter determination
3. Study of sub-leading neutrino processes

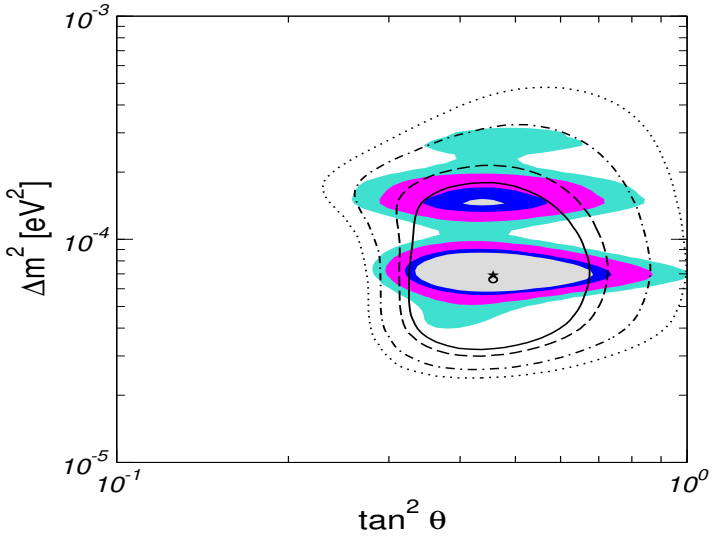

Figure 1.9: *Allowed 90%, 95%, 99% and 99.73% (3σ) C.L. regions. The hollow lines are the allowed regions from solar and CHOOZ data alone. The star and the dot represent the best-fit point with and without KamLAND. Figure from "M. Maltoni et al.", ref. [FMB02]*

4. Astrophysics

In this section we briefly explain what is meant by the above issues. In reference [BP03] Bahcall and Peña-Garay have recently given an exhaustive state-of-the-art analysis of what we presumably will know in the near future with better statistics from SNO and KamLAND and the goals and potential of the future of solar neutrino physics in this context.

SK and SNO have measured the total flux and the flavor composition of ^8B neutrinos, confirming the SSM predictions. With the next completion of the SNO scientific program, it is likely that the study of the ^8B flux will be close to the limit of its potential. The low energy part of the solar neutrino spectrum has been explored only by radiochemical experiments, which cannot disentangle the different neutrino components. Future experiments have to complete the present survey, by measuring *pp*, ^7Be, *pep* and CNO neutrinos in real time and with energy information.

Ultimate Test of the LMA Flavor Oscillation Solution Although the evidence for the "standard" MSW-LMA oscillation scenario now seems compelling, this is based on the observation of a negligible fraction of the solar neutrino flux and on the plausible assumption that neutrinos do not violate CPT. It is desirable to confirm the physics of LMA with *neutrinos* only and in a different energy range. It was often pointed out in the literature that all the pre-KamLAND allowed oscillations solutions have distinctive features in the sub-MeV range (e.g. [BGP02]), while they give similar predictions at $E_\nu > 5\,MeV$ (as an effect of the strong parameter selection operated by SK and SNO). The observation of a rate consistent with the LMA prediction below $1\,MeV$ would be a proof that neutrinos do *flavor-oscillate* and not simply *flavor-convert*[9]. If a detailed study of solar ν_e at low energy will not support LMA, new

[9]The oscillatory character of the ν flavor transitions might be soon revealed by spectral distortions in KamLAND.

physics might be revealed (CPT violation and more "exotic" flavor conversion mechanisms).

Precision Parameter Determination If indeed LMA is the correct solution, fundamental physics requires the mixing parameters Δm^2_{sol} and θ_{sol} to be determined with the highest precision. Reactor experiments, KamLAND *in primis*, have much better sensitivity to Δm^2_{sol} than solar experiments. On the other hand, the precision of the reactor experiments on θ_{sol} is limited by statistics, while solar neutrino experiments offer better sensitivity (at present $\tan^2\theta_{sol}$ is mainly constrained by solar data). If we trust the SSM, the most intense solar source, $pp-\nu$, is known to 1%. A comparison between expected and measured interaction rate can decrease the present uncertainty in $\tan^2\theta_{sol}$. However, it is shown in [BP03] that a new $pp-\nu$ experiment can contribute significantly only with a rate measurement at $\sim 3\%$ precision, while a ^7Be experiment alone is not expected to improve the actual constraints on θ_{sol}.

Sub-leading Neutrino Processes So far, the analysis of solar neutrino flavor conversion has been reduced for simplicity to the case of 2ν oscillations between active families. Future $pp-\nu$ and $^7Be-\nu$ experiments can further constrain the admixtures with the third mass eigenstate (θ_{13}) and with sterile neutrinos, ν_s. In both cases the departure of the oscillation from the basic "2ν - active" model will manifest in an apparent deficit of the detected ν fluxes. This deficit would be detected through the comparison of the experimental rates with the SSM predictions or, dropping the SSM and assuming only the luminosity constraint, through the comparison of the solar " nuclear" luminosity, calculated from the measured neutrino fluxes, with the observed photon luminosity. However, a significant improvement of the actual limits requires the low energy neutrino interaction rates to be measured with a precision of $\sim 1\%$ [BP03].

Astrophysics Neutrino physics and solar astrophysics are tightly coupled: the precise determination of the oscillation parameters requires the SSM predictions or at least the minimal assumption of the luminosity constraint. Conversely, the inference of the total solar ν fluxes from the measured experimental rates requires the knowledge of the oscillation parameters, which determine the flavor conversion factors at all ν energies and hence the detector response.

Unfortunately, there is no equivalent of the SNO NC reaction at low energy, therefore the comparison of CC and ES rates in two separate experiments is the only viable model-independent method for the experimental determination of pp, ^7Be and the other low energy ν fluxes. However, the precision attainable with this method is limited by the weak sensitivity of ES to $\nu_{\mu,\tau}$ and the relatively low conversion probability for ν_e at low energy, according to the best fit LMA solution ($P_{ee}\sim 0.63$). Therefore CC and ES rates need to be determined with very high accuracy: for a $\sim 10\%$ determination of the total ν_x flux, both the CC and the ES experiment have to attain a precision of $\lesssim 1\%$.

If the LMA scenario with the current parameter uncertainty is assumed (Fig. 1.9), and any *a priori* astrophysical assumption dropped, the only solar neutrino flux that is experimentally determined with comparable or better accuracy than the SSM estimations is the ^8B flux, measured by the SNO NC reaction and through the comparison between the CC rate in SNO and the ES rate in SNO and SK. All the other components, especially the fundamental $pp-\nu$ and $^7Be-\nu$, can be indirectly estimated from the global analysis of all the past and present experiments with very poor precision [BP03]. However, Bahcall and Peña-Garay have pointed

Table 1.4: *Comparison between ES and real time inverse-EC experiments (CC).*

	ES	CC
sensitivity	$\nu_e + \sim \frac{1}{6}\nu_{\mu,\tau}$	ν_e
cross section	well known	$\gtrsim 5\%$ uncertainty
calibration artificial ν source	not necessary	indispensable
ν - tag	directionality	$e^- - \gamma/\beta$ delayed coincidence
critical backgrounds	natural radioactivity	target specific
strategy background reduction	purification, self-shielding	ν- tag

out that if the luminosity constraint is added, the *pp* flux is determined with $\sim 2\%$ accuracy with the existing solar and reactor data (especially with the results of the gallium experiments plus the assumption of LMA). Furthermore, if a $\sim \pm 5\%$ ^7Be experiment will be performed in the future, the *pp* flux would be determined with $\sim 0.5\%$ accuracy, even without a new $\nu - pp$ experiment. Conversely, a precise measurement of the $pp - \nu$ interaction rate would test the validity of luminosity constraint, i.e. of the assumption that the sun is in a steady state and produces all of its irradiated energy via the hydrogen-burning reactions described in Sec. 1.2.2. As for the ^7Be and CNO neutrinos, the current bounds from global analysis, with or without the luminosity constraint, are so loose that any reasonably precise direct experimental determination would dramatically reduce the uncertainty and provide a fundamental test of our theory of stellar physics.

Conclusions The largest and most fundamental part of the solar neutrino spectrum has not been explored with comparable precision as the high energy ^8B spectrum. Predictions for the low energy solar neutrino fluxes, especially for *pp* and *pep,* are very robust, therefore the MSW-LMA physics established by the existing data can receive the ultimate confirmation or otherwise unexpected results might reveal new physics beyond the current simplest hypothesis. In case of no major surprises, the measurement of low energy solar neutrinos, especially of the $pp - \nu$ flux, could provide valuable contributions to the understanding of neutrino physics. However, future *pp* experiments have to demonstrate that they can give a superior scientific output than that of GALLEX-GNO and SAGE, combined with the results of the other experiments. This is only possible if a high precision is achieved (3% or better).

Last, once neutrino physics will be better understood, solar neutrino detection will eventually come back to its original goal: to probe the core of the sun and test in detail the theory of stellar energy generation.

1.5.2 Upcoming Experiments, Proposals and Ideas for Future Experiments

Upcoming and proposed future solar neutrino experiments aim at the real time and energy resolved measurement of the low energy fluxes [Sch02]. Either ES and CC experiment are considered and it is desirable that the same energy range could be covered with both methods and high precision, to test fundamental physics and stellar astrophysics (see previous section). The ES and inverse-EC detection techniques have advantages and disadvantages over each other (Table 1.4), some of which have been discussed in Sec. 1.3.1 and 1.3.2.

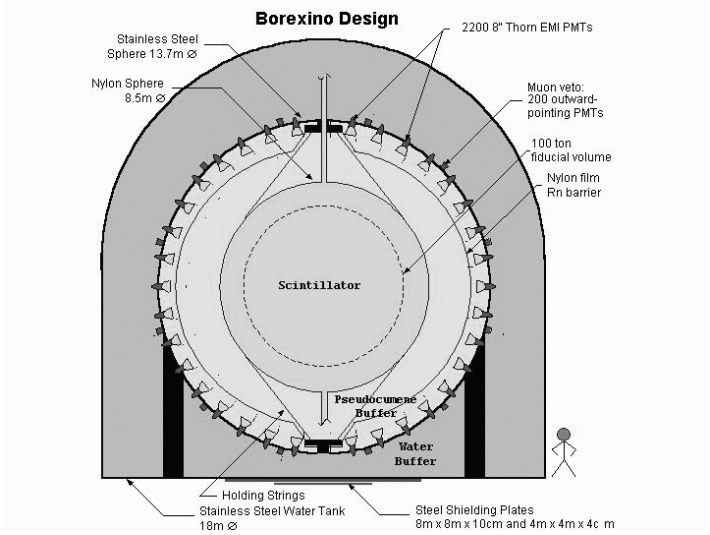

Figure 1.10: *Schematic view of the Borexino detector. Outside to inside: water-Cherenkov outer detector, serving as a passive shield for the internal volume and as a muon track detector; stainless steel sphere, where 2200 PMTs with light concentrators are mounted; buffer of* $1\,kton$ *of Pseudo-Cumene (PC); nylon Rn barrier, to prevent* ^{222}Rn *from diffusing toward the fiducial volume; nylon inner vessel, containing* $300\,ton$ *of ultra pure organic scintillator (PC with 1.5g/l PPO). Only the innermost* $100\,ton$ *of scintillator will be selected for the solar neutrino analysis.*

ES experiments The Cherenkov effect utilized in SK and SNO for the detection of ES interactions has too poor light yield to be used for sub-MeV solar neutrino spectroscopy. For this reason most of the future experiments consider using scintillation light, either from organic scintillators or from liquefied noble gases. Scintillation is isotropic and hence the information about the direction of the recoil electron is lost. As a consequence, there is no specific signature that can distinguish a ν-scattered electron from any β particle or γ Compton. The success of scintillation ES experiments is based on the achievement of unprecedented low background levels. This is the route pioneered by the Borexino experiment [Bor02]. **Borexino** is the only approved and funded project for sub-MeV solar ν detection and is currently near completion of the installation phase at Gran Sasso, Italy. The detector is described in Fig. 1.10 and the relevant caption. The primary goal of Borexino is the measurement of the $0.862\,keV$ $^7Be-\nu$ line, a task of fundamental importance to test LMA: the $0.862\,keV$ $^7Be-\nu$ line is particularly sensitive to the best non-LMA pre-KamLAND solutions; to the VAC, through seasonal rate modulations; and to the LOW, via day-night rate asymmetry. Beside, the ^7Be ν flux is a fundamental astrophysical datum, which is at the moment very weakly constrained by existing data. Moreover, Borexino's measurements will indirectly reduce the current uncertainty in the estimation of the $pp-\nu$ flux. The threshold of the experiment will be at $250\,keV$ and the ^7Be rate will be determined by analyzing the Compton-like recoil spectrum of the scattered electrons. In order to achieve a favorable signal to background ratio in the $[250\,keV - 800\,keV]$ neutrino energy window, the internal background rate must be $\lesssim 1\times10^{-6}s^{-1}m^{-3}$, which translates to limits of $\lesssim 10^{-16}g/g$ for uranium and thorium (with progenies assumed in secular equilibrium), $\lesssim 10^{-14}g/g$ for potassium, $\lesssim 10^{-10}g/g$ for argon and $\lesssim 10^{-16}g/g$ for krypton. Special care is dedicated to the purification of the scintillator

from the radioactive noble gases ^{222}Rn, ^{39}Ar and ^{85}Kr and to the treatment of all the surfaces in contact with the scintillator. The detector concept and the achievable background levels have been tested in the Counting Test Facility (CTF), a $\sim 4\,ton$ scale Borexino prototype [Bor98]. Particularly attractive is the possibility of measuring the *pep* flux with Borexino. *Pep* neutrinos are predicted with high accuracy by the SSM (1.5%) and, most important, their ratio to the *pp* neutrinos is known with much better precision and is nearly model-independent. The limiting background is the in-situ production of ^{11}C ($t_{1/2} = 20.4\,min$) by cosmic ray muons and secondary particles, which cannot be suppressed by a prompt μ - veto, due to the long lifetime. Suitable spallation cuts based on the muon track reconstruction in the outer detector are under careful investigation [Pei03]. With a larger Borexino-like detector, **KamLAND** may also try to measure the $0.862\,keV$ ^{7}Be. KamLAND has been optimized for reactor $\bar{\nu}_e$ detection, whose purity demands are less stringent than for solar neutrinos. The experiment has shown to have reached levels of contamination for uranium, thorium and potassium which would enable the detection of $^{7}Be - \nu$ [Shi03], however other backgrounds (^{85}Kr and ^{210}Pb) are still several order of magnitude higher than required.

The contamination of radiogenic ^{14}C (β end-point: $156\,keV$) in organic scintillators, measured in CTF at the level of few $10^{-18} C^{14}/^{12}C$, represent the ultimate irreducible background for $pp - \nu$ detection in Borexino-like detectors. Unless a low-^{14}C scintillator with $C^{14}/^{12}C \lesssim 10^{-20}$ can be produced, ES detection of $pp - \nu$ must use another technique. A promising approach is to use liquefied noble gases, which often exhibit higher light yields than organic scintillators. The **XMASS** collaboration considers using liquid xenon as target and aims at a ES measurement of the *pp* flux at $\sim 1\%$ precision ([Sch02] and refs. therein). Xenon has high density ($\rho = 3.06\,g/l$), which provides good self-shielding, excellent photon yield ($42000\,phs/MeV$) and a suitable scintillation wavelength ($\lambda = 175\,nm$). The detector would have a similar geometry as Borexino with $\sim 10\,ton$ of Xe. The strategy for Xe purification envisages distillation. The most dangerous backgrounds for solar neutrino detection are ^{85}Kr and the $2\nu - \beta\beta$ decay of ^{136}Xe (isotope separation might be necessary). The project is in a pilot phase, with the operation of a $100\,kg$ prototype. Important goals of the pilot phase will be the study of the $2\nu - \beta\beta$ decay of ^{136}Xe and the determination of the optical properties of liquid Xe. Other projects based on noble gases (e.g. liquid neon in **CLEAN** and super-fluid helium in **HERON**, see [Sch02] and refs. therein) have not yet moved from the study and R&D phase to the realization of real pilot experiments. Another option under investigation is the use of a Time Projection Chamber (TPC). The advantage of a TPC is that the reconstruction of the recoil electron track combined with the information on the solar position allows a full kinematic reconstruction of the incoming neutrino energy. **Super-MUNU** is one of such proposed TPC experiments: the detection concept has been tested in the MUNU detector [Bro01], which has performed $\bar{\nu}_e$ spectroscopy in the MeV energy region.

CC experiments Few isotopes exist suitable for the *pp* and ^{7}Be solar neutrino detection by means of the charge current reaction 1.13. They are listed in Table 1.5 . ^{100}Mo is the target chosen by the **MOON** project [Eji00]. The threshold for the reaction $^{100}Mo(\nu_e, e^-)^{100}Tc$ is $168\,keV$, sufficiently low for $pp - \nu$ detection. The ν signature consists of the prompt e^- and a coincidence β-decay, with end-point energy of $3.2\,MeV$ and half life of $15.8\,s$. For the energies of *pp*, ^{7}Be and *pep* neutrinos, only $0^+ \rightarrow 1^+$ ground to ground state transitions are possible and the Gamow-Teller (GT) strength is known with 4% uncertainty from the inverse EC decay and charge exchange reactions. In a target of $100\,ton$ of natural molybdenum about

Table 1.5: *Candidate nuclei for real time spectroscopy of pp and/or ^{7}Be solar neutrinos. Neutrino detection is based for all of the listed nuclei, but ^{100}Mo, on eq. 1.13. ^{100}Mo is converted to ^{100}Tc via a ground to ground state transition and ^{100}Tc subsequently β decays to ^{100}Ru. $T_{1/2}$ is the half life of the target nucleus, E^* the energy released (the Q) in the γ (β) de-excitation (decay) of the populated isomeric state (unstable nucleus), $T^*_{1/2}$ the half life of the neutrino-produced nuclear state. ^{100}Mo, ^{82}Se, ^{160}Gd and ^{176}Yb are all $\beta\beta$ unstable nuclei. Table from ref. [Sch02].*

Isotope	Abundance (%)	$T_{1/2}$	Q (keV)	$E^*(keV)$	$T^*_{1/2}$
^{115}In	95.7	$6 \times 10^{14}\,y$	114	116 + 498	$3.26\,\mu s$
^{100}Mo	9.6	$8 \times 10^{18}\,y$	168	3209	$15.8\,s$
^{82}Se	9.4	$9 \times 10^{19}\,y$	173	29	$10\,ns$
^{160}Gd	21.9	$\beta\beta$	244	75+64	$6 + 60\,ns$
^{176}Yb	12.7	$\beta\beta$	301	72	$50\,ns$
^{71}Ga	39.9	stable	404	175	$79\,ns$
^{123}Sb	42.7	stable	541	330 + 159	$31\,ns$
^{159}Tb	100	stable	543	177 + 121 + 56	$9.3\,ns$
^{137}Ba	11.2	stable	611	11	$89\,ns$

1 event per day is expected from $pp-\nu$ and 3.3 from $^{7}Be-\nu$. The major challenge of the MOON concept seems to be achieving in a $\sim 100\,ton$ detector the extremely high granularity that is required to reject the background from accidental coincidences in the long time window of the ^{100}Tc lifetime. The background from $2\nu-\beta\beta$ decay of ^{100}Mo is not expected to exceed the ν signal.

^{82}Se, ^{160}Gd, ^{176}Yb and ^{115}In have been investigated within the **LENS** project, which is described in detail in the next chapter.

Chapter 2

LENS

2.1 Introduction

The acronym LENS stands for Low Energy Neutrino Spectroscopy. It contains the main goal of the project: detecting low energy ($< 2\,MeV$) solar neutrinos, decomposing the flux into the individual contributions: *pp*, ^7Be, *pep, CNO*.

2.1.1 Motivations: Old and New Objectives

In Sec. 1.4 it was pointed out that after the first and second generation of solar neutrino experiments the global ensemble of data was consistent with the predictions of the SSM combined with the hypothesis of mass-driven neutrino flavor-oscillations. However no irrefutable proof could confirm this scenario and moreover the global fit of the experimental data still allowed several solutions spanning orders of magnitude in the oscillation parameter space (Fig. 1.6 on page 27). It was recognized that the low energy part of the solar neutrino spectrum plays a crucial role, since all the oscillation solutions consistent with data predicted peculiar signatures in the sub-MeV range (see Sec. 1.5.1). It was in this scientific context that the LENS collaboration formed. The aim of the project was to investigate the feasibility of a new solar neutrino detector with the potential of giving the ultimate answer to the solar neutrino problem [LENS99].

After the results of SNO and KamLAND there is almost unanimous consensus that solar neutrinos flavor-oscillate according to the MSW-LMA solution, with mixing parameters shown in Fig. 1.9 on page 31. Concerning fundamental particle physics, the field of solar neutrino detection has now to shift from the discovery phase to a phase of confirmation and precision parameters determination [Sch02]. At the same time, solar neutrino physics can address again its original astrophysical motivations with the new acquired insight on the fundamental neutrino properties. In Sec. 1.5.1 it was pointed out that, after the upcoming measurement of the ^7Be flux with Borexino, the scientific impact of a direct experimental determination of the $pp-\nu$ flux will be significant only if a very high precision is achieved: $\sim 3\%$ at least, $\lesssim 1\%$ desirable. A lower precision experiment would be able to confirm the currently favored oscillation solution, however without providing new significant physics and astrophysics inputs, unless surprise scenarios are revealed. High precision is therefore the goal of the next generation of low energy solar neutrino experiments.

2.1.2 Detection Principle and Candidate Target Nuclei

The idea of detecting low energy solar neutrinos in real time and with spectroscopic information, via charge current interactions on suitable nuclei was proposed in 1976 by Raghavan [Rag76]. The detection principle has been introduced in Sec. 1.3.1 and its implementation briefly discussed in Sec. 1.5.2. Table 1.5 on page 36 lists all the nuclei suitable for low energy solar ν detection via the reaction 1.13, sorted by energy threshold. Only the first 5 isotopes can enable the $pp-\nu$ detection. ^{115}In was the first target considered for this purpose [Rag76]. In 1997 Raghavan proposed three of the remaining four target candidates [Rag97]: ^{82}Se, ^{160}Gd and ^{176}Yb. The last nucleus, ^{100}Mo, is considered by the MOON collaboration (see Sec. 1.5.2).

^{82}Se and ^{160}Gd have been soon discarded by the LENS collaboration due to unresolved target-specific difficulties. The ν-tag of ^{82}Se poses severe technical challenges, due to the very low energy ($29\,keV$)and short time window ($\tau = 10\,ns$). A detection technology is required not yet developed for large scale ν experiments. Concerning ^{160}Gd, the main obstacle is the background due to the α-unstable ^{152}Gd, present in natural Gd with 0.2% isotopic abundance. ^{152}Gd decays with emission of a $2.2\,MeV$ α particle, which produces in scintillators an electron-equivalent observable energy in the pp range, due to α-quenching. Furthermore, a precise calibration of the experiment is problematic, because the total reaction cross section has contributions from transitions to several excited states of ^{160}Tb.

After this preliminary selection, the LENS collaboration has focused on the two most promising targets: ^{176}Yb and ^{115}In.

2.2 Experimental Concept

2.2.1 Detection Technique

With the major technological breakthroughs accomplished by the Borexino experiment in matter of large scale ν scintillation detectors and ultra-low background techniques, a natural approach to implement the LENS detection principle is to use organic liquid scintillators. A key point of the LENS concept is the development of an organic liquid scintillator in which the required mass of target element is dissolved. Basic demands for such a scintillator are:

- **High "Metal" Loading**: the weight fraction of the ν-target should be as high as possible, in order to minimize the total mass of the experiment. The optimal loading is the best compromise between costs, which scale with the total detector mass, and scintillator performance, which degrade with increasing concentration of non-scintillating components. A further constraint on the metal loading is set by the calibration of the detector with an artificial ν source, because the statistical precision of the measurement increases with the detector "compactness". The LENS working hypothesis envisages a metal loading in the range $2-10\%$ by weight.

- **Chemical Stability**: the dilution of the ν-target element in the scintillator has to be realized in a chemical form that ensures long term stability (several years). Furthermore, the final scintillator formulation has to be chemically "robust", i.e. it has to maintain stability also in the presence of other chemical species (e.g. water) and for a wide range of physical conditions (temperature, humidity, etc.).

- **Good Optical Performance**: for a useful energy spectroscopy it is necessary that the final metal loaded scintillator maintains an adequate *Light Yield* (LY), defined as the number of primary photons emitted per unitary energy deposition (upon electron excitation). The design goal is $\sim 50\%$ of the LY of standard, high-performance liquid scintillators ($\sim 10000\, ph/MeV$). The attenuation length[1] (μ) around the emission peak wavelength has to be sufficient to allow the transport of a substantial fraction of the light to the detection site. The goal is $\mu \gtrsim 3\, m$. Last, it is also important that the scintillation light is emitted with the usual fast timing typical of the fluorescence in organic scintillators (a few ns), so that an event can be spatially reconstructed via the photons time-of-flight distribution at the PMTs.

The minimal composition of a LENS scintillator consists of:

1. **Fluorescent Aromatic Solvent**. This is the base ingredient of all organic scintillators. It has a typical UV fluorescence response to the excitation of energy-deposing charged particle. Typical solvents considered are: PC (Pseudo-Cumene, 1,2,4-Trimethylbenzol), PXE (Phenyl-ortho-XylylEthane), Anisole (1-methoxybenzene), MN (Methyl-Naphthalene).

2. **Fluor**. A fluorescent molecule that couples *non-radiatively* to the solvent and shifts the original UV emission to the near UV - optical band. The most employed fluors are: PPO [2,5-diphenyloxazole], BPO [2-(4-bi-phenyl)-5-phenyloxazole], p-TP [1,4-diphenyl-benzol].

3. **Metallorganic Compound**. This is the molecule that brings the target element in the organic solution. Inorganic metallic compounds (like nitrates or chlorides) do not have good solubility in aromatic solvents, hence the target element must be bound by suitable ligands in a metallorganic "molecule" or "complex"[2].

In some formulations further chemicals are added, to stabilize the metal complex in the organic solution.

The presence of the metallorganic compound (and of other additives in some cases), at the high required concentration, degrades the scintillator transparency. For this reason the scintillator formulation is tuned to shift the light emission to a spectral region where self-absorption is reduced. The strategy is to intercept the primary fluorescence and shift it to longer wavelengths before absorption from the metal-compound and other optical impurities intervenes. Wavelength shifters are used (WLS, or λ-shifter), whose absorption band overlaps with the fluor emission. The most used WLS is bis-MSB [1,4-bis(2-methylstyryl)benzene]. At a concentration of a few tens mg/l, photons with $\lambda \lesssim 400\, nm$ are typically absorbed and re-emitted by bis-MSB within few mm or less[3]. The primary fluor emission is eventually shifted by bis-MSB to a range $\lambda \gtrsim 420\, nm$. Fig. 2.1 shows the emission spectra of the single fluorescent molecules most used: PPO, BPO and bis-MSB. A model of the physics of light emission and interaction in the scintillator will be presented in Sec. 6.4. The physics of energy transfer from the solvent to the fluors in a special class of LENS scintillators is studied experimentally and theoretically in refs. [MPI03, Buc04].

[1] Defined as the distance at which the intensity of a light beam has decreased to $1/e$ of its original value.

[2] We define here "molecule" a chemical species with own stoichiometric identity, like a metallorganic salt; "complex" a bound equilibrium state in an organic solution.

[3] Energy transfer to the λ-shifter can also be non-radiative. See Sec. 6.4 for a detailed discussion.

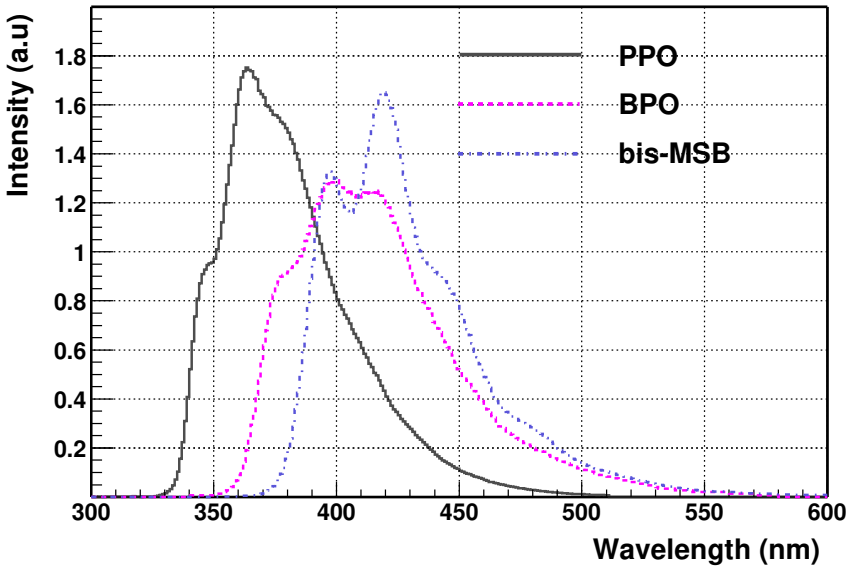

Figure 2.1: *Fluorescence spectra of PPO, BPO, bis-MSB, obtained via UV excitation at the wavelength of maximum absorption. All spectra were measured by us with a "Varian-Eclipse" fluorimeter (see ref. [MPI03, Buc04]).*

2.2.2 Design

As in Borexino and KamLAND, ν interactions are revealed through the detection of the scintillation light. Photons propagate outward from the ionization site and are eventually detected by PMTs. For each event energy and position are reconstructed. The former by measuring the total charge collected at the PMTs, the latter by analyzing the photons time of arrival distribution at the different PMTs. The detector performance largely depends on its energy and spatial resolution and on the homogeneity of those parameters within the sensitive volume.

For a large scale scintillator detector two alternative designs are possible: homogeneous and segmented. In the former case the target mass is enclosed in a unique volume and the scintillation light is collected at the surface of this volume. A segmented detector consists of a matrix of individual units and light is collected independently in each of such units. The homogeneous design, chosen for Borexino and KamLAND, has the advantage that less surfaces and containment materials are needed for the same sensitive mass. Moreover, an internal fiducial volume can be defined, self-shielded by the outermost region against external background sources. For these reasons the homogeneous design is the best strategy to achieve the lowest absolute background rate. In LENS, however, the key issue is to lower the detection energy threshold by benefiting from the ν-tag and hence it is not the absolute background rate the parameter to minimize, but rather the rate of events mimicking the ν-tag. In the LENS concept, the neutrino signature is based on a coincidence between a prompt and a delayed energy deposition (eq. 1.13 on page 21). A common background to all targets is the accidental spatial and temporal coincidence of uncorrelated single background events. For

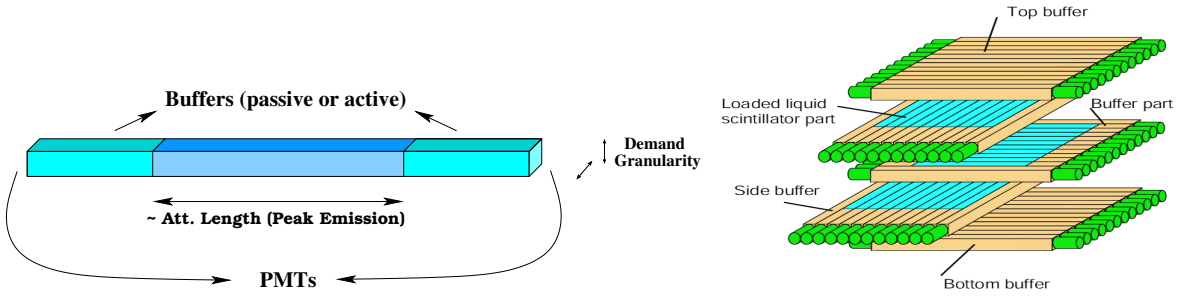

Figure 2.2: *Left: typical geometry considered for a LENS cell. The innermost region is the sensitive volume. Its length is of the order of the effective attenuation length in the cell for the wavelength range of the scintillation emission peak. The external sections at both sides (light guides or buffers) shield the sensitive volume from the external radioactivity. Two PMTs are coupled to the ends of the cell to detect the scintillation light. The sum of their signals provide a measurement of the total energy deposited in the scintillator; the difference in the photon time of arrival localizes the interaction site in the longitudinal coordinate. The side dimension of the cell is fixed by the target-specific demand in granularity (in the considered design there is no handle for the determination of the transversal position of an event).*
Right: Schematic layout of a homogeneous modular scintillation detector.

sources uniformly distributed the rate of random coincidences is proportional to the mass contained in the reconstructed volume, i.e. to the spatial resolution. It is noted that the rate of accidentals as a function of the coincidence time is nearly constant, while the ν-induced signal decays exponentially with time constant equal to the isomeric state lifetime. This allows to separate signal and background statistically by fitting the data with an exponential signal plus a constant background, in a similar way as in the radiochemical experiments (Sec. 1.3.1). Therefore a sizable background rate can be tolerated, up to $S/N \sim 1$ within the first few ν-tag lifetimes. A general demand of the LENS concept is the achievement of the minimal "granularity" (volume in which an event can be delimited) necessary to reduce the random-coincidence rate to this level. High granularity is best achieved with a segmented design, because of the physical separation of the single modules. The event location within a cell is further constrained by the differential measurement of the photon time of arrival at both ends. The modular concept is illustrated in Fig. 2.2. The exact demand on granularity is target specific and will be discussed separately for ^{176}Yb and ^{115}In.

2.3 Yb-LENS

2.3.1 The Target

The level scheme of the ν-induced $^{176}Yb \rightarrow {}^{176}Lu$ transitions is shown in Fig. 2.3. Electron neutrinos with $E_\nu > 301\,keV$ can be captured by ^{176}Yb (12.7% i.a. in natural Yb), leading to $0^+ \rightarrow 1^+$ transitions to an isomeric state of ^{176}Lu with $\tau = 50\,ns$. This decays to the first excited state of ^{176}Lu with the emission of a $72\,keV$ γ. Neutrinos with $E_\nu > 445\,keV$ can also induce transitions to another 1^+ exited state, which promptly decays to the isomeric state with the emission of a $144\,keV$ γ. The ν-tag consists of the spatial and temporal coincidence

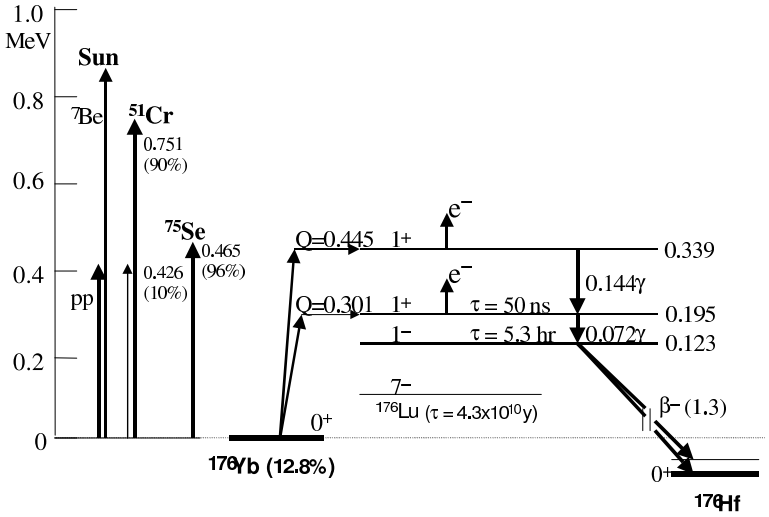

Figure 2.3: *Level scheme of the $^{176}Yb \rightarrow {}^{176}Lu$ ν-transitions. The arrows on the left side of the diagram indicate the energy range of pp and ^{7}Be solar neutrinos, and of the considered calibration sources ^{51}Cr and ^{75}Se.*

of the prompt e^- (or $e^- + 144\,keV$ γ, for transitions to the higher energy state) with the $72\,keV$ γ from the decay of the isomeric 1^+ state of ^{176}Lu. Electrons with a few hundreds keV give a very localized energy deposition. Gammas with $\sim 100\,keV$ have a short range, especially due to photo-absorption from Yb, and deposit their energy near the ν-interaction site. Therefore the sequence of the ν-signature is: prompt energy deposition ($\Leftrightarrow \nu$ energy) $\rightarrow$ delay ($\tau = 50\,ns$) $\rightarrow 72\,keV$ energy deposition in spatial coincidence with the prompt event. In most cases the two reaction channels of Fig. 2.3 are experimentally indistinguishable.

The strength of the Gamow-Teller transition $[B(GT)]$ has been derived with (p, n) and (^3He, t) charge-exchange experiments: $B(GT) = 0.21 \pm 0.04$ for the ^{176}Lu level at $195\,keV$; $B(GT) = 0.11 \pm 0.02$ for the next level at $339\,keV$ [FB00]. With these results, $\sim 20\,t$ of natural Yb are necessary to obtain a total ν interaction rate of $\sim 1\,ev/d$ (full SSM, 100% detection efficiency). The SSM simulated spectrum for this target mass is shown in Fig. 2.4. The ν cross section on Yb is calculated with sufficient accuracy to estimate the necessary detector mass, however the present $\sim 20\%$ precision must be reduced of one order of magnitude to achieve the LENS scientific goals. It is envisaged to calibrate the transitions to the two 1^+ levels of ^{176}Lu by exposing the detector to two intense (several MCi) artificial ν sources, for example ^{51}Cr and ^{75}Se (Fig. 2.3)

2.3.2 Detector Concept

An irremovable background in organic scintillators is ^{14}C (see Sec. 1.5.2), which decays β with $156\,keV$ end-point. Accidental coincidences of ^{14}C events can be a limiting background at low energies for neutrino targets with a non highly specific tag, like ^{176}Yb (simple double coincidence). In the CTF of Borexino the ^{14}C contamination in several samples of liquid organic scintillators has been measured: $^{14}C/^{12}C \sim 10^{-18} - 10^{-17}$ [Bor98]. It has been

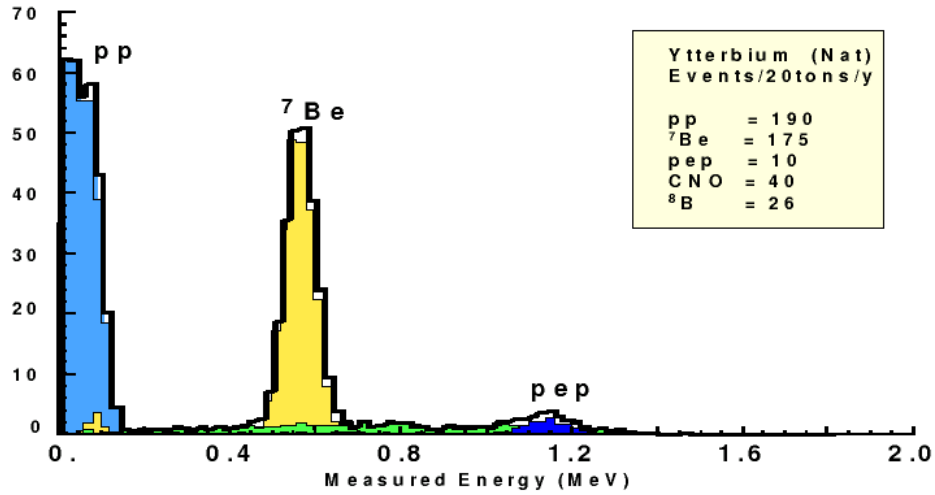

Figure 2.4: *SSM spectrum simulated for a* $20\,ton \times year$ *natural ytterbium target, folded tentatively with energy resolution. Neither the background nor the detection efficiency are simulated. Figure from [Sac].*

calculated that at these concentrations the accidental background rate for $pp-\nu$ detection is acceptable if two $\sim 100\,keV$ events truly occurring in the same position can be reconstructed within a volume of $\lesssim 10^{-1}\,m^{-3}$ [Sch00]. This goal is unfeasible in a large homogeneous detector, where the three spatial coordinates are reconstructed via time of flight difference at the PMTs. This granularity is however achievable in a modular detector, provided that the module cross-section surface is sufficiently small. In this case an event is delimited in the volume of the cell generated by the spatial resolution in the longitudinal coordinate. The working hypothesis for an Yb cell considers a geometry as the one shown in Fig. 2.2, with $\sim 20\,cm$ side and $\sim 300\,cm$ length.

The best performing Yb-loaded scintillators have been produced by using carboxylic acids as ligand. Yb has 3+ valence and forms equilibrium carboxylate complexes YbA_3 in organic solution, where HA represents the carboxylic acid utilized. In the empirical approach pursued at Bell Labs, light non-linear carboxylic acids are used [e.g. "isovaleric acid", $(CH_3)_2 - CH - CH_2 - COOH$] and long-term stability requires the addition of other suitable chemicals [Rag01a]. These are thought to stabilize the chemical form YbA_3 by "plugging" gaps around Yb and thus preventing hydrolysis and polymerization. Used stabilizers are heavier carboxylic acids and organo-phosphorous $(P = O)$ compounds. At MPIK a more methodical approach was followed, aiming at synthesizing Yb-loaded scintillators with single carboxylic acids. The stabilization is ensured by controlling the pH during the synthesis [Har04]. An alternative to the Yb-carboxylates is the use of neutral organo-phosphorous compounds as ligand [INR01].

2.3.3 Technological Challenges and Critical Issues

As discussed in Sec. 2.3.1, the ν-tag consists of a spatial and temporal coincidence of two events, a prompt e^- with $E_e = E_\nu - 301\,keV$, and a delayed $72\,keV\,\gamma$, with a typical delay of the order of $50\,ns$. The neutrino signature with ^{176}Yb is therefore:

1. Not highly specific, because based on the correlation of only two localized energy depositions

2. Technologically challenging, because of the low tag energy and short time window

Both items make the ^{176}Yb ν-tag weak and allow a wide range of possible correlated backgrounds[4]. The most dangerous are ^{235}U, ^{176}Lu and ^{169}Yb, which all have decay branches that mimic the ν-tag. Fakes due to self-correlation in single events are another serious background.

Uranium-235 This isotope decays α to ^{231}Th ($\tau = 37\,h$), which in turn decays β to an excited state of ^{231}Pa, with β end-point energy of $305\,keV$. This decay populates with 64% total probability an isomeric state of ^{231}Pa with $\tau = 65\,ns$, which de-excites to the ground state of ^{231}Pa with emission of a $84\,keV$ γ. Therefore the $^{231}Th \rightarrow {}^{231}Pa$ decay leads in 64% of the cases to an event sequence that is experimentally indistinguishable from a $pp-\nu$ capture on ^{176}Yb.

With a 0.72% isotopic abundance of ^{235}U in U_{nat}, $S/N > 1$ requires an uranium contamination $\lesssim 10^{-15}\,gU_{nat}/g$. Borexino and KamLAND have demonstrated that this level is achievable in aromatic scintillators, though very challenging. However, the feasibility of such a purity after the additional load of Yb and its organic ligand must be proven.

Lutetium-176 Lutetium is chemically very similar to ytterbium and therefore the standard industrial rare-earth technology delivers Yb compounds with sizable admixture of Lu (at the level of $\sim 1\,ppm$). The long lived ^{176}Lu (2.6% i.a.) β-decays to an excited state of ^{176}Hf and, after a γ cascade, an isomeric state is populated, with lifetime of $2\,ns$. This de-excites to the ground state of ^{176}Hf with emission of a $88\,keV$ γ. The energy released in the prompt $\beta-\gamma$ is in the range of the $^{7}Be-\nu$ signal, the delayed γ can mimic the ν signature, even though the time scale is much shorter. The purification of the Yb material to a level of $\sim 10\,ppb$ of Lu has been shown to be in principle feasible [GK01], however even at this concentration the rate of ^{176}Lu fake events is overwhelming compared to the ν signal and a minimum delay cut $\tau \gtrsim 30\,ns$ for the tag coincidence must be introduced. This implies a loss of $\sim 50\%$ of the solar ν rate.

Ytterbium-169 $^{169}Yb\,(\tau = 46\,d)$ is formed by resonant capture of thermal neutrons from ^{168}Yb (0.13% i.a.). It decays via EC to (predominantly) a metastable state of ^{169}Tm at $379\,keV$ with $72\,ns$ lifetime. The atom de-excites radiating a $\sim 50\,keV$ X photon, while the metastable nuclear state decays to the next long-lived excited level at $316\,keV$ ($\tau = 952\,ns$), with emission of a $63\,keV$ γ. Last, $^{169}Tm^{*}(316\,keV)$ decays to the ground state with the emission of one or more gammas. The sequence $X\,(50\,keV) \rightarrow$ delay $\rightarrow \gamma\,(63\,keV)$ mimics the interaction of a $pp-\nu$.

The ^{169}Yb equilibrium activity at sea-level is $\sim 10^{8}$ decays per day in $20\,t$ of natural Yb and hence a storage underground for $\sim 2\,y$ is needed to cool the ^{169}Yb activity to the same level of the ν interaction rate [Cri01]. In addition, a neutron shield against *in situ* neutron activation of ^{168}Yb would be necessary.

[4]It has been considered to strengthen the ν signature by detecting the β decay of the long lived ^{176}Lu 1^{-} state at $123\,keV$ (the level fed by the ν capture reaction) to the ground state of ^{176}Hf. However the time window of this additional tag is so long ($\tau = 5.3\,h$) that the demand in single rate background and detector granularity must be dramatically tightened.

In principle, the ^{169}Yb decay results in a triple coincidence that can be tagged imposing a cut on the late deposited energy. However an inefficiency must be expected, due to the escape of all or a part of the $316\,keV$ from the last de-excitation. MC simulations have shown that the rejection efficiency can be $\sim 10^3$ [Mey01] and hence a long cooling time is in any case necessary and probably the detector design must be improved to increase the efficiency of the ^{169}Yb cut.

Self-Correlated background The low energy and short lifetime of the ^{176}Yb ν-tag can generate a different kind of background: the "self-correlations" (SC). In a large volume scintillation detector the integral charge produced by an event is collected in a typical time of several tens of ns. The rise time can be fast (a few ns), however the signal pulse shape is expected to contain sizable late components. With $\tau = 50\,ns$, the probability that the coincidence γ of the ^{176}Yb tag overlaps with the tail of the prompt signal is very high. This makes the identification of the ν signature to a certain extent difficult, especially due to the very low tag energy. Conversely, a statistical fluctuation of the pulse shape of a single event (in coincidence on both PMTs) can be misidentified as a sequence of a prompt and a delayed energy deposition. This is a serious background for solar neutrino detection. The rate of such SC events is controlled by 4 parameters:

1. It is proportional to the rate of single background events in the considered energy window
2. It is a strong function of the energy, because the larger the signal amplitude the higher is the probability of generating a fluctuation consistent with the $72\,keV$ of the ^{176}Yb ν-tag
3. It is a strong function of the photoelectron yield at the PMTs (PY, measured in pe/MeV), since the higher the photoelectron statistics, the lower is the probability of a large fluctuation relative to the mean pulse shape
4. It is a strong function of the average fraction of charge collected from a single event at a later time than a proper cut

Point 1 says trivially that the rate of singles has to be minimized. Because of point 2, the SC background is likely to be a more severe problem for $^7Be - \nu$ (ratio prompt-to-delayed energy ~ 8) and higher energy fluxes, than for $pp - \nu$ (ratio ~ 1). Point 3 remarks that the ν-tag quality benefits from a high PY. Point 4 implies that the SC background can be reduced by increasing the delay threshold for accepting a coincidence as a ν-candidate event, however at the cost of a loss of efficiency for the solar signal.

For any given PY, the minimum delay cut to impose depends on the "late" component of the pulse shape of a single event. For the chosen detector concept, the following sources of late charge are identified:

1. Late fluorescence of the scintillator
2. Tail of the photon time of arrival distribution at the PMTs[5]
3. Photon trapping before detection, due to reflections at the PMTs side

[5]In the LENS modular geometry most of the collected light is not direct and the photons can travel a wide range of path-lengths to reach the PMTs.

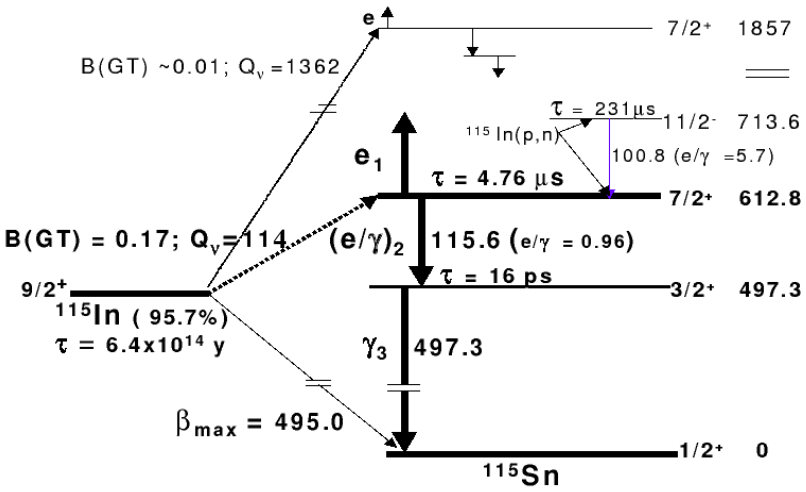

Figure 2.5: *Level scheme of the* $^{115}In \rightarrow {}^{115}Sn$ *ν-transitions. The last update for the Q value of the* ^{115}In *β-decay is* $Q = (499 \pm 4)\,keV$ *[AWT03]. The figure reports an older evaluation.*

4. PMT late pulses

The late component of the signal pulse shape in a LENS cell has been deeply investigated during this work. Chapters 3 and 5 are devoted to experimental studies of the decay-time of scintillator samples and the reflectivity of PMTs, respectively. Results are implemented in a model of a scintillation cell developed to perform Monte Carlo simulations of photon propagation, interaction and detection in a LENS module. This model is described in Chapter 6. In Chapter 7 the conclusive results of MC studies on the Yb ν-tag and the SC background are presented and commented.

2.4 In-LENS

2.4.1 The Target

The level scheme of the ν-induced $^{115}In \rightarrow {}^{115}Sn$ transitions is shown in Fig. 2.5. Electron neutrinos with $E_\nu > 114\,keV$ can be captured by ^{115}In (95.7% i.a. in natural indium), populating the second excited level of ^{115}Sn at $613\,keV$. This state is metastable, with lifetime $\tau = 4.76\,\mu s$. It decays emitting a $116\,keV$ γ or a conversion e^- (with nearly the same probability) to the first excited state of ^{115}Sn, which in turn promptly de-excites to the ground state with emission of a $497\,keV$ γ. Therefore a neutrino interaction results in the sequence:

1. prompt e_1^- ($\Leftrightarrow \nu$ energy)
2. delay ($\tau = 4.76\,\mu s$)
3. $(e^-/\gamma)_2$ with localized deposition of $116\,keV$ in spatial coincidence with e_1^-

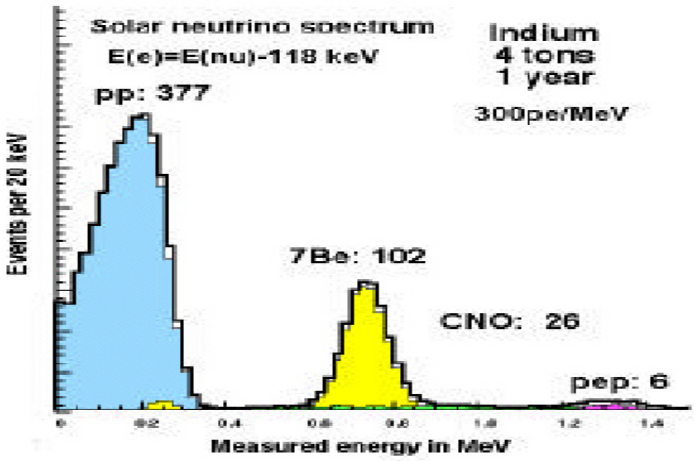

Figure 2.6: *SSM spectrum simulated for a* $4\,ton \times year$ *natural indium target, folded with the statistical energy resolution corresponding to* $300\,pe/MeV$*. Neither the background nor the detection efficiency are simulated. Figure from [Sac].*

4. γ_3 in prompt coincidence with $(e^-/\gamma)_2$, depositing $497\,keV$ via multi-Compton interactions in a larger volume around the e_1^- and $(e^-/\gamma)_2$ ionization sites.

The ν-signature in ^{115}In is very rich (≥ 3 point-like energy depositions), has an optimal delay (neither too long, nor to short) and a specific topology (two events in the same micro-volume plus an extended multi-Compton shower).

Only one level is involved in the ν-induced $^{115}In \rightarrow {}^{115}Sn$ transitions for energies below $1\,MeV$. The relevant Gamow-Teller matrix element has been estimated via $(p,\ n)$ reaction: $B(GT) = 0.17(1 \pm 0.2)$ [Rap85]. This implies an interaction rate of $\sim 1\,ev/d$ from $pp-\nu$ and $\sim 0.3\,ev/d$ from $^7Be-\nu$ in $\sim 4\,t$ of natural In (full SSM, 100% detection efficiency). The SSM simulated spectrum for the same mass of In is shown in Fig. 2.4. Also in this case it is necessary to calibrate the reaction cross-reaction with an artificial ν source. A ^{51}Cr source alone would be sufficient.

^{115}In has several favorable features as a target for low energy solar neutrino detection: high isotopic abundance, very low threshold, ν transitions to a single level, strong and highly specific ν-tag. The reason why this detection technique has not yet been implemented in a real experiment is that the target ^{115}In is β-unstable and can decay directly to the ground state of ^{115}Sn, with a β end-point energy of $495\,keV$ (Fig. 2.5). The decay involves a highly depressed $9/2^+ \rightarrow 1/2^+$ transition and this explains the very long lifetime of ^{115}In ($\tau = 6.4 \times 10^{14}\,y$). Nevertheless, the specific activity of natural indium is $0.26\,Bq/g$, which translates to a rate of $2.6\,MHz$ in a $10\,t$ indium detector. The In β-spectrum overlaps with the $pp-\nu$ signal, the $(e^-/\gamma)_2$ and γ_3 tag energies. Thus indium itself is the major irremovable source of background. The various backgrounds in a In detector are discussed in the next two sections.

2.4.2 Detector Design

^{115}In has a much more specific ν-tag than ^{176}Yb, with higher event multiplicity and tag energy. This suppresses the background from ^{14}C and any other non-indium source of random

coincidences. However, the intrinsic ^{115}In β-radioactivity sets such a high rate of singles that the control of the background from In-accidentals requires a even finer detector granularity than what is needed with ^{176}Yb.

A simple triple coincidence is not sufficient in any practical design and hence it is requested that the $497\,keV$ γ_3 must produce at least two separate "hits". This implies a modest loss of efficiency for the solar signal, but strengthens the tag from 3-fold to 4-fold. Obviously, the powerful ^{115}In ν-tag can be fully exploited only if each hit of the prompt $(e^-/\gamma)_2$ + γ_3 coincidence ($\geq$ 3 hits for the 4-fold tag) is separately identified. This is unfeasible in a homogeneous detector, where the light from each ionization site piles up at the PMTs. Consequently, the only viable design for In-LENS is a highly segmented detector, where it is required that the $(e^-/\gamma)_2 + \gamma_3$ tag triggers ≥ 3 cells in prompt coincidence and in a small volume surrounding the prompt ν event. It is found that even with the 4-fold ν-tag, the background rate from random coincidences of In β-decays requires a detector granularity of a few liters (the exact value depends on the In loading). This implies that the section of a module (Fig. 2.2) needs to be in the range $5 - 10\,cm$.

It is noted that in the background from random coincidences the prompt ν event is faked by an In decay, which can deposit in the detector an energy $E_\beta < 499\,keV$. Therefore, with a reasonable energy resolution, this background does not affect the detection of solar neutrinos of higher energy than the *pp*.

2.4.3 Technological Challenges and Critical Issues

Scintillator The approach followed by Raghavan for the production of In-loaded scintillators is to repeat the procedure invented for the Yb-loaded scintillators [Rag01b] (indium has also 3+ valence). However it is found that indium has a much higher chemical reactivity to OH^- than to the carboxylic acids: In^{3+} begins to react with water to form hydroxy species even at pH 1 [Har04]. This means that during the synthesis indium-hydroxy-compounds are formed, InA_xOH_{3-x}, rather than pure carboxylates InA_3. Furthermore, even once InA_3 is formed, the indium in the organic solution readily hydrolyzes in the presence of water (or in general of OH^- cations) and precipitates.

Hydrolysis is a severe problem towards the realization of a stable and robust indium-loaded scintillator (ILS). Two groups in LENS have produced stable ILS following two different approaches. At Gran Sasso a formulation has been developed, based on the chemistry of carboxylic acids [INR03]. Indium is bound into strongly hydrolyzed equilibrium compounds ($\sim InA_{0.6}OH_{2.4}$), which however do not precipitate out of the organic solution because of polymerization (polymer chains form, with 9 to 115 In atoms). A single carboxylic acid is used, and the *α-Methyl-Valeric* acid gives the best results.

The idea pursued at MPIK is rather to encapsulate the In atom in a stable metallorganic molecule that preserves its identity in the organic solution. This is accomplished by using β-diketones as ligand [BHS03]. The β-diketone molecule has a structure $R1 - (C = O) - CH_2 - (C = O) - R2$ consisting of two ketones $(C = O)$ that "sandwich" a methylene carbon CH_2. $R1$ and $R2$ are two carbon-based side chains. At basic pH the methylene carbon can lose a hydrogen and a delocalized negative charge is left. The positive metal ion is then bound at the center of the $[(C = O) - CH - (C = O)]^-$ diketone group, in a form stabilized by resonance. The carbon side chains promote solubility in the organic scintillator base solvent. Many indium β-diketonates have been synthesized and studied. The β-diketone molecule finally chosen for the LENS prototype is the simplest one, in which $R1$ and $R2$ are both methyl groups. This is

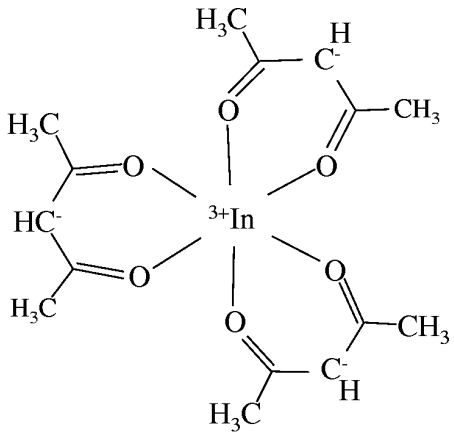

Figure 2.7: *Molecular structure of $In(acac)_3$. The In^{3+} at the center is fixed by three "acac" cations, through delocalized resonant bindings. The resulting molecule is very stable and has very low reactivity to OH^-.*

named *Hacac*, and the In β-diketonate $In(acac)_3$ (Fig. 2.7). $In(acac)_3$ is produced as a white crystalline powder, purified by sublimation and finally dissolved in the scintillator solvent (see [BHS03] for the details about the synthesis). Due to the strong chelate bound, the indium β-diketonates preserve their molecular identity in the organic solution, opposite to the case of the carboxylic complexes, which are more vulnerable equilibrium states. Consequently, the indium atoms are protected against hydrolysis and the scintillator formulation results inherently stable and robust. The solubility of $In(acac)_3$ in most of the standard organic scintillator base solvents (including PC and PXE) is found to be rather poor (translating to $\lesssim 1.5\%$ indium concentration by weight). Only anisole ensures high solubility, with a corresponding indium loading limit of 7.9% [BHS03].

The most critical issue in the β-diketonate scintillator formulation is that the $In(acac)_3$ molecule has an absorption band overlapping with the anisole UV emission and thus interfering with the energy transfer anisole $\rightarrow$ fluor, by opening a concurrent quenching channel anisole $\rightarrow In(acac)_3$. $In(acac)_3$ is not fluorescent and hence the energy diverted to this molecule is lost. This issue is discussed in detail in refs. [MPI03, Buc04]. The problem of optimizing the scintillator composition in a LENS cell is studied through MC simulations in Chapter 8. The experimental characterization of the optical performance of full-scale $In(acac)_3$-based prototype cells are also presented in Chapter 8. Preliminary results of the ongoing background measurements at Gran Sasso are reported in Chapter 9.

Bremsstrahlung and other In-Related Backgrounds The background due to uncorrelated In β decays can be effectively reduced with a highly segmented detector and the additional request of a 4-fold coincidence. More dangerous, however, are the backgrounds due to a simple double coincidence between an indium decay and a multi-hit event with similar characteristics as the $(e^-/\gamma)_2 + \gamma_3$ sequence. Two classes are identified:

1. backgrounds related to In decays only
2. backgrounds due to coincidences of an In decay and another source.

Correlated backgrounds with no In events are negligible compared to the above cases, due to the very strong ν-tag. In all the cases that will be discussed the prompt ν event is faked by an In decay and hence also these backgrounds do not significantly affect the detection of ^7Be and higher energy solar neutrinos.

A simple coincidence of two indium decays can mimic the ν-tag if the second β emits Bremsstrahlung (BS) gammas[6]. The sequence most similar to a ν-event is given by a first β, mimicking the prompt e^- from the ν capture, followed by a second β in spatial and temporal coincidence, where a large fraction of the decay Q is converted into a single BS γ. The residual energy deposition from the latter β mimics the $(e^-/\gamma)_2$ event, the BS photon γ_3. This background is called *hard-BS*, because the sequence can be misidentified as a ν event only if the BS photon carries most of the available energy in the β-decay. The hard-BS background is controlled by three parameters:

1. **Granularity**, due to the space-time coincidence between the two In β decays.

2. **Indium Bremsstrahlung Spectrum**, in particular the integral probability $P_{BS}(E)$ that an In decay is accompanied by a BS photon with higher energy than E. The probability of hard BS emission is doubly depressed, because it is the product of two low probabilities: 1) that the β carries most of the available decay energy and 2) that most of this energy is transferred to a single hard BS photon. The function $P_{BS}(E)$ has been theoretically calculated for external BS in metallic In [Cri84]. Its experimental determination in ILS is one of crucial goals of the In-LENS pilot phase.

3. **Energy Resolution**. The total energy available for the hard-BS is the Q of the In decay, $Q = 499\,keV$, which is lower than the total ν-tag energy $E_{\nu-tag} = 613\,keV$. In fact the hard-BS is dangerous only due to the detector finite energy resolution. It is envisaged to apply a double cut: on the reconstructed energy of γ_3 alone and on the total tag energy. For the efficiency of both cuts the energy resolution is the key parameter.

   For an order of magnitude estimation of the required detector performance, if we ask that the reconstructed energy $\pm 2\sigma$ of a $490\,keV$ $\beta + \gamma_{BS}$ event is incompatible with $613\,keV^{+x\sigma}_{-1\sigma}$ (asymmetric cuts ensure a better rejection), than the limit energy resolution corresponds to $\sim 300\,pe/MeV$ (for comparison, Borexino has $\sim 400\,pe/keV$, with $\sim 30\%$ PMT coverage and unloaded scintillator).

Also *soft-BS* can produce a dangerous background to the $pp-\nu$ signal, however with a different event structure. A β can emit a few (≥ 2) soft BS photons, or a single medium-energy BS γ that undergoes multi-Compton scattering before photo-absorption. In either case, there exist at least three separate ionization sites in prompt temporal coincidence. If an In decay has taken place few μs before this event, in spatial coincidence with one of the low energy depositions from the BS gamma(s), the observed sequence can mimic the ν-tag. This background is similar to the hard-BS and hence has a similar dependence on the achievable spatial granularity and energy resolution. It has however a much higher probability, because the emission of less energetic BS photon(s) is involved. Detailed MC simulations [Mey02] have shown that, in any realistic detector based on the geometry of Fig. 2.2, the soft-BS background overwhelms the ν-signal, unless the minimum energy cuts on the ν signature are so much tightened that the efficiency for solar neutrinos drops to $< 10\%$.

[6] *Internal* Bremsstrahlung is considered, as well as *external*.

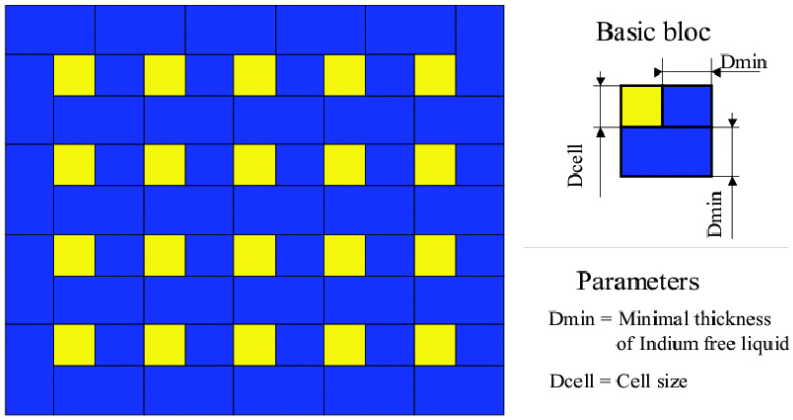

Figure 2.8: *Schematic layout of the In-LENS "hybrid" detector concept. Each In-cell (yellow/light-shaded) is surrounded by an unloaded scintillation volume (blue/dark-shaded).*

A key point helpful for rejecting this background is that soft BS photons are much more limited in range than γ_3, so that in most of the cases a fake needs the first β-decay of the sequence to occur in a neighbouring cell of the second β-BS event. The remedy is to change the detector concept from *homogeneous-segmented* to *hybrid-segmented*: any In-cell should be surrounded by an unloaded portion of detector (Fig. 2.8). The soft-BS photons are attenuated in the unloaded volume, where no In decays can occur. MC simulations indicate that the hybrid design can effectively suppress the soft-BS background with the same detector segmentation imposed by the accidentals[7] [Mey03]. However such a geometry implies much higher hardware costs and a lower attainable precision in the cross-section calibration with an artificial ν source, due to the effective indium "dilution".

A last dangerous background related to the In radioactivity is the coincidence of an In decay, mimicking the prompt ν event, with a $\beta-\gamma$ cascade from another source, or a partially contained multi-Compton shower from a high energy γ. Detailed MC studies have been carried out for the case of the ^{40}K contamination in the PMT glass envelope [Mey03]. Results indicate that the sensitive volume of each cell must be protected by very long or dense buffers ($> 1\,m$ acrylic), or otherwise an active shielding must be considered.

Light Piping It has been stressed that the In-LENS concept needs a high detector granularity to reduce the background from random and correlated coincidences associated with ^{115}In β decays. This requires the In-cells to have a small geometrical cross section. On the other hand, the detector modules need to be as long as allowed by the scintillator attenuation length, to minimize the total number of PMTs and electronic channels, i.e. the costs. The LENS working hypothesis envisages dimensions of $\approx 5-10\,cm \times 5-10\,cm \times 100-300\,cm$. With such a geometry, guiding the scintillation light from the ionization site to the PMTs with high efficiency is a challenging issue: whatever the piping mechanism, photons must un-

[7] Very recently our colleagues at Gran Sasso have reported evidence for the experimental observation of a decay branching of ^{115}In to the excited state of ^{115}Sn at $497.3\,keV$ [Cat04], which seems now energetically allowed after the last update in [AWT03]. If this discovery is confirmed, and the decay has a non-negligible rate, a new dangerous background could derive. Work is in progress to check this result and evaluate the impact on LENS.

dergo many reflections and even a small inefficiency can result in large light losses. This has an obvious impact on the detector performance, namely on the energy and space resolution, which are the essential parameters towards the background reduction.

Light piping in optical modules has been experimentally characterized during this work. This topic is covered in Chapter 4. The effect of the measured piping inefficiency on the performance of LENS cells is studied via MC simulations in Chapter 7.

Trigger In a detector of $10\,t$ In mass, the β-decay rate is $\sim 2.6\,MHz$. The detection of the solar signal requires a very low-threshold first-level hardware trigger. Managing the resulting huge acquisition rate is unfeasible and hence a high level trigger must be developed, with a buffer depth of several μs.

2.5 The LENS Pilot Phase

The LENS collaboration formed in 1999 with the aim of studying the feasibility of a low energy, real time, charge current solar neutrino experiment based on the ideas discussed in Secs. 2.1 and 2.2. The first phase of the R&D focused on detector design, development of metal-loaded scintillators, study of the expected detector performance and backgrounds via MC simulations, and lastly on the definitive choice of the most promising ν-target.

However, the ultimate goal of the LENS collaboration was to test the experimental concept in a prototype detector. The MPIK has financed, designed and installed the *LLBF,* a low background facility for LENS at the Gran Sasso underground laboratory [Mot03], and an array of prototype cells to house in the LLBF.

The LENS pilot phase program has addressed in parallel two complementary questions:

1. The comprehensive study of the "optical" performance of a single LENS prototype cell. This includes the characterization of the light attenuation in the module, the measurement of the photoelectron yield at the PMTs, the measurement of energy and spatial resolution. These parameters are interpreted by comparing the results of the final metal-loaded scintillator cell with the benchmarks measured with the same cell filled with a standard, high performance organic liquid scintillator and with the predictions of MC simulations. This experimental program has been simultaneously carried out in two laboratories within the LENS collaboration: at Gran Sasso and at MPIK, for different indium-based scintillator formulations (In carboxylate for the former case, In β-diketonates for the latter). Chapter 8 reports on the measurements performed at MPIK. The data are compared with the predictions of photon-tracing MC simulations, also developed during this work (Chapters 6 and 7).

2. The final test of an array of optical modules simulating a "block" of the LENS detector, in the ultra-low background environment of the LLBF at Gran Sasso. Preliminary results are presented in Chapter 9.

2.6 The Contribution of this Work

In this section the structure of the thesis is outlined, with emphasis on the relationship of this contribution with some of the critical issues of the LENS concept discussed in this chapter.

The primary purpose of this work was to address basic questions about the detector performance, in particular energy resolution, spatial resolution, and pulse shape. In the first R&D phase this program has been pursued by modeling the physics of a single LENS detector unit (a scintillator cell). The aim was to set benchmarks for the achievable detector performance, single out the most critical problems and provide feed-back for the prototype design. These goals have required the experimental measurements of key detector parameters, which serve as input data for the aforementioned model. Two experimental lines of research have been pursued:

1. Study of the effects that influence the signal pulse shape, in particular in the time window of the ^{176}Yb ν-tag. This issue is critical to estimate and control the background from self-correlated events, as discussed in Sec. 2.3.3.

2. Study of the effects that influence the photoelectron yield and hence the energy and spatial resolution.

Concerning point 1:

- The scintillator fluorescence timing has been measured, in benchmark unloaded organic scintillator samples and as well in metal-loaded samples synthesized during the LENS R&D. Chapter 3 is devoted to these measurements.

- The optics of PMTs has been experimentally investigated with several techniques. The measurements have been interpreted by fitting the data with a theoretical description of light interaction with a PMT. The result is a model able to predict the PMT reflectance as a function of the wavelength and angle of incidence, for any optical coupling (e.g. to air or to scintillators). As a by-product, the model also predicts the angular dependence of the PMT sensitivity. Chapter 5 covers this topic.

Concerning point 2:

- Light piping via total internal reflection (scintillator to air) and specular reflection (via giant birefringent multilayer polymer mirrors) have been experimentally studied in prototype optical modules. An effective reflection efficiency has been deduced for both piping mechanisms at two representative wavelengths. These studies are reported in Chapter 4.

- A detailed model of light interaction with the scintillator has been developed, including absorption and radiative energy transfer, separately for each component of the scintillator. This is covered in Chapter 6.

All the theoretical and experimental inputs discussed above have been implemented in a model of light emission, propagation, interaction and detection in a LENS cell, which is the subject of Chapter 6. This model is the base for Monte Carlo simulations, which have been used to investigate some of the crucial issues of the LENS concept, either for ^{176}Yb and for ^{115}In. This R&D phase has led to results that have contributed to:

- Disfavor the ^{176}Yb option, due to the problem of self-correlation in the proposed design

- Validate the technical part of the In-LENS concept related to light piping and optical performance

The above items are studied in Chapter 7, which concludes the part of this thesis devoted to the "Detector Modeling".

Next the LENS project has fully entered the pilot phase, with the construction and operation of full-scale detector prototypes, as outlined in Sec. 2.5. Chapter 8 describes first the preliminary studies to optimize the MPIK $In(acac)_3$ scintillator formulation for use in full-scale optical modules. Then results are given of the experimental characterization of the optical performance of a LENS prototype cell filled with a benchmark scintillator and with $In(acac)_3$-based scintillators, for different metal and fluors concentrations. The measured detector parameters are: total number of collected photoelectrons per unit of deposited energy, energy resolution and spatial resolution. Their dependence on the location of the ionization site along the cell length was also characterized. The results are then compared with the full photon-tracing MC simulation of the cell and used to select the scintillator composition for low background counting in the final LENS prototype.

Chapter 9 describes the LLBF facility at Gran Sasso. The performance of the shielding are reported and the prototype set-up is described. A matrix of 3×3 scintillation modules, all identical to the one optically characterized at MPIK, has been installed in the LLBF and operated in a ultra-low background environment. Background data are shown and preliminary analysis presented for the first campaign of measurements, in which the prototype array was filled with a benchmark PXE scintillator, also measured in CTF [Bor04]. Recently 4 of the 9 PXE cells have been filled with In-loaded scintillators synthesized at MPIK and Gran Sasso, and background measurements of this prototype set-up are ongoing. First preliminary data will be shown.

Chapter 10 reviews briefly the major achievements of this work and in general of the LENS pilot phase, and gives an outlook about the future of the project.

Part II

LENS Detector Modeling

Chapter 3

Measurement of the Fluorescence Time in Organic Liquid Scintillators

3.1 Introduction

When a charged particle excites a scintillator molecule, this de-excites (when radiatively) following an exponential decay law that has the lifetime of the excited state as time constant. In fact, several molecular states can be populated by the primary energy deposition, therefore the emission time distribution is the sum of various exponentials, each with a different time constant. A fluorescence probability density function (PDF hereafter) $P(t)$ can be defined, giving the probability that a single excited molecule emits a photon in dt after a delay t from the excitation. $P(t)$ depends on the scintillator solvent and is influenced by the properties and concentration of the fluors. It can be described as a multi-exponential decay function, where each time constant can be thought of as the effective lifetime of a populated excited state[1]. Therefore the simplest parametrization is:

$$P(t) = \sum_{i=1}^{n} \frac{q_i}{\tau_i} e^{-t/\tau_i} \tag{3.1}$$

where τ_i is the decay constant of the i^{th} component and q_i its statistical weight, i.e. the probability for a molecule to de-excite radiatively with a τ_i decay constant[2]. The number of exponentials n is chosen as the minimum giving a good fit to data, in the considered time window. The fastest decay constants, τ_1, has normally the largest weight and contributes substantially to determine the rise-time of signals in scintillator detectors. The requirement for many applications in nuclear physics aiming at an event spatial reconstruction is that such rise-time is comparable to (or shorter than) the maximum time of flight difference for light to reach the detector PMTs. If the scintillator response is too slow, the event position can be only inferred by charge division, which has limited performance with low photons statistics

[1] In fact this interpretation turns out to be too simplistic: the first decay component is indeed in relation with the lifetime of the lowest fluor singlet excited state, but is also determined by the efficiency of the energy transfer from the solvent to the fluor itself, hence by the concentration of the latter. The slower components are due to de-excitation of metastable triplet states, through processes involving interactions between two molecules. In this case the decay constants are rather an effective mathematical parametrization of the fluorescence time PDF. The theory of scintillation is treated, for example, in the textbooks [Bir64, Kno89].

[2] With the parametrization in eq. 3.1 q_i is the integral of the i^{th} exponential, i.e. $\sum_{i=1}^{n} q_i = 1$

and transparent scintillators. Standard organic liquid scintillators are known to be sufficiently fast for use in large volume detectors, with main decay constants of the order of magnitude of few ns (the speed of light in a liquid with $n = 1.5$ is $20\,cm/ns$). In this case, the pulse rise-time is rather dominated by the detector geometry, light transport and electronics jitter. The slow fluorescence components are influenced by the energy loss mechanism of the exciting particle. This effect allows the statistical identification of the detected radiation, by means of pulse shape discrimination [RWH64].

In the LENS project the experimental determination of the fluorescence time distribution of metal-loaded scintillators, as well as benchmark unloaded scintillators, is of great importance. It must be understood whether the presence of the metal and its ligands, at the high required concentrations, interferes with any of the steps that lead to light emission, in such a way that the scintillator time performance is degraded. If this was the case, spatial reconstruction, essential in LENS for background rejection, may be severely limited. Furthermore, in Yb-LENS it is crucial to characterize the delayed fluorescence, because it contributes to increase the probability that, due to statistical fluctuations in the pulse shape, a single ionization event is misidentified as a ν-event candidate. For this reasons, we have set up a system to characterize the fluorescence time of liquid organic scintillators under γ irradiation. Samples of interest for the LENS project have been measured and, for comparison, scintillators used in Borexino. Our goal was to determine the decay time of the prompt scintillation fluorescence and as well to study the late emission, over a time range of $\sim 1\,\mu s$.

3.2 Experimental Technique

The measurement of the fluorescence decay time of scintillators has been accomplished by using the *start-stop* method based on the single photon sampling technique, which is briefly described in this section (a detailed treatment is also found in [Ran94] and references therein).

The goal of the measurement is to determine with which probability the excitation of a single scintillator molecule at time $t = 0$ results in the emission of a photon at a delayed time t. An ionizing particle losing energy in a scintillator will typically excite a large number of molecules. Ideally, it would be necessary to be blind to all the de-exciting molecules but one, and to measure the delay between the primary excitation and the detection of the emitted photon. An implementation consists in watching a scintillator sample irradiated by a radioactive source with two PMTs. The optical coupling must be such that one PMT can see a large number of photons per event. If the sample is sufficiently small, it can be assumed that any interaction of a charge particle excites the scintillator molecules all at the same time, so that the onset of the analogical signal delivered by the high rate PMT defines the time of the energy deposition (disregarding the insignificant constant delay for signal forming and detection). If the second PMT is coupled to the sample in such a way that it can detect only one photon from the event, the delay of the detection time of this photon relative to the other PMT gives the actual decay time of a single molecule. The fluorescence PDF is then determined by repeating the procedure, until sufficient statistics for each time bin is acquired.

Summarizing, the method requires a set-up consisting of the scintillator sample to measure, a radiation source, two PMTs and a suitable "chronometer". One PMT, strongly coupled, gives the *start* to the chronometer, the other, weekly coupled, must trigger on a single photoelectron and provides the *stop* signal.

Let us consider the case of an ideal system, having a δ function of time as response and no

Table 3.1: *Effective decay time of the PDF of the first pe, calculated by fitting eq. 3.3 with a simple exponential function, for the case of* $F' = \frac{1}{\tau}e^{-t/\tau}$. *The input decay time is* $\tau = 3\,ns$ *and the fit is performed in the interval* $[0,\ 6\,ns]$.

m	1	0.2	0.1	0.05	0.01	0.001
τ from fit (ns)	2.01	2.74	2.87	2.93	2.986	2.9986

background (the corrections to apply for a real detector will be discussed in the next sections). In principle, a delay measurement can be biased by systematics on both *start* and *stop* signals. Both have been studied and the latter will be first considered.

Biases from the statistics of the *start* signal The number of photons detected by the *stop* PMT follows a Poisson distribution parametrized by the mean number of detected photons per event, m. The Poisson statistics biases the measured PDF, since whenever the low rate PMT detects more than one photon the stop signal has an effective shorter decay time. In order to minimize this bias, the coupling must be tuned until the mean number of detected photons per event is $\ll 1$ (*sub-Poisson* statistics). This implies:

$$\sum_{n>1} P(n) \ll P(1) \tag{3.2}$$

where $P(n)$ is the probability that n photoelectrons (*pe* hereafter) are detected. Following [Ran94], the requirement expressed by eq. 3.2 can be further quantified, by considering the PDF of the first *pe*, when the average number of *pe* is m:

$$P_{first}(t) = \frac{me^{-mF(t)}F'(t)}{1-e^{-m}} \tag{3.3}$$

where the time t is measured from the scintillator excitation, $F'(t)$ is the detection time PDF for the single *pe* and $F(t) = \int_0^t F'(s)ds$. In the ideal case considered here (infinite resolution, no background), the distribution $F'(t)$ is equal to the scintillator fluorescence PDF.

In a real experiment, $P_{first}(t)$ is the probability that is directly measured with the *start-stop* technique, not $F'(t)$. Assuming for simplicity that the scintillator fluorescence PDF is an exact single exponential with $\tau = 3\,ns$, eq. 3.3 has been evaluated for different values of m and compared to the original PDF. The results are shown in Fig. 3.1. It can be seen that working at an average of one detected *pe* per event leads to a highly biased distribution. For an average of one *pe* in 20 events a small departure from the real PDF is still observable.

Previous determinations on organic liquid scintillators of interest in neutrino physics have shown that typically the first exponential has a decay time of a factor 10 shorter than the second, and also about a factor 10 greater weight [Ran94, RGL98]. Therefore the fast component dominates the scintillator response for a time of the order of $\sim 2\tau_1$. In Table 3.1 it is calculated how large the systematic error of the scintillator decay time is, when this is experimentally determined through $P_{first}(t)$ in the time interval $[0,\ 2\tau]$, as a function of the level of illumination of the low rate PMT. This illumination-dependent systematic can be analytically corrected by using eq. 3.3, as in ref. [Ran94]. However, Table 3.1 shows that for $m \sim 0.01$ this bias is $< 0.5\%$, which we consider negligible for the level of accuracy we aim

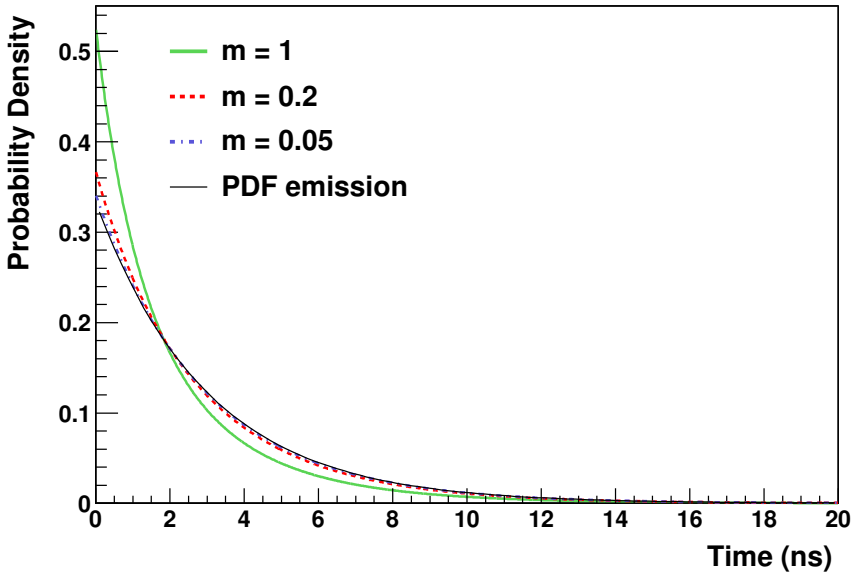

Figure 3.1: *Probability density functions for the time of detection of the first detected photon, calculated for* $m = 1,\ 0.2$ *and* 0.05 *under the assumption of exponential emission PDF, with* $\tau = 3\,ns$.

at. Consequently, in all our measurements we have tuned the coupling of the low rate PMT to reduce the illumination to $m \sim 0.01$.

Biases from the statistics of the *stop* signal So far, the assumption was made that the time zero is the instant of the energy deposition in the scintillator. In reality, this time is the moment in which the analogic signal from the high rate PMT goes over the threshold, which in turn has its own PDF with respect to the real time-zero. If $P_{stop}(t)$ is the PDF for the detection of the first photon in the low rate PMT (equal to $P_{first}(t)$ in eq. 3.3) and $P_{start}(t)$ the probability distribution of the trigger time for the high rate PMT, the measurement of the delay $\Delta t = t_{stop} - t_{start}$ will provide an effective measured PDF, $P_{meas}(t)$, given by:

$$P_{meas}(t) = \int_0^\infty P_{start}(s) P_{stop}(s+t) ds \tag{3.4}$$

It is important to note that, if $P_{stop}(t)$ is an exact exponential, then $P_{meas}(t) \propto P_{stop}(t)$, irrespective of $P_{start}(t)$. This is a consequence of the exponential statistics, which is insensitive to time shifts, and can be easily verified by replacing $P_{stop}(s+t)$ with $ke^{-(s+t)/\tau}$ and evaluating eq. 3.4 at $t + dt$.

Eq. 3.4 has been evaluated for the base case of P_{stop} given by eq. 3.3, with an exponential fluorescence PDF, $\tau = 3\,ns$ and $m = 0.01$. P_{start} has been given several distributions: eq. 3.3 with high values of m (ideal case), gaussian (simulating a jitter), constant (the "worst" case). The resulting $P_{meas}(t)$ functions have been analyzed in the interval $[0,\ 6\,ns]$ to determine the effective decay time that would be measured under the above assumptions. Table 3.2 shows the results. Since in our case $P_{stop}(t)$ is "very similar" to an exponential distribution the conclusion valid for an exact exponential still holds: the measured PDF is nearly independent

Table 3.2: *Effective decay time for the calculated PDF of the measured start-stop delay, for some example $P_{start}(t)$: statistics of the first detected photoelectron for $m = 100$ and $m = 10$, gaussian distribution with $\sigma = 1ns$, step function with $P_{start} = 1$ for $t \in [-6\,ns,\ 6\,ns]$, 0 elsewhere. The $P_{stop}(t)$ distribution is fixed to the function given by eq. 3.3 for $m = 0.01$ and $F' = \frac{1}{\tau}e^{-t/\tau}$. The input decay time is $\tau = 3\,ns$ and the fit is performed with a simple exponential function, in the interval $[0,\ 6\,ns]$.*

$P_{start}(t)$	eq. 3.3 $m = 100$	eq. 3.3 $m = 10$	gauss $\sigma = 1ns$	step [-6,6]
τ from fit (ns)	2.986	2.987	2.989	2.993

of the time distribution of the *start* signal and almost indistinguishable from the PDF of the first detected photoelectron.

The conclusion of this analysis is that setting the experiment such that the low rate PMT has the proper sub-Poisson statistics automatically makes the time distribution of the *start* signal unimportant.

3.3 Backgrounds, Instrumental Artifacts and Resolution

In the previous section the biases of the *start-stop* technique with single photon sampling have been studied for a system with ideal response. In a real experiment several other problems can bias the measurement. These can be classified as *backgrounds* or *instrumental artifacts*, depending whether they originate from background start-stop sequences or from the response function of the system, respectively. In this section these problems are described and it is discussed how they have been reduced in our measurements. The response function of the system is also related to the time resolution, which is discussed in the last part of the section.

3.3.1 Backgrounds

Both PMTs are affected by dark noise counts, which can interfere with the measurement by giving fake *start* or *stop* signals:

Dark Counts from the *start* PMT It can happen that a dark count from the *start* PMT opens a gate that is stopped by a signal in the low rate PMT. In this case a time interval is acquired, which is not related to the scintillator fluorescence. This background has been suppressed by simply increasing the threshold of the *start* PMT above the end-point of its dark noise spectrum, with no drawbacks for the decay time measurement.

Dark Counts from the *stop* PMT This case is more dangerous than the previous one because:

1. Real signals (single *pe*) and dark noise have the same range of amplitude, so that the background cannot be suppressed by increasing the threshold

2. The condition of low illumination expressed by eq. 3.2 worsens the signal-to-noise rate ratio of the *stop* PMT

As a consequence, if the low rate PMT has a high dark counts rate, the background becomes overwhelming at large t, severely limiting the time depth of the measurement. The only solution for this problem is to use a PMT with an intrinsic dark noise rate R_{dark} satisfying;

$$R_{dark} D \ll m \tag{3.5}$$

where D is the time depth of the measurement and m the average number of detected photoelectrons per event in the time interval [0, D]. If $D = 1\,\mu s$ and $m \sim 0.01$, eq. 3.5 gives: $R_{dark} \ll 10\,kHz$. Since the PDF of a *stop* signal has a fast decay, whilst the background is nearly constant, the condition in eq. 3.5 has to be interpreted in a strong sense to preserve an acceptable signal-to-noise ratio in the tail of the distribution. Standard PMTs with $\sim 1\,kHz$ dark noise rate are therefore not suitable. The PMT we have used, a Hamamatsu R1527P, is specially designed for single photon counting applications and shows a dark noise rate $< 10\,Hz$.

Background from Misidentified Sequences In our measurements, the *start* trigger rate is comparable to D^{-1} and the low rate tube is operated in sub-Poisson statistics. In this case, since our electronics is *non-updating* (a new *start* does not reset the system), another background must be considered: it has been observed that after a first *start* signal sometimes a second interaction can occur in the scintillator within the time depth of the measurement and the latter is followed by a *stop*. In such cases it is more likely that the *pe* detected by the low rate PMT is associated with the second *start* event, but the recorded sequence $t_1^{start} \rightarrow t_2^{start} \rightarrow t_2^{stop}$ results in the acquisition of the wrong delay $t_2^{stop} - t_1^{start}$. We have suppressed this background by adding a hardware logic condition that vetoes the acquisition whenever the *stop* signal is preceded by more than one *start* within the time window D.

3.3.2 Instrumental artifacts

Instrumental artifacts related to the time response function of the *stop* PMT to a single photon can add fake structures to the measured distribution:

Late Pulses Between the PMT illumination and the subsequent detection of the resulting avalanche a typical time elapses, which is called "transit time". This delay corresponds to the dynamic of the photoelectron focusing on the first dynode and of the succeeding multiplication through the dynode chain. The transit time shows a gaussian-like spread, which adds a time jitter to the measurement. With a certain PMT-dependent probability (typically few percent) the photoelectron can follow a much longer path before undergoing multiplication, resulting in a delayed signal. Such events are called *late pulses*. For a given PMT, the late pulses time distribution shows a well defined peak (see Fig. 6.3 on page 135, with typical delays of $20 - 100\,ns$, depending on the size of the PMT. In a fluorescence time measurement the late pulses of the *stop* PMT add a delayed peak to the distribution, a lower amplitude mirror of the principal peak at $t = 0$. This effect can thus jeopardize the analysis of the tail of the distribution. A possible solution is to determine precisely the response function of the *stop* PMT to a single photon and then to deconvolve it from the measured curves. However this procedure is technically difficult and gives results of limited precision. The best option is to choose a special PMT, with very low intrinsic probability of generating late pulses. The Hamamatsu R1527P is a "side-window" PMT and it is found that this geometry is particularly favorable to reduce the rate of late pulses [RGL98].

After Pulses Contrary to late pulses, *after pulses* are not due to the *pe* itself, but to positive ions from the residual gas inside the PMT produced during the avalanche, which move upstream, strike the photocathode and induce a second delayed avalanche. In this case two correlated pulses are detected: the original and the ion induced one. The delays are longer than for late pulses, of the order of few $10^2\,ns$ to microseconds. After pulses are always preceded by the corresponding prompt signal, nevertheless after pulses of the low rate PMT are of nuisance, because in some cases it happens that the prompt *pe* gives a sub-threshold pulse, whereas the following after pulse triggers, providing a delayed *stop*. The solution we applied is to introduce a hardware logic condition triggered by a very low *stop* threshold, which vetoes the acquisition whenever two such *stop* signals occur in the gate opened by a *start*.

3.3.3 Resolution

Several components contribute to determine the time resolution of the system. The transit time spread of the PMTs has been mentioned above. Both our PMTs have been selected among the types with the fastest rise-time and lowest jitter[3]. The next step in which a time uncertainty is introduced is the analogic-to-logic conversion of the signals (*discrimination*). For this reason a "constant fraction" (CF) discriminator was preferred to a higher walk "leading edge". The outputs of the CF discriminators need to be shaped and delayed, which adds another time jitter. Last, further uncertainties are associated with the *chronometer*, in our case a Time to Pulse Height Converter (TPHC). Due to all these effects, what is really measured is the fluorescence PDF of the scintillator sample convoluted with the response function of the whole experimental apparatus. In order to facilitate the deconvolution of the scintillator performance, the total resolution of the system should be $\lesssim \tau$ and the response function as regular as possible (i.e. gaussian-like).

3.4 Experimental Set-Up

The concepts described in the previous sections have been implemented in the set up shown in Fig. 3.2. It consists of a black, light-tight box where the scintillator sample and the source are placed. The inner walls are covered with a Teflon layer to improve light collection for the high rate PMT. The holders of the two photomultipliers are screwed into this black box. The high rate PMT is a fast $2''$ "front-window" Photonis XP2262, the low rate PMT is a "side-window" Hamamatsu R1527P. Some important features of the two PMTs are reported in Table 3.3. The very low dark counts rate of the R1527P PMT enables the measurement of the decay time over a time range of $\sim 1\,\mu s$, with very low background. The neutral (non wavelength dependent) filter in front of the *stop* PMT decreases the illumination to the desired level.

A simplified scheme of the logic of the electronics is shown in Fig. 3.3. The analogic signals from the PMTs are discriminated by a CF discriminator. When the pulse from the high rate tube goes over the threshold, a logic signal of the duration of $1\,\mu s$ is generated and sent as a

[3] In Sec. 3.2 it was shown that the time distribution of the *start* signal has a very modest impact on the decay time measurement, provided that the *stop* PDF does not differ very much from an exact exponential. However, the real PDF of the stop signal is the convolution of eq. 3.3 with the response function of the low rate PMT and subsequent electronics, which is no longer "very similar" to an exact exponential. Therefore the conclusion that the time distribution of the start signal is unimportant is not necessary true for a system with finite resolution.

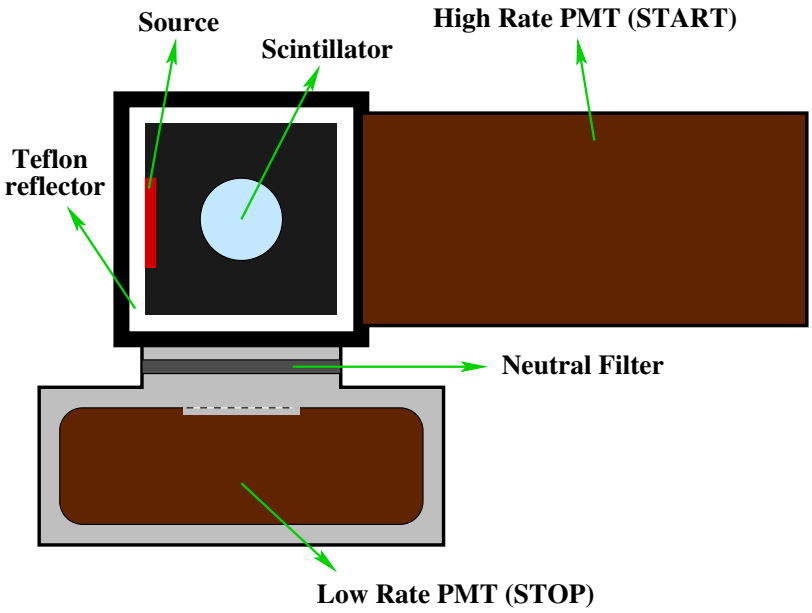

Figure 3.2: *Scheme of the experimental set up used to measure the decay time of scintillator samples.*

Table 3.3: *Some figures of merit of the two utilized PMTs. The dark noise rate have been measured by us, at operating voltage and with a threshold of* $\simeq 0.2\,pe$. *The other parameters are the manufacturer's specifications.*

	High rate	Low rate
Type	Photonis XP2262	Hamamatsu R1527P
Rise Time	$\simeq 2.0\,ns$	$\simeq 2.2\,ns$
Jitter (1σ)	$\simeq 0.5\,ns$	$\simeq 0.5\,ns$
Dark counts	$\simeq 1\,kHz$	$\simeq 7\,Hz$

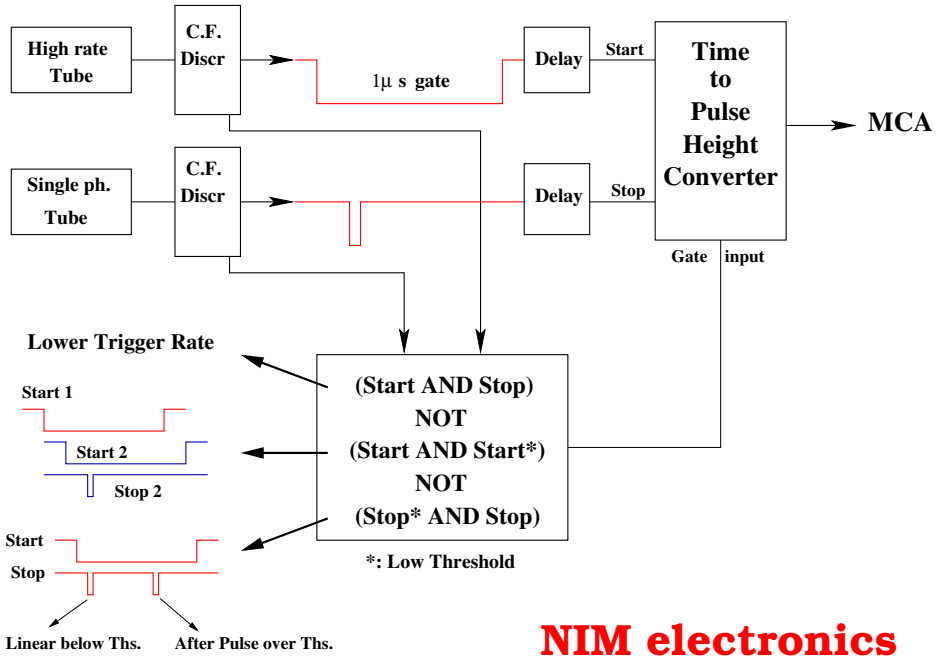

Figure 3.3: *Simplified scheme of the logic of the electronics used to measure the decay time of scintillator samples.*

Table 3.4: *Thresholds for acquisition and veto, in units of the single pe amplitude peak.*

	Start PMT	Stop PMT
Acquisition	$\sim 10\,pe$	$\sim 0.7\,pe$
Veto/Monitor	$\sim 3\,pe$	$\sim 0.1\,pe$

start signal to a TPHC. Similarly, a pulse above threshold from the low rate PMT produces a logic signal that stops the TPHC. Both logic signals are delayed to let the trigger take the decision whether to accept or not the occurring sequence. For each PMT two sections of a CF discriminator are used, with different thresholds settings: higher for the acquisition and lower for veto and monitor purposes (see Table 3.4). The outputs of the CF are used to form a trigger logic that opens a gate for the TPHC whenever:

1. Start and Stop are in coincidence within a time depth of $1\,\mu s$
2. Within this interval there is no other low-threshold *start* before a *stop* has come
3. Within this interval there is no low-threshold *stop* before the effective high-threshold *stop*.

Condition 1 is trivial, conditions 2 and 3 veto the backgrounds due to misidentified sequences and after pulses of the low rate PMT, respectively, as explained in Secs. 3.3.1 and 3.3.2. The

threshold for the acquisition of the *start* signal is high enough to suppress the dark noise triggers and make sure that the signals used for the reference time-zero have a regular pulse shape and high statistics. For the *stop* PMT, it is necessary to trigger on a single-*pe*. However, it has been noticed that the discrimination of low amplitude single-*pe* pulses is affected by a large jitter, hence the threshold chosen is the lowest preserving an accurate discriminator output. The veto and monitor systems have to trigger on the highest possible number of physical events: the threshold of the *start* PMT is set such to accept a large fraction of source events, while cutting most of the dark counts; the veto threshold of the *stop* PMT sits just above the baseline noise. The trigger rates of the two PMTs are monitored through a scaler-timer unit, to check whether the low illumination regime of eq. 3.2 is fulfilled.

Once an event sequence meets the conditions 1, 2 and 3 above, the TPHC is enabled and converts the start-stop delay into a pulse of proportional amplitude, which is sent to a Multi-Channel Analyzer (MCA). The MCA was set to cover its dynamic range with 2048 channels, corresponding to an instrumental sensitivity of $\sim 0.5\, ns/ch$.

The calibration of the channel-to-time scale was obtained by measuring the MCA response to a series of fixed delays in the range $50\, ns - 1\, \mu s$. The *start* and *stop* have been provided by a couple of coincident signals from a Gate & Delay generator. The various delay between the two signals were set on the module and measured with a digital oscilloscope (TDS 7000, Tektronix).

3.5 Data Analysis

The scintillator fluorescence PDF can be parametrized by eq. 3.1. The MCA output spectra are the convolution of the scintillator PDF with the response function of the system. The latter includes the channel-to-time calibration of the TPHC-MCA sub-system and the time response to a single photon of PMTs and electronics. The analysis is carried out by fitting the measured curves with the function:

$$f(x_i) = [kP(t - t_0) + b] \otimes R(t) \tag{3.6}$$

where the right hand term has to be evaluated at the time t_i:

$$t_i = c_0 + c_1 x_i + c_2 x_i^2 \tag{3.7}$$

where x_i is the MCA i^{th} channel, t_i the corresponding time. In eq. 3.6 $P(t - t_0)$ is the multi-exponential function of eq. 3.1 with an overall time offset t_0 given by the sum of all the offsets between the *start* and *stop* signals; k is an absolute normalization, b a constant rate describing the total contribution of the unvetoed backgrounds[4] (cf. Sec. 3.3.1); $R(t)$is the response function of the system and the symbol $\otimes$ represents the convolution product. The response function $R(t)$ has not been experimentally measured and was approximated with an asymmetric gaussian (different standard deviations on the left and right side of the peak). This assumption is justified by the observation that the response of a PMT around 0 is always

[4]The background rate is here assumed constant, thought it is in principle time-dependent. It can be shown (see e.g. [Ran94]) that the relative variation of the background rate on a time scale of the order of the fluorescence lifetime is of the order of $1 - e^{-m}$, while asymptotically it scales as $e^{-R_d t}$, R_d dark counts rate. In both cases the variation is negligible, due to the high signal/background ratio at short times, the smallness of m and the very low background rate R_d.

Table 3.5: *Free parameters of the fit of the fluorescence time spectra (eq. 3.8, see also the definition of the fit function in eq. 3.6). For n free decay constants, only n-1 weights are free parameters, due to the normalization constraint:* $\sum_{i=1}^{n} q_i = 1$.

Parameter	Explanation
$\tau_1, \ldots, \tau_n$	Decay Constants
$q_1, \ldots, q_{n-1}$	Weights of the Components
t_0	Time Offset
k	Global Normalization
b	Background Rate
σ_{dx}	Right Instrumental Resolution
σ_{sx}	Left Instrumental Resolution

well approximated by a gaussian function and that side-window PMTs show a negligible rate of late pulses.

The channel-to-time scale has been calibrated as described in the previous section and interpolated with a second order polynomial (eq. 3.7). The coefficient of the quadratic term c_2 is negative and the non-linearity of the scale modest: $|c_2/c_1| \sim 10^{-6}$, implying a maximal relative correction associated with the quadratic term of $\sim 10^{-3}$. The polynomial gives a good fit to the calibration points and two independent calibrations performed at a distance of several days have given similar results. The resulting relative uncertainty in the channel-to-time conversion[5] is lower than 0.002 over the whole $1\,\mu s$ measurement depth, which has a negligible effect on the determination of the fluorescence parameters.

Eq. 3.6 has been implemented in a computer program that minimizes the χ^2 function of the fit to the data, defined as:

$$\chi^2(p_j) = \sum_{i=l}^{h} \frac{[N(x_i) - f\,(x_i,\ p_j)]^2}{N(x_i)} \tag{3.8}$$

where $\{p_j\}$ is the set of free parameters of the fit (see Table 3.5), $N(x_i)$ is the number of counts in the MCA i^{th} bin and $f\,(x_i,\ p_j)$ is given by eq. 3.6. The error used for the single bin is the square root of the bin content: $\sigma(x_i) = \sqrt{N(x_i)}$. The interval of fit $[x_i,\ x_h]$ excludes, on the left side of the peak, the range which is not well described by the fit function due to the non gaussian tail of the PMT response; on the right side, the last overflow channels. The χ^2 minimization is performed by the MINUIT package of the CERN libraries. All the measured curves could be described with the sum of 3 to 4 exponentials.

3.6 The Measured Samples

Five samples have been measured: three of them where non metal loaded, benchmark organic liquid scintillators of interest in neutrino physics; two samples were high metal loaded scintillators synthesized during the early phase of the LENS R&D program. Before measuring, all

[5]For this comparison the difference of the constant terms c_0 in eq. 3.7 has been corrected, since the fit function has an additional time-offset free parameter.

the samples were bubbled with N_2 for $5\,min$ to remove oxygen, which is known to decrease the light yield and at the same time to attenuate the slow time components (see [Bir64]). The samples have been irradiated with pure γ emitters: ^{137}Cs and ^{54}Mn. Gammas from these sources have Compton interactions in the scintillator, so that the measured fluorescence curves refer to the scintillator excitation by electrons. The neutral filter in front of the low rate PMT was tuned such to have $m \sim 0.01$, so that the systematic distortion of the fluorescence PDF due to the statistics of the *stop* signal was negligible (cf. Sec. 3.2). The parameter m was estimated by monitoring the ratio (*start* & *stop* rate)/(*start* rate): typically $R_{start\,\&\,stop} \sim 10 - 20\,Hz$ and $R_{start} \sim 2\,kHz$, measured with the "acquisition" thresholds of Table 3.4.

3.6.1 Benchmark Scintillators

The unloaded scintillator samples measured were:

- **BC505**: high light yield, fast response, standard organic scintillator produced by the BICRON corporation. Its exact composition is not published, however its characteristic odor reveals the use of PC as solvent and fluorimetric measurements show that bis-MSB is also employed as WLS [Buc04]
- **PC + PPO(1.5 g/l)**: a sample of identical composition as the scintillator proposed for the Borexino experiment [Bor02, Bor98]. The PC was purchased by Aldrich and has slightly different properties compared to the PC delivered by Enichem for Borexino ([Buc04]).
- **PXE + p-TP (2.0 g/l) + bis-MSB (20 mg/l)**: a scintillator deeply studied by the Borexino collaboration. The sample investigated is the same PXE-based scintillator measured in CTF [Bor04].

3.6.2 Metal Loaded Scintillators

Both the investigated scintillator samples, one loaded with ytterbium, the other with indium, have been synthesized by R. Raghavan at Bell Labs in 2001 and are based on the chemistry of carboxylic acids [Rag01a, Rag01b]. The In sample turned out to fail essential demands in matter of transparency and especially of chemical stability, therefore it is not representative of the kind of scintillator suitable for the LENS experiment. Nevertheless its limitation did not prevent the reliable measurement of the decay time and the study of the influence of the metal and its ligands on the scintillator fluorescence. A measurement of stable In-loaded scintillators, available only at a later time, has not been carried out, because the decay time is much less critical for the indium project than for ytterbium, due to the very long tag-time. Table 3.6 gives a description of the two investigated samples.

3.7 Results and Conclusions

The experimental fluorescence time PDF and the fit obtained with the function of eq. 3.6 are shown in figs. 3.4 to 3.8. Table 3.7 reports the best fit values for the most significant parameters. All the measured curves are regular over the entire time depth, which confirms that late and after pulses from the *stop* PMT have been reduced to a negligible level and no other major instrumental artifacts are present. The low dark noise counts rate of the R1527P

Table 3.6: *Data of the measured Yb and In loaded scintillators [Rag01a, Rag01b]. The Light Yield was measured by us with a Compton-Back-Scattering (CBS) technique on a 20 ml sample, under irradiation with ^{137}Cs and ^{54}Mn sources (CBS will be described in Sec. 8.3) TMMA: Tri-methyl-acetic Acid. TBPO: Tri-Butyl-Phosphine-Oxide.*

Name	BL Yb #260F1	BL In #381MP
Date of Synthesis	1/22/2001	8/8/2001
Metal Loading (In wt.)	$\sim 10\%$	$\sim 12.5\%$
Light Yield (rel. BC505)	$\sim 45\%$	$\sim 39\%$
Carboxilic Acid	Iso-Valeric	Iso-Valeric
Solvent	PC	MN
Fluor	BPO ($8\,g/l$)	BPO ($8\,g/l$)
λ-shifter	bis-MSB ($10\,mg/l$)	bis-MSB ($10\,mg/l$)
Further Ingredients	TMMA	TMAA; TBPO
Comment	viscous	low transparency, chemically unstable

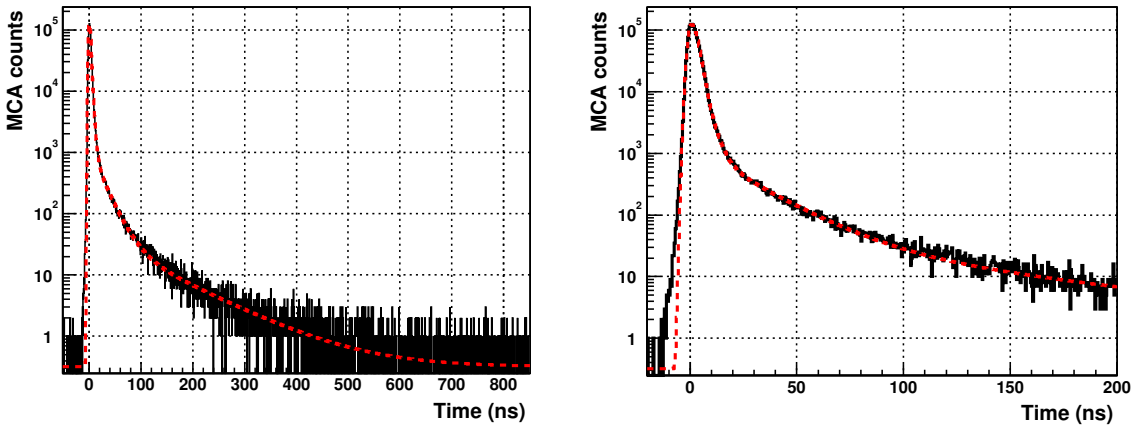

Figure 3.4: *BC505: experimental (black solid histogram) and best fit (red dashed curve) fluorescence time PDF. The right plot displays the first 200 ns.*

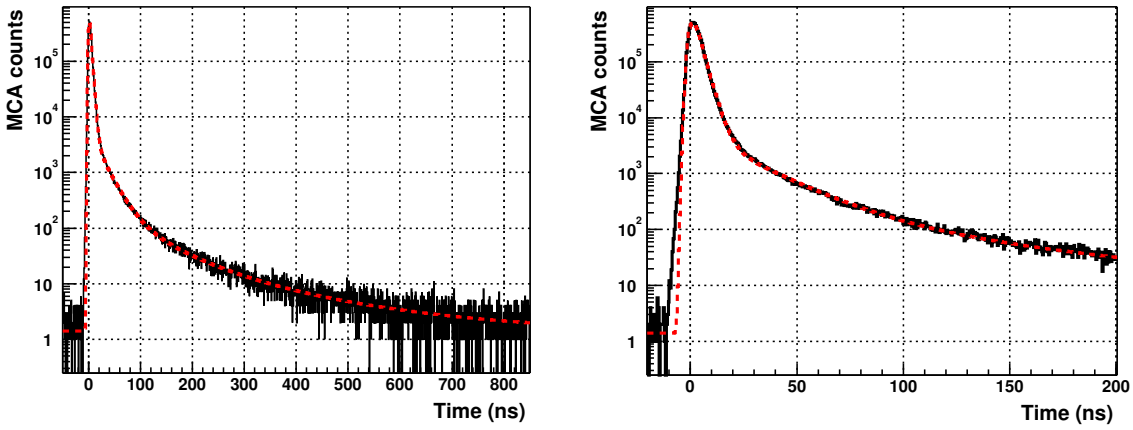

Figure 3.5: *Fluorescence curve of the PC + PPO*($1.5\,g/l$) *sample.*

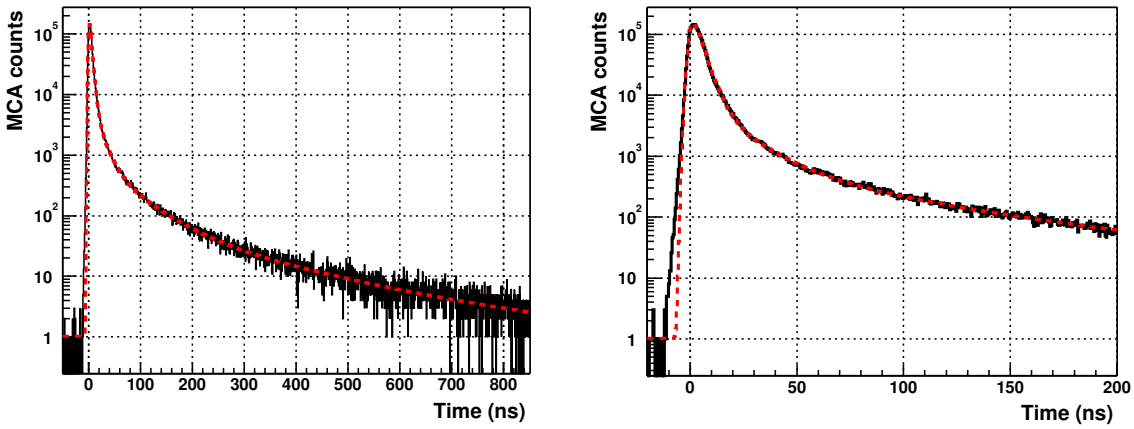

Figure 3.6: *Fluorescence curve of the PXE+p-TP*($2.0\,g/l$) *+bis-MSB*($20\,mg/l$)*sample.*

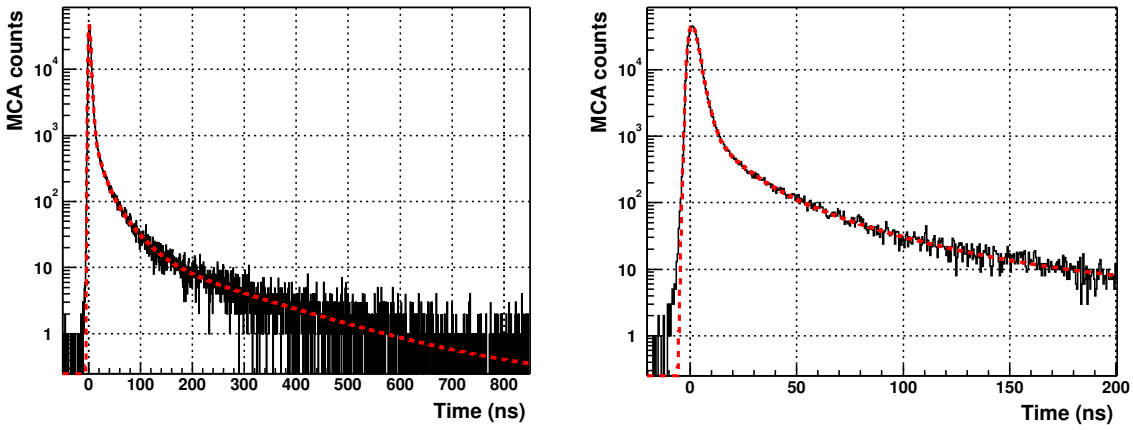

Figure 3.7: *Fluorescence curve of the Yb-loaded scintillator.*

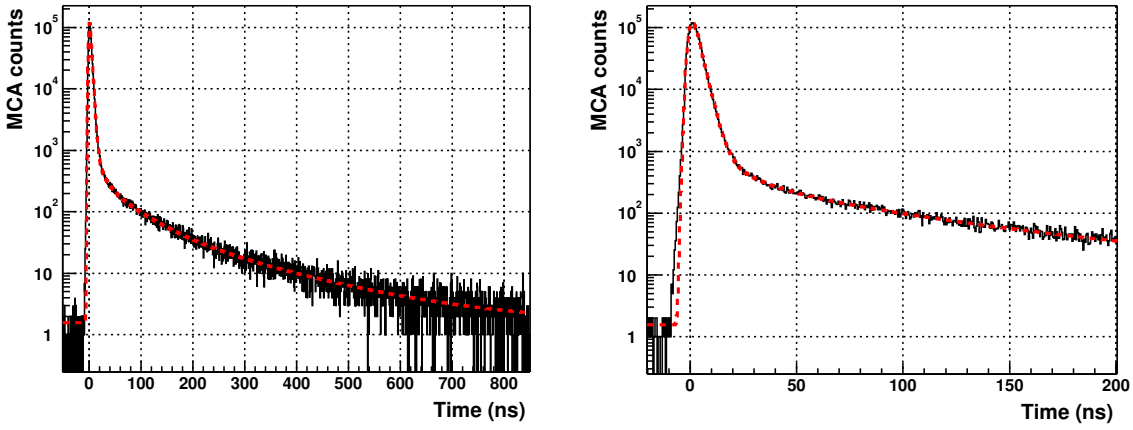

Figure 3.8: *Fluorescence curve of the In-loaded scintillator.*

Table 3.7: *Parameters of the fit of the fluorescence curves. The decay times τ_i and the resolutions $\sigma_{sx,dx}$ are given in ns. Results are presented from either a 3-exp and a 4-exp fit: in some cases 4 exponentials are necessary and with 3 only the fit tries to compensate the missing term by increasing the background. On the other hand, when 3 exponentials are sufficient, the fourth is rather used to fine tune the fit and can lose its physical meaning.*

	τ_1	τ_2	τ_3	τ_4	q_1	q_2	q_3	q_4	σ_{sx}	σ_{dx}
BC505 (3 exp)	1.96	14.1	87.1	/	0.935	0.056	0.009	/	1.4	1.9
BC505 (4 exp)	1.63	3.36	21.4	103	0.716	0.242	0.035	0.007	1.4	1.9
PC + PPO (3 exp)	3.09	23.2	121	/	0.956	0.038	0.006	/	1.3	1.8
PC + PPO (4 exp)	3.09	21.6	73.1	209	0.955	0.037	0.006	0.002	1.3	1.8
PXE (3 exp)	3.87	20.7	127	/	0.853	0.115	0.032	/	1.4	1.8
PXE (4 exp)	3.78	15.4	59.7	215	0.831	0.114	0.040	0.015	1.4	1.8
BL Yb 260F1 (3 exp)	2.31	20.5	144	/	0.893	0.089	0.018	/	1.2	1.5
BL Yb 260F1 (4 exp)	2.23	11.1	34.5	173	0.872	0.070	0.043	0.015	1.2	1.6
BL In 381MP (3 exp)	2.86	28.9	142	/	0.946	0.028	0.026	/	1.3	1.6
BL In 381MP (4 exp)	2.81	13.5	58.0	185	0.939	0.020	0.024	0.017	1.3	1.7

Table 3.8: *First decay time τ_1 for the Borexino PXE scintillator. The entry † is our determination, all the other decay times have been measured by the Borexino collaboration (ref. [Bor04]). The fluorimeter measures the decay time upon UV-excitation. No triplet states are populated, resulting in a reduced late light fraction. However, the fast component is expected to be the same as for electron excitation.*

p-TP concentration	τ_1 fluorimeter	τ_1 γ-source
$2.0\,g/l$	$3.7 - 4.0\,ns$	$3.8\,ns^{\dagger}$
$3.0\,g/l$	$3.2\,ns$	$3.1\,ns$

PMT, has ensured adequate signal-to-background ratio up to $\sim 1\,\mu s$ from the excitation time. Moreover, the background level on the left of the time zero seems reasonably compatible with the count rate in the tail of the fluorescence curve, proving the absence of unaccounted backgrounds. All the fits extrapolate from the experimental curves consistent time resolutions (last two columns in Table 3.7), which are adequate, though the system was not optimized to this regard.

The standard BC505 shows the fastest scintillation response. The main decay constant, $\tau_1 \sim 2\,ns$, is consistent with the BICRON specifications. The PC + PPO ($1.5\,g/l$) mixture exhibits a slower decay time, as a consequence of the low fluor concentration (see [Bir68]). Our results are however not completely consistent with those reported in [RGL98] for Borexino, where the authors find a still slower first decay constant ($\tau_1 \simeq 3.6\,ns$) and a larger fraction of late light. The PXE + p-TP ($2.0\,g/l$) + bis-MSB ($20\,mg/l$) sample shows the slowest response. Our results are consistent with those reported in [Bor04], as shown in Table 3.8.

The performance of both metal-loaded samples from Bell Labs is in the same range of the benchmark scintillators, either for the main decay constant and for the relative fraction of

slow light, in spite of the high metal concentration, the large non-aromatic volume fraction and the presence of other chemicals. Thus there is no experimental evidence that the metal loading degrades the scintillator fast response or leads to a larger fraction of late light. The consequence is that spatial resolution and signal pulse shape in LENS are not degraded by the presence of the metal. However, the measured total weight of the slow components in the Yb sample is non negligible, $\sim 10\%$. A large fraction of this light is emitted in the time window of the ν-tag ($t \gtrsim 30ns$), enhancing the probability of fake ν identification from statistical fluctuations of the pulse shape of single events, as discussed in Sec. 2.3.3. The impact of late fluorescence on this background will be studied in Sec. 7.1.

Chapter 4

Measurements of Light Piping for Application in LENS Cells

4.1 Introduction

In Sec. 2.4.3 the problem of guiding light to the PMTs in the Indium-LENS concept has been introduced. As an example, in Fig. 4.1 the results of a Monte Carlo simulation of a $5\,cm \times 5\,cm \times 200\,cm$ cell are reported, where light propagation is based on Total Internal Reflection (TIR), the medium has $n = 1.5$ and an absorption length of $4\,m$. The figure displays the expected distribution of the number of reflections at the cell-to-air interface before a photon reaches a PMT (ideal TIR is assumed). The mean is 48 reflections, the most probable number $\simeq 35$. For an order of magnitude estimation, if R is the real TIR reflectance, I the light intensity at the PMT, I_0 the limit intensity for $R = 100\%$, then $I \sim I_0 R^n$, where n is the average number of reflections. For $n = 48$, $I/I_0 > 0.5$ requires $R \gtrsim 98.5\%$. The In-LENS concept is therefore very demanding in matter of light piping. For this reason a campaign of measurements has been carried out, aiming at testing whether such stringent demands can be met with commercially available technology.

In Sec. 4.2 the main mechanisms useful for light guiding in a scintillation cell are outlined: TIR and Specular Reflection (SR). Sec. 4.3 describes the samples that have been measured for both TIR and SR. Sec. 4.4 reports on the measurements of absolute mirror-like reflectance of samples suitable for SR light guiding in LENS cells. Sec. 4.5 gives a description of the method employed to measure and analyze light piping via TIR and SR in optical modules. The results of these measurements are reported in Secs. 4.6 and 4.7. The conclusions follow in Sec. 4.8.

4.2 Light Piping Mechanisms

In the geometry of a LENS module (Fig. 2.2 on page 41), the solid angle for direct illumination of the PMTs is very small in a large fraction of the volume. Therefore it is necessary to have some other mechanism to guide light to the PMTs. The only two such mechanisms are *total internal reflection* and *specular reflection*.

Total Internal Reflection A natural possibility for light guiding is offered by the change of refractive index at the boundary with air (Fresnel reflection). The efficiency for unpolarized

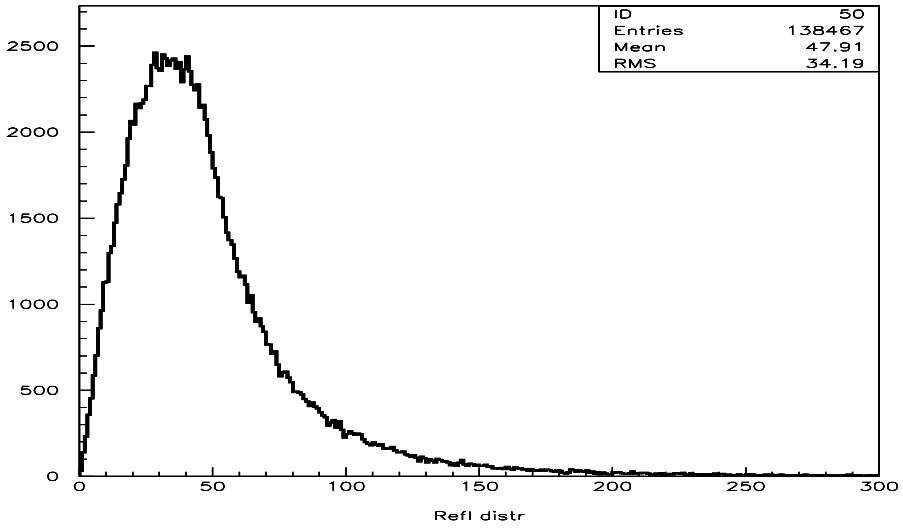

Figure 4.1: *Distribution of the number of reflections before PMT, for a source* $2\,m$ *distant in a* $5\,cm \times 5\,cm \times 200\,cm$*cell with absorption length of* $4\,m$*. A square geometry and ideal TIR piping are assumed (the MC simulations of optical modules are described in Chapter 6).*

light is given by (see e.g. [BW64]):

$$R = \frac{1}{2}\left[\left(\frac{\tan(\theta_i - \theta_r)}{\tan(\theta_i + \theta_r)}\right)^2 + \left(\frac{\sin(\theta_i - \theta_r)}{\sin(\theta_i + \theta_r)}\right)^2\right] \tag{4.1}$$

where $\theta_{i,r}$ are the angle of incidence and refraction respectively, related with each other and with the refractive index by the Snell's law. For a medium with $n \sim 1.5$ (typical range of many organic liquids and as well of materials that can be used for a cell, such as glass, quartz or acrylic), eq. 4.1 has a plateau at $\simeq 4\%$ for $\theta_i \lesssim 35°$, then goes up to 100% at the *critical angle* θ_c:

$$\theta_c = \arcsin(1/n) \tag{4.2}$$

which gives $\theta_c \simeq 42°$. Fresnel reflection is very poor for light piping below θ_c, whereas for $\theta_i \geq \theta_c$ TIR ensures in principle a perfect light guiding. In a TIR-based cell light striking the interfaces with $\theta_i < \theta_c$ is lost after a very short distance, while the rest propagates theoretically without attenuation (as far as light guiding only is concerned). The efficiency of a real system is $< 100\%$, because of losses due to absorption in the cell walls, surface defects and roughness.

Specular Reflection An other option considered for LENS is the design of cells based on specular reflection, nearly equally efficient at all angles. The advantage of SR over TIR is the bonus of recovering the solid angle lost with TIR ($\sim 50\%$ of the total 4π) and, from the point of view of the detector design, the implementation of SR does not need modules physically separated by air gaps. On the other hand, it is hard to find mirrors competing with TIR in matter of reflectance. With a photon survival probability $P = R^n$, the LENS geometry is extremely sensitive to even small departures of R from 100%, as argued in Sec.

4.1. Conventional metallic reflectors with typical $R \lesssim 90\%$ are not suitable. However, the recent development of multi-layer dielectric foils with reported $R \gtrsim 99\%$ at all wavelengths above cut-off and all angles (VM2000 from 3M, ref. [Web00], application in optical modules reported in [Ste02, Bog01]) has made SR appealing for LENS.

Mixed Light Guiding In case $R_{TIR} > R_{SR}$, a design can be chosen that takes the best of the two methods: light should be guided via TIR above the critic angle, otherwise via SR. This is realized by wrapping an optical module in a non-coupled mirror profile. In the implementation in a segmented detector, this solution has also the advantage of isolating neighbouring cells against light cross talk.

4.3 Description of the Samples

4.3.1 VM2000 Reflective Foils

The optical properties of three samples of VM2000 foils by 3M have been studied:

1. The standard version first put on the market by 3M
2. A UV-extended version
3. An improved standard version on the market since 2002

It will be referred to these samples as *old*, *UV* and *new* VM2000, respectively.

4.3.2 Quartz Tubes

Two quartz tubes have been used for the measurements of light piping. One $\simeq 55\,cm$ long, the other $\simeq 110\,cm$ long. Their section is square with rounded corners, with $\simeq 15\,mm$ external dimension, $\simeq 2\,mm$ quartz thickness and $\simeq 2\,mm$ curvature radius at the rounded corners (shown in Fig. 4.4 on page 80). The tubes have been provided by *Heraeus Quartz Glas GmbH*. Materials and surface finishing are similar to those of the final LENS prototype cells (Chapter 8). At one side of the tube a *suprasil* quartz window has been glued for liquid containment.

4.4 Measurements of Reflectance of Mirror Foils

In order to study the reflectance of the VM2000 foils, a *V-W* accessory mounted on a Varian Cary-400 spectrophotometer has been used. The V-W technique allows to measure the specular reflectance of a flat sample, with no need of calibrated references. Fig. 4.2 and its caption describe the principle of the method. The experimental systematics limit the precision of the measurement at the level of $\sim 1\%$ (declared instrumental specification). Reflectance was measured in air, at an incidence angle of 7°, in the near-UV to visible spectrum. In Fig. 4.3 a representative measurement for each one of three investigated VM2000 samples is reported. It has to be remarked that measurements of the same sample can differ from each other up to $\sim 2\%$. This error includes non uniformities of the samples (different spots were probed), as well as the intrinsic systematics of the instrument and the method.

The features of the *old* VM2000 are: cut-off at $\sim 400\,nm$, plateau of $R \simeq 97\%$ in the range $[400\,nm - 440\,nm]$, dip down to $R \simeq 94\%$ in the interval $[440\,nm - 520\,nm]$, $R \gtrsim 98\%$

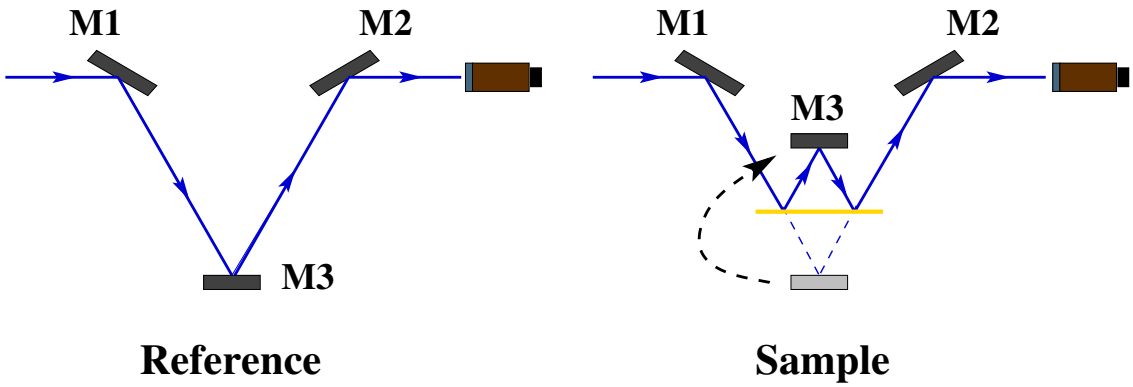

Figure 4.2: *Schematic diagram of the V-W technique applied to measure the absolute reflectance of a sample. The light intensity with the apparatus in the "Sample" configuration (I_S) is compared to the one measured in the "Reference" configuration (I_R). The mirrors M1 and M2 are in a fixed position, while the mirror M3 can be moved as shown on the right side of the figure. The sample to measure is located exactly half way between the two slots for M3. The optical length is the same in the two configurations, as well as the reflectance at the mirrors M1, M2 and M3. The only difference is that light in the right side configuration must reflect twice on the sample. Thus:* $R = \sqrt{I_S/I_R}$. *The result is an average of the sample reflectance in the two illuminated spots. In the V-W accessory of the Varian Cary 400 spectrophotometer the angle of incidence on the sample is* $7°$ *and the instrument is designed to operate in air.*

for longer wavelengths. The *UV* VM2000 has cut-off at $\sim 310\,nm$, a similar spectrum above $400\,nm$, however with slightly lower reflectance in the interval $[400\,nm - 460\,nm]$.

These results are in good agreement with previous measurements [Bog01] and confirm that, above cut-off, *old* and *UV* VM2000 are superior to the best conventional metal-coated mirrors. However their performance is not sufficient for the LENS demands: in LENS the scintillator composition is tuned to shift the emission in the "blue-green" spectrum, $420\,nm \lesssim \lambda \lesssim 500\,nm$, which combines a higher scintillator transparency and good photo-sensitivity of standard PMTs. In that wavelength range the measured average reflectance is $\sim 96\%$.

The *new* VM2000 performs substantially better: the dip has disappeared and the reflectance is constantly $\gtrsim 98\%$ above $420\,nm$, which is of great interest for light piping applications in LENS.

The spectrophotometric V-W measurements of the VM2000 gives important preliminary indications, but further scrutiny is needed, because the systematic uncertainty of the method is too large. The performance of a scintillation module have a very strong dependence on R and hence an error as large as the estimated $\pm 1\%$ results in a huge uncertainty. Furthermore, V-W reflectance is measured in air at near-normal incidence, while in a cell light reflects with a continuous angular distribution from a medium with $n \sim 1.5$. Last, obviously TIR reflectance cannot be measured with the same technique. In order to give a more precise and realistic characterization of TIR and SR, we have set up a system in our dark room for the measurement of light piping in prototype cells, which is described in the next section.

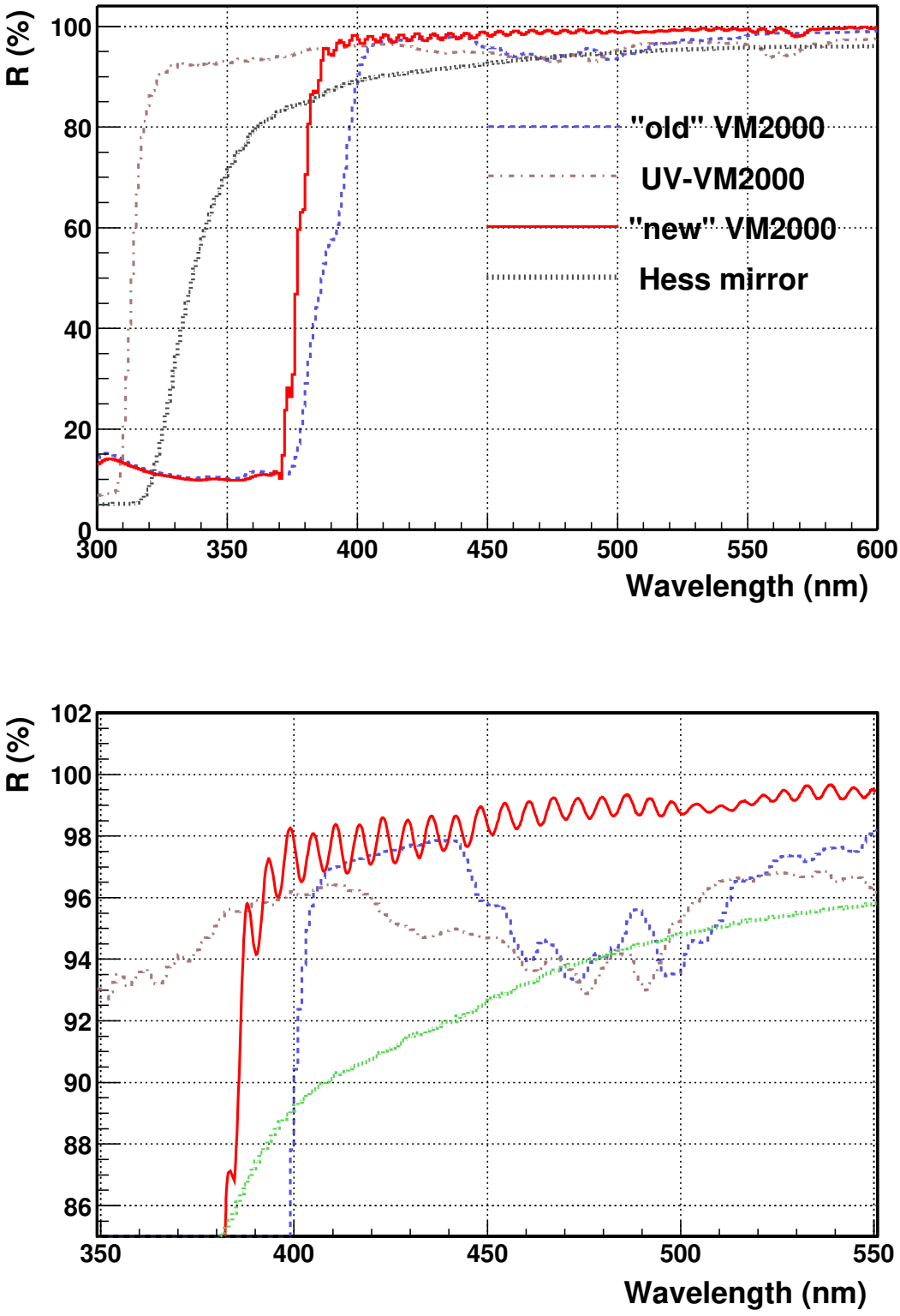

Figure 4.3: *Reflectance spectra of the 3 samples of VM2000 foils. The bottom graphics is the magnification of the top one in the region of interest. For comparison, we also reported the spectrum of an aluminum-coated mirror employed in the "Hess" γ-ray Cerenkov telescope [HES03], measured by us.*

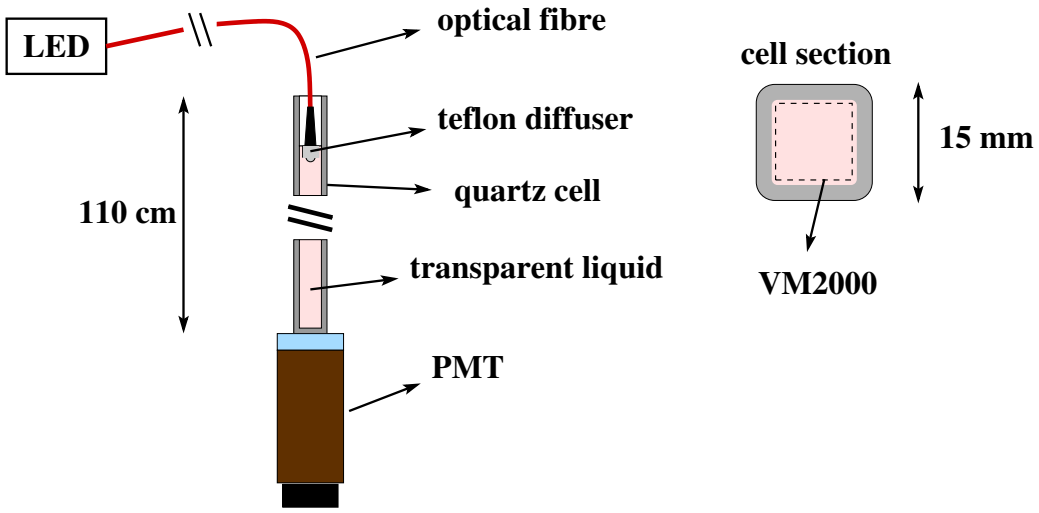

Figure 4.4: *Schematic view of the experimental set-up for light piping measurements. Pulses of monochromatic light are generated with a LED. An optical fiber is coupled to the LED and guides light into a prototype quartz cell. The light intensity is read-out by the PMT at the bottom. The cell is filled with a transparent liquid, which provides the refractive index necessary for TIR light piping. For the measurements of SR piping the cell was lined with a profile of VM2000.*

4.5 Method for the Measurement of Light Piping

4.5.1 The Experimental Set-Up

The aim of the measurements was to characterize light guiding in cells based either on TIR or SR (via VM2000). In order to decouple the light losses due to imperfect reflection from those due to absorption in the liquid, short cells ($l \sim 1\,m$) have been used and optical media featuring very high transparency in the wavelength region of interest (absorption length $\gtrsim 20\,m$). The required high sensitivity in R was obtained by using pipes of small cross-section ($d = 15\,mm$), thus increasing the number of reflections. Only the best performing *new* VM2000 was tested.

A drawing of the setup used for light piping characterization is shown in Fig. 4.4. It consists of a quartz tube coupled to a PMT on one side and open on the other side for filling and insertion of a light fiber, which is coupled to a LED. The LED is connected to an electric circuit developed by the electronic department of the MPIK [Pei03]. Light is emitted in form of fast pulses when the circuit is triggered with an external logic TTL signal. At the free side of the fiber a Teflon diffuser is connected, to isotropize the light direction distribution inside the cell.

The same system has been adapted for the measurement of a SR-based cell: a long square profile of VM2000 is inserted into the quartz tube, so that the quartz internal surface is entirely lined with reflective foils. Dimensions of the VM2000 pipe are: $\sim 9.3\,mm \times 9.3\,mm \times 600\,mm$.

The PMT used is a Photonis XP2262; it is read out by a VME acquisition system (DAQ described in ref. [Las02]). The trigger logic is very simple: a couple of gate & delay generators produces a periodic TTL signal for the LED and a time gate synchronous with the PMT pulse for the VME electronics. Each LED pulse produces a signal in the PMT, that is measured by

an ADC.

The light fiber is deployed at various distances from the PMT. For each position typically 50000 pulses are acquired and the light intensity is determined as the average ADC signal. Each measurement consists of a scan of the light intensity as a function of the distance.

As light source two LEDs have been used, with emission peaked at $380\,nm$ and $430\,nm$. The former delivers pulses very sharp in time, with few ns width (details in ref. [Pei03]), while the latter exhibits a much broader pulse shape ($\sim \mu s$ fall time). In the first case the PMT signal was read by a VME integrating charge-sensitive ADC, in the second it was necessary to use a shaping amplifier and then a peak sensitive ADC. The data acquired with the $430\,nm$ LED are particularly significant for LENS, because the metal loaded scintillators are tuned to have an emission peaked at $\lambda \sim 430\,nm$. Wavelength-shifters are used, such as bis-MSB, which have very high absorption for $\lambda < 400\,nm$, so that typically light primarily emitted in this range is shifted to longer wavelengths before the first reflection. Nevertheless, data for $\lambda = 380\,nm$ provide interesting indications of the reflectance wavelength dependence and give a cross-check for systematics, since the acquisition of the nanosecond LED pulses requires an electronics set-up different from the one used for the slow $430\,nm$ LED.

The cell must be filled with a liquid to simulate a scintillator-like refractive medium. We have chosen "Uvasol" cyclohexane ($n \simeq 1.42$), "Uvasol" ethanol ($n \simeq 1.37$) and "99+%" dodecane ($n \simeq 1.42$), all showing excellent optical properties. All these liquids turned out to be chemically aggressive against the cable of the light fiber and exhibited a degradation of their transparency after prolonged contact with it. Therefore the adopted procedure was to measure the light intensity from the bottom to the top, gradually filling the cell and making sure that at any step only the Teflon diffuser was immersed in the liquid (as in Fig. 4.4). In addition, at the end of each scan the absorbance of the liquid was checked at our spectrophotometer in a $1\,cm$ vial and the measurement validated only if no worsening of the transparency in the wavelength region of interest was observed. The VM2000 was found chemically compatible with ethanol and dodecane, but not with cyclohexane, whose absorbance in the visible increased after contact with the foils.

4.5.2 Data Analysis

A measurement consists of a scan of the light intensity measured by the PMT as a function of the source distance. Due to the small cross section, the solid angle for direct illumination of the PMT is negligible for a large fraction of the cell length and hence the light attenuation curve tests the efficiency of light piping.

Data analysis is not trivial, because many photons are emitted and each propagates in the cell differently, depending on the initial direction. There are paths to the PMT involving a small number of reflections at near grazing incidence, others spiralizing forward, with many reflections at $\theta_i \sim \theta_c$. The observed result is the superposition of all the possible propagation scenarios.

Strategy The measurements have been analyzed by comparing the experimental light attenuation curves with MC simulations, in which the surface reflectance has been tuned to reproduce most closely the data. The simulations are photon-tracing MCs based on a simplification of a more elaborated optical model that will be presented in Chapter 7. Important features implemented in the simulations are:

- Cell geometry, described as a square tube with rounded corners, as in Fig. 4.4
- Two defined volumes: liquid and quartz. They are assumed optically coupled[1], but may have different absorption lengths
- Light reflection at the external surface via Fresnel reflection (eq. 4.1) plus TIR, or SR. The TIR and SR efficiencies are assumed for simplicity constant at all angles and are the "free parameters" of the MC
- Photon interaction with the media, through the definition of an absorption length in liquid and quartz. Interacting photons are considered lost (elastic scattering is neglected)

In the standard analysis a $20\,m$ "guess" attenuation length is assumed for both quartz and liquid, while different values are used to investigate the systematics of the method. *Suprasil* quartz has "virtually" no absorption in the visible range. The liquids utilized have been measured by us at the spectrophotometer and none of them has shown a detectable absorption at the considered wavelengths. In both cases $20\,m$ attenuation length is rather the lower limit given by the sensitivity of the measurement.

Simplified Analysis Both experimental and simulated curves are fitted with a double exponential function:

$$f = I_1 e^{-(x-x_0)/\mu_1} + I_2 e^{-(x-x_0)/\mu_2} \tag{4.3}$$

where x_0 is the distance of the closest data/simulation point (normally $x_0 = 5\,cm$). The empirical fitting function 4.3 has no direct physical meaning and is just intended to give an effective parameterization of the attenuation curves.

Eq. 4.3 fits well both data and MC simulations in all the cases considered. In Fig. 4.5 an example of double exponential fit to data is shown.

The fit returns two effective attenuation lengths (μ_1 and μ_2), the weights at the reference distance x_0 (I_1 and I_2) and the uncertainties for those parameters. The amplitude parameters I_1 and I_2 are not physically meaningful, because the absolute normalization of the light attenuation curves -for data as well as simulations- is not significant in this context. Only the ratio $W_{1,2} = I_{1,2}/(I_1 + I_2)$ is meaningful: it gives the fraction of the intensity measured by the PMT at x_0, which is attenuated with a $\mu_{1,2}$ attenuation length.

The correct modeling of the system behaviour near the PMT can be difficult, because many factors beside pure guiding efficiency can influence the light intensity curve, such as: geometry, anisotropies, optics at the interfaces and interactions with the PMT. In many cases, most important for this study is the longest attenuation component, say μ_2, which characterizes light piping at a distance from the PMT where the effect of such other light-loss mechanisms has decayed out. In a first simplistic analysis procedure the best estimation of the effective reflectance is given as the value producing the simulation with predicted attenuation length closest to data:

$$\mu_2^{sim}(R_{best}) \simeq \mu_2^{data} \tag{4.4}$$

[1] At the wavelengths of the measurements, quartz has $n \simeq 1.47$, the optical liquids used to fill the cell $n \simeq 1.42$. Since $n_{liquid} < n_{quartz}$, the critic angle for TIR depends only on the ratio of the refractive indices of liquid and air, as a consequence of the Snell's law. Light refraction at the liquid-quartz crossing causes a small deviation of the ray path in quartz, which is considered negligible.

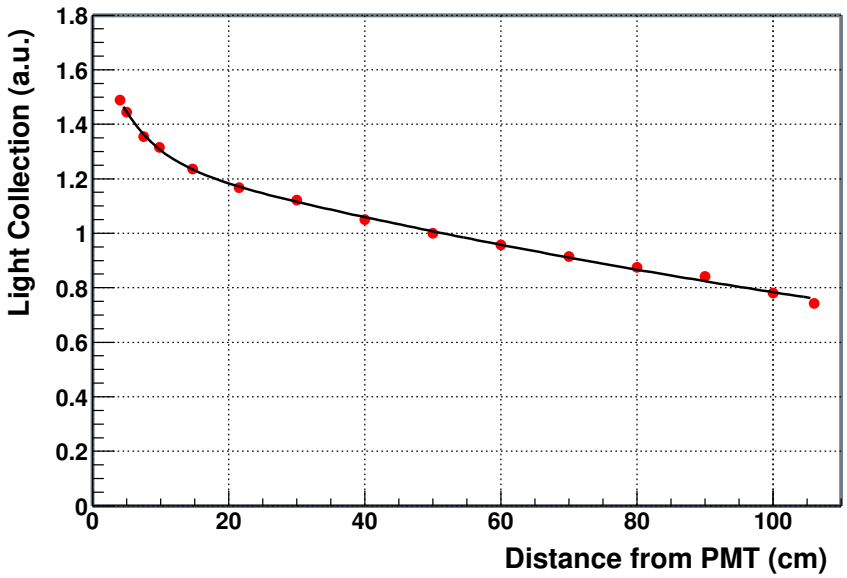

Figure 4.5: *Example of double exponential fit (solid black line) on real data (red markers). Data are normalized to 1 for* $d = 50\,cm$.

The $\pm 1\sigma$ error is estimated from the reflectance interval at either sides of R_{best} for which μ_2^{sim} is still compatible with μ_2^{data}. This procedure simplifies the analysis, compared to fitting data with a parametrized MC, and has the advantage not to depend on the normalization of data and simulations (only attenuation lengths are used).

χ^2 Analysis An other data-analysis approach, technically more correct, however posing some more difficulties, is the standard χ^2 fit to data with a MC, with the effective reflectance R as free parameter. The MC simulations are used only to predict the shape of the light attenuation curves, hence there is still a free normalization between data and simulations. For simplicity, not to introduce a new fit parameter, both experimental and predicted curves are normalized to 1 at a central position of the scan (for instance at $d = 50\,cm$, as in Fig. 4.5).

Due to computation time, only a few simulations for a limited set of values of R, $\{R_j\}$, are performed and for each one the χ^2 of the fit is evaluated as:

$$\chi^2\left(R_j\right) = \sum_{i=i_0}^{n} \left(\frac{data(x_i) - MC_j(x_i)}{\sigma} \right)^2 \tag{4.5}$$

The first used data-point x_{i_0} is chosen at a distance where the simulations reproduce correctly the shape of the experimental attenuation curve.

The set of $\chi^2\left(R_j\right)$ is fitted with a parabolic function of R and the point of minimum is chosen as a best estimation of the effective pipe surface reflectance.

In order to use the χ^2 analysis also to estimate confidence intervals, two conditions must be fulfilled:

1. The model must reproduce exactly the data, for a proper choice of the free parameters.

2. The error σ at denominator in eq. 4.5 must be precisely known. This is the sum in quadrature of the statistical error of the simulation and the experimental error of the light intensity.

The first condition has indeed to be proven and cannot be simply assumed. In many cases we observed that the model is in good qualitative agreement with the experimental curves, however there are statistically significant departures between MC and data, namely simulations reproducing well the tail of the attenuation curves are often in less good agreement with the first part, and vice versa. It is for this reason that the χ^2 function 4.5 is evaluated from x_{i_0}, assuming that the tail of the curves is more significant for the estimation of the reflectance. For condition 2, the calculation of the statistical error of the simulation is trivial, whereas it is more difficult to make a precise experimental determination of the error of the single light intensity in a scan sequence. This error is systematic-dominated, because the number of acquired LED pulses per position is sufficient to limit the statistical error to $< 0.1\%$, while data show a much larger scatter. Unfortunately not enough data was collected to estimate the standard deviation from repeated measurements. Therefore a usual statistical procedure is applied, which consists in fitting data with a suitable function and evaluate *a-posteriori* the mean standard deviation from the point-to-point scatter with respect to the best fit:

$$\bar{\sigma}_{data} = \sum_{i=1}^{n} \frac{(data(x_i) - f_{best}(x_i))^2}{n - p} \tag{4.6}$$

where n is the total number of data-points and p the number of parameters of f.

Eq. 4.6 gives a good approximation of the real experimental error only if the fit function is an exact model of the data, otherwise the error is overestimated, because it includes the systematic departure of the fit function from data. Besides, it makes sense to apply eq. 4.6 only if all the measured points are expected to have the same error. Given the χ^2 definition in eq. 4.5, it is obviously not possible to use a MC simulated curve as fit function for eq. 4.6, hence eq. 4.3 is used and it is pragmatically assumed that eq. 4.6 holds.

Both the methods described above, $\mu_2(R)$ and $\chi^2(R)$, are applied for the analysis of the TIR measurements and lead to consistent results. However, it turned out that none of them is suitable for the analysis of the SR data (a discussion will be found in the relevant section). For this case the analysis relies on a qualitative "visual" comparison of data and MC simulations, with estimated errors correspondingly enlarged.

4.6 Measurements of TIR

Several light collection scans have been acquired, both at $380\,nm$ and $428\,nm$ wavelength. Only those satisfying the following criteria were selected:

1. System stable during the measurement (no gain drifts, good reproducibility)
2. Liquid used not optically degraded after the measurement (transparency checked at the spectrophotometer)

The two items are closely related, since most of the times the measurement was not reproducible because the liquid had been contaminated by accidental contact with the light fiber cable.

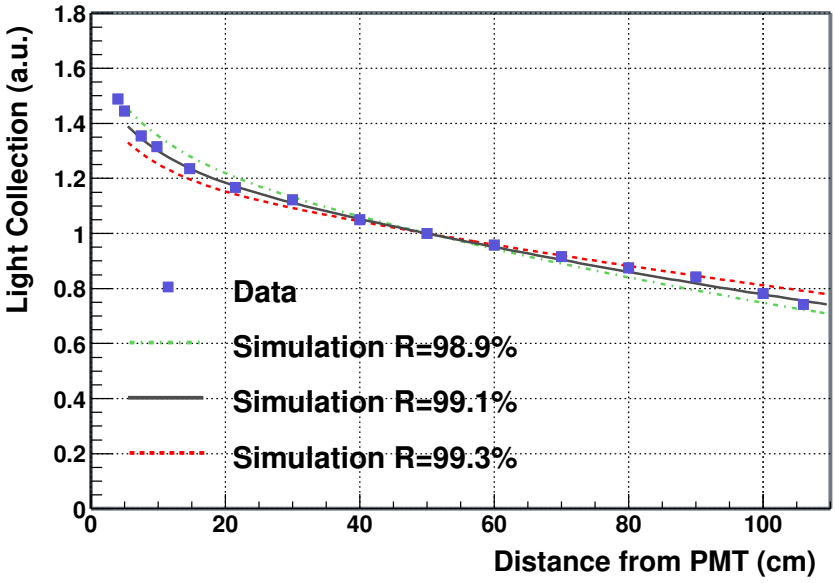

Figure 4.6: *Measurement of light intensity as a function of distance from the PMT, at* $\lambda = 380nm$. *The filling liquid is cyclohexane. Three MC simulations are shown, for TIR reflectance of* 98.8%, 99.0% *and* 99.2% *and an assumed attenuation length* $\mu = 20\,m$, *both in liquid and quartz. The curves are arbitrarily normalized to 1 at* $d = 50\,cm$. *The mean standard deviation of the single measured point, calculated with eq. 4.6, is* $\sigma_{data} \simeq 0.01$, *i.e.* $\sigma_{data}/data \sim 1\%$.

4.6.1 Measurements at 380 nm

Fig. 4.6 shows the results of the measurement at $380\,nm$ and for comparison three MC simulations of the system. The quality of data is good: no jumps or irregularities are present, thus proving that the cell has a homogeneous surface quality. The rms of the measured light intensities with respect to the best fit with eq. 4.3 is $\sim 1\%$ and the experimental curve is well reproduced by the MC simulations. Table 4.1 reports the parameters of the fit to data and simulations with eq. 4.3.

A simple "visual" analysis of the figure suggests that the best estimation for the effective reflectance is $R_{TIR}(380\,nm) \simeq 99.1\%$. This is confirmed by a comparison between the measured and simulated attenuation length. Making a linear extrapolation for the function $\mu_2(R)$ from data in Table 4.1 and considering only the statistical error of μ_2 for data and MCs, it is found:

$$R_{TIR}(380\,nm) = (99.11 \pm 0.04)\% \tag{4.7}$$

The $\chi^2(R)$ function for the fit with the MC is shown in Fig. 4.7. For this analysis the first two points are not used, because they are not well fitted by the simulations.

The reflectance giving the minimum χ^2 is $R = 99.12\%$ and $\chi^2_{min}/dof = 0.981$ for (13 points$-$2 constraints) $= 11\,dof$. If the first two rejected data-points are also included, it is found $R = 99.06\%$ and the fit is less good ($\chi^2/dof = 3.99$ with $13\,dof$).

Since the MC fit without the first two data-points is statistically good, it makes sense to

Table 4.1: *Fit parameters of data and MCs for the TIR light piping measurement at* $\lambda = 380nm$. *See Sec. 4.5.2 for the definition of the parameters.*

	W_1	$\mu_1(cm)$	W_2	$(\mu_2 \pm \sigma)\,(cm)$
Data	0.126	5.5	0.874	199 ± 6
MC $R = 98.9\%$	0.109	8.1	0.891	168 ± 2
MC $R = 99.0\%$	0.105	7.5	0.895	180 ± 2
MC $R = 99.1\%$	0.104	7.7	0.896	197 ± 2
MC $R = 99.2\%$	0.102	7.5	0.898	215 ± 2
MC $R = 99.3\%$	0.108	8.2	0.892	244 ± 4

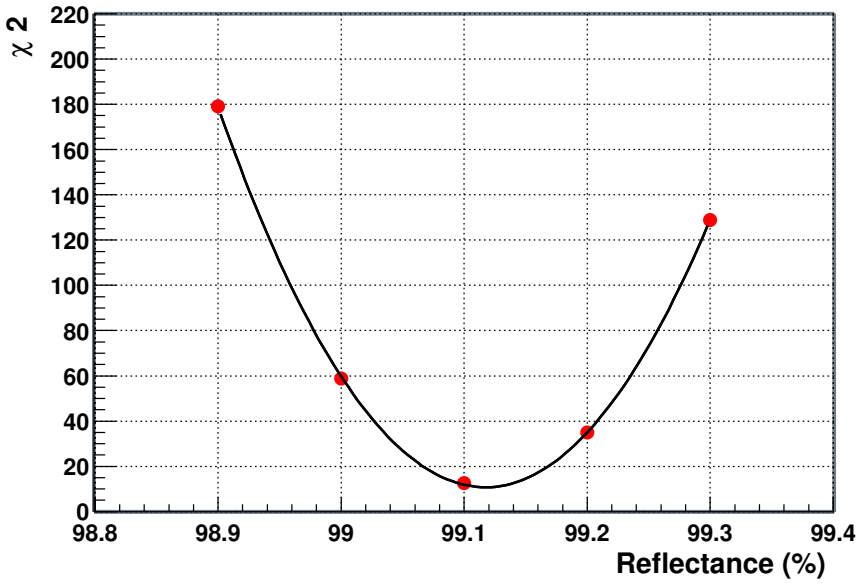

Figure 4.7: $\chi^2(R)$ *function for the fit of the measured light intensity scan with MC simulations. The markers represent the* χ^2 *values for the simulated reflectances, the solid line is a parabolic fit. The* χ^2 *was calculated with eq. 4.5, where* $i_0 = 3$ *(the first two points are not used). The minimum of the curve is found for* $R \simeq 99.12\%$.

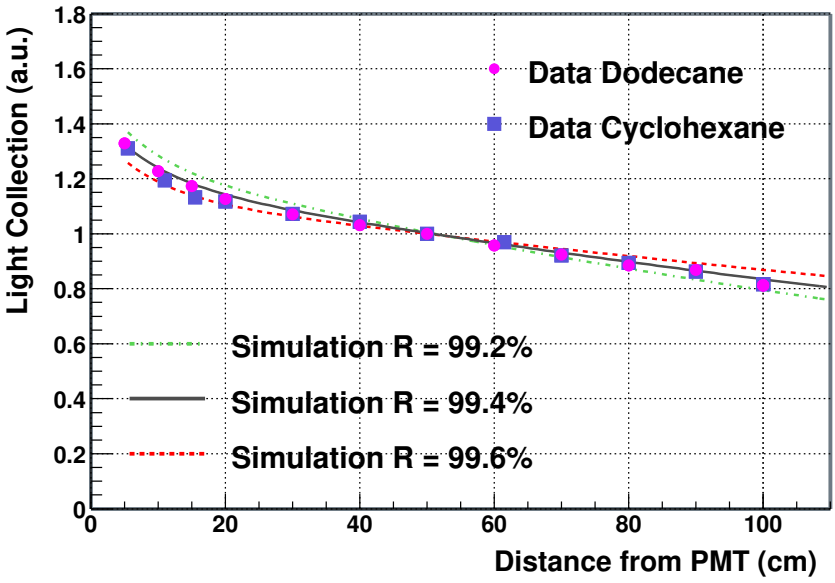

Figure 4.8: *Measurement of light intensity as a function of distance from the PMT, for* $\lambda = 430\,nm$. *For this wavelength two measurements are available, one with cyclohexane and the other with dodecane as filling liquid. Three simulations for different TIR reflectance are superimposed. The curves have been arbitrarily normalized to 1 at* $d = 50\,cm$.

estimate the $\pm 1\sigma$ interval, by solving for $\chi^2(R) = \chi^2_{min} + 1$. It is found:

$$R = (99.12 \pm 0.02)\% \tag{4.8}$$

which is in good agreement with the estimation of eq. 4.7.

Both parameters used in the analysis, $\mu_2(R)$ and $\chi^2(R)$, are very steep functions of R, so that the sensitivity of the measurement is at the level of few 10^{-4} in σ_R/R. This is a consequence of the chosen set-up, in particular of the small cross-section of the quartz tube, which turns into a high sensitivity in R. The systematics are however not included. In Sec. 4.6.3 it is discussed how the systematic errors can be estimated and a final result will be given.

4.6.2 Measurements at 430 nm

Fig. 4.8 shows the measurements with the $430\,nm$ LED, carried out in cyclohexane and dodecane. In Table 4.2 the same analysis is reported, as in Table 4.1.

We observe that the two sets of measurements are consistent with each other and this is significant, since different liquids have been used. The agreement with the MC predicted attenuation curves is also good, though the measurements show in comparison a systematic faster attenuation in the first part of the scan.

The analysis of the long attenuation length leads to:

$$R = (99.35 \pm 0.05)\% \tag{4.9}$$

Table 4.2: *Same as Table 4.1, for* $\lambda = 430\,nm$

	W_1	$\mu_1\,(cm)$	W_2	$(\mu_2 \pm \sigma)\,(cm)$
Data Cyclohexane	0.110	3.6	0.890	260 ± 7
Data Dodecane	0.110	6.4	0.890	257 ± 7
MC $R = 99.2\%$	0.102	7.6	0.898	213 ± 3
MC $R = 99.3\%$	0.109	8.4	0.891	244 ± 5
MC $R = 99.4\%$	0.109	8.5	0.891	274 ± 9
MC $R = 99.5\%$	0.113	9.0	0.887	320 ± 7
MC $R = 99.6\%$	0.106	8.0	0.894	359 ± 9

The χ^2 analysis is in this case more difficult, because the MC reproduces data sufficiently well only at far distances, $d \gtrsim 20\,cm$. For example, a combined analysis of the two measurements, in which only data for $x \geq 30\,cm$ are used, leads to:

$$R = (99.36 \pm 0.02)\% \tag{4.10}$$

with $\chi^2_{min}/dof = 1.56$. Using all available data-points would lead to $R = 99.43\%$ and a bad fit ($\chi^2_{min}/dof = 3.3$).

4.6.3 Discussion on Systematics and Final Results

The results given in the preceding sections do not include systematic errors. These are now discussed.

This data analysis is based on the comparison with MC simulations and hence depends on the assumed input parameters and on the approximations of the model. A large model inaccuracy is unlikely, because the system has a relatively simple geometry, a single wavelength and a very high attenuation length. Nevertheless, the simulations may not reproduce correctly the reality, for example because the light pipe may not behave as an ideal system (e.g. due to non-uniformities) and because the model itself may be too simplistic or its assumptions wrong.

The effect of two such systematics are considered:

1. Departure of the real geometry from the simulated one

2. Attenuation length in the propagation media

The model first used to carry out a preliminary analysis assumed for simplicity a perfect square geometry. It is interesting to evaluate how such inaccurate simulations compare to those presented in the previous sections, in which the more realistic geometry with rounded corners is implemented.

For point 2, $\mu = 20\,m$ in quartz and optical liquid has been simply assumed. Measuring very low absorbance at the spectrophotometer free-of-systematics is very hard, either because the sensitivity of the instrument is not sufficient and because there is no reference to com-

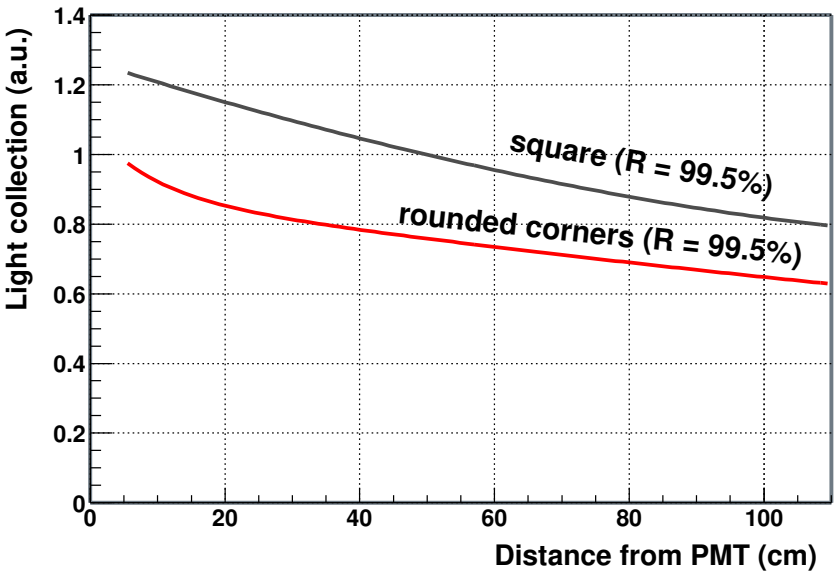

Figure 4.9: *MC predictions of light attenuation curves. The dark gray line is the output for a perfect square geometry* $15\,mm \times 15\,mm \times 1060\,mm$*, the red line that for a cell with rounded corners (radius of curvature* $2\,mm$*). The former is arbitrarily normalized as in preceding figures, the latter is scaled accordingly (so that their ratio is preserved). The same attenuation length* ($20\,m$) *and surface TIR reflectance* (99.5%) *is assumed.*

pare the sample with[2]. Also in this case it is interesting to test how the MC predictions change when the attenuation length in the media varies within the interval allowed by the spectrophotometric measurements.

Geometry Fig. 4.9 shows the MC simulation calculated for the perfect square geometry and for the base case of square geometry with rounded corners. Both curves are computed for a common TIR reflectance, $R = 99.5\%$.

The model predicts that the effect of the rounded corners on light propagation is dramatic: already at $5\,cm$ distance, more than 20% of the light that would otherwise be detected is lost. However, the surviving light propagates with longer attenuation length. This happens because it is mostly the "spiralizing" photons that escape at the corners (those with incidence little above the critic angle and small forward component, which need to reflect the most before getting to the PMT). Light surviving the corners selection is more "forward-oriented" and hence weaker attenuated.

In Table 4.3 the fit parameters of some examined variant MC simulations are reported. A comparison with Table 4.2 shows that using the perfect square geometry would lead to a $\sim 0.25\%$ higher TIR reflectance estimation (data consistent with $R \simeq 99.25\%$ would be best

[2] A standard analysis procedure uses "self-referencing", i.e. the absorbance of a sample at a certain wavelength is compared with the minimum of absorbance in the spectrum, assumed to be 0 (see ref. [Buc04]). This procedure cannot be applied for the case of very transparent samples, since the absorbance spectra are nearly flat and the effect of the wavelength-dependent Fresnel light losses are a dominant systematics.

Table 4.3: *MC predictions for a common TIR reflectance, $R = 99.5\%$. The "base case" is the one discussed in the text. In the other rows variations are considered: square section, infinite attenuation length, poor attenuation length (5 m in liquid, 10 m in quartz).*

	W_1	$\mu_1\ (cm)$	W_2	$\mu_2 \pm \sigma\ (cm)$
MC base case	0.113	9.0	0.887	320 ± 7
MC square	~ 0	...	~ 1	229 ± 3
MC $\mu = \infty$	0.101	7.3	0.899	372 ± 8
MC $\mu = 5m/10m$	0.111	8.8	0.889	228 ± 4

fitted by the "wrong" simulation with $R = 99.5\%$). We also observe that the predicted shape of the light attenuation curve without rounded corners is nearly a perfect single exponential and does not fit the data, which prefers a double exponential function, as the "best" simulations do.

The case studied above is an example that shows to which extent wrong assumptions on the geometry can affect the analysis. It might be argued that the idealization of the geometry as square with circular corners, which was assumed to derive the best reflectance values, still departs from reality. Considering that the perfect square section model is certainly a much rougher approximation, we conclude that the systematic error due to the departure of the real geometry from the simulated one must be much smaller than 0.25%: $\sim \pm 0.1\%$ seems a reasonable guess.

Attenuation In Fig. 4.10 the effect of the assumptions on the liquid and quartz attenuation lengths is studied. Data in Tables 4.3 and 4.2 show that for a real TIR reflectance $R = 99.5\%$ the considered uncertainty in the attenuation length would lead to a $^{+0.15}_{-0.25}\%$ systematic error. However, an attenuation length as short as $5\,m$ would be clearly at reach of the spectrophotometer sensitivity in a $1\,cm$ vial and an infinite attenuation length is not a realistic assumption. Therefore, it seems reasonable to reduce such error to $\sim \pm 0.1\%$.

Other Systematics and Conclusions Other possible systematics related to the model dependent analysis are: non perfect source isotropy, light elastic scattering, unimplemented optics at the liquid to quartz and quartz to PMT interfaces, etc. Their total contribution is estimated not to exceed the one of the systematics examined, hence $\sim \pm 0.1\%$.

Last, an experimental error might come from drifts in the gain of the PMT and subsequent electronics. The high voltage for the PMT had to be switched off and on before any new measured point to move the light fiber and fill the cell. It is then questionable whether the PMT could recover each time to the same gain. However, it was observed by repeated tests at constant distance that the results were reproducible.

In conclusion, the estimated TIR reflectance at the two investigated wavelengths is:

$$\begin{aligned} R_{380} &= (99.1 \pm 0.2)\% \\ R_{430} &= (99.35 \pm 0.2)\% \end{aligned} \tag{4.11}$$

where the estimated errors are the sum in quadrature of the four considered uncertainties (statistic, systematic related to the geometry, systematic related to the absorption, other systematics).

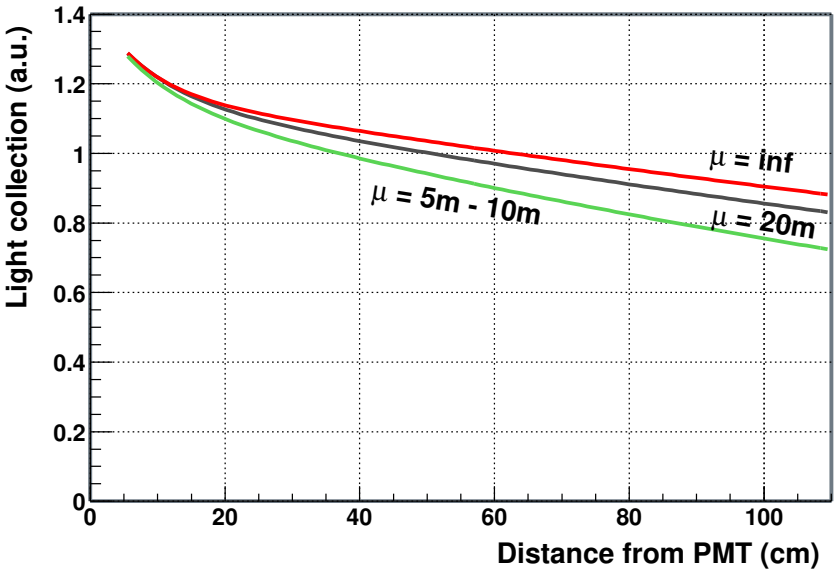

Figure 4.10: *MC predictions of light attenuation curves. The dark gray line is the output for the base case $\mu = 20\,m$; the red line that for a cell with infinite attenuation length; the green curve was calculated for $\mu = 5\,m$ in liquid, $\mu = 10\,m$ in quartz. The curve with no attenuation is arbitrarily normalized as in preceding figures, the others are scaled accordingly. In all the MCs the same surface TIR reflectance is assumed ($R = 99.5\%$).*

In principle, there should be no reason why for TIR $R(380\,nm) \neq R(430\,nm)$, however the two measured values in eq. 4.11 do differ from each other, though they are compatible within the uncertainties. In fact, all the considered systematic errors are wavelength independent, except the contribution related to the absorption length. Considering only this systematic error and summing in quadrature with the statistic error of each measurement (where the more conservative estimation from the $\mu_2(R)$ method is used), it is found: $R_{430} - R_{380} = (0.25 \pm 0.16)\%$, which is statistically compatible with zero at $\sim 12\%$ of confidence level.

4.7 Measurements of VM2000-SR

The measurements of specular reflectance have been carried out in a similar way, as described for TIR. Data were also collected at $\lambda = 380\,nm$ and $\lambda = 430\,nm$. Since SR piping does not necessarily need a medium with refractive index $n > 1$, measurements were performed either in liquid (ethanol and dodecane) and in air. This permits to test whether the VM2000 performance is medium-independent, which might be not true, because the giant reflectance is based on birefringence [Web00], therefore it may be affected by the optics of the medium coupled to the foils. Besides, the measurements in air, which are free of possible biases related to the liquid and its optical properties, offer an independent check of the spectrophotometric results for the reflectance at near normal incidence, reported in Sec. 4.4, however probing a wider angular range.

The model used to interpret data is simpler than for TIR, because neither quartz walls, nor rounded corners must be implemented. On the other hand, the foils are flexible and hence the VM2000 pipe has no perfectly flat surfaces, nor a strictly constant section.

4.7.1 Measurements at 380 nm

We expect from the V-W measurement (Sec. 4.4) the *new* VM2000 reflectance at $\lambda = 380\,nm$ to be rather poor. The spectrum has a sharp cut-off around this wavelength, hence a precise determination from the spectrophotometric data is difficult. In fact, assuming that the LED spectrum is a narrow peak at $\lambda = (380 \pm 5)\,nm$, the mean reflectance from the V-W data could be any value between $\sim 30\%$ and $\sim 90\%$.

Figs. 4.11 and 4.12 report the measured light intensity scans for the cell filled with air and dodecane respectively, together with the predictions of MC simulations. At a first glance, data either in air and in liquid seem consistent with reflectance between 95% and 97%.

It has to be remarked that in this case, due to the relatively poor reflectance and smaller pipe cross section, the short distance part of the curves gives the highest sensitivity to the reflectance parameter, while the tail contributes less. This is clearly seen by comparing the predictions of the MC simulations for $R = 95.0\%$ and $R = 97.0\%$. We conclude *a posteriori* that it would have been desirable to have more data points in the first part of the curves, even at a shorter distances than $5\,cm$.

A full analysis of these measurements is not carried out, because the VM2000 reflectance at $\lambda = 380\,nm$ does not play an important role for the LENS project. The conclusion from a visual qualitative analysis is that $95.0\% \lesssim R_{VM2000}(380\,nm) \lesssim 97.0\%$, with no apparent difference between reflectance in air and in dodecane.

This result is much better than expected. An explanation for this "too good" performance is given by the observation that some of the plastic layers of the foils scintillate [Lor02]. Further

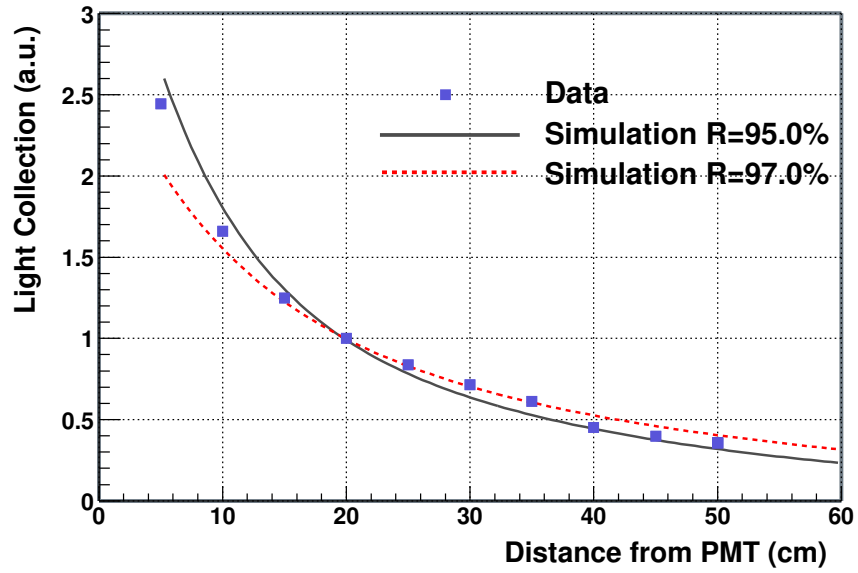

Figure 4.11: *Measurement of light intensity as a function of distance from PMT, for a VM2000 light pipe in air, at* $\lambda = 380\,nm$*. The predictions of MC simulations for SR reflectance of* 95% *and* 97% *are also shown. The light intensity curves are arbitrarily normalized to 1 at* $d = 20\,cm$*.*

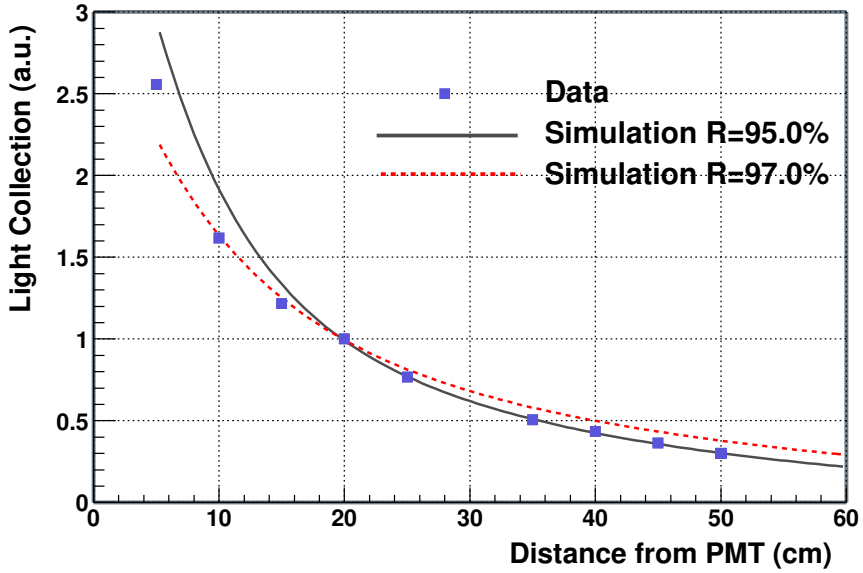

Figure 4.12: *Measurement of light intensity as a function of distance from PMT, for a VM2000 light pipe in dodecane, at* $\lambda = 380\,nm$*.*

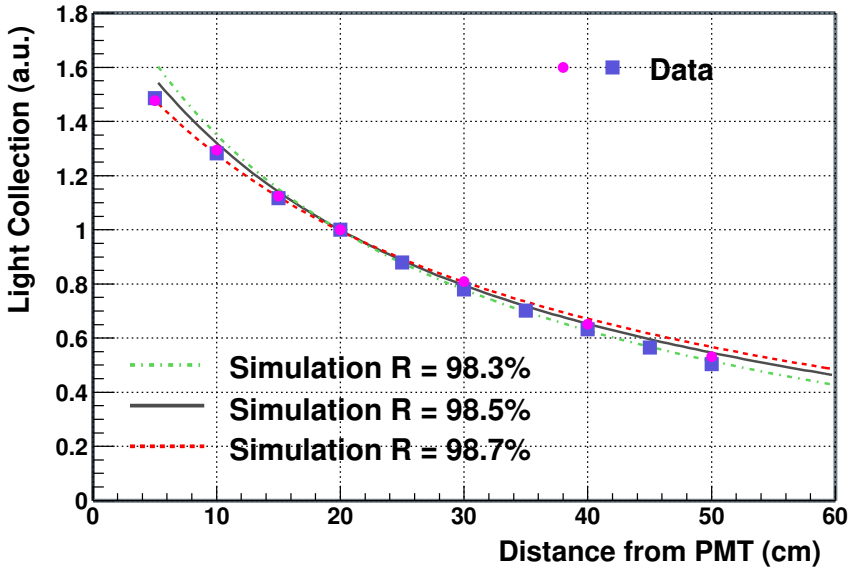

Figure 4.13: *Measurement of light intensity as a function of distance from PMT, for a VM2000 light pipe in air, at* $\lambda = 430\,nm$. *The predictions of MC simulations for SR reflectance of* 98.3%, 98.5%, *and* 98.7% *are also shown. The light intensity curves are arbitrarily normalized to 1 at* $d = 20\,cm$.

investigations carried out at MPIK have confirmed that the VM2000 do act as a wavelength-shifter below the cut-off for giant reflection [MS04]. In this wavelength range absorption dominates (transmission is at the level of $\sim 4\%$) and the λ-shifting quantum efficiency can be as good as $\sim 50\%$ of that of a standard fluor like BPO. This means that light absorbed by the VM2000 is reemitted at longer wavelength about half of the times BPO does (BPO has virtually $QE \sim 100\,\%$). The peak of the emission is at about $420\,nm$. The MC simulations in figs. 4.11 and 4.12 do not include such a feature. It is likely that a large part of the light surviving the $5\,cm$ distance of the first data point has already been shifted to a range where the VM2000 is an efficient reflector.

4.7.2 Measurements at 430nm

Also for $\lambda = 430\,nm$ data were taken in air and in optical media. Figs. 4.13 and 4.14 report the results and the MC predictions. In Tables 4.4 and 4.5 the parameters of the 2-exp fit to data and MC simulations are reported, in analogy with tables 4.1 and 4.2.

It is first observed that the simulations do not reproduce perfectly the data. The experimental curves tend to behave as "high" reflectance models predict at short distances and as "low" reflectance models at further distances, with turning point around $d \sim 20\,cm$. It is not possible to find a unique simulation reproducing data equally well over the entire range of probed distances. The interpretation of data is in this case more difficult and ambiguous. Using only the tail of the curves to estimate the reflectance is in this case less appropriate, for two reasons:

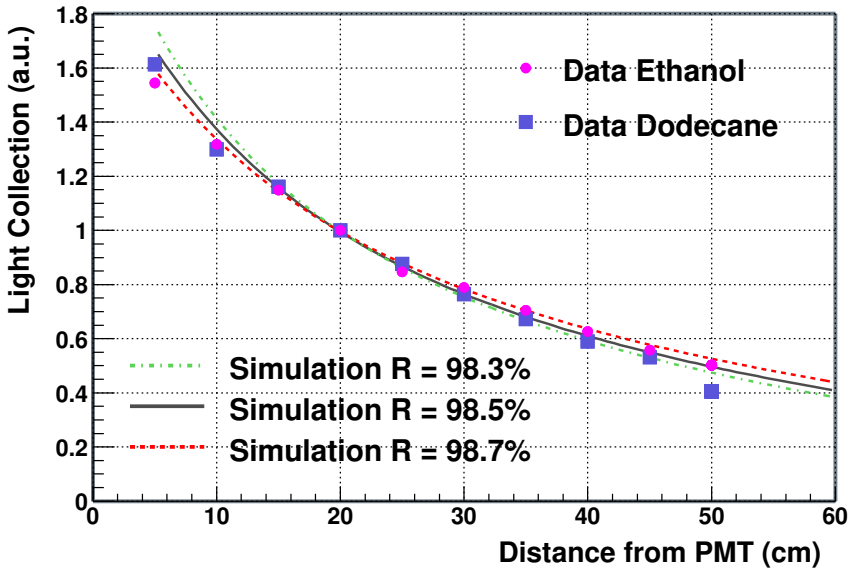

Figure 4.14: *Measurement of light intensity as a function of distance from PMT, for a VM2000 light pipe, at* $\lambda = 430\,nm$. *The pipe was filled with ethanol (round markers) and dodecane (square markers).*

Table 4.4: *Fit parameters of data and MCs for VM2000-SR light piping in air at* $\lambda = 430\,nm$

	W_1	$\mu_1\ (cm)$	W_2	$(\mu_2 \pm \sigma)\ (cm)$
Data run1	0.095	7.9 ± 1.9	0.905	45.8 ± 1.0
Data run2	0.129	10.6 ± 3.0	0.871	50.5 ± 2.6
MC $R = 98.3\%$	0.302	11.6 ± 1.2	0.698	55.9 ± 3.2
MC $R = 98.5\%$	0.322	13.1 ± 0.3	0.678	65.2 ± 1.0
MC $R = 98.7\%$	0.281	13.9 ± 0.3	0.719	68.4 ± 0.9

Table 4.5: *Fit parameters of data and MCs for VM2000-SR light piping in liquids at* $\lambda = 430\,nm$. *The fit of the dodecane curve was done excluding the point at* $d = 50\,cm$.

	W_1	$\mu_1\ (cm)$	W_2	$(\mu_2 \pm \sigma)\ (cm)$
Data dodecane	0.082	0.40 ± 0.03	0.918	38.7 ± 0.3
Data ethanol	0.243	13.0 ± 1.7	0.757	51.9 ± 2.5
MC $R = 98.3\%$	0.325	10.0 ± 0.4	0.675	48.5 ± 1.2
MC $R = 98.5\%$	0.331	11.4 ± 1.2	0.669	54.0 ± 3.7
MC $R = 98.7\%$	0.303	11.8 ± 1.8	0.697	58.6 ± 5.1

1. the dimension of the pipe is smaller and the reflectance of the foils lower, hence the dynamics of light attenuation is much faster and the first measured data points are as important as the others

2. in the measurement of TIR piping the first attenuation constant was dominated by a geometric effect, i.e. the rounded corners (see figure 4.9), rather than by reflectance, while for the VM2000 profile only reflectance matters

If the long-range attenuation length μ_2 is used to derive the reflection coefficient, then the qualitative "visual" analysis from Figs. 4.13 and 4.14 does not agree with the quantitative evaluations reported in Tables 4.4 and 4.5. The experimental light attenuation curves, either in air and in liquid, are consistent with the predictions for $R = 98.7\%$, at $d \lesssim 20\,cm$, and with those for $R = 98.3\% - 98.5\%$, at $d \gtrsim 20\,cm$, however data are fitted by a shorter effective attenuation length μ_2.

The reason for the mismatch between visual and numerical analysis is that the shape of experimental and simulated curves are slightly different and hence the attenuation lengths cannot be directly compared. In particular, the simulations need more weight in the short-range attenuation component. Since μ_1 is not much shorter than $\mu_2$for this case, the two parameters correlate in the fit, so that a longer μ_2 is required to fit the tail. In the TIR analysis such an ambiguity was not found, because the two exponentials of eq. 4.3 have very different attenuation lengths, thus they do not correlate strongly with each other during the fit.

Similarly, a χ^2 analysis would not be appropriate for this case, either, since the MC does not give a good fit to data in a sufficiently large interval of distances.

For all these reasons, it seems more appropriate to rely on a visual comparison of the measured curves with the simulations, in the entire range of distances. The estimated effective reflectance of the *new* VM2000 is then: $R_{VM2000}(430\,nm) = (98.5 \pm 0.2)\%$, where the error is large enough to accommodate the systematic uncertainty related to the departure of the model from data. Other systematics are not included.

Systematics A systematic error that has been studied is the effect of the uncertainty of the transverse dimension of the VM2000 pipe, which had neither a strictly constant cross section, nor a perfectly square shape. Moreover, the foils are flexible and the surfaces not perfectly flat, which makes the unambiguous determination of the dimensions difficult, in absence of an internal support. The measured transverse dimension is $s = (9.3 \pm 0.3)\,mm$ (the error is a conservative estimation from repeated measurements). For a given reflectance, the larger is the pipe, the less the attenuation.

MC simulations have been carried out, whose outcome is that, for the above uncertainty in the pipe transverse dimensions, the corresponding error of the reflectance is much lower than the $\pm 0.2\%$ estimated above. This also implies that non uniformities in the pipe transverse dimension cannot explain the difference between observed and predicted shape. A possibility that has been considered is that the VM2000 reflectance is not constant at all angles, as assumed in the model. For example, a higher reflectance at near normal incidence than at larger angles can reproduce the experimental trend. Light would be first guided with the highest effective efficiency, then with a lower and lower efficiency, the further the source is, because it is mostly the "grazing" photons, which need less reflections per unit length, to reach

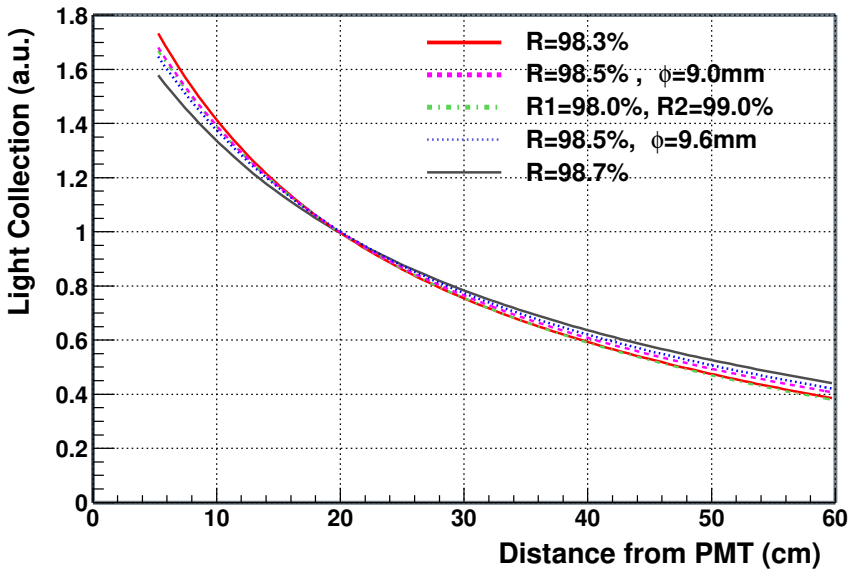

Figure 4.15: *Predictions of "variant" MC simulations, for light transport through VM2000 foils in liquid. The red and dark gray solid curves correspond to the standard simulations also shown in Fig. 4.14 for $R = 98.3\%$ and $R = 98.7\%$, respectively. The dashed magenta and dotted dark blue curves are calculated for $R = 98.5\%$ and pipe dimension of $s = 9.0\,mm$ and $s = 9.6\,mm$. The dashed-dotted light green simulation correspond to a model with $R_1 = 98.0\%$ for $\theta > 45°$ and $R_2 = 99.0\%$ for $\theta < 45°$, where θ is the angle of incidence on the foil. All curves are normalized to 1 at $d = 20\,cm$.*

the PMT and these are piped with a lower reflection coefficient[3].

This hypothesis has been checked with a MC simulation, which assumed $R = 99.0\%$ for $\theta < 45°$ and $R = 98.0\%$ for $\theta > 45°$. The calculated light attenuation curve is similar to the standard one for $R = 98.5\%$ at short distances and to the one for $R = 98.3\%$ in the tail, thus matching better with the observations.

The simulations of all the the "variant" cases discussed above (different transverse dimension, bi-modal reflectance) are shown in Fig. 4.15, together with two base-case simulations for reference. The figure confirms that the reflectance determination reported in the previous section is robust against the considered variations. The final estimation is:

$$R_{VM2000}(430\,nm) = (98.5 \pm 0.3)\% \tag{4.12}$$

for reflectance from air as well as from media with higher index of refraction. The error in eq. 4.12 has been slightly enlarged compared to the previous $\pm 0.2\%$ for conservativeness, since it is likely that not all the sources of systematics have been identified. Eq. 4.12 is in good agreement with the near-normal mirror-reflectance measured with the V-W technique for the same wavelength (Fig. 4.3). The latter has however a much larger uncertainty.

[3]It is assumed that the supposed angular dependence of the reflectance is not sufficiently strong to have a selective effect on the photons direction distribution at a far distance from the source. This would primarily depend on the number of reflections necessary to reach that distance, instead (long-propagating photons are on average more grazing).

4.8 Conclusions

Guiding the scintillation light to the PMTs is a critical issue for the LENS concept, due to the small geometrical cross section of the detector elementary unit, compared to the length. Light piping via total internal reflection on finished quartz surfaces and via specular reflection of VM2000 super-reflective foils from 3M has been studied at $\lambda = 380\,nm$ and $\lambda = 430\,nm$ in prototype cells. Data have been analyzed by comparing with photon-tracing MC simulations. The results are expressed in terms of angle-position averaged reflection coefficient and are summarized in eqs. 4.11 and 4.12. The method developed has shown a very high sensitivity to the light piping efficiency, with an achieved precision of $\sigma_R/R \sim 2 - 3 \times 10^{-3}$, as required by the strong expected dependence of the LENS optical performance on R.

Notable efficiency for TIR reflection has been found, which promotes TIR as the base high efficiency light piping mechanism for LENS. The reflectance of the VM2000 foils at $430\,nm$, a wavelength representative of the typical emission spectrum of secondary fluors in organic scintillators, is remarkably high, though lower than TIR, thus making VM2000 a powerful tool for light guiding applications in optical modules.

Based on these results, the expected optical performance of TIR, SR and mixed TIR/SR LENS cells is studied with MC simulations in Chapter 7.

Chapter 5

Optical Measurements of Bialkali Photocathodes

5.1 Introduction

Photomultipliers based on bialkali photocathodes are widely used in astrophysics, nuclear and particle physics. In many cases, the only optical property of a PMT a user is interested in is its spectral sensitivity, i.e. the fraction of photons converted into detected photoelectrons as a function of the wavelength (Fig. 5.1). Recent developments in particle physics, especially in neutrino physics, have led to the construction or proposal of several kiloton detectors in which the interactions are detected either via Cherenkov light in water or via scintillation light from organic liquid scintillators, as outlined in Secs. 1.3 and 1.5.2. Data analysis in these experiments often relies on the comparison with the predictions of MC simulations, which have to implement the response of the detector as precisely as possible, including the non trivial description of light interaction with the PMTs. Three processes are possible for a photon impinging on a PMT:

1. Absorption in the photocathode, with probability $A(\lambda, \theta)$
2. Reflection off the PMT window or off the photocathode, with probability $R(\lambda, \theta)$
3. Transmission inside the PMT, with probability $T(\lambda, \theta) = 1 - A(\lambda, \theta) - R(\lambda, \theta)$

Fig. 5.2 illustrates the three cases. In case of absorption, a photoelectron is produced, which has a certain chance to escape the layer toward the interior of the PMT, where it is accelerated to the first dynode. An avalanche then begins, resulting in a final detectable signal. It is convenient to express the probability that a photon contributes to a signal as the product of two probabilities:

$$QE(\lambda, \theta) = A(\lambda, \theta) \times P_{conv}(\lambda) \tag{5.1}$$

where $A(\lambda, \theta)$ is the probability that the photon is absorbed in the photocathode, which is a function of the wavelength λ and the incidence angle θ, and P_{conv} is the conversion factor for such absorption to result in an avalanche, which is assumed independent of θ and only dependent on λ (due to the different kinetic energy transferred to the photoelectron in the absorption process) and - not shown in eq. 5.1 - on the location of the photon absorption on the PMT surface (typically photoelectron collection is less efficient at the PMT border).

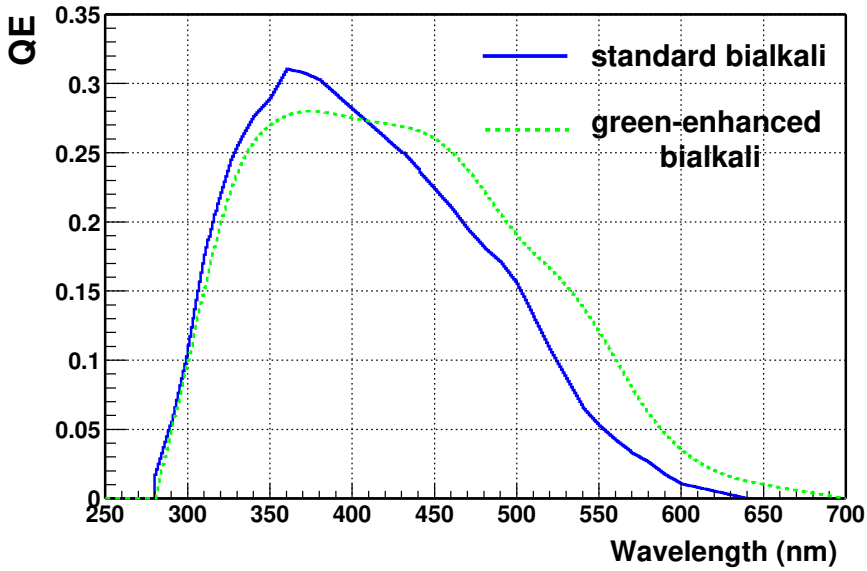

Figure 5.1: *Spectral response of standard and green-enhanced bialkali photocathodes. The ordinate gives the probability for a photon to produce a detected photoelectron. The curves are measured by the PMT manufacturer (see e.g. [Pho94]) by illuminating the PMT center in air, at normal incidence. The cut-off at* $\sim 310\,nm$ *is due to the absorption by the PMT glass window.*

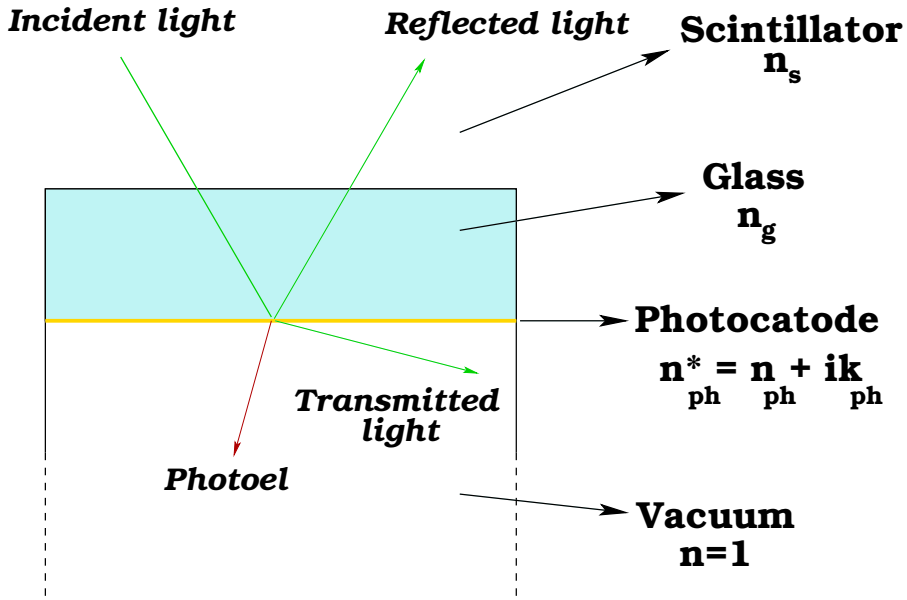

Figure 5.2: *Simplified model of a PMT immersed in medium (e.g. in a scintillator). Perfect match of the refractive index of medium and glass window is assumed.*

The probability $QE(\lambda, \theta)$ is called *Quantum Efficiency* and is one of the most important figures of merit of a PMT. It depends on the window glass (for the short-wavelength cut-off), the photocathode material and its thickness. In Fig. 5.1 the typical QE spectra are shown of two of the most employed photocathodes: the standard *bialkali* ($KCsSb$) and the *green-enhanced bialkali* ($RbCsSb$). The curves are measured by the PMT manufacturer in air for light impinging at near normal incidence ($\theta \sim 0$).

For most applications the information in Fig. 5.1 is sufficient, since it characterizes the PMT detection efficiency for "standard" operation. However the physics of light interaction with the PMT is more complex than that. First because the QE is not only a function of λ, but also of θ, second because in neutrino detectors PMTs are typically coupled to liquids and not to air, last because the probabilities $R(\lambda, \theta)$ and $T(\lambda, \theta)$ are not implicit in eq. 5.1. In any close-volume PMT-based detector, like LENS and other solar neutrino experiments described in Secs. 1.3 and 1.5.2, light reflected off the PMT is not lost: it keeps on propagating and can eventually be detected at a later time. This has two consequences: 1) more light is collected; 2) this extra-light deforms the pulse shape, adding a contribution to the signal tail.

In spite of the great importance of this topic for detector-modeling, surprisingly very little is documented in the literature. A major breakthrough was accomplished by Moorhead and Tanner [MT92] (hereafter referred to as M&T), who measured the optical constants of a $KCsSb$ bialkali photocathode at the wavelength of $\lambda = 442\,nm$, for implementation in the MC simulation of the SNO experiment. The method they used gave them the ability to break the ambiguity typical of this kind of determinations. In their work M&T also tried to deduce the wavelength dependence of the photocathode optical constants, by reinterpreting and reanalyzing earlier measurements at discrete wavelengths in the visible spectrum, reported in [Tim76]. Later on, Lang has used M&T's set-up to check their measurements on the same photocathode and to extend the investigation to several other photocathodes [Lan93], including the $RbCsSb$.

Our purpose was to extend M&T's and Lang's measurements on the $KCsSb$ and $RbCsSb$ photocathodes, by covering the whole visible spectrum. The two investigated photocathodes are the most usual choice in neutrino physics. The former is suitable for the detection of Cerenkov light and scintillation light from primary fluors, the latter ensures good blue-green sensitivity and matches better the emission spectra of secondary fluors (wavelength-shifters) in three-components organic scintillator mixtures.

The original motivation for this work was the study of the impact of light reflections off PMTs on the Yb-LENS experiment. In the assumed detector concept it is not possible to avoid that a fraction of the primary light reflects off the PMTs and is eventually detected at a later time, with a delay given by the time of flight inside the volume. In a typical LENS cell, for a length of $\sim 4\,m$, this delay is of the order of $\sim 30\,ns$, with a large spread corresponding to all the possible photon paths, hence this late light falls in the time-window of the ^{176}Yb ν-tag coincidence. Consequently reflections, as any other source of late photoelectrons, contribute to increase the probability that single events are misidentified as correlated double events, i.e. ν-candidates. In a similar way, also the performance of the Borexino detector could be affected by light reflections: this effect might for example weaken the $\alpha - \beta$ discrimination power, which is based on the fact that α-excitation in organic scintillators leads to a larger fraction of late light (see refs. [RWH64, RGL98]).

These examples clarify in two specific cases the importance of characterizing the optical properties of photocathodes. However, several other applications of an optical model of PMTs are conceivable, for example the prediction, based on eq. 5.1, of the angular dependence of

the QE, for a PMT in air as well as in liquid.

5.2 Theory and Methodology

5.2.1 Introduction

The photocathode of a PMT is a thin layer of a multi-alkali semiconducting alloy, which is evaporated onto the back plane of the glass window during production. Light impinging on a photocathode is in part reflected, in part absorbed and in part transmitted, due to the very thin thickness of the layer (Fig. 5.2). The thickness is a compromise aiming at maximizing the probability that a photon results in a signal: if the photocathode is too thin, little light can be absorbed; if it is too thick, the resulting photoelectrons cannot efficiently escape the photocathode.

The description of such and similar systems is covered by the "optics of thin metallic films", a wide field on which a very rich literature exists (see e.g. the textbook [Hea91]). The theoretical model merges the optical description of an absorbing material, through its complex refractive index, and the optics of thin layers, where the series of wave fronts of different orders of reflections are added coherently to calculate the resulting reflected wave amplitude. Assuming that the surface of a photocathode is regular and uniform enough that the model of thin metallic films is applicable, then the functions $A(\lambda,\theta)$, $R(\lambda,\theta)$, $T(\lambda,\theta)$ are predictable in any condition, once the three parameters of the problem are known: real and imaginary part of the refractive index, $n^* = n+ik$ (i imaginary unit, both n and k function of the wavelength) and thickness of the layer, d. The challenge is to invert the results of optical measurements performed under certain specific conditions (angle of incidence, polarization, refractive index of the medium in coupled to the PMT) in order to infer the constants (n,k,d). This is done by fitting the experimental results with the optical model of the photocathode, with (n,k,d) as free parameters.

Unfortunately the problem has often a high degeneracy: for a single measurement (for example absolute reflectance at a certain incidence angle) there exist infinite solutions for (n,k,d) able to reproduce the data. For each considered wavelength at least 3 independent measurements are needed, but this is often still insufficient to guarantee the convergence to a unique solution.

Several techniques have been developed for the study of thin solid films, which might be applied to this particular case (see refs. [Hea91, TMG99] for a review). However, the photocathode of a PMT is a challenging sample. It cannot be directly studied, because it is not chemically stable when exposed to air, therefore some information is either unaccessible, like transmittance, or only in part available, like reflectance: only the reflectance from the glass side can be measured, which is not the same as the reflectance from the photocathode side. Furthermore, any polarization analysis of the light reflected off the photocathode is disturbed by the birefringence that is induced on the glass window by the mechanical stress due to the pressure difference (the interior of the PMT is under vacuum).

5.2.2 The Model

Dealing with light reflection off a PMT, four regions can be defined, each characterized by its own refractive index: the medium where the light originates, with n_1; the PMT envelope, with n_2; the photocathode, with $n_3^* = n_{ph} + ik_{ph}$, and the vacuum inside the PMT, with $n_4 = 1$.

The amplitudes of the reflected and transmitted waves at the interface glass-photocathode (n_2 to n_3^*) are given by the following formulas (see e.g. [BW64] for a derivation):

$$\begin{aligned} a_R(\lambda,\theta) &= r_{23} + \frac{t_{23}t_{32}r_{34}\exp(-2i\delta)}{1+r_{23}r_{34}\exp(-2i\delta)} \\ a_T(\lambda,\theta) &= \frac{t_{23}t_{34}\exp(-i\delta)}{1+r_{23}r_{34}\exp(-2i\delta)} \end{aligned} \tag{5.2}$$

where

$$\begin{aligned} r_{ij} &= \frac{n_i\cos\left(\theta_{i(j)}\right)-n_j cos\left(\theta_{j(i)}\right)}{n_i\cos\left(\theta_{i(j)}\right)+n_j cos\left(\theta_{j(i)}\right)} \\ t_{ij} &= \frac{2n_i\cos(\theta_i)}{n_i\cos\left(\theta_{i(j)}\right)+n_j cos\left(\theta_{j(i)}\right)} \\ \delta &= \frac{2\pi d n_3^*}{\lambda}\cos(\theta_3) \end{aligned} \tag{5.3}$$

In eq. 5.3, n_l is the complex refractive index of the l^{th} region, θ_k the angle of the propagating light beam with respect to the normal in the same region, calculated using the Snell's law starting from the angle of incidence on the PMT window, $\theta_1 \equiv \theta$. Eq. 5.2 holds for both the light polarizations, perpendicular and parallel relative to the photocathode plane (s and p waves respectively), providing that the definitions for r_{ij} and t_{ij} are changed by swapping the i and j indices as indicated in eq. 5.3 (the formulas with first indices apply to p-wave).

Eq. 5.2 can be used to predict the total reflectance of the PMT by adding the Fresnel reflection on the medium-to-window interface (n_1 to n_2) to the reflectance from the photocathode:

$$\begin{aligned} R_{tot}(\lambda,\theta) &= \tfrac{1}{2}\left[R_s^{tot}(\lambda,\theta)+R_p^{tot}(\lambda,\theta)\right] \\ R_{s,p}^{tot}(\lambda,\theta) &= F_{s,p} + \frac{R_{s,p}(1-F_{s,p})^2}{1-F_{s,p}R_{sp}} \\ R_{s,p}(\lambda,\theta) &= \left|a_R^{s,p}\right|^2 \end{aligned} \tag{5.4}$$

where the quantities:

$$\begin{aligned} F_s(\lambda,\theta) &= \left[\frac{\sin(\theta_1-\theta_2)}{\sin(\theta_1+\theta_2)}\right]^2 \\ F_r(\lambda,\theta) &= \left[\frac{\tan(\theta_1-\theta_2)}{\tan(\theta_1+\theta_2)}\right]^2 \end{aligned} \tag{5.5}$$

represent the Fresnel reflectance at the interface with the PMT window (see [BW64] and cf. eq. 4.1 on page 76). Eq. 5.4 is derived by solving the series: $R = F + (1-F)^2R + (1-F)^2FR^2... + (1-F)^2F^nR^{n+1} = F + (1-F)^2R\sum_{n=0}^{\infty}(FR)^n$, which represents the infinite sum of the intensities of the waves reflected from window and photocathode. Similarly for the transmittance:

$$\begin{aligned} T_{tot}(\lambda,\theta) &= \tfrac{1}{2}\left[T_s^{tot}(\lambda,\theta)+T_p^{tot}(\lambda,\theta)\right] \\ T_{s,p}^{tot}(\lambda,\theta) &= \frac{T_{s,p}(1-F_{s,p})}{1-F_{s,p}R_{sp}} \\ T_{s,p}(\lambda,\theta) &= \frac{n_4\cos(\theta_4)}{n_2\cos(\theta_2)}\left|a_T^{s,p}\right|^2 \end{aligned} \tag{5.6}$$

The last optical function, absorption, is deduced from eqs. 5.4 and 5.6, by using the identity:

$$A(\lambda,\theta) = 1 - R(\lambda,\theta) - T(\lambda,\theta) \tag{5.7}$$

A computer code has been written to implement eqs. 5.2 to 5.7.

5.2.3 Experimental Approaches

Preliminary Remarks The angle at which a ray of light with a given incidence angle emerges after crossing a series of parallel layers depends only on the refractive index of the first and last medium, as a consequence of the Snell's law. If $n_1 = 1$ (PMT in air) there is no critical angle in the system of Fig. 5.2. The part of the PMT reflectance due to the direct Fresnel contribution of the window is trivial. In a large region of the (n,k,d) parameter space the photocathode reflectance for both polarizations (given by eqs. 5.4 after subtraction of the window contribution $F_{s,p}$) is nearly constant for $\theta \lesssim 60^\circ$ and then drops to zero (simply because the Fresnel-reflectance of the window rapidly increases to 100% for θ approaching 90° and less light can refract and reach the photocathode). Therefore, reflectance measurements in air, even at different angles, provide a weak constraint on the solution of the fit, as pointed out by M&T in [MT92].

On the other hand, if $n_1 > 1$ (for example PMT in water or scintillator), then there is a critical angle θ_c above which no light can be transmitted. In this case the photocathode reflectance shows a plateau until θ_c and then a peculiar shape, very different for parallel and perpendicular polarization. The optical model of the photocathode shows that, in this case, the free parameters (n,k,d) are strongly constrained by the angular dependence of the reflectance, in particular by the shape around θ_c.

An example is reported in Fig. 5.3 for the two cases discussed above: PMT in scintillator and in air.

Previous Measurements Based on this fact, M&T have built an experimental set-up to measure the photocathode reflectance as a function of the angle of incidence for a PMT immersed in water, at the wavelength of $\lambda = 442\,nm$, provided by a *He-Cd* laser. With this technique they were able to establish unambiguously the three optical constants of the *KCsSb* bialkali photocathode they investigated: $n = 2.7 \pm 0.1$, $k = 1.5 \pm 0.1$, $d = (23 \pm 2)\,nm$ [MT92]. The result was obtained by fitting the data with the same optical model summarized in eqs. 5.2 to 5.5. The goodness of the best fit was sufficient to demonstrate that the assumed theoretical model is an acceptable description of the photocathode.

This Work Our strategy was to investigate the optical properties of bialkali photocathodes by scanning the whole visible spectrum with commercial equipments, instead of following M&T and setting up an ad-hoc system at a single wavelength. All our measurements had to be performed in air, therefore we tried to break the degeneracy of the problem by performing a global fit to a set of independent measurements. This kind of approach is quite "standard" in the study of thin solid films, as discussed in [TMG99]. For a photocathode of a PMT, light reflected from the glass window side is the only accessible observable. Beside simple reflectance determinations, we also performed *ellipsometric* measurements.

Ellipsometry (see [TMG99]) is an optical technique devoted to the the analysis of surfaces and in particular thin films. It is based on the measurement of the change in the polarization state of light upon reflection off a plane surface. In short, an ellipsometer consists of a polarizer and an analyzer: light is linearly polarized, sent to a sample and finally the reflected beam is analyzed. In general the reflection changes the polarization from linear to elliptic, in a way that depends on the three optical constants (n,k,d). Any linear polarization can be thought

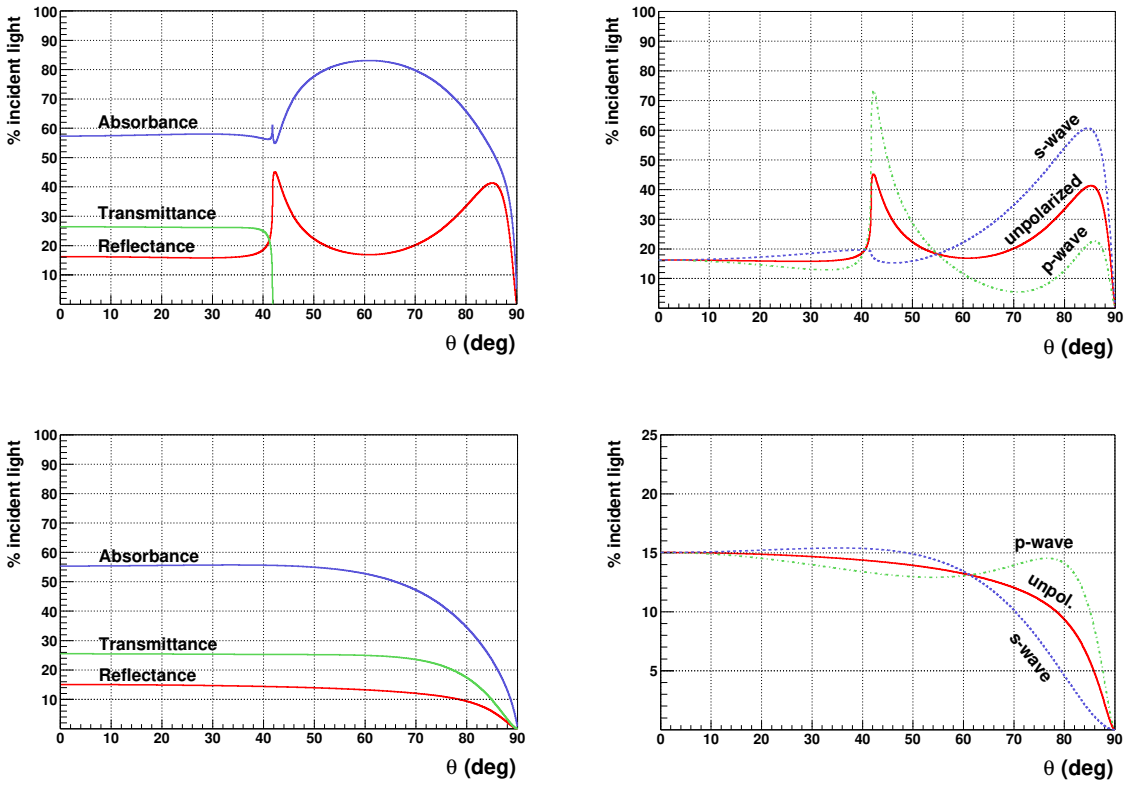

Figure 5.3: *Top left: predictions of the optical model of thin films for absorption, reflectance and transmittance from the photocathode of a PMT, assuming the following parametrization:* $n_1 = 1.5$ *(scintillator),* $n_2 = 1.51$ *(glass),* $n_3 = 2.7 + 1.5i$ *(photocathode),* $n_4 = 1$ *(vacuum);* $d = 20\,nm$*;* $\lambda = 442\,nm$*.*
Top right: reflectance for unpolarized light, perpendicular and parallel polarization for the same case. The discontinuity of all the optical functions at $\theta \simeq 42°$ *corresponds to the onset for the condition of total internal reflection: transmittance to vacuum drops to zero, reflectance shows a peak for the p-wave (in a dielectric reflectance would rise to* 100%*). It is found that in this case the reflectance spectra constraint effectively the parameters* n_2*,* n_3^* *and* d*.*
Bottom left: predictions for the same parameters, but PMT in air: $n_1 = 1$*. The absence of a critical angle for total internal reflection gives no special features to the curves and an optical measurement in this condition provides a very weak constraint for parameters determination.*
Bottom right: reflectance for unpolarized light, perpendicular and parallel polarization for the same case.
In all the graphics, the ordinates are given in percent of the incident light and the first order Fresnel reflection from the glass is not included (for this reason the sum $A+R+T$ *drops to zero, for* $\theta \to 90°$*).*

of as the superposition in phase of two orthogonal components. The frame of reference is chosen relative to the sample plane, which defines the parallel *p-wave*, and the perpendicular *s-wave*. The reflection off a surface changes the relative intensity ratio between p and s waves and introduces a phase delay. This can be expressed by the ratio of the complex reflected amplitudes, which translates to an angle and a phase:

$$\frac{a_R^p}{a_R^s} = \tan\Psi e^{i\Delta} \tag{5.8}$$

where a_R^p and a_R^s are the same amplitudes appearing in the first row of eq. 5.2. The angle Ψ and the phase Δ are the two parameters measured by ellipsometry.

Ellipsometry is one of the most sensitive methods for the analysis of thin films and has the advantage over conventional reflectometry to be independent of absolute determinations, where systematics are often not under control. To our knowledge, this technique has been applied here for the first time to the study of PMT photocathodes.

5.3 Optical Measurements of Photocathodes

Two $1,5''$ PMTs from ETL have been investigated: a 9102B and a 9902B, the former endowed with a standard *KCsSb* bialkali photocathode, the second with a *RbCsSb* "green-enhanced" bialkali photocathode. Both PMTs have a flat photocathode, with a geometry similar to the one of the schematic model in Fig. 5.2. The measurements performed are:

1. Absolute reflectance for unpolarized light at $\theta = 7°$ in the wavelength range $[250\,nm - 700nm]$
2. Relative reflectance for p and s polarizations at $\theta = 45°$, $55°$, $65°$ in the wavelength range $[390\,nm - 700nm]$
3. Ellipsometric measurement of (Ψ, Δ) in the wavelength range $[420\,nm - 740nm]$

5.3.1 Absolute Reflectance at a Fixed Angle

The absolute reflectance of glass plus photocathode has been measured in air, at near normal incidence ($\theta = 7°$), with a V-W accessory of a Varian Cary 400 spectrophotometer. The V-W technique, described in Fig. 4.2 on page 78 and relevant caption, allows the measurement of the absolute specular reflectance of a flat sample without the use of any reference mirror. A precision of $\sim \pm 1\%$ is attainable (instrument specification). At this level of accuracy, the fluctuations within our sample PMTs due to non homogeneities of the surface are the dominant uncertainty. Consequently, in fig 5.4 the average spectra from several measurements of both PMTs are reported (relative deviations of $\sim 10\%$ are observed).

It is remarkable that both PMTs show a $\sim 20\%$ reflectance in the visible region. This means that roughly 20% of the light interacting with the PMTs remains in the detector. The same range of reflectance has also been measured by us in other investigated samples. From other investigations, it seems to be typical of all the bialkali PMTs [Lan93].

Moreover, we found that the spectral shape of the reflectance is reproduced in other PMT equipped with the same bialkali photocathodes.

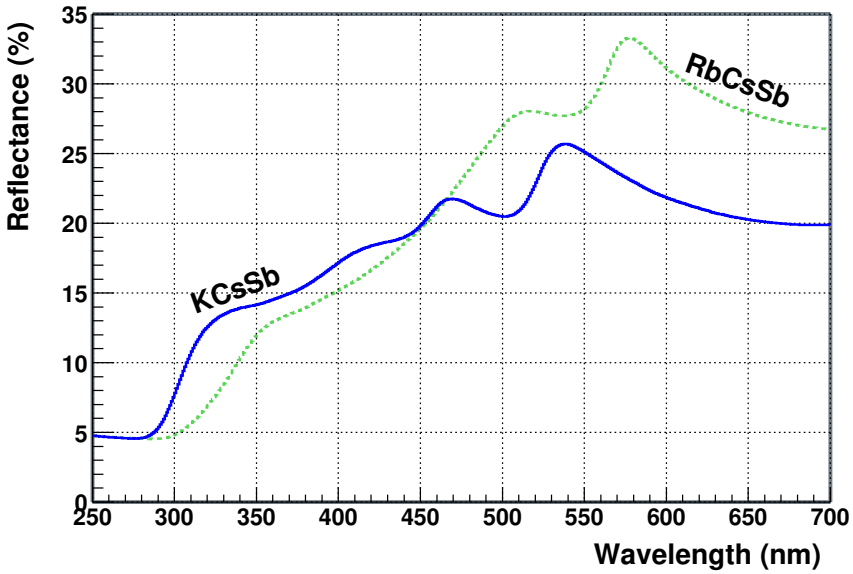

Figure 5.4: *Average PMT absolute reflectance spectra of an ETL 9102B (blue solid curve) and an ETL 9902B (green dashed curve). The former has a standard KCsSb bialkali photocathode, the latter a RbCsSb "green-enhanced" bialkali photocathode. The reflectance is the sum of the Fresnel component from the glass window and the dominant photocathode contribution. The short-wavelength cut-off is in both cases due to the absorption from glass.*

5.3.2 Relative Reflectance at Variable Angle

Experimental Technique The reflectance of the samples has also been investigated with a VASRA accessory (Variable Angle Specular Reflectance Accessory) of our Varian Cary 400 spectrophotometer, which allows to measure the specular reflectance of a sample tuning the angle of incidence in 0.5° steps in the interval $20° \leq \theta \leq 70°$. The VASRA has no self-referencing capabilities, contrary to the V-W accessory, therefore any measurement needs to be referenced to a calibrated standard.

Unfortunately the instrument exhibited very poor reproducibility: the repetition of a scan after resetting the accessory often resulted in a large discrepancy in the absolute scale of the spectrum (the shape, however, was reproducible). It has been figured out that this systematics is due to the fact that the VASRA sample holder was not very stable. Each time the angular setting of the instrument was changed or reset, the holder was not able to restore exactly the same orientation in the plane perpendicular to the optical path. The optics of the device is very sensitive to such small displacements of the reflection plane and hence the effect was a dramatic change in the collection efficiency of the reflected light. Several attempts to fix the vertical orientation of the holder were unsuccessful. For this reason, the VASRA measurement is used for spectral shape data only, while the absolute normalization is considered as an indeterminate parameter.

In order to correct for the instrument spectral baseline the VASRA is referenced with the response to a VM2000 sample, which is known from the V-W measurements to have a nearly flat (at $\sim 1\%$) reflectance spectrum above cut-off at near normal incidence (see Sec. 4.4). A polarizer is employed to select the p ans s waves before reflection off the sample, and a depolarizer is mounted at the end of the optical path, to avoid biases related to the sensitivity of the spectrophotometer light sensor to the polarization state of the outgoing light.

Summarizing, the procedure adopted for the VASRA measurements is:

1. Select with the polarizer the perpendicular or parallel polarization
2. Set the instrument in sequence to $\theta = 45°$, 55° and 65° and take a reference spectrum for each angle of incidence with a VM2000 reflective foil sample
3. Mount the PMT in the sample holder, set the instrument in sequence to $\theta = 45°$, 55° and 65° and acquire a reflectance spectrum for each of the three angles of incidence
4. Normalize the spectra acquired at point 3 by the reference spectra taken at point 2, assuming $R_{VM2000}(45°) = R_{VM2000}(55°) = R_{VM2000}(65°) = 100\%$ for both parallel and perpendicular polarization[1]

The above VASRA angles are chosen because the strongest constraints in the determination of the photocathode optical parameters are expected from measurements at high angles of incidence. Furthermore, the investigated angular range lays around the Brewster's angle for Fresnel's reflection off the glass, so that the PMT reflectance of the parallel polarization is largely dominated by the photocathode contribution.

[1]Since the foils have $\sim 98\% - 99\%$ reflectance, this implies an absolute error of $\lesssim 2\%$. However this error is insignificant, since the absolute scale of the measurement is free. The only significant systematic error implicit in this procedure is related to the wavelength dependence of the foil reflectance. The former was measured at near-normal incidence (see Sec. 4.4), where it was found $R_{max} - R_{min} \simeq 1\%$ in the wavelength range used for the analysis.

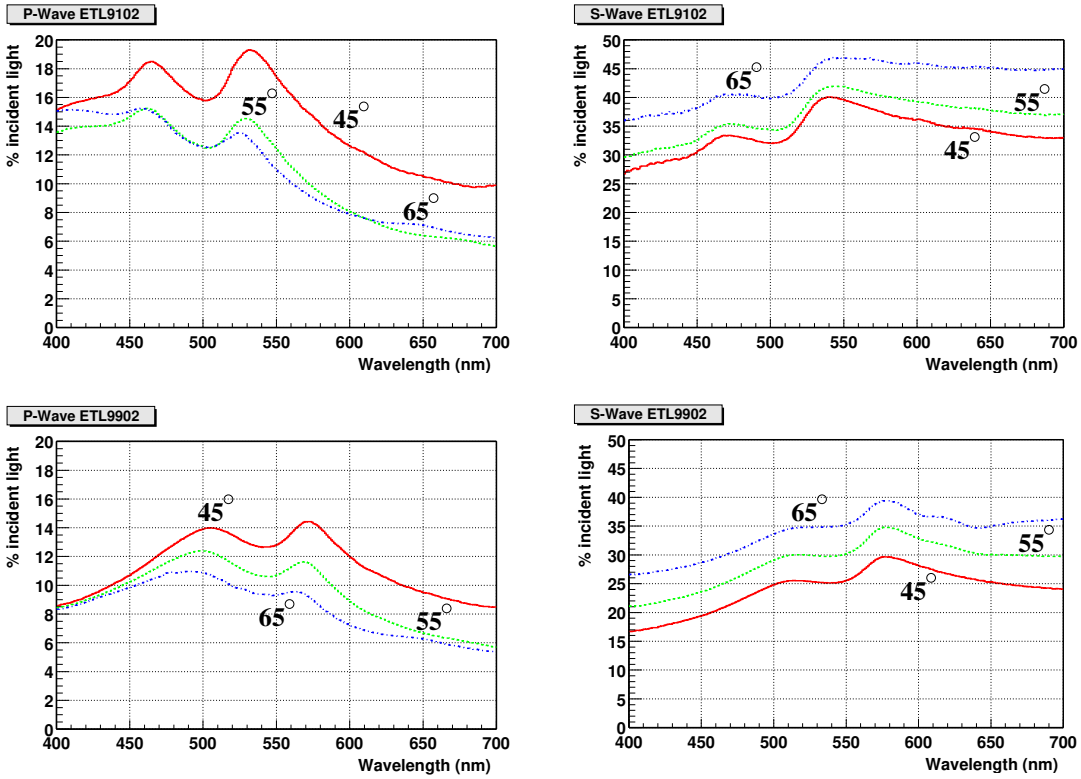

Figure 5.5: *Reflectance spectra of the PMTs ETL 9102B (top) and ETL 9902B (bottom) for parallel (left) and perpendicular (right) polarized light, recorded with a Varian Cary400 spectrophotometer by using a variable angle specular reflectance accessory. Ordinates are given in percent of the incident light, but the uncertainty in the absolute normalization of the measurements is very large (see text). The three shown spectra per PMT and polarization state correspond to different angles of incidence: $\theta = 45°$ (red), $55°$ (green dashed), $65°$ (blue dot-dashed). The measurements were limited to $\lambda > 400\,nm$ because the reference VM2000 foils have their reflectance cut-off at $\lambda \sim 390\,nm$.*

Results and Discussion Fig. 5.5 displays the measured reflectance spectra. We observe that the main features observed with the VASRA accessory (peaks and dips) are also found in the V-W absolute reflectance measurements (Fig. 5.4).

In Fig. 5.6 the V-W reflectance spectrum of the PMT ETL 9102B at the fixed $\theta = 7°$ is shown, together with the average VASRA spectrum of the two polarization for $\theta = 45°$. The optical model described in Sec. 5.2.1 predicts a negligible difference for this case between $\theta = 7°$ and $45°$. The two spectra are in good agreement, except the normalization constant.

5.3.3 Ellipsometric Measurements

Experimental Technique The ellipsometric measurements on our two sample PMTs have been performed at the Institute for Applied Physical Chemistry (Angewandte Physikalische Chemie) of the University of Heidelberg, with a *M-44 J.A. Woolam* spectral ellipsometer[2].

[2]The support of Prof. Grunze and the help of Dr. T. Bastuck for the realization of the measurements is acknowledged.

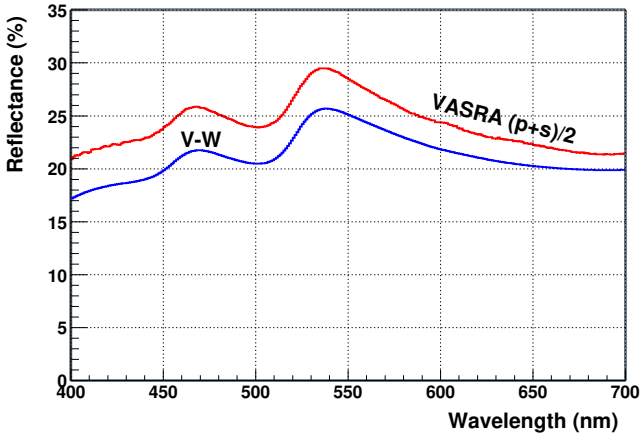

Figure 5.6: *Comparison between the absolute reflectance of the PMT ETL 9102B measured with the V-W accessory of our spectrophotometer ($\theta = 7°$, $\sim 1\%$ precision) and the average of the reflectances for p and s waves, measured with the VASRA accessory at $\theta = 45°$.*

The ellipsometric angle of incidence on the sample was $\theta = 60.75° \pm 0.01°$, measured by ellipsometry itself on a reference SiO_2 film. Light was linearly polarized and the polarization state of light upon reflection was then analyzed by decomposing the elliptical polarization into the parameters Ψ and Δ of eq. 5.8. The thickness of the PMT glass window was sufficient to allow a clear separation of the beams reflected off the glass and the photocathode, so that it was possible to select only the photocathode-reflected light to the analyzer. This selection facilitates the succeeding interpretation of data. For both PMTs three ellipsometric scans have been performed in the wavelengths interval $420\,nm < \lambda < 740\,nm$, corresponding to the illumination of different spots of the photocathode.

Results and Discussion The results are shown in Fig. 5.7. It can be seen that for the PMT ETL 9102B the three scans of the $\Psi(\lambda)$ function are in excellent agreement with each other, while the $\Delta(\lambda)$ spectra measured in different positions are similar, but shifted by nearly constant phases. This is likely to be an artifact introduced by the PMT glass window, which has to be crossed twice by light before the analyzer. As mentioned in Sec. 5.2.1, the glass of a PMT is under stress due to the pressure difference at the two sides. Mechanical stresses in dielectrics induce birefringence, which results in a phase shift between the two orthogonal polarization states. The latter adds to the shift due to reflection. The stress on the PMT envelope is different in different positions, and this can explain the observed phase shifts between the different measurements of $\Delta(\lambda)$. Differences are also observed in the $\Psi(\lambda)$ scans of the ETL 9902B PMT, where this effect cannot be explained by glass birefringence. It is likely that the photocathode of this sample is not homogeneous, for example in thickness.[3]

Before performing any quantitative analysis, we observe that the ellipsometric spectra show clear features (peaks and "bumps") where the reflectance spectra have their local maxima (compare Fig. 5.7 with Fig. 5.4 and 5.5).

[3]The process of photocathode growth through evaporation is not under complete control and some non homogeneities in the deposition are in general to be expected.

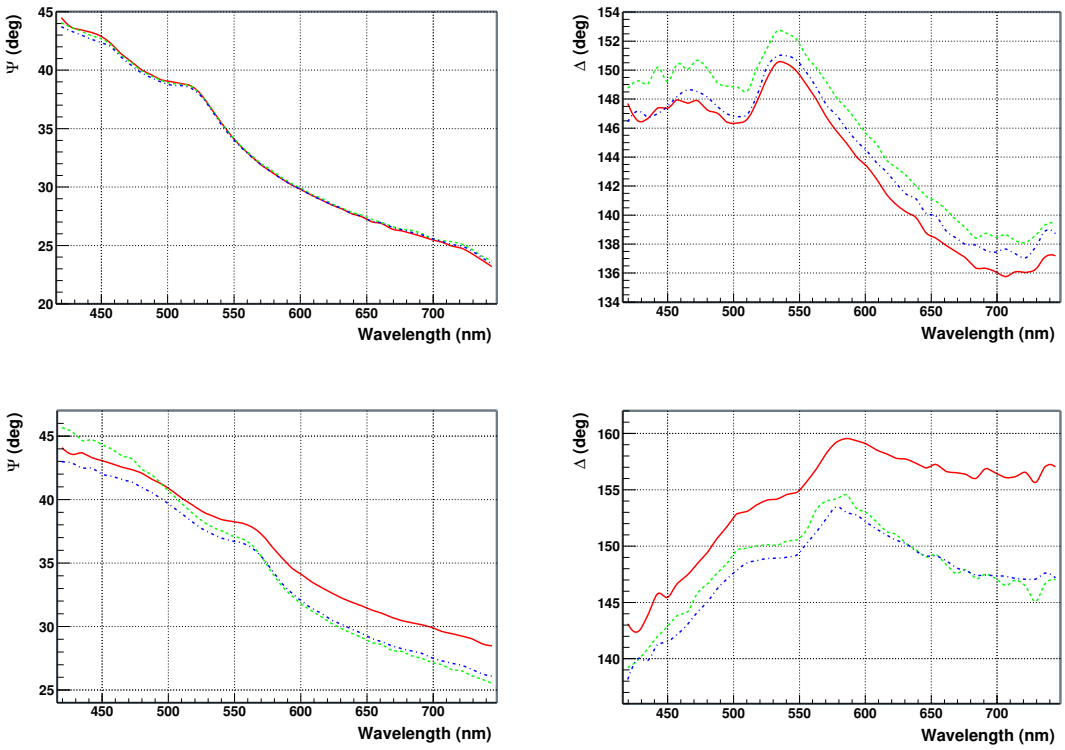

Figure 5.7: *Ellipsometric measurements on a ETL 9102B (top, KCsSb bialkali photocathode) and a ETL 9902B (bottom, RbCsSb green enhanced bialkali photocathode) PMT. The graphics show the wavelength spectra for the* Ψ *and* Δ *functions (equation 5.8. The three curves correspond to different spots on the PMTs (red solid: center; green dashed and blue dashed-dotted: close to the edge, at* $\sim 90°$ *from each other). The measurements refer to light reflected from the back-plane of the PMT window, where the photocathode layer sits. The instrument was set at an ellipsometric angle of* $\theta = 60.75°$.

5.4 Data Analysis

In Sec. 5.2.1 the equations describing the optical model of a thin metallic film have been introduced and in Sec. 5.3 all the optical measurements performed on two sample PMTs have been reported. The purpose of data analysis is to combine theory and experiments to derive the unknowns of the problems, so that the theoretical model can be used to predict the behaviour of a PMT under any condition. Those unknowns are:

1. The photocathode refractive index, $n^*(\lambda) = n(\lambda) + ik(\lambda)$
2. The photocathode thickness, d

For simplicity, it will be assumed that the glass refractive index, also entering the model as an unknown parameter, is indeed a known constant: $n_{glass} = 1.50$.[4]

A computer program has been written, implementing eqs. 5.2 to 5.5, which is used to perform a global fit of the experimental data based on a least square minimization. The program uses the package MINUIT of the CERN software libraries to perform such minimization. The global parameter d is easily included, while real and imaginary part of the photocathode refractive index are in principle continuous functions of the wavelength. They are implemented in the global fit as a table of parameters at discrete wavelengths, with a step of $15\,nm$, and then interpolated at each data-point wavelength by using a cubic *spline* function. As mentioned in Sec. 5.3, some of our measurements suffer from systematics implying a partial loss of information. This forces the introduction of new unknown free parameters in the fit:

1. Six normalization factors for the variable angle reflectance measurements (Fig. 5.5), expressing the systematic uncertainty in the absolute scale of the scans.
2. One constant phase offset for the Δ ellipsometric spectrum, accounting for the average shift introduced by the glass birefringence

The fit is performed in the wavelength range $410\,nm \leq \lambda \leq 680\,nm$. The lower limit is due to the lack of ellipsometric data at shorter wavelengths (an extension down to $\lambda = 390\,nm$ would be possible, by using reflectance data only). The least-square fit is preferred over the standard χ^2 fit, because the errors of the photometric and ellipsometric measurements are difficult to evaluate. Furthermore, it was not possible to find a unique solution (to be discussed in the next section) and in this case a complete χ^2 analysis is not meaningful.

The function *FCN* minimized by MINUIT is expressed as the sum of 4 contributions: $FCN = FCN_{V-W} + FCN_{VASRA} + FCN_{\Psi} + FCN_{\Delta}$. Each one, FCN_l, is defined as:

$$FCN_l(p_j) = \frac{1}{n}\sum_{i=1}^{n}\left[y_i - model(\lambda_i,\ p_j)\right]^2 \tag{5.9}$$

where the values y_i are the optical measurements at the wavelength λ_i and $model(\lambda_i,\ p_j)$ are the predictions of the theory, for a particular choice of the parameters set $\{p_j\}$. Eq. 5.9 is normalized to the total number of data-points n to have each measurement contributing the global fit the same statistical weight.

[4] The refractive index of the borosilicate glass employed in the two investigated PMTs is measured by many manufacturers to be in the range $1.48 \lesssim n \lesssim 1.52$ in the visible spectrum.

5.5 Results

It turned out that the inversion of the experimental data by using the described fitting procedure does not lead unambiguously to a unique solution. In Sec. 5.2.1 it was pointed out that at least three independent measurements per wavelength are necessary to determine the three free parameters (n, k, d). The thickness d is common to all wavelengths, so that even a weaker constraint might be sufficient with a multi-wavelength data-set. However, our measurements are not independent: the V-W absolute reflectance spectrum strongly correlates with the variable angle reflectance data, which in turn correlate with each other for the different probed angles and with the ellipsometric measurements (in particular with Ψ). Furthermore, some measurements provide only partial information. Last, measurements in air give admittedly poor constraints, being the model highly degenerate in the optical parameters for this case (see Sec. 5.4). In conclusion, the FCN function does not show a well defined minimum, so that the problem is mathematically indeterminate. A way of breaking the degeneracy is to fix some parameters and check how the fit converges varying the value of the fixed parameters. It is found that fixing the thickness to a guess-value during the fit leads to a unique solution, stable against changes in the parameters initialization. M&T have found $d = (23 \pm 2)\,nm$ as best fit value for their sample [MT92]. Lang has derived for 12 different PMTs values of the thickness typically laying in the interval $10\,nm \lesssim d \lesssim 40\,nm$[Lan93][5]. Therefore the PMT thickness has been fixed to $d = 15\,nm,\ 20\,nm,\ 25\,nm,\ 30\,nm$ and a global fit to the data performed, with all the other fit parameters free.

5.5.1 *KCsSb* Bialkali Photocathode

An example of global fit to the optical measurements performed on the PMT ETL 9102B is shown in Fig. 5.8, while Fig. 5.9 reports the best fit solutions for the complex refractive index.

The goodness of the global fit cannot be statistically evaluated, since a reliable estimation of the measurement errors is missing. The fit seems however good for the V-W absolute reflectance, the set of VASRA spectra for the perpendicular polarization and the ellipsometric $\Psi(\lambda)$ curve. The fit to the VASRA parallel polarization spectra and the $\Delta(\lambda)$ curve is less good and this is a hint either for the presence of systematic errors in the measurements, or for the non ideal behaviour of the photocathode. In Secs. 5.3.2 and 5.3.3 the known systematics affecting the VASRA and the Δ ellipsometric measurements have been discussed. It is likely that the reason for the bad fit is related to further experimental problems, which are still not compensated by the introduction of the free normalization parameters (VASRA) and the free phase shift parameter (Δ). In this regard, it is interesting to check the robustness of the results of the analysis by dropping some experimental data. An example is reported in Fig. 5.10, where the optical constants derived by the global fit are compared with those obtained by fitting only $R_{V-W}(\lambda)$ and $\Psi(\lambda)$[6], i.e. the most robust experimental data. It is remarkable that the results do not differ very much, which implies that data are consistent with each other. On the other hand, it is shown that the measurements performed do not really contribute independent information and thus the indetermination of the problem is the consequence of such strong correlations.

[5] The manufacturers give no specification for this parameter.

[6] One measurement does not provide alone a sufficient constraint for the convergence to a unique solution, even with fixed photocathode thickness.

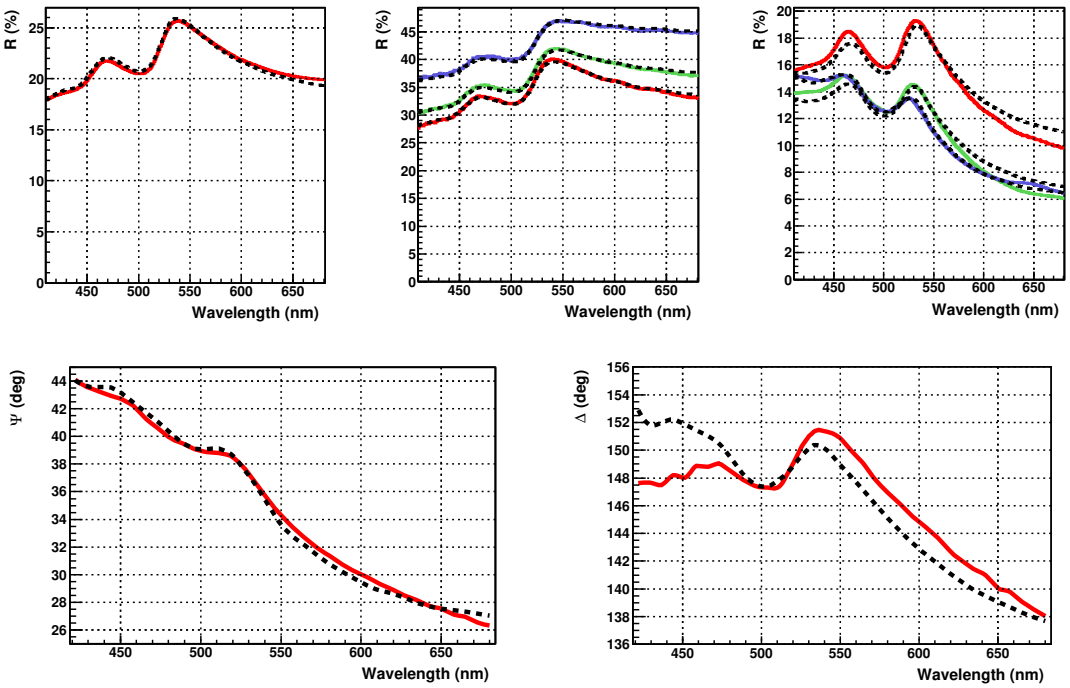

Figure 5.8: *Best global fit to the optical measurements on the ETL 9102B sample PMT, for the particular case of photocathode thickness fixed to* $d = 20\,nm$*. Top: V-W absolute reflectance spectrum (left); VASRA reflectance spectra, perpendicular polarization (center); VASRA reflectance spectra, parallel polarization (right). Bottom: ellipsometric* Ψ *(left) and* Δ *(right) parameters. The measured spectra are displayed in colored solid line (see figs. 5.4, 5.5 and 5.7), the fits in black dashed line. The fits obtained after fixing* d *to the other considered values are all very similar to the one shown here.*

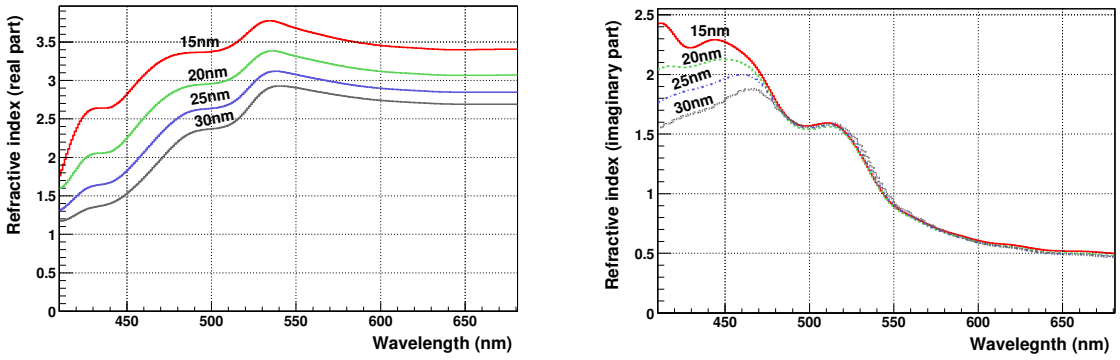

Figure 5.9: *Best fit spectra for real (left) and imaginary (right) part of the complex refractive index of a KCsSb photocathode. The four displayed curves correspond to different assumed photocathode thickness:* $d = 15\,nm$ *(red),* $20\,nm$ *(green),* $25\,nm$ *(blue),* $30\,nm$ *(gray), fixed during the fit.*

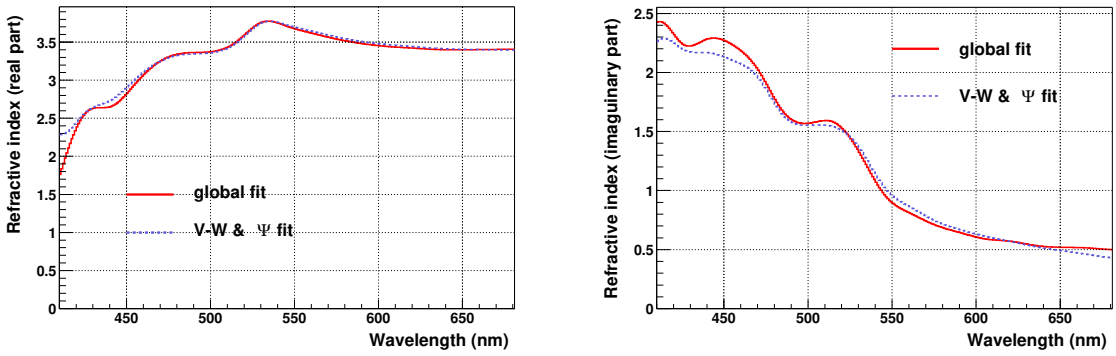

Figure 5.10: *Spectra of the complex refractive index of a KCsSb photocathode deduced by the fit of optical measurements with fixed* $d = 15\,nm$. *Comparison between the results of the global fit (red solid curves, also shown in Fig. 5.9) and those of a partial fit that uses only the V-W reflectance measurement and the ellipsometric* Ψ *data (blue dashed curves).*

The results in Fig. 5.9 show that the spectral shape of the real part of the photocathode refractive index is well constrained by the data, while the absolute normalization anti-correlates with the thickness in the fit. The solution for the imaginary part is nearly independent of assumptions of the photocathode thickness for $\lambda \gtrsim 480\,nm$, while at shorter wavelengths k anti-correlates with d. In fact, M&T have observed that the χ^2 of their fit increases the least steep in the parameter region around the minimum with constant $|n^*|^2\,d$ and n/k, because the reflectance below the critical angle remains constant over this surface.

A direct comparison of our results with those of other authors [MT92, Lan93] is not straightforward, because our data are not fitted by a unique solution. Table 5.1 reports the published results for $\lambda = 442\,nm$, the only wavelength investigated with M&T's method, together with examples of our determinations. The three measurements from M&T and Lang are in agreement with each other within the quoted errors. Despite the indetermination intrinsic in our estimation, it is difficult to reconcile our results with those of the other authors: Fig. 5.9 and Table 5.1 show that our estimation of n is consistent with the results of M&T and Lang for $d \simeq 15\,nm$, while a good agreement for k requires $d \simeq 30\,nm$. Fig. 5.11 shows a graphical comparison of our results and those of M&T, including a re-analysis that M&T propose of previous measurements by Timan at few other wavelengths in the visible region [MT92]. Our spectrum of the real part of the refractive index seems consistent with M&T calculations, assuming a low value of the photocathode thickness ($d \sim 15\,nm - 20\,nm$). Our curves of the imaginary part are systematically higher, instead, irrespective of d. The wavelength dependence is however in qualitative agreement.

5.5.2 *RbCsSb* Bialkali Photocathode

A similar analysis has been carried out with the optical measurements on the PMT ETL 9902B (*RbCsSb* bialkali). For this sample as well the global analysis leads to a bad fit to the VASRA and Δ measurements, hence the results of the fit of only the V-W and Ψ spectra are reported, following the indications of the previous analysis that those two measurements are sufficient. The estimated real and complex part of the refractive index as a function of the

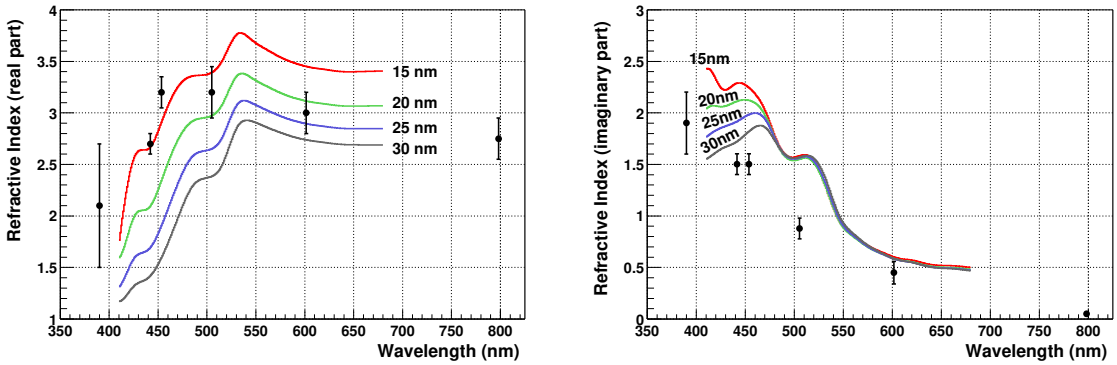

Figure 5.11: *Real and imaginary part of the KCsSb bialkali photocathode. The solid curves are our results, for different fixed photocathode thickness (as in Fig. 5.9). The markers show M&T analysis of their own data at $\lambda = 442\,nm$ and their re-analysis of Timan's measurements [MT92].*

Table 5.1: *Optical parameters of the KCsSb bialkali photocathode, for $\lambda = 442\,nm$, from [MT92, Lan93] and our analysis. Our estimations are obtained with arbitrarily fixed photocathode thickness, therefore they cannot be given a significant $\pm 1\sigma$ error.*

PMT	$n \pm 1\sigma$	$k \pm 1\sigma$	$d \pm 1\sigma$ (nm)	ref.
ETL 9124	2.7 ± 0.1	1.5 ± 0.1	23 ± 2	[MT92]
ETL 9125	2.71 ± 0.10	1.62 ± 0.06	18.1 ± 1.2	[Lan93]
ETL 9125	2.27 ± 0.19	1.68 ± 0.13	38.4 ± 3.5	[Lan93]
ETL 9102	2.69	2.28	15 (assumed)	our analysis
ETL 9102	2.12	2.11	20 (assumed)	our analysis

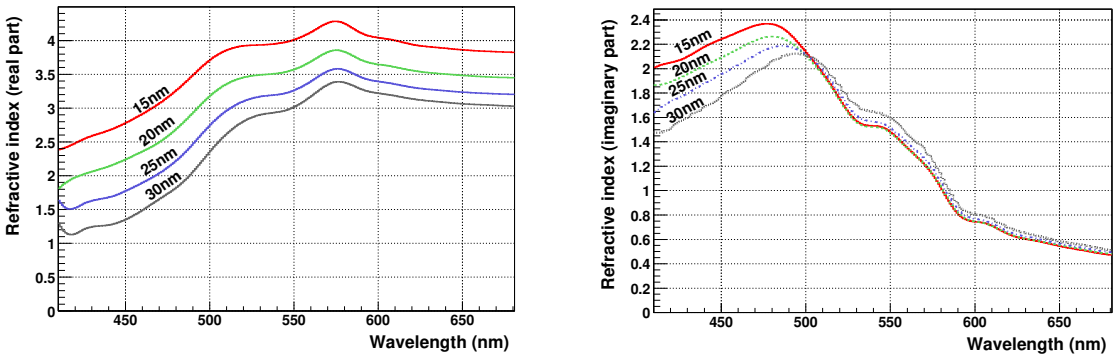

Figure 5.12: *Best fit spectra for real (left) and imaginary (right) part of the complex refractive index of a RbCsSb photocathode. The four displayed curves correspond to different assumed photocathode thickness: $d = 15\,nm$ (red), $20\,nm$ (green), $25\,nm$ (blue), $30\,nm$ (gray), fixed during the fit.*

Table 5.2: *Optical parameters of the RbCsSb bialkali photocathode for $\lambda = 442nm$, from [Lan93] and our analysis. Our estimations are obtained with arbitrarily fixed photocathode thickness, therefore they cannot be given a significant $\pm 1\sigma$ error.*

PMT	$n \pm 1\sigma$	$k \pm 1\sigma$	$d \pm 1\sigma$ (nm)	ref.
ETL 9124	2.73 ± 0.15	1.37 ± 0.08	18.8 ± 2.0	[Lan93]
ETL 9124	2.38 ± 0.10	1.32 ± 0.06	24.3 ± 1.6	[Lan93]
Hamamatsu R268 3	2.29 ± 0.10	1.65 ± 0.07	35.0 ± 1.8	[Lan93]
Hamamatsu R268 1	3.15 ± 0.26	2.16 ± 0.17	14.4 ± 2.5	[Lan93]
ETL 9902	2.70	2.20	15 (assumed)	this analysis
ETL 9902	2.16	2.04	20 (assumed)	this analysis

wavelength are plotted in Fig. 5.12.

The solutions show similar features to the case of the *KCsSb*: the same kind of anti-correlation with d is found, for the function $n(\lambda)$ as well as for $k(\lambda)$. Lang has used M&T's method to determine the optical parameters of the *RbCsSb* photocathode, at $\lambda = 442\,nm$. His results on four PMTs are summarized in Table 5.2, which also reports some of our determinations for the same wavelength. In the comparison with our curves another indication is found of systematic higher values for the imaginary part of the refractive index. Lang's results show however such a large scatter that it is not possible to conclude that our estimations are not consistent.

5.6 Discussion and Applications

In the previous section it has been pointed out that our measurements on the two investigated PMTs are not sufficient to determine unambiguously the photocathodes optical parameters. Nevertheless, data provide strong constraints, which are expressed as unique solutions for a fixed photocathode thickness. It should be noted that even with a precise determination of the

photocathode optical parameters in one PMT, the problem of predicting the behaviour of any other similar PMT would still remain indeterminate, because the thickness of the photocathode can vary of a factor ~ 2 from one PMT to another, as shown by Lang's measurements. Last, it is questionable whether it is really possible to assign a well determined refractive index to the photocathode material: in [Hea91, TMG99] the authors point out that the parameters measured for a thin film differ from those of the bulk material and that they can also differ in layers of different thickness, i.e. $n^*(\lambda) = n^*(\lambda, d)$. Furthermore, a PMT-to-PMT variation is to be expected, because the photocathode material is an alloy, rather than a well defined chemical species. In fact, the optical parameters obtained by Lang on PMTs equipped with the same photocathode show sometimes variations inconsistent with the experimental errors [Lan93]. For these reasons, any investigation of the optical properties of photocathodes should aim only at an approximate understanding of the PMT optics.

The original purpose of this study was to provide a model able to make predictions on the optics of a PMT, under any experimentally relevant condition. In the following, we try to probe the degree of predictability of our model and to evaluate the uncertainties originating from the ambiguity left in the problem, with the aid of some selected examples. The aim is to provide some "rules of thumb", which are believed to be useful in detector modeling. In all the calculations it will be assumed that light impinging on the PMT is unpolarized, as for scintillation light.

5.6.1 Qualitative Understanding of the PMT Sensitivity

First we check whether the model is able to predict the main features of a quantity that the PMTs manufacturers measure: the quantum efficiency QE in air, at near normal incidence. QE is related to the photocathode absorption, as expressed in eq. 5.1 on page 99. Fig. 5.13 shows the wavelength dependence of the absorption, deduced from our model after selecting the solutions for fixed photocathode thickness $d = 15\,nm$ and $d = 25\,nm$. A direct absolute comparison between the two PMTs from Fig. 5.13 is not obvious, because the two thicknesses may be different and fixing them to a common value would not be correct. However, Fig. 5.13 shows clearly that the green-enhanced bialkali photocathode is expected to have a plateau of maximum absorption extending further into the "green" visible region, compared to the standard bialkali. Absorption is largely determined by the imaginary part of the refractive index, so that the features of the calculated spectra reflect the shape of the $k(\lambda)$ functions in figs. 5.9 and 5.12, where it is also found that the *RbCsSb* photocathode spectrum peaks at longer wavelengths than the *KCsSb* photocathode. The figure also shows that changing the assumed photocathode thickness and correspondingly the best fit optical parameters has no effect on these qualitative assertions, mostly resulting in an offset for the calculated absorption spectra.

The correct prediction of the sensitivity of the two photocathodes, though only qualitative, is non trivial, because it has been based on the study of the reflected light only. However, the calculated absorption spectra are in disagreement with the reported QE (see Fig. 5.1 on page 100), especially in the tail, where the QE drops to zero, while the model predicts only a factor ~ 2 reduction. This may be explained with the hypothesis that the conversion factor $P_{conv}(\lambda)$ in eq. 5.1 on page 99 goes to zero at long wavelengths: photoelectrons are indeed produced, but with insufficient kinetic energy to escape the photocathode.

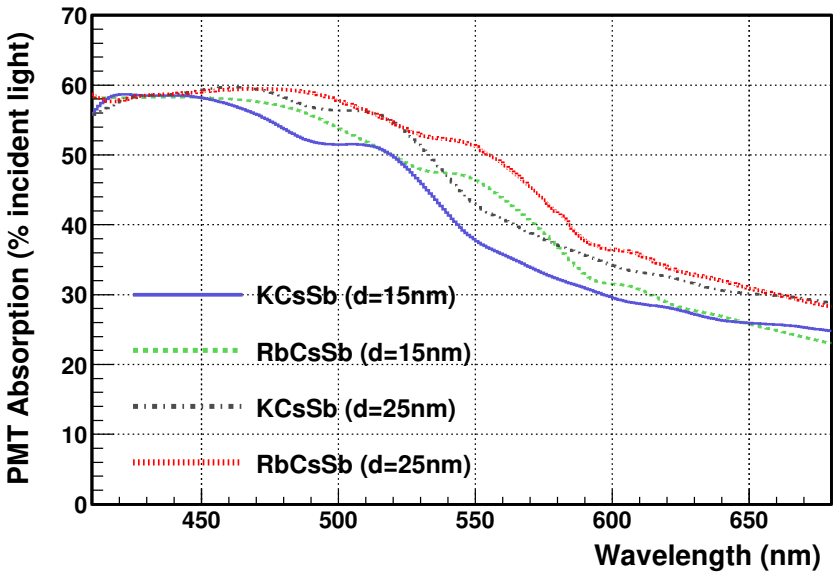

Figure 5.13: *Absorption calculated for PMTs in air and light impinging with $\theta = 5°$. The photocathode thickness is fixed to $d = 15\,nm$ and $d = 25\,nm$ and the corresponding best fit optical parameters are used (see figs. 5.9, 5.12).*

5.6.2 Predicted PMT Reflectance and Absorption as a Function of λ and θ

One of the main motivations for this study was the determination of the typical reflectance of a PMT optically coupled to a scintillator, as a function of wavelength and angle of incidence. This information is of great importance for the ^{176}Yb-LENS and Borexino experiments, as explained in the introduction.

Reflectance Wavelength Dependence Fig. 5.14 reports the wavelength dependence of the reflectance at various angles, calculated for our sample ETL 9102B in (or coupled to) liquid scintillator ($n = 1.5$) by choosing the optical solutions for $d = 15\,nm$.

At near normal incidence the spectrum is very similar to the one measured in air (cf. Fig. 5.4) and does not change much until θ approaches θ_c ($\simeq 42°$). Above the critical angle the spectrum behaves differently, with higher reflectance at longer wavelength: since transmission is suppressed at $\theta > \theta_c$ and absorption decreases with λ (cf. Fig. 5.13), the reflectance must necessarily compensate, to preserve $A + R + T = 1$.

The predictions for the *RbCsSb* green-enhanced photocathode are qualitatively very similar. The only visible difference is that the main features of the reflectance spectra (peaks below θ_c, slope change above) appear $\sim 40\,nm$ shifted to longer wavelengths coherently with all the optical measurements.

In Fig. 5.15 it is shown how the indetermination in our model affects the predictions: for $\theta < \theta_c$ the models with $d = 15\,nm$ and $d = 25\,nm$ give the same results, whereas at higher angles the differences can be quite large. This is related to the fact that the behaviour of a

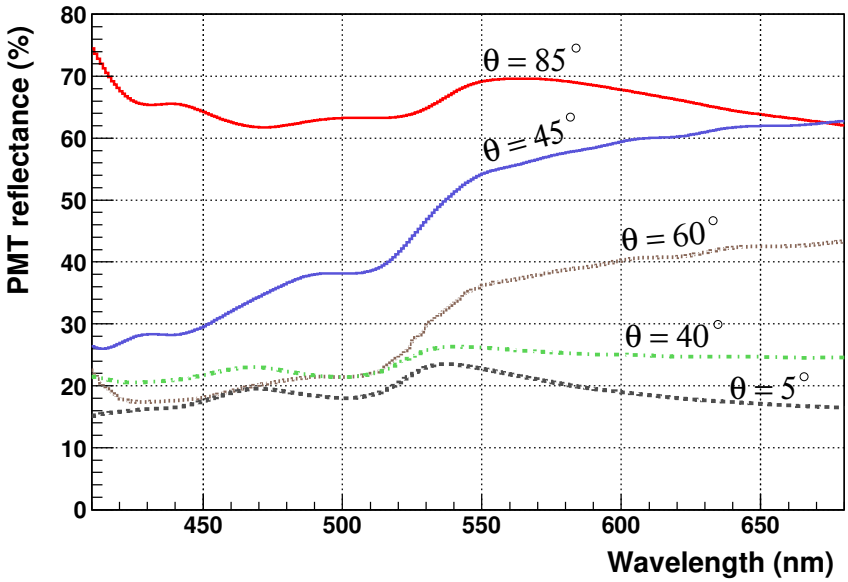

Figure 5.14: *PMT reflectance as a function of the wavelength at some angles of incidence, calculated for the sample ETL 9102B in a medium with $n = 1.5$, choosing a photocathode thickness $d = 15\,nm$ and the corresponding optical parametrization in Fig. 5.9.*

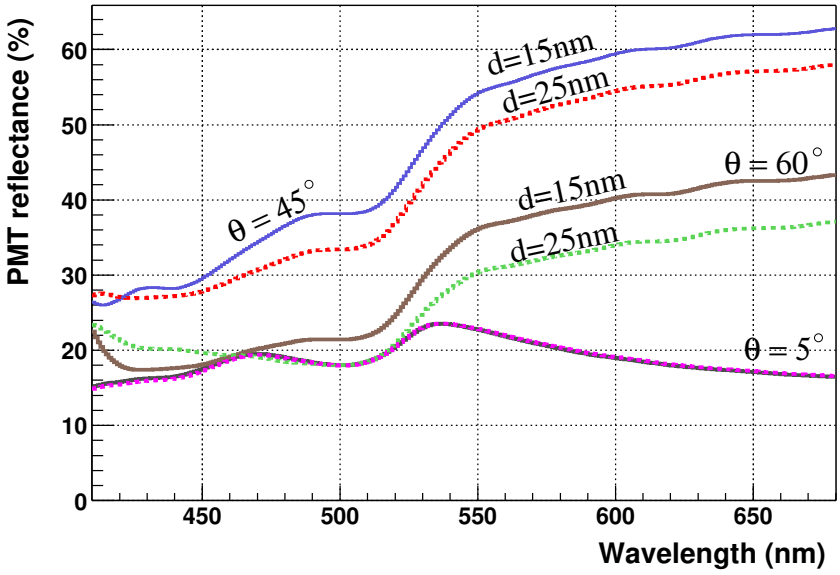

Figure 5.15: *Comparison between the PMT reflectance spectra (ETL 9102B) calculated using the solutions for photocathode thickness $d = 15\,nm$ (solid lines) and $d = 25\,nm$ (dashed line), for PMT in scintillator ($n = 1.5$). The two curves for $\theta = 5°$ are hardly distinguishable in the graphics.*

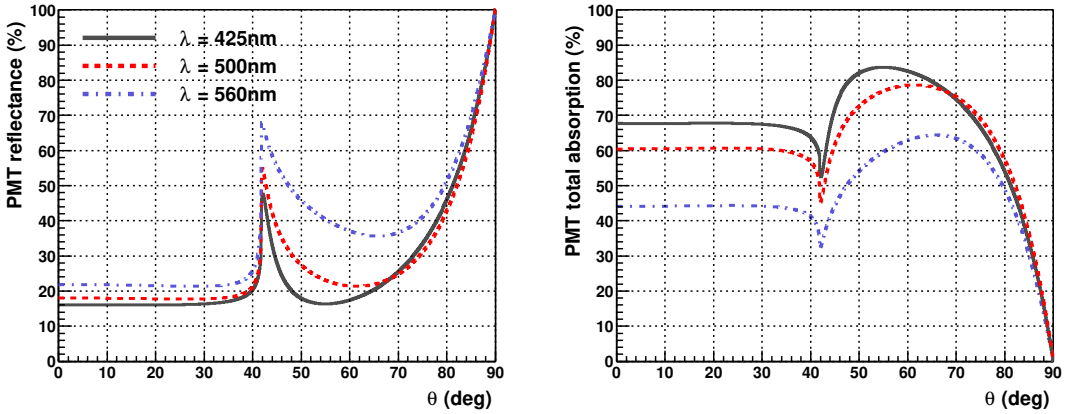

Figure 5.16: *Predicted angular dependence of reflectance and total absorption (see footnote on the current page for the definition), for the investigated ETL 9102B PMT in optical contact with a scintillator ($n = 1.5$), at three representative wavelengths. For the calculations the model from figure 5.9 for $d = 15\,nm$ was employed.*

PMT in liquid below the critical angle does not differ very much from that of a PMT in air (after the Fresnel reflection off the glass is corrected). The selected solutions are those best fitting the measurements in air, consequently they also make very similar predictions for a PMT in liquid at $\theta < \theta_c$. On the other hand, Fig. 5.15 corroborates the statement that the degeneracy of the model is most effectively broken by measuring the reflectance of a PMT in liquid, above the critical angle for total internal reflection.

Angular Dependence of Reflectance and Absorption In Fig. 5.16 the angular dependence of reflectance and total absorption[7] is shown, for three representative wavelengths. In all cases the reflectance has a plateau below θ_c, then a sharp peak at the critical angle, followed by an extended angular region where R has similar or higher values than at near normal incidence; finally the spectrum has a fast increase to 100% for $\theta \to 90°$. Similarly the total absorption has a flat angular dependence for $\theta < \theta_c$, a sharp dip at the critical angle, followed by a broad peak and it finally goes to zero to keep $A + R = 100\%$ ($T = 0$ for $\theta > \theta_c$). At different wavelengths the branching between reflection and absorption changes, as well as the shape of the peak around the critical angle. The analysis of the $RbCsSb$ photocathode leads to very similar predictions.

It is important to note that, since the conversion factor $P_{conv}(\lambda)$ in eq. 5.1 is not expected

[7]The total absorption also includes the fraction of transmitted light that is back reflected onto the photocathode by the aluminized internal surface of the PMT and eventually absorbed. Since simulating optics inside the PMT would be too complicated, it is assumed for simplicity that on average a fraction ~ 0.7 of the transmitted light (T) hits the photocathode again. The probability for absorption is given by the same optical model whose equations are presented in Sec. 5.2.1, simply by exchanging the order of the refractive indices, going from vacuum to scintillator. Absorption from the photocathode side is a very flat function of θ. Using the model for the PMT ETL 9102B corresponding to $d = 15\,nm$, it is found: $A(425\,nm) \sim 0.42$, $A(500\,nm) \sim 0.36$, $A(560\,nm) \sim 0.25$. These values are multiplied by $0.7T$ and added to the absorption from the scintillator side to obtain the total absorption function. The effect of this correction is to increase absorption below the critical angle, resulting in a higher QE. As a by-product, the PMT efficiency has a more uniform angular dependence.

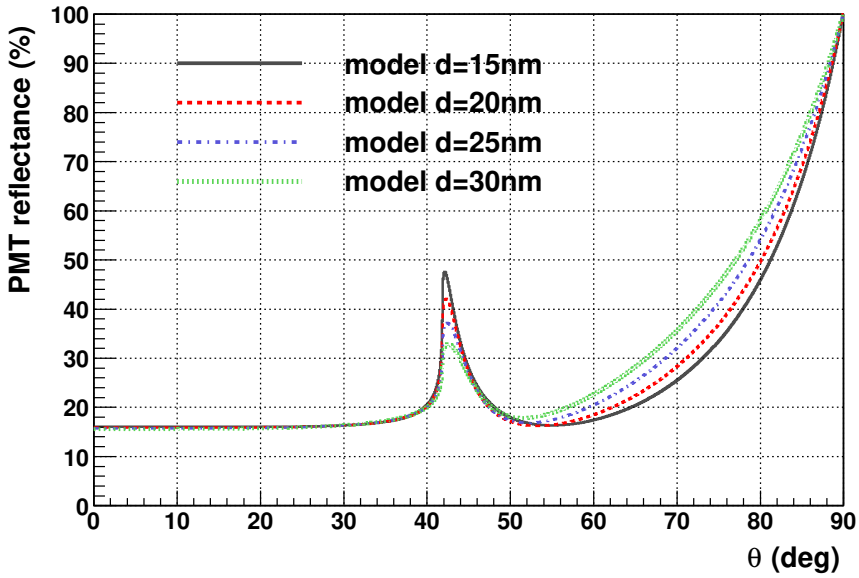

Figure 5.17: *Reflectance calculated for the investigated PMT ETL 9102B operating in optical contact with a scintillator ($n = 1.5$), at the wavelength $\lambda = 425\,nm$. The different curves correspond to the choice of each of the four best fit solutions obtained for fixed photocathode thickness: $d = 15\,nm,\ 20\,nm,\ 25\,nm,\ 30\,nm$.*

to depend on θ, the angular dependence of the total absorption function is the same as that of the PMT QE. As a consequence, the efficiency of a PMT can be predicted for any angle of incidence and wavelength, by rescaling the calculated absorption with the ratio $QE(\lambda)/A(\lambda)$ at near-normal incidence.

In Fig. 5.17 the impact of the indetermination of the optical parameters is studied, for the example of the PMT ETL 9102B at $\lambda = 425\,nm$, which is representative of the typical wavelength range of the light emitted by scintillators doped with bis-MSB. It is again found that all the models give the same predictions for $\theta < \theta_c$, whereas they slightly differ from each other at larger angles of incidence, even though the angular dependence is qualitatively the same. We remark that a single reflectance measurement with the test PMT in liquid, at a single wavelength, by $\theta \simeq 43°$ or $60° \lesssim \theta \lesssim 80°$, would probably be sufficient to break the degeneracy left over by the entire set of optical measurements performed.

5.7 Conclusions

The optical properties of two test PMTs, an ETL 9102B and an ETL 9902B, the former endowed with a standard *KCsSb* bialkali photocathode and the latter with a *RbCsSb* "green-enhanced" bialkali photocathode, have been investigated, through the measurement in air of the absolute reflectance at near normal incidence, the relative reflectance at variable angles of incidence for both polarization and the study of the polarization of light upon reflection off the photocathode (ellipsometry). The experimental data have been fitted with a model based on the optics of thin films to determine the photocathode optical parameters. The problem

turned out not to have a unique solution, however data provided sufficient constraint for the fit to converge to a class of solutions depending on a single free parameter, for example the photocathode thickness. Based on this observation, the optical properties of both PMTs could be predicted in the wavelength region $410\,nm \leq \lambda \leq 680\,nm$, and the uncertainty originating from the degeneracy of the model was evaluated and discussed. The latter is sufficiently small, to allow the formulation of "rules of thumb" for the prediction of the angular and wavelength behaviour of reflectance and absorption from a bialkali PMT in contact with any medium. As an example, the case of *KCsSb* PMT coupled to a scintillator was studied in detail. The model predicts that the reflectance is nearly constant for light with incidence $0° < \theta \lesssim 40°$, with values of $R \sim 15\% - 25\%$ depending on the wavelength, according to the spectra shown in Fig. 5.14. Figs. 5.15 and 5.17 show that in this angular range, the predictions of the model are robust, because strongly constrained by the direct measurement of the PMT reflectance (shown in Fig. 5.4). Above the critical angle ($\theta \gtrsim 42°$) the degeneracy is broken and the uncertainty of the model larger. However, figs. 5.15 and 5.17 show that also in this case quantitative predictions are made at the level of $\lesssim 10\%$ precision. This accuracy is fully adequate for the simulation of light propagation in large Cherenkov and scintillation detectors. A simplified model based on this work has been already implemented in the Borexino light tracing MC. Fig. 5.16 shows that the quantum efficiency of a PMT, normally measured for near-normal illumination, can be predicted at any angle, through the angular dependence of the photocathode absorption. It is found that the PMT has nearly constant sensitivity for $\theta < \theta_c$, a $\sim 20\%$ higher efficiency for $45° \lesssim \theta \lesssim 70°$ and an efficiency dropping to 0 for $\theta \to 90°$, where the PMT reflectance goes to 100%.

The optical model of a PMT discussed in this chapter is implemented in the simulations of light transport in a LENS cell, which are described in Chapter 6 and whose results are presented in Chapters 7 and 8.

Chapter 6

Optical Model of a LENS Cell

6.1 Introduction

The demands of the Yb-LENS and In-LENS experiments are quite different, however they share many features of the proposed designs (Sec. 2.2), such as: segmented liquid scintillator detector, cuboid unitary cell, energy and time of flight read-out through two PMTs, one at each side. These similarities allowed a unified approach to the problem of light transport and detection in the detector. A detailed optical model for implementation in Monte Carlo (MC) simulations of a single scintillator cell is a fundamental tool for LENS, toward:

- Identification the most crucial detector parameters
- Prediction and understanding of the performance of the detector in different configurations
- Determination of the optimum design, the best cuts strategy, the ν-tag efficiency, etc.

The above goals are achieved by predicting the two fundamental observables of the detector:

- Photon arrival time distribution, which determines the signal pulse shape
- Photon collection efficiency, which determines the detector energy and space resolution

These parameters are determined as a function of the event position inside the sensitive volume.

Starting from a core of simple geometrical photon tracing, the model was continually improved, through the introduction of "second order effects" and the implementation of a more refined physical description. At each stage, the prediction of the "state of the art" simulation was compared to experimental data, leading on one hand to the identification of features requiring a more appropriate implementation in the model, on the other hand to the optimization of the detector design. In several cases the need to improve the model or to feed it with the most appropriate input data has led to self-standing experimental studies of single detector elements that cover an important part of this work (Chapters 3, 4 and 5). The final result of this development is a model that has been used to:

1. estimate the performance and the instrumental background of an Yb cell
2. optimize the design of an In cell

3. interpret the results of the optical measurements of the MPIK In-LENS prototype cell.

These studies will be reported in Chapters 7 and 8. In the next sections the final result of such development is described, while other "precursor" and intermediate models will be neglected, though for many applications the use of all of the implemented features is not necessary and many of them can be "switched off", leading to simpler descriptions (this is for instance the case of the simple photon-tracing simulations used to analyze the light piping measurements, as discussed in Chapter 4).

This model is a multipurpose tool easily adaptable to any detector based on the LENS design. The aim of this chapter is to set the general physical framework, the definitions, conventions and assumptions. Only the input parameters and the physics common to all the simulations will be discussed here. More detector-specific input parameters and the results of various applications of the model for LENS are given in the next chapters.

6.2 Simulation Strategy

The "optical" performance of the LENS detector depends entirely on pulse shape and photon collection efficiency. This is true for ^{176}Yb as well as ^{115}In, however there are peculiarities of the two isotopes, which make each one particularly sensitive to specific aspects of the problem. For Yb-LENS one critical point is the short lifetime of the $\nu-$populated $^{176}Lu^*$ metastable state and the low energy of the coincidence γ, which can lead to misidentification of the ν-tag from statistical fluctuations or instrumental self-correlations of single events (Sec. 2.3.3). Therefore in the model several features are included that affect the pulse shape of a signal and in particular its tail, over few hundreds nanoseconds: scintillator decay-time, light reflection off the PMTs and late pulses from the PMTs. At this regard, important inputs come from the specific experimental studies reported in Chapters 3 and 5.

For the Indium case, the tag is much less sensitive to the signal pulse shape, which plays a (modest) role only for the spatial resolution. Here, it is crucial to show that in the frame of a realistic detector design energy and spatial resolution are sufficient to reject the *In-bremsstrahlung* and other backgrounds. In this case the focus is on the details of light transport and interaction, with the inclusion of all known effects leading to photon loss, absorption and scattering. Particular important for these issues are the results of the light piping study reported in Chapter 4, the implementation of a faithful detector geometry and of the optics of scintillators. The last two items are described in this chapter.

The optical model developed is used to run "single-photon-tracing" Monte Carlo simulations. Each cycle of a MC loop starts with the generation of a new photon and finishes with either its detection or its loss. At generation a set of observables are assigned to the photon, chosen randomly from input probability density functions (PDF). The photon is propagated inside the detector volume according to its table of observables and the "laws of propagation and interaction", to be soon described. The photon evolution proceeds step by step, where each step can either be a reflection-refraction-transmission at the interface between different regions, or an elastic-inelastic scattering in the medium, or an absorption in the medium as well as at an interface. Photons impinging on the photocathode of the PMTs can either be detected, back-reflected or lost, according to well defined probabilities.

Two options can be followed to implement a model of light propagation in a MC: to use existing simulation toolkits, such as GEANT4, for the general framework of the simulation and introduce the specific physics which is not provided; or writing a simulation code, to have

a more direct control on the most critical issues. The latter strategy has been followed, since the physics of light interaction with scintillators and PMTs is only very roughly implemented in GEANT4. The MC code is written in FORTRAN programming language and makes use of the CERN libraries for the random number generator and other useful mathematical functions.

6.3 Geometry

During the development of the model, two main geometry frameworks have been implemented: parallelepiped and cylindric. The Monte Carlo has been optimized for the former, while the latter has been developed mostly to test the cylindric geometry and compare it with the square one. Fig. 2.2 on page 41 shows the typical geometry considered for In-LENS and the detector prototypes. The simulated volume is divided in regions, each characterized by specific optical and physical properties. In the most general implementation, such regions are:

1. Scintillator
2. Air gap (inside the cell, on top of the scintillator)
3. Cell walls
4. Buffers
5. PMTs

The cell is described at first approximation as a square parallelepiped with free dimensions (Fig. 2.2 on page 41). After the first prototype quartz cells were built, the simplified square geometry has been improved to obtain a more realistic description. For example, the measurements of light piping reported in Chapter 4 have been carried out using a square cell with rounded corners, as shown in Fig. 4.4 on page 80. In that analysis it was stressed that the implementation of the rounded corners for the case of TIR-guiding improves significantly the agreement between simulated and experimental light intensity curves (cf. Fig. 4.9). In general, the features of the implemented geometry are detector specific and are tuned to reproduce the real geometry of the LENS prototype cells (cf. Fig. 8.4 on page 167). The buffers are usually defined as simple solid bars. Some examples of PMT coupling in a simple square geometry are shown in Fig. 6.2 on page 134.

6.4 Scintillator and Other Media

Light is first emitted by the scintillator, then has to propagate through it before being detected. Consequently several properties of the scintillator enter the model. The physics of the scintillator (and of other media in a cell) is a fundamental issue for the LENS concept and as well for the optical model described in this chapter.

Refractive Index As any dielectric medium, all scintillators are characterized by a refractive index spectrum $n(\lambda)$. For a medium with normal dispersion law, n decreases smoothly with increasing λ over the near UV-visible spectrum (Cauchy's law). This variation is a few percent over the scintillator emission spectrum and is negligible compared to other uncertainties in the model, therefore a single value for n is assumed. Typically $n \sim 1.5$ in organic

scintillators. The same arguments apply to the walls and light guides materials. For example, the Borexino scintillator has $n \simeq 1.505$, *suprasil* quartz $n \simeq 1.47$, acrylic $n \simeq 1.49$. For simplicity it is assumed that all the regions of the cell are perfectly coupled: $n_{walls} = n_{lg} = n_{scint}$.

The refractive index of the medium determines the speed of light and hence influences the signal pulse shape and the left-right time of flight difference. Most importantly, it determines the condition for *total internal reflection* at the interface to air (see Sec. 4.2). The higher the refractive index, the larger the solid angle for efficient light transport.

Scintillator Light Yield The Light Yield (LY) is defined as the number of emitted photons per unitary energy deposited by an electron. It represents the efficiency of conversion of the deposited energy into a form suitable for detection, i.e. photons. It is one of the most important figures of merit of a scintillator. Measuring the LY of a scintillator free of systematics is difficult, hence the light output relative to a well known and reproducible standard is normally measured (see e.g.. [Buc04]). The LY enters the model as a multiplicative normalization factor, either for estimations of the total collected light corresponding to a given deposited energy, or for comparison between different scintillators, whose relative yields are known. The MC simulations predict the fraction of primary photons that is eventually detected at the PMTs. This efficiency can be multiplied by the LY to calculate the total number of detected photoelectrons per unitary deposited energy, often given in units of pe/MeV. This number gives the limit of the achievable detector energy resolution.

Scintillation Decay Time The fluorescence decay time of organic scintillators has been defined in Chapter 3, where the experimental technique and the results of measurements carried out on several samples are also reported. The fluorescence PDF can be approximated with the multi-exponential function of eq. 3.1 on page 57. Three exponents are in most of the cases sufficient, therefore the input data of the model are the three time constants τ_1,τ_2, τ_3 and the three relative weights q_1, q_2, q_3. The scintillator decay time enters the optical model in the determination of the signal pulse shape: each photon has an associated "generation" time, randomly chosen using the multi-exponential PDF. This time is an offset which is added in the calculation of the photon time of arrival.

Scintillation Emission Spectra The physics of light emission from a composite solvent-fluor-shifter system is rather complex and will not be treated here in detail (see e.g. the textbook [Bir64]). Each component is characterized by its own pure emission spectrum, normally measured by exciting the molecules in an optically inert solution at their absorption peak and observing the corresponding emission. In an aromatic scintillator mixture the primary deposited energy excites the solvent, whose emission is typically in the UV. The fluor molecules are tuned to have their absorption band overlap with the solvent emission spectrum, so that they intercept the solvent excitation and reemit light at a longer wavelength. The same is done (when needed) by a secondary fluor (Wave Length-Shifter, WLS, or λ-shifter), which converts the primary excitation into a final "blue" spectrum, where the scintillator has a high transparency and the PMTs sensitivity is good.

Two mechanisms can apply for the wavelength shift: *radiative* and *non radiative* energy transfer. In the former case the transfer from a *donor* to an *acceptor* molecule (solvent $\rightarrow$ fluor, or fluor $\rightarrow$ λ-shifter) is mediated by a real photon, in a process of emission-absorption-reemission. In the non-radiative case, the donor transfers its excitation energy to a neigh-

bouring acceptor without emission-absorption of real photons. When the energy transfer is radiative, the initial scintillation spectrum is the one of the donor molecules. Photons then propagate out of the production region and are absorbed and reemitted at longer wavelengths by the acceptor molecules. The longer the distance, the more the spectrum results shifted. In case of non radiative energy transfer, the initial scintillation spectrum is directly the one of the acceptor. It is desirable to have non radiative energy transfer dominating, because the efficiency of wavelength shifting is higher in this case.

The understanding of the mechanisms of energy transfer from the solvent to the fluor and finally to the WLS is a key issue in LENS, especially for the luminescent properties of the β-diketonates scintillators developed at MPIK [MPI03, Buc04]. Experimentally, an energy transfer has been considered radiative when in a solution containing both molecular species, donor and acceptor, the excitation of the donor results in the direct emission of the acceptor spectrum, when fluorescence is measured in "front-face geometry". In this geometry the light is observed from the same side where the sample is excited, so that self-absorption and wavelength shifting are negligible. Conversely, the energy transfer is considered radiative when in front-face geometry the fluorimeter output is the emission spectrum of the donor. It is found that the transfer from any scintillator solvent (Anisole, PC, PXE) to suitable fluors at usual concentrations (order of few g/l) is mostly non-radiative. The transfer to the WLS at typical concentrations (few tens of mg/l) is predominantly radiative, instead. Non-radiative transfer becomes important at much higher concentrations, which are however not suitable for scintillation detectors due to intense self-absorption of light.

The model requires the initial spectrum of the emitted light to be known. This is the spectrum that "propagates" in the simulation. Therefore, it is necessary to know how energy is transferred from the solvent to the final fluorescent molecule. In the model the assumption is made that the initial spectrum is the measured emission spectrum of the last non-radiatively populated component. This is an approximation, since in the case radiative and non radiative energy transfer have comparable importance, the fluorescence light has an intermediate spectrum between donor and acceptor, but this effect is in part accounted for by including the radiative energy transfer in the model, as explained in the next section.

The experimental spectra implemented in the model are those of PPO and BPO for the primary fluors; bis-MSB as WLS. They are shown in Fig. 2.1 on page 40.

Extinction The basic interactions of optical photons in a medium are:

1. **absorption**: the photon is lost, its energy dissipated

2. **elastic scattering**: the photon scatters off an electron or off non homogeneity of the medium. It continues to propagate in a new direction with the same wavelength. In case of Rayleigh scattering the new direction is statistically correlated with the one of the incoming photon according to a $\propto \frac{1}{\lambda^4}(1+\cos^2\theta)$ law, where θ is the angle to the original direction

3. **inelastic scattering**: the photon is absorbed by a molecule, which de-excites emitting a photon of longer wavelength (see discussion above about the *radiative* energy transfer). The fluorescence is isotropic and there is no correlation between the old and new photon direction

In a system in which different chemical species are present, each molecule contributes to all three processes. It would be desirable to know the cross sections of every single interaction mechanism as a function of the wavelength, for each component of the scintillator mixture. However, a spectrophotometer measures simply the fraction of light which is lost from a collimated beam, whatever the mechanism, in a nearly mono-dimensional set-up. This "light loss" is calculated by comparing the residual light intensity measured after crossing of a thickness d of a solvent and after crossing of the same thickness of a solution of the same solvent and the substance under investigation. This information converts into a molar extinction coefficient, which is used to calculate an attenuation length, $\mu(\lambda)$, for any given solute concentration. This is the quantity that enters the *Lambert-Beer's* law of attenuation:

$$I(x) = I_0 e^{-x/\mu} \tag{6.1}$$

where $I(x)$ is the residual light intensity in the beam after a distance x and I_0 the unattenuated intensity. Eq. 6.1 holds independently for each component of the scintillator mixture and assuming that the attenuation processes are independent of each other, the attenuation is still given by the Lambert-Beer's law, with:

$$\mu = \mu_{tot} = \left(\sum_i \frac{1}{\mu_i} \right)^{-1} \tag{6.2}$$

where μ_i are the contributions from the single components.

With the experimental procedure outlined above, absorption, elastic and inelastic scattering are indistinguishable, as they all result in removing photons from their original direction. This is the reason why μ is called the *attenuation length* and not *absorption* or *scattering* length: attenuation is what can be most easily measured. In the optical model of a LENS cell, absorption, elastic and inelastic scattering are all implemented, but since their individual cross sections are not experimentally known, it is necessary to use the measured attenuation lengths μ_i and make assumptions on the relative probability of the three processes. Elastic scattering has usually been "switched off", since it is sub-dominant in most cases. Consequently, the measured extinction spectra are considered composed of two contributions: absorption and inelastic scattering. The model must implement the relative probability of those two processes. These probabilities are estimated based on the knowledge of the fluorescence properties of the molecules involved and on the measurements performed with our fluorimeter [Buc04]. In general the materials of a scintillation detector belong to two categories: pure absorbers and fluorescing components. For the former the attenuation length is in reality an *absorption* length: any interaction with a photon results in its destruction. For the fluorescing species, a fluorescence quantum yield, ϕ, must be defined, which is the probability that an absorption is followed by a prompt photon re-emission, i.e. the probability that an absorption is indeed an inelastic scattering. In Table 6.1 the values assumed for the LENS simulations are reported. In case of inelastic scattering, a new photon is generated, with the emission wavelength PDF relevant to the absorbing molecule, with the energy-conserving constraint $\lambda_{new} > \lambda_{old}$.

Other Media The walls of the cell and the light guides are defined in the model as separate regions of the detector, having the same refractive index of the scintillator and a constant attenuation length, due to pure absorption, of $20\,m$. The latter attenuation length is simply assumed as a lower limit for a highly transparent medium (see discussion in Secs. 4.5.2 and

Table 6.1: *Estimation of the probability distributions between absorption and inelastic scattering for all the detector component of a LENS cell. ϕ is the probability that an absorption results in a new photon emission, λ the wavelength of the absorbed photon. It is assumed $\phi = 0\%$ for the solvent at all wavelengths because the solvent emission spectrum has typically a negligible overlap with the emission of the fluors [Buc04]. Therefore the fluor scintillation light absorbed by the solvent is not reemitted. Fluors (BPO was chosen for most simulations) are known to have very high quantum yield for absorption of photons in their absorption band, virtually $\phi = 100\%$. However a more conservative 90% is chosen, because the yield for photons overlapping with the emission band may be lower and because the scintillator may contain impurities that quench the emission. For an exciting radiation with $\lambda \gtrsim 410\,nm$ (for BPO) no measurable light output is found at the fluorimeter [Buc04], therefore it is assumed $\phi = 0\%$above this threshold. Similar arguments are used to justify the parameters chosen for the bis-MSB. The organo-metallic compounds bringing the ν-target metal in solution have never shown fluorescence in the optical band [MPI03, Buc04]. Similarly, quartz and buffers are pure absorbers.*

	Solvent	Metal-Compound	Fluor (BPO)	bis-MSB	Quartz & Buffers
ϕ	$0\%\ \forall\lambda$	$0\%\ \forall\lambda$	$90\%\ \lambda < 410\,nm$ $0\%\ \lambda > 410\,nm$	$95\%\ \lambda < 450\,nm$ $0\%\ \lambda > 450\,nm$	$0\%\ \forall\lambda$

4.6.3). The materials for the LENS prototype cells and the buffers are quartz and acrylic respectively, both extremely transparent in the visible and near UV spectrum. In general, the implementation of the quartz walls in the model has the effect of increasing the effective attenuation length, especially in small cells, where the quartz volume is a non negligible fraction of the total volume available for light transport: photons are reflected at the boundary with air and hence they travel part of their way to the PMTs in an optically inert medium. A similar argument holds for the air gap above the top scintillator surface, where $n = 1$ (light refraction at the interface is correctly implemented) and no absorption is assumed.

6.5 Light Piping

Light piping in optical modules has been studied in Chapter 4. This issue is strongly related to the detector energy resolution, which is a critical for the LENS concept toward high ν-tag efficiency and especially background reduction. Therefore light piping must be implemented in the model with the highest precision. The main options for light piping, defined and discussed in Chapter 4, are reconsidered in the next sections, with focus on the application in scintillation modules.

Total Internal Reflection The TIR reflectance off quartz finished surfaces has been experimentally determined and the results reported in Sec. 4.6. It was found $R_{TIR} = (99.35 \pm 0.2)\%$ at $\lambda = 430\,nm$. In a cell of larger dimensions than the one used for the light piping measurement this efficiency may even be higher, due to better surface homogeneity. TIR offers therefore a high piping performance when a large number of reflections are necessary to guide light to the PMTs. Fresnel reflection is implemented in the model (eq. 4.1 on page 76), as well as TIR with its efficiency parameter.

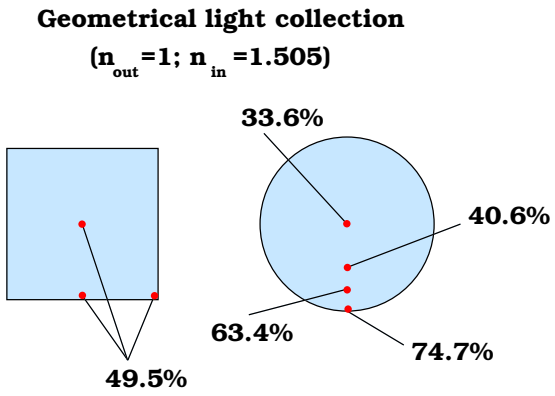

Figure 6.1: *MC-calculated geometrical light collection in some representative positions in the plane transversal to the longitudinal axis of the cell, for a square parallelepiped and a cylinder.*

In a three-dimensional model, even for a simple square geometry, as the one in Fig. 2.2, it is not trivial to calculate analytically the solid angle for TIR acceptance, which is found solving the integral:

$$\Omega_{TIR} = \int_{|u|,|v|<cos\theta_c} d\Omega \tag{6.3}$$

where u and v are the cosines of the photon direction in the plane transversal to the cell axis. Once a photon is generated with direction in the acceptance solid angle of eq. 6.3, in any square geometry the condition for TIR will be always satisfied, providing no other processes intervene.

First Results of "Geometric" Simulations Eq. 6.3 has been numerically estimated with a Monte Carlo for the particular case $n = 1.5$. It is found:

$$\Omega_{TIR}/4\pi \simeq 0.491 \tag{6.4}$$

It is important to note that eq. 6.4 is not dependent on the light source location in the cell transversal plane. This is a consequence of the square geometry and eq. 6.3. On the contrary, in a cylindric cell the geometrical light acceptance for TIR is strongly dependent on the position of the light emission site in the transversal section. In fact, for a source in the cylinder axis the component of the photon momentum in this transversal plane cannot contribute to TIR and the angle of incidence to the cylindric surface depends only on the component of the photon direction along the cell axis. In this case, the acceptance is given by $\Omega_{TIR}/4\pi = 1-\sin\theta_c = 1-1/n$. The more the source moves toward the external circumference, the larger becomes the solid angle for TIR, as more and more "spiralizing" paths enter the TIR acceptance expressed by the eq. 6.3. In Fig. 6.1 the results of MC calculations of the geometrical collection efficiencies for several positions are reported, for a typical $n \sim 1.5$. This means that in a cylindric geometry based on TIR light piping the same energy deposited at different radial positions results in signals of different amplitudes. Since in a longitudinal cell there is no handle for reconstructing the position of an event in the transversal plane,

a cylindric geometry would jeopardize the energy resolution of a TIR-based detector. The geometry in Fig. 4.4 (see also Fig. 8.4 on page 167) is an intermediate case between the two cases discussed above, due to the rounded corners. Light in the acceptance solid angle of eq. 6.3 can lose the TIR condition at a corner or just after reflection off a corner. In Sec. 4.6.3 it was discussed how this departure from the square case can affect the performance of an optical module. This subject will be further studied in the frame of the simulations of an In cell in Sec. 7.2.

Specular Reflection and Mixed TIR-SR SR light guiding is also implemented in the model, through the effective surface reflectance measured for VM2000 light pipes, as reported in Chapter 4. The result of this measurement is $R_{VM2000} = 98.5 \pm 0.3$ at $\lambda = 430\,nm$. The spectral dependence of the reflectance was measured at the spectrophotometer to vary of $\sim \pm 0.5\%$ in the wavelength range of interest for LENS (Fig. 4.3 on page 79). Intuitively, it is expected that pure SR-piping has absolute better performance than TIR when the number of reflections is not too high, because of the $\sim 50\%$ loss of acceptance solid angle with TIR. However, the higher TIR reflectance ensures a longer piping attenuation length and is more suitable when light has to reflect many times before detection. Quantitative conclusions on the relative comparison between TIR and SR in optical modules require a full MC study, which is carried out in Sec. 7.2.

As suggested in Sec. 4.2, since $R_{TIR} > R_{SR}$, the solution for the optimal light piping consists in using TIR whenever possible, SR otherwise. A TIR-based cell wrapped in non-coupled VM2000 foils implements this concept. Beside maximizing the piping efficiency, the reflectors outside the cell can also partly compensate for a non ideal cell behaviour, due e.g. to local surface non homogeneities, roughness, etc. Considering whether or not such irregularities are also the primary cause for the $\sim 0.65\%$ TIR reflectance inefficiency, two opposite scenarios are conceivable:

- TIR *or* SR: light is guided via TIR or SR, depending on whether the angle of incidence is larger or smaller than θ_c. Light lost due to inefficient TIR-guiding is not recoverable.
- TIR *and* SR: light missing TIR reflection, even for $\theta > \theta_c$, is simply transmitted across the quartz and can be still reflected by the foils around the cell. As a result, the effective reflectance efficiency is increased to $R_{TIR\&SR} \simeq 99.99\%$ for $\theta > \theta_c$.

Mixed TIR+SR light piping has not been investigated with the technique described in Chapter 4, however reality is likely to lay somewhere between those two extremes. In the model the effect of the VM2000 for recovering light escaping TIR at $\theta > \theta_c$ is simulated by artificially increasing the TIR effective reflectance, with the condition $R_{TIR} \leq R_{TIR\&SR}(\theta > \theta_c) \leq R_{TIR} + (1 - R_{TIR})R_{SR}$.

6.6 Light Interaction with the PMTs

Photons that are not absorbed, nor lost due to inefficient piping, will eventually strike the photocathode of one of the two PMTs, where they can be converted into a useful signal. Assuming that the glass of the PMT couples perfectly to the quartz - scintillator system, the whole physics of the light interaction with the PMTs reduces to the understanding the processes that a photon can undergo when it hits its photocathode. This topic is the subject

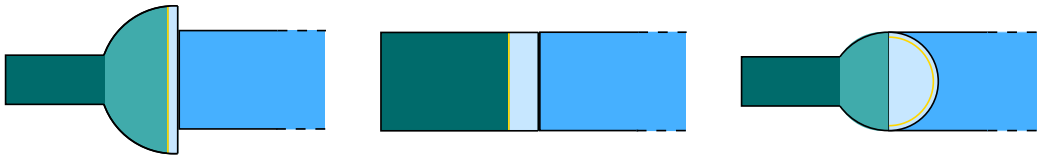

flat PMT/photocatode full coverage | **flat PMT/photocatode partial coverage** | **hemispherical PMT partial coverage**

Figure 6.2: *The three implemented PMT-to-cell interfaces. The PMT has always rotational symmetry, while the cell has square section.*

of Chapter 5, where the theory of light interaction with a PMT is presented and the optical measurements performed on two different photocathodes presented. The result is an optical model of the photocathodes, which is able to predict the functions $A(\lambda,\theta)$, $R(\lambda,\theta)$, $T(\lambda,\theta)$ (see Sec. 5.1 for definitions) for a PMT in any medium. This model has been implemented in the description of a scintillator cell to calculate the probabilities for a photon to be detected, reflected or lost at the PMT:

$$\begin{array}{ll} P_D(\lambda,\theta) & = QE(\lambda,\theta) = QE'(\lambda,0) \times \frac{A^*(\lambda,\theta)}{A^*(\lambda,0)} \\ P_R(\lambda,\theta) & = R(\lambda,\theta) \\ P_L(\lambda,\theta) & = 1 - P_D(\lambda,\theta) - P_R(\lambda,\theta) \end{array} \tag{6.5}$$

with the following meaning for the symbols used:

$P_{D,R,L}(\lambda,\theta)$: probability for photon detection, reflection and loss, as a function of λ and θ.

$A^*(\lambda,\theta)$: effective absorption probability, defined as $A^*(\lambda,\theta) = A(\lambda,\theta) + 0.3 \times T(\lambda,\theta)$, following the arguments in the footnote 7 on page 121. The assumed efficiency factor 0.3 comes as the product of two probabilities: $0.3 \sim 0.7 \times 0.4$, where 0.7 is the assumed mean probability that a transmitted photon is eventually back reflected to the photocathode, 0.4 the typical probability that this event results in an absorption.

$QE'(\lambda,0)$: Quantum Efficiency function measured in air at $\theta = 0$ (Fig. 5.1 on page 100), corrected with a $\simeq 4\%$ factor, which takes into account the slight increase expected due to the PMT optical coupling with the medium where the light originates (no loss due to Fresnel reflection at the PMT glass window).

It is noted that the equation for P_D in eq. 6.5 makes use of eq. 5.1, which states that the angular dependence of the quantum efficiency is the same as the one of the absorption.

The geometrical shape of the photocathode plays an important role in this context, for two reasons: 1) all the probabilities in eq. 6.5 depend on θ, thus also on the photocathode geometry; 2) light back reflected has an angular distribution that depends on the photocathode shape. Two photocathode geometries have been implemented in the model: flat (with complete or partial coverage of the surface area) and hemispherical (Fig. 6.2).

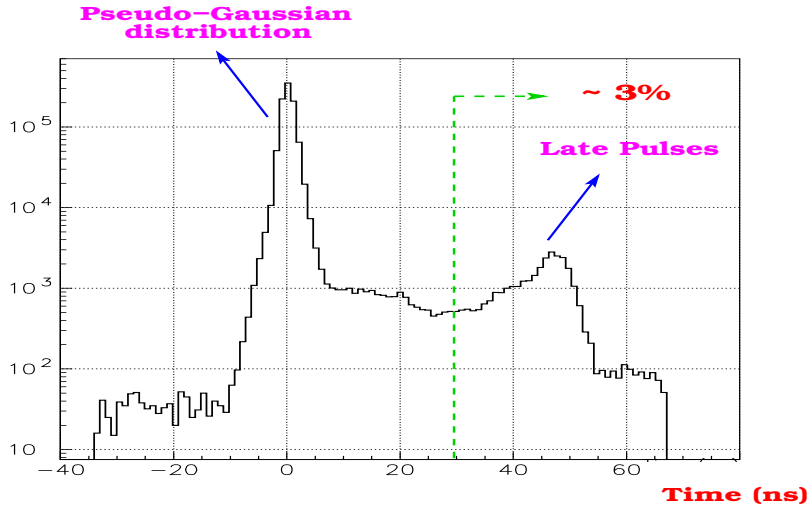

Figure 6.3: *Response function to a single photon of a Borexino 8" PMTs (courtesy Oleg Smirnov for the Borexino Collaboration). The shown distribution is the one with the lowest fraction of late pulses in an ensemble of* ~ 100 *measured samples. About* 3% *of the total charge is collected after* 30 *ns from the time-0.*

6.7 Electronics

So far light interaction with the PMTs has been discussed only from the point of view of optics. Photoelectrons that are successfully accelerated to the first dynode start an avalanche, which is collected at the anode as a current pulse. The latter typically undergoes a filtering and shaping (due to the presence of cables, impedances and capacitors). The signal is then integrated, to lead to a "charge signal" proportional to the initial light pulse, and discriminated, to get a time that is used for event spatial reconstruction by comparing with the time of the second PMT. The electronic signal building from the PMT to the digitization is not implemented in this optical model: charge signal and pulse shape are simply assumed to be equivalent to the total number of photoelectrons and to their time-of-detection distribution.

The only feature of the electronics that is implemented is the system time response to a single photon. This includes the *time jitter* from PMT and electronics and the PMT *late pulsing*. The former is given by the spread in time intrinsic to the photoelectron collection, multiplication and detection process (a gaussian distribution to a good approximation). The *late pulses* occur a few tens of nanoseconds after the reference time and are not preceded by any correspondent prompt pulse (late and after pulses are also defined in Sec. 3.3.2). The time jitter contributes to worsen the time resolution of the detector, while late pulses represent a potential danger for the ^{176}Yb LENS concept, since their timing typically overlaps with the coincidence time window of the ν-tag. In Fig. 6.3 an example of PMT time response to a single photon is shown, as measured for one of the Borexino 8″ PMTs. The implications of late pulses and are sources of late light in a Yb cell will be studied in Sec. 7.1.

6.8 Tracing a Photon

In Sec. 6.2 the MCs based on of the optical model described in this chapter were defined "single-photon-tracing" simulations. In this sections this definition is clarified, by showing how a simulation works, step by step.

Input Data First the simulation framework and its input parameters have to be chosen:

- detector geometry (shape, dimensions, PMT interface, etc.)
- scintillator (refraction index, decay time, composition, emission and extinction spectra)
- light transport (TIR, SR, or mixed; reflection coefficients)
- PMTs (QE, optical constants of the photocathode, time response)

It is also possible to "switch off" any of the implemented physical processes for debugging or interpretation purposes, but in the following the running of the complete simulation will be assumed.

Photon Generation As a photon is generated, a table of observables is assigned to it:

- **Position**: the (x, y, z) coordinates inside the sensitive volume. They can be all fixed, to study the expected detector response at a given position. Otherwise the longitudinal coordinate can be fixed and the position in the transversal plane randomly chosen with uniform distribution, to simulates the effect of a collimated external γ source (when attenuation is negligible).
- **Direction**: two random numbers are generated to select isotropically the photon direction cosines.
- **Wavelength**: the photon is given a random wavelength, according to one of the emission spectra shown in Fig. 2.1.
- **Attenuation Length**: the selected wavelength determines the photon attenuation length in the scintillator.
- **Delay**: two random numbers are generated, which are used to define the emission time of the photon, following a triple exponential decay. The first decides the time branching (τ_1, τ_2, or τ_3, through the weights q_1, q_2, or q_3), the second the emission time.
- **Jitter**: a random number is generated to produce a jitter-time, either following a measured time distribution (as the one in Fig. 6.3), or using a simple gaussian function with the standard deviation given by the PMT specification from the manufacturer. Thus, the offset for the photon detection time is $t_0 = delay + jitter$

Propagation Regions The simulated volume is divided into physical *regions*, characterized by different propagation-absorption properties. The regions are defined as:

- Scintillator
- Cell frame (walls)
- Air gap (between scintillator and top wall)
- Buffers (light guides)
- PMTs
- "Outside"

The regions are separated from each other by planes and/or more complex surfaces, which are all individually defined and numbered and are called *interfaces*. Given the photon initial position and direction, the code determines the closest interface, the distance to be traveled to reach it, the intersection coordinates and the angle of incidence θ_i. The hit interface connects two regions that can have either different or equal refractive index. Those two main cases are considered in turn.

Propagation between Regions of Different n If the interface separates regions with different refractive index, two sub-cases must be considered:

1. light comes from an optically denser medium (cell/buffer-to-outside or scintillator-to-air gap)
2. light comes from an optically less dense medium (only realized at the air gap-to-scintillator interface)

When the condition 1 is met, it is evaluated whether θ_i is smaller or greater than θ_c. If $\theta_i < \theta_c$ 4 cases are possible:

1. a Fresnel reflection takes place, with probability given by eq. 4.1 on page 76
2. no reflective foils outside the interface are simulated, no Fresnel reflection occurs, hence the photon leaves the region
3. reflective foils are included, which reflect back the photon
4. although mirror foils are present, the photon is not reflected, due to $R_{SR} < 100\%$

In the cases 1 and 3 the photon is ready to propagate further in the same region; the new direction of propagation is calculated and the intersection point is assumed as the new photon position. In case 2, the photon exits the cell and is lost, unless the crossed interface is the scintillator-to-air gap, in which case it undergoes refraction and continues propagating. In case 4 the photon is definitively lost.

If $\theta_i > \theta_c$ (TIR condition) the two following possibilities are given:

1. the photon is TIR-reflected

2. the photon misses TIR reflection due to $R_{TIR} < 100\%$. R_{TIR} can incorporate the positive contribution from reflective foils behind the interface, in case "TIR and SR" piping is simulated (see Sec. 6.5)

Here similar considerations hold, as in the previous discussion for $\theta_i < \theta_c$.

In the second case considered in this paragraph, i.e. light crossing an interface coming from an optically less dense medium, it is simply assumed that light is entirely transmitted, with a change in direction according to the refraction law (for simplicity Fresnel reflection at these interfaces is neglected).

Propagation between Regions of Equal n For simplicity, it is assumed that scintillator, walls, buffers and PMT envelope have the same refractive index, therefore all interfaces between those regions belong to this case. The direction of motion remains unchanged, the geometric and physical properties of the new region will be considered from the next propagation step.

Attenuation At this point it is known where the photon will strike, whether it will reflect off the interface or will propagate into a new region or whether it will be lost due to inefficient guiding. Before continuing the propagation an absorption distance is randomly generated using eq. 6.1 and the total photon attenuation length $\mu_{region}(\lambda)$. If such distance-to-interaction is shorter than the distance to be traveled to reach the next interface, the interaction position is determined. For interactions in the scintillator, it is then decided which of the scintillator components was responsible for the absorption, making use of the absorption probabilities $P_i = \frac{1/\mu_i}{1/\mu_{tot}}$. It is then decided whether or not such absorption eventually results in a re-emission, with the parameters given in Table 6.1. In case pure absorption takes place, the photon is lost and the loop starts again with a new photon. Otherwise the photon is "recreated" and its list of observables reset: the start position coincides with the interaction position, a new wavelength is randomly selected out of the emission spectrum of the absorbing molecule (or of the corresponding acceptor fluor, for effective non-radiative energy transfer), with the constraint $\lambda_{new} > \lambda_{old}$. A new absorption length is derived and the photon is assigned a new isotropic direction of propagation and a further random scintillator decay time is added to t_0.

Interaction with the PMTs In case an inelastic scattering has occurred, or the photon has been reflected, the propagation continues for another step: the next intersection is calculated and, again, either the closest interface is reached or the photon undergoes an interaction.

This propagation loop continues until the photon is either lost (at the interfaces or by absorption) or reaches one of the detector PMTs. In the latter case, the probabilities of eq. 6.5 are evaluated for the actual (λ, θ). A random number is generated, which decides whether the photon is converted into a photoelectron, reflected or lost. In case of detection the time of arrival, defined as $t_d = flight\ time + t_0$, is stored in a histogram, the counter of detected photons incremented, and the loop starts again with a new photon. If a reflection at the photocathode occurs, the new direction is calculated and the photon is propagated until it gets lost or has a new encounter with a PMT.

MC output At the end of the loop on the chosen number of generated photons several distributions are obtained:

- Total number of photoelectrons at each PMT
- Distribution of the photon time of arrival at each PMT
- Number of photons lost due to inefficient light piping, absorption in the detector, incomplete PMT area coverage, etc.
- Wavelength spectrum of the detected photons at each PMT
- Photon angular distribution at the PMTs
- Distribution of number of reflections off PMT before detection.
- Time of arrival for photons once, twice, etc. reflected off the PMTs, or inelastic-scattered
- Others ...

The first two give the prediction of light collection and pulse shape, the others are important information for debugging and interpreting the results.

6.9 Conclusions

A model of light propagation and detection in a scintillator cell has been developed. A faithful detector geometry and a detailed description of the physics of scintillators are implemented, the latter based on the measurements reported in refs. [MPI03, Buc04]. The model also implements the inputs from the experimental studies reported in Chapters 3, 4 and 5, for the scintillation decay time, the light piping efficiency and the physics of photon interaction with the PMTs. The purpose of the model is to run MC simulations of a LENS cell and therefore, due to the segmented design, to predict and understand the performance of the whole detector. A simplified simulation based on this model was already used in Chapter 4 to analyze the measurements of TIR and SR light piping. In the next chapter the application of this model for the investigation of fundamental issues of the Yb and In LENS concepts are presented. In Chapter 8, devoted to the optical measurements of full-scale LENS prototype cells, the prototypes performance will be compared with the MC predictions.

Chapter 7

MC simulations for Yb-LENS and In-LENS

7.1 MC simulations for the Ytterbium Target

7.1.1 Introduction

The LENS detection concept based on ^{176}Yb as a ν target was introduced in Sec. 2.3. During the LENS R&D the ytterbium project has lost momentum, due to the concurring effect of two factors:

1. Several backgrounds were identified (Sec. 2.3.3) and some of them put the feasibility of the Yb-LENS concept in serious doubt
2. The proposal of the ^{115}In isotope as a target for ^{7}Be and possibly pp solar neutrinos offered a very attracting alternative to ^{176}Yb for the realization of the LENS goals

In this section one of the most critical issues of the Yb-LENS concept is studied: the background from self-correlated (SC) events. This problem is studied by MC simulations and the analysis involves the experimental and theoretical modeling covered in the previous chapters.

For a better understanding of the following analysis, the key points of the discussion in Sec. 2.3.3 are recalled. The most critical detector parameters controlling the SC are:

- The final photoelectron yield at the PMTs
- The signal mean late charge

The latter is meant as the fraction of the signal charge acquired after a minimum delay cut for the observation of the tag γ. Three main factors are identified, which determine the single-pulse late charge:

1. scintillator fluorescence time
2. photons time-of-flight distribution, including reflections off the PMTs
3. PMT late pulses

At this stage other sources of late charge are not considered (e.g. electronic noise and signal reflections).

7.1.2 Simulation of the Signal Time PDF for a Single Energy Deposition

Input Parameters of the MC The first step towards the study of SC in Yb-LENS is the simulation of the single pulse PDF. As a benchmark case, the typical geometry considered for an Yb cell is simulated and a reasonably transparent metal-loaded scintillator. The assumptions and input parameters of the MC are:

- Parallelepiped cell geometry with external dimensions $20\,cm \times 20\,cm \times 300\,cm$, square section, $5\,mm$ wall thickness and $5\,mm$ air gap on top of the scintillator. Two $20\,cm \times 20\,cm \times 50\,cm$ buffers are coupled to the cell ends.

- Light source at the cell center.

- Scintillator decay-time as measured in this work for an Yb-loaded sample (Chapter 3).

- The scintillator base corresponds to the choice of anisole as solvent, PPO at $6\,g/l$ as primary fluor, with $20\,mg/l$ bis-MSB as λ-shifter[1]. For the metal complex, it is simulated that Yb is in solution as $Yb(acac)_3$ and the extinction coefficients measured for $In(acac)_3$ are used[2]. The metallorganic compound is simulated at the concentration required for a $50\,g/l$ Yb loading.

  The total attenuation length at $\lambda = 430\,nm$ is $\mu \sim 2.7\,m$, dominated by the absorption from the $Yb(acac)_3$ molecule ($\mu \sim 4.1\,m$). The parameters in Table 6.1 are used for the relative probabilities of absorption and inelastic scattering. It is assumed that buffers and cell walls have a constant absorption length of $20\,m$.

- The emission spectrum of bis-MSB is assumed as primary scintillation spectrum (Fig. 2.1 on page 40), because of the good overlapping of the PPO emission with the bis-MSB absorption band.

- Light piping via TIR and SR. The refractive index of scintillator, walls and PMT window is $n = 1.5$. The reflection coefficients are $R = 99.7\%$ for $\theta > \theta_c$ and $R = 98.5\%$ for $\theta < \theta_c$. This choice corresponds to an intermediate case between the limits "TIR or SR" and 'TIR and SR" defined and discussed in Sec. 6.5. SR piping can be switched off and in this case $R_{TIR} = 99.4\%$.

- PMT coupled to the cell ends with flat photocathode and complete surface coverage. The "green-enhanced" QE is chosen (Fig. 5.1 on page 100). The optical model of the PMTs is implemented, as described in Sec. 6.6.

- The experimental response of the PMTs to a single photon, including the late pulses, as measured in Borexino (Fig. 6.3 on page 135). This can be switched off and in this case a gaussian time-jitter with $\sigma = 1\,ns$ is simulated.

The geometry and the scintillator attenuation lengths implemented in the simulations are shown in Fig. 7.1.

[1] All attenuation and emission data used for the simulation reported in this chapter come from spectrophotometric and fluorimetric measurements performed by us at MPIK [Buc04].

[2] This is simply an exercise, because no real $Yb(acac)_3$ molecule has been synthesized and measured.

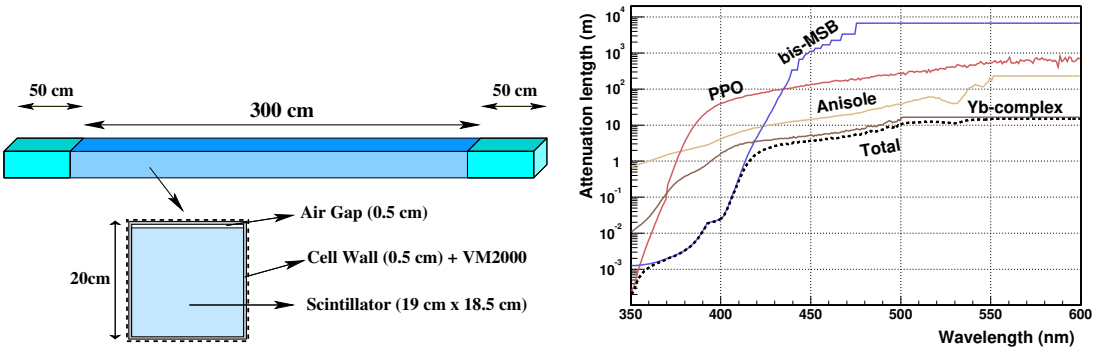

Figure 7.1: *Left: Geometry simulated for the Yb-cell. Right: Simulated attenuation lengths in the scintillator.*

Results Several single-pulse PDFs have been generated via MC, obtained by "switching on" one by one all the investigated effects that are related to the signal pulse shape. The results are shown in Fig. 7.2. In the "basic TIR" case only the dispersion of the distance traveled to the PMTs determines the pulse shape. The features observed in the other simulations are:

- The introduction of the reflective foils determines a sizable enhancement of the signal tail, due to the opening of the geometrical acceptance to photons with large transverse momentum.
- The implementation of the scintillator fluorescence time produces a dramatic effect: the late charge increases of one order of magnitude and the signal tail extends for several hundreds of ns (reflecting the measured fluorescence PDF, see Fig. 3.7 on page 71).
- The PMT reflections contribute a "bump" in the signal PDF for $\Delta t \sim 25\,ns - 60\,ns$, corresponding to the first reflection peak (one reflection, then detection at the opposite side).
- The late pulses contribute a further charge accumulation at $\Delta t \sim 50\,ns - 70\,ns$ (as in Fig. 6.3 on page 135).

The integral of these PDFs above various minimum delay cut has been computed and is reported in Table 7.1. It can be seen that the considered sources of late charge provide contributions of the same order.

7.1.3 Estimation of the Detector Photoelectron Yield

The information on the signal PDF has to be combined with the detector photoelectron yield (PY). This is the product of the scintillator LY times the photon detection probability (called *PDP* hereafter). The latter is the fraction of primary photons converted into *pe* and includes light transport to the PMTs and photo-conversion probability. The PDP is also predicted by the MC. Table 7.2 shows a breakdown of the calculated PDP. The full simulation predicts a PDP of $\sim 9.6\%$, under the assumption that the entire end side of the cell is covered by the PMT, with uniform response. However, in a real modular detector it is difficult to have

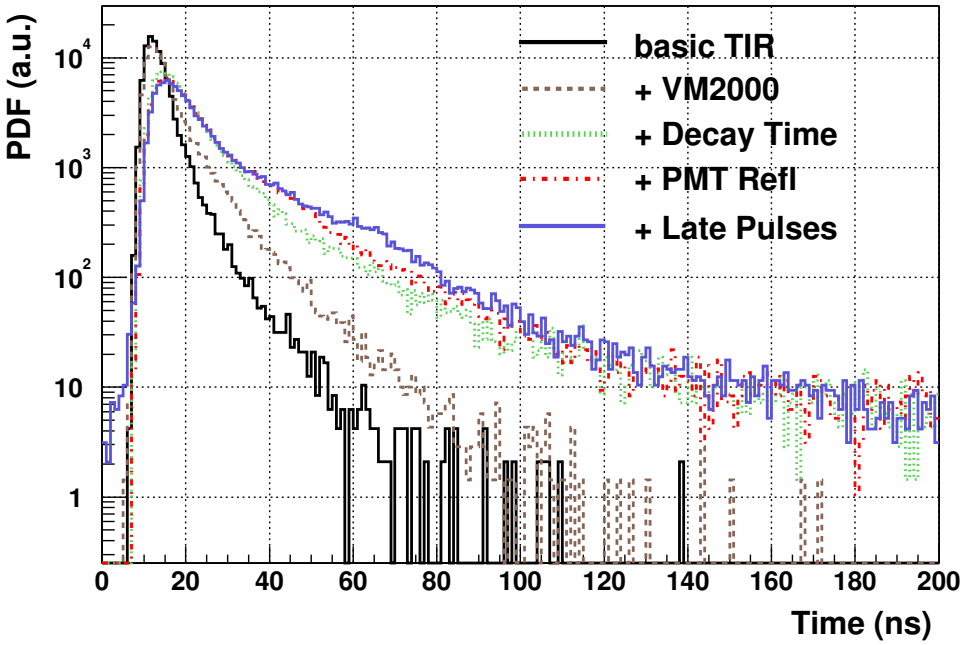

Figure 7.2: *Simulated single-pulse PDFs for a source in the cell center. The "basic TIR" simulation (black solid) includes geometry, TIR light piping ($R_{TIR} = 99.4\%$), absorption and inelastic scattering, and a gaussian time-jitter ($\sigma = 1\,ns$). In the brown-dashed simulation the TIR plus SR piping is implemented. The other simulations add one by one: the scintillator decay-time (green-dotted histogram); the PMT reflectance, (red-dotted-dashed histogram); and the experimental response of the PMTs to a single photon. All the histograms are normalized to the same total integral. The time $t = 0$ is the instant of photon generation (the minimum time of flight to the PMT is $10\,ns$).*

Table 7.1: *Integral fraction of late charge predicted by the simulations in Fig. 7.2, for various lower integration limits. The delay is calculated from the bin on the left side of the peak where the signal is $\sim 10\%$ of the peak value. This corresponds to $\sim 10\,ns$ in the figure.*

	Late Charge (%)			
Delay / Simulation	$> 30\,ns$	$> 40\,ns$	$> 50\,ns$	$> 60\,ns$
basic TIR	0.61	0.24	0.11	0.06
+ Mirror Foils	2.35	0.99	0.47	0.24
+ Decay Time	10.1	6.59	4.68	3.48
+ PMT reflections	14.4	8.72	5.77	4.19
+ Late Pulses	17.8	11.8	8.12	5.35

Table 7.2: *Predicted photo-detection probability (fraction of photons converted to photoelectrons) for a source in the cell center. The value in the first column represents the pure TIR geometrical acceptance (Eqs. 6.3 and 6.4 on page 132). The results in the other columns are obtained by "switching on" in sequence: the experimental TIR efficiency; VM2000 foils; attenuation (absorption and inelastic scattering); "standard" PMT Quantum Efficiency (as in Fig. 5.1) for the "green-enhanced" photocathode; and full PMT optics, including reflectance and $QE(\lambda, \theta)$, according to Eq. 6.5 and the optical model covered in Chapter 5. The last column corresponds to the full "best" simulation. It is assumed that the PMTs have flat photocathode and full surface coverage.*

Simulation	Geo TIR	TIR efficiency $R_{TIR} = 99.4\%$	+ SR $R_{SR} = 98.5\%$	$+\mu(\lambda)$	$+QE$	+ PMT optics
PDP (%)	49.1	45.1	72.8	33.1	6.94	9.58

complete PMT surface coverage. Moreover, the PMTs are not so efficient over their whole surface as they are at the center, where the QE is measured, and furthermore the manufacturer-specified QE implemented in the simulation is likely to be an upper limit of the achievable PMT response. It can be assumed that the PMT coverage is $\pi/4$ (a disk inscribed in a square) and that the mean QE over the covered surface is a factor ~ 0.9 of the maximum QE[3]. In conclusion, a more conservative estimation is $PDP \sim 6.5\% - 7\%$.

7.1.4 Analytical Calculation of the Self-Correlation Probability

We try now to use the results of the simulations to make an order of magnitude estimation of the SC probability in the Yb-LENS experiment, i.e. the probability that a single event has a pulse shape that is not distinguishable from that of a ν-capture event. An approximate analytical calculation is developed, which is described step by step for a particular choice of the input parameters.

Input Parameters A detector with $PDP \sim 6.7\%$ is assumed, as deduced from a conservative interpretation of the MC output. The scintillator LY is taken to be 50% of BC505 (the best synthesized Yb-loaded scintillators have $LY \sim 40\%$, for $\sim 8\%$ Yb loading [Har04, Rag01a]). This translates to an absolute primary photon yield of $\sim 6000\, ph/MeV$[4]. The final PY is then $\sim 400\, pe/MeV$. A background event with sufficient energy to fake a $^7Be - \nu$ interaction must have $E \sim 600\, keV$ (it is reminded that the ν capture threshold in ^{176}Yb is $301\, keV$), which produces $\sim 120\, pe/PMT$. From Table 7.1 it is deduced that on average $\sim 21\, pe$ are collected later than $30\, ns$ after the signal onset. In this time window we look for the $72\, keV$ coincidence γ, which would produce $\sim 14.5\, pe/PMT$ (neglecting a possible low energy quenching in the scintillator). The above inputs are summarized in Table 7.3

[3] This last assumption will be rediscussed in Chapter 8, where the optical performance of a real prototype cell are measured and compared with the MC. An experimental "quality" factor will be deduced.

[4] The BICRON specification for BC505 is $LY = 80\%$ relative to Anthracene. The BC505 measured by us is $\sim 105\%$ of the Borexino mixture reported in [Eli97] as giving $(11500 \pm 1000)\, pe/MeV$. However the latter estimation relies on the comparison of the experimental performance of a scintillation detector with MC simulations. The absolute estimation of scintillators LY is very uncertain.

Table 7.3: *Input parameters of the analytical calculation of the SC probability.*

PY	E_{event}	Δt	*Late Charge*	E_{tag}
$400\,pe/MeV$	$600\,keV$	$> 30\,ns$	17.8%	$72\,keV$
	$(120\,pe/PMT)$		$(21\,pe/PMT)$	$(14.5\,pe/PMT)$

Tag Condition To tag a neutrino we ask that at least $E \sim (72\,keV - 1\sigma)$ is detected, that is $E_{tag} = 11\,pe$. We consider the probability P_{PMT}^{charge} that a statistical fluctuation of an average of $(21/120)\,pe$ at one PMT leads to an excess charge compatible with a delayed $72\,keV$ energy deposition:

$$P_{PMT}^{charge} = \sum_{N \geq 32} P(N) \tag{7.1}$$

where N is the number of pe. The probabilities $P(N)$ are given by the binomial distribution, for the case of 120 "trials" and 0.178 "success" probability. It is found: $P_{PMT}^{charge} \sim 8 \times 10^{-3}$. In addition, it can be asked that this excess photoelectrons form a "cluster" with similar time distribution as a real single pulse. The simulations predict that a signal collects $\sim 70\%$ of the total charge in the first $20\,ns$, while for the integral charge collected at $t > 30\,ns \sim 55\%$ comes in the interval $[30\,ns, 50\,ns]$. It can be asked that in the first $20\,ns$ of the candidate correlated event there are $\sim 55\%$ of the underlaying $21\,pe$ and $> 65\%$ of the excess pe. Also in this case the binomial distribution is used and it is found that the clustering is:

$$P_{PMT}^{cluster} \sim 0.4 \tag{7.2}$$

We have then:

$$P_{PMT} \sim P_{PMT}^{charge} \times P_{cluster} \sim 3 \times 10^{-3} \tag{7.3}$$

The total probability that a self-correlated event gives a fake is given by the probability that both PMTs see the same fluctuation, in either side consistent with a delayed deposition of $72\,keV$. This is the product:

$$P_{SC} = P_{PMT}^2 \times P_{Sum} \times P_{time} \tag{7.4}$$

where P_{Sum} is a possible additional cut on the sum energy measured by the two PMTs and P_{time} the probability that the two fluctuations are consistent with an event in spatial coincidence with the prompt. For simplicity, we consider that no further cut on the sum energy is applied, since $\geq (11 \times 2)\,pe$ of the tag is only $\lesssim 1.3\,\sigma$ away from the expected total $29\,pe$ from $72\,keV$; and that $P_{time} \sim 1$, because with the highest probability both fluctuations will occur short after the $30\,ns$ cut and the space resolution for a low energy event sitting on the tail of a higher amplitude pulse is not expected to be very good for real coincidences, either. Therefore we end up with:

$$P_{SC} \sim 10^{-5} \tag{7.5}$$

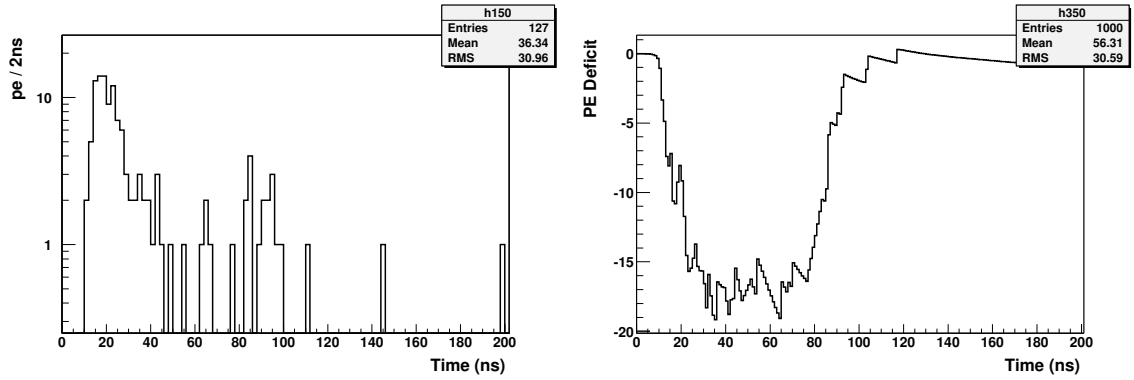

Figure 7.3: *Left: simulated signal at one PMT, for a* $^7Be-\nu$ *event at the cell center. The abscissa is the pe detection time in 2 ns bins, the ordinate the number of pe per bin. The generated delay between prompt and correlated signal is* $\Delta t = 69\,ns$*. The average PY at each side is* $200\,pe/MeV/PMT$*. Right: distribution for the deficit function 7.7. Since the simulated signal consists of two time-separate energy depositions, the prompt "misses" the delayed charge (*$\sim 16\,pe$*, consistent with the expectations for a* $72\,keV$ *energy deposition). This charge is collected when the burst of pe from the second event arrives. The deficit function indicates that the coincidence occurs at* $t \sim 80\,ns$*, which translates to* $\Delta t \sim 70\,ns$*, consistent with the generated delay.*

7.1.5 MC Calculation of the Self-Correlation Probability

Tag Algorithm In order to verify eq. 7.5, a ν-tag algorithm has been written. The algorithm computes first the cumulative *pe* distribution for the observed time sequence:

$$C(t_i) = \sum_{j \leq i} n(t_j) \tag{7.6}$$

where t_i is the i^{th} time bin and $n(t_j)$ is the number of *pe* detected in the time bin t_j. Eq. 7.6 is the discrete equivalent of the time integral of a continuous signal.

The algorithm compares the function 7.6 with the time integral of the single-pulse PDF $[I_{PDF}(t)]$, normalized to the total number of detected *pe* (N_{pe}), so that for $t \to \infty$ $C(t_i) = I_{PDF}(t) = N_{pe}$. A "deficit" function is defined:

$$D(t_i) = C(t_i) - I_{PDF}(t_i) \tag{7.7}$$

If the signal time of arrival distribution is consistent with a single energy deposition, eq. 7.7 will fluctuate around 0 at all times. Conversely, if an event consists of two energy depositions separated by a delay, the function 7.7 will have a negative value, until the burst of photon from the second event arrives. The signature for a "double" is a deficit of *pe* observed at the end of the prompt signal, followed by a fast zeroing of the deficit as the second pulse comes. The concept is illustrated with an example in Fig. 7.3.

If both PMTs observe a deficit compatible with $72\,keV$ after a minimum delay cut from the signal onset, the event is tagged. To increase the background rejection efficiency, the algorithm imposes the same cuts on number of missing *pe* and "clustering" of delayed charge discussed for the approximated analytical calculation, plus a relaxed constraint on the sum energy and the time consistency (corresponding to the factors P_{sum} and P_{time} discussed above).

Results of the MC This algorithm has been implemented in a MC simulation that generates single events with $E \sim 600\,keV$ and mean time PDF given by the full simulation of light transport (Fig. 7.2). The energy is converted into pe/PMT by assuming $PY = 200\,pe/MeV/PMT$ (Poisson statistics included). The tag algorithm imposes a cut of $\Delta t > 30\,ns$ on the coincidence delay. The result of the MC is 116 tags in 10^7 events. Thus:

$$P_{SC} = \sim 1.2 \times 10^{-5} \tag{7.8}$$

which is in excellent agreement with eq. 7.5. Fig. 7.4 shows an example of such a fake tag due to SC.

A similar simulation has been performed generating real ^7Be events, also for $\Delta t > 30\,ns$. The tagging efficiency is $\varepsilon^{tag}_{^7Be} \sim 0.42$. Including the loss of efficiency due to the minimum delay cut, this translates to:

$$\varepsilon^{tot}_{^7Be} \sim 0.23 \tag{7.9}$$

7.1.6 Self-Correlated Background Rate in Yb-LENS

For this specific case studied in detail, it has been found $P_{SC} \sim 10^{-5}$, with good agreement between analytical and MC calculations. In order to evaluate the corresponding absolute SC background rate in Yb-LENS, this information has to be combined with the rate of singles in the considered energy window. The background of single counts in a Yb detector in the range of the $^7Be - \nu$ energy is dominated by ^{176}Lu (see Sec. 2.3.3). It has been calculated that for a Lu contamination in Yb of $0.1\,ppm$ (the lowest level measured in Yb samples during the LENS R&D), the integral background rate above $\sim 500\,keV$ (energy deposited in a single cell) is $\sim 10^7\,y^{-1}\,ton^{-1}_{Yb}$ [Mal01], while the $^7Be - \nu$ interaction rate is $\sim 10\,y^{-1} ton^{-1}_{Yb}$. With the calculated ν efficiency and P_{SC}, it turns out that:

$$S/N \sim 2 \times 10^{-3} \tag{7.10}$$

.

To improve this number it is necessary to decrease the self-correlation probability, by acting on one or more of the following directions:

1. Increase the minimum delay cut, however at the cost of a further loss of ν efficiency
2. Increase the detector PY, by improving the scintillator primary LY, or the PDP efficiency (e.g. with a higher scintillator transparency and a better light collection at the PMTs)
3. Reduce the single background rate, i.e. the Lu contamination
4. Reduce the mean late charge from a single ionization event

As an exercise, the S/N ratio in the ^7Be and pp window has been estimated for various minimum delay cuts and PY. The results are reported in Table 7.4. The tag efficiency in the $pp - \nu$ energy range was estimated with the tag algorithm and is slightly higher than for ^7Be: $\varepsilon^{tag}_{pp}(E_{prompt} = 100\,keV,\ \Delta t > 40\,ns,\ LY = 400\,pe/MeV) \sim 0.49$. This value could be improved by relaxing the cuts on the tag energy. However Table 7.4 shows that the self-correlations are not completely negligible even at for pp neutrinos, due to the much higher background rate.

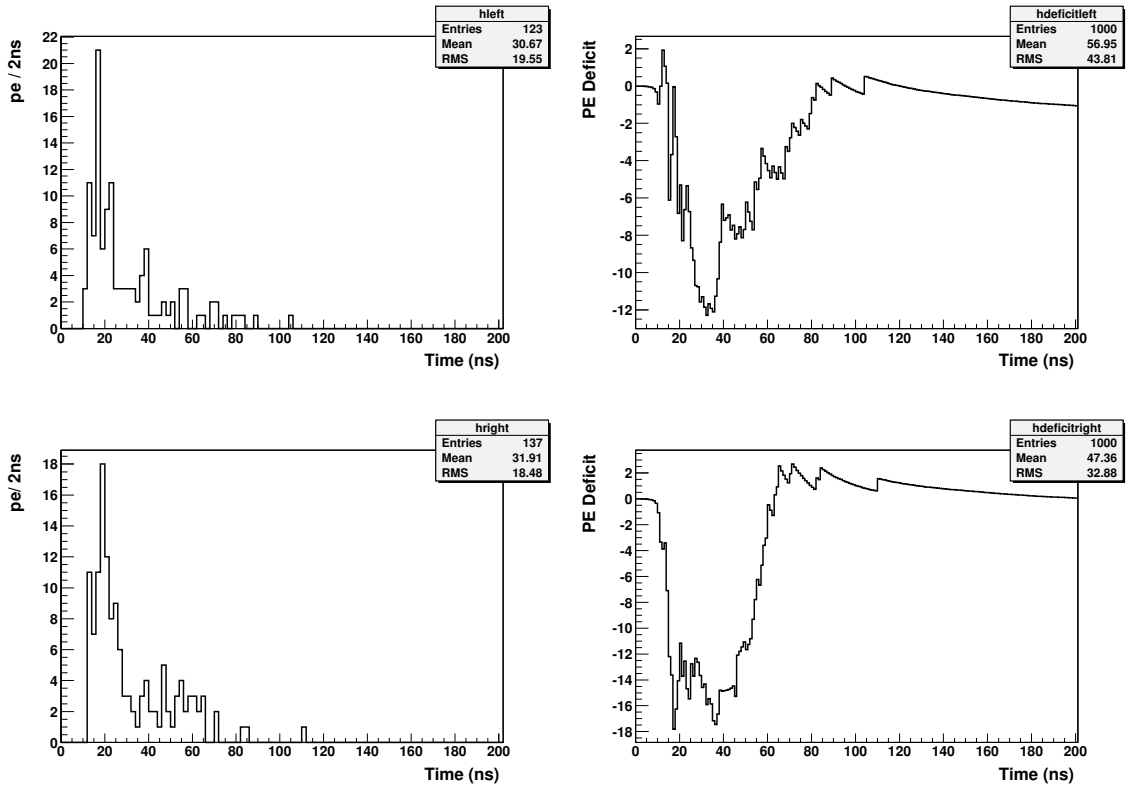

Figure 7.4: *An example of falsely tagged simulated single event, with* $E = 630\,keV$ *and* $PY = 400\,pe/MeV$. *The photoelectron time of detection distribution was generated by using the average PDF given by the full MC simulation (Fig. 7.2).*
Top-Left: distribution of pe detection time ($2\,ns$ *bins) at one PMT.*
Top-Right: plot of the corresponding deficit function 7.7.
Bottom: same distributions at the opposite PMT.
A two-fold statistical fluctuation has generated a fake delayed event at $t \sim 40\,ns$, *corresponding to a delay of* $\sim 30\,ns$ *with respect to the prompt event. The deficit function shows that on both PMTs a stable deficit of pe has occurred in the first* $\sim 30\,ns$ *of the event. At a delay* $\Delta t \sim 30\,ns$, *a cluster of photons is detected in coincidence on both sides. All the event features are consistent with the late detection of the* $72\,keV$ *coincidence* γ $(\sim 14\,pe/PMT)$ *and the resulting event cannot be distinguished from a genuine* $^7Be - \nu$ *interaction. The probability for such an event is roughly* 1 *in* 10^5 *(see text).*

Table 7.4: *Calculated SC background for different minimum delay cuts and detector performance. P_{SC} is the probability of self-correlation for an event with deposited energy $E = 600\,keV$, given by eq. 7.4 and calculated analytically as described in Sec. 7.1.4. The column "Simulation" reports the number of MC-generated singles that are tagged as ν candidates. ε is the total detection efficiency for solar ν. It is the product of the trivial loss of statistics due to the cut on Δt and the MC-calculated tag efficiency. The latter weakly increases with increasing Δt_{min} and PY, from ~ 0.42 in the first row to ~ 0.50 in the best cases. The column S/N reports the estimated signal-to-background ratio due to SC, assuming a rate of singles of $10^7\,y^{-1}\,ton_{Yb}^{-1}$ in the relevant energy interval, dominated by ^{176}Lu [Mal01].*
In the last row a similar calculation is reported for the case of pp neutrinos. A deposited energy of $200\,keV$ is considered, which in case of SC would be observed as $\sim 130\,keV$ prompt plus $\sim 70\,keV$ delayed. The estimated background rate of single events at these energies is $\sim 10^{10}\,y^{-1}\,ton_{Yb}^{-1}$[Mal01].

Δt_{min} (ns)	pe/MeV	P_{SC}	Simulation	ε	S/N
30	400	10^{-5}	$116/10^7$	0.23	2×10^{-3}
40	400	2×10^{-6}	$17/10^7$	0.21	5×10^{-2}
50	400	7×10^{-8}		0.18	3
60	400	5×10^{-9}		0.16	30
40	450	7×10^{-7}		0.21	0.3
40	500	6×10^{-8}	$1/10^7$	0.22	4
40	400, $E = 200\,keV$	5×10^{-12}		0.22	50

7.1.7 Discussion

The analysis presented in this section has shown that in a Yb detector with fairly good performances ($400\,pe/MeV$, the Borexino yield with an unloaded scintillator) a minimum delay cut of $\gtrsim 60\,ns$ must be imposed for the safe detection of ^7Be neutrinos, and $\gtrsim 40\,ns$ for *pp* neutrinos. The expected total efficiency for ν detection is low, in the range of 20%.

It is recalled that for simplicity the analysis has been carried out for the particular case of a source at the cell center. In general a source is closer to one PMTs and this affects both pulse shape and PY at the two sides. Concerning the pulse shape, the scintillator decay time and the late pulses affect the PDF in a way independent of the source position, whereas the delay in the detection of photons reflected off the PMTs is different at the two sides if the source is not at the cell center. For the PY, obviously more photoelectrons are measured by the closest PMT. Therefore the probability P_{PMT} of eq. 7.3 is lower for the near PMT and vice versa.

As a guideline for a discussion about the SC background in Yb-LENS the scheme in Table 7.5 is considered.

Late Charge Concerning the reflections off the PMTs, there seems to be not much room for an improvement, as far as conventional PMTs are considered. The reflectivity is an intrinsic property of the photocathode layer, as discussed in Chapter 5, and cannot be lowered without affecting the PMT sensitivity. Nevertheless, the impact of PMT reflections can be decreased by making shorter cells, so that the first reflection peak falls at a shorter delay. This would also improve the PY, however increasing the cost of the experiment, as more PMTs and electronics

Table 7.5: *Guidelines for the evaluation of the critical SC background.*

What can (must) be improved	What can worsen the situation
signal late charge	low energy β-quenching
detector PY	noise/reflections electronics
detector radiopurity	detector performance worse than expectations

channels would be needed.

In the MC a PMT with hemispherical photocathode has been implemented, as in Fig. 6.2 on page 134. The simulations show that this geometry reduces the amount of late-detected reflected light of a factor ~ 4 in a TIR based cell. The reason is that the reflection off a flat surface in a "box" geometry does not change the angle for TIR, whereas photons reflected off a hemispherical PMT lose with high probability the condition for TIR. However, in a mixed TIR-SR cell, which ensures a much higher light collection efficiency (to be discussed in detail in Sec. 7.2), the photons that are not piped by TIR are reflected by the mirror foils with high efficiency and hence the difference between a flat and a hemispherical PMT is expected to be modest.

The scintillator late fluorescence is a major contributor of late charge. There can be some room for an improvement of this parameter, by careful choice of solvents and fluors. However, the results of Chapter 3 have shown that there are no huge differences in the late scintillation of all the samples and that the decay curves measured for the metal-loaded scintillators are not significantly different than those of benchmark unloaded scintillators.

An R&D on PMT technology should be undertaken to explore the possibility of reducing the late pulsing.

Photoelectron Yield The estimations in Table 7.4 show that even if it turns out that the late part of the signal PDF cannot be reduced, an improvement of S/N can be achieved by increasing the PY. This means that the scintillator needs to have higher LY and transparency, or the detector a better PDP. However, the benchmark value of $400\,pe/MeV$ seems an optimistic rather than a conservative estimation. The possibility to achieve a better performance in a real detector must be experimentally proven.

Detector Radiopurity A fundamental parameter that controls the SC background is the rate of single events, which is dominated by ^{176}Lu. It would be important for the Yb project to demonstrate that an admixture of natural Lu in Yb significantly lower than $0.1\,ppm$ is feasible at a reasonable cost.

The right column in Table 7.5 is a remind that effects not included in this simplified analysis may in fact further worsen the situation. Signal pulse-shape and final PY must be eventually measured in a full scale prototype detector.

7.1.8 Conclusions

Due to the low energy and short delay of the ^{179}Yb ν-tag, the self-correlations are expected to be a critical background for the observation of solar neutrinos, especially for the main $^{7}Be - \nu$

line and higher energy fluxes. The S/N ratio depends on several detector parameters: late charge, PY, background rate of single energy depositions. The PDF of a single pulse and the PY have been estimated via MC simulation of an Yb-loaded scintillation cell. These results have been used to predict the probability for fake ν-tag from SC of single energy depositions and consequently the expected S/N. This analysis has shown that the SC background is in fact a very severe problem for Yb-LENS. With the present detector concept and assuming a benchmark PY and lutetium contamination, S/N>10 requires a minimum-delay-cut of $\Delta t \gtrsim 60\,ns$ for ^{7}Be and $\Delta t \gtrsim 40\,ns$ for pp. The corresponding ν efficiency would be ~ 0.16 and ~ 0.22 respectively, found as the product of the probability for a $^{176}Yb^{*}$ de-excitation with $\Delta t > cut$ and the tag efficiency (other sources of detection inefficiency are not considered). This implies that a larger detector mass is required to compensate this loss of statistics.

Further comments on the feasibility of an Yb solar neutrino experiment are given in the conclusions of this work, in Chapter 10.

The efforts of the LENS R&D and the final pilot phase have focused on ^{115}In as a ν target. Indium has a much more favorable ν-tag, a much higher ν interaction rate per unit mass and a clearer background rejection strategy: high granularity and energy resolution.

7.2 MC Studies of Benchmark Light Collection for an Indium Cell

In Chapter 4 the efficiency for the two main light piping mechanism, TIR and SR, has been experimentally determined in prototype light guides. It is now possible to address the question that opened that chapter (Sec. 4.1): is light piping a limiting factor for the Indium-LENS project? Is the commercial technology (quartz finished surfaces and VM2000 mirror foils) sufficient to meet the LENS demands? Which between TIR and SR ensures a superior performance in a LENS module, given the results in Eqs. 4.11 and 4.12? These questions will be here addressed through MC simulations.

7.2.1 MC Study of a Benchmark Ideal Detector

Input Parameters of the MC To answer the question whether (or to which extent) the In-LENS concept is limited by light piping efficiency, an ideal case is assumed for the simulations:

- Parallelepiped cell geometry with external dimensions $5\,cm \times 5\,cm \times 300\,cm$, with a $5\,cm \times 5\,cm \times 50\,cm$ buffer at each side and perfect square section.
- No light attenuation in the propagation media, BPO emission spectrum.
- Light piping via TIR and/or SR. The refractive index of scintillator, walls and PMT window is $n = 1.5$. The reflection coefficients are $R_{TIR} = 99.4\%$ and $R = 98.5\%$ (assumed constant over λ and θ), as measured in Chapter 4. The specific conditions for light piping are varied.
- PMT coupled to the cell ends with flat photocathode and complete surface coverage. The "green-enhanced" bialkali sensitivity is chosen and the optical model of the PMTs is implemented, as described in Sec. 6.6.

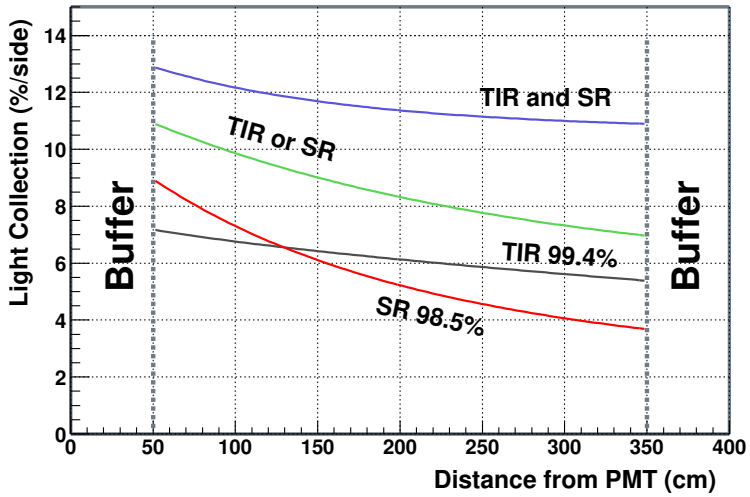

Figure 7.5: *MC predictions for some ideal scintillator cells: PDP per PMT as a function of the source distance. The ordinate is given in percent of the primary light converted to photoelectrons. The total charge collected at the distance d is then* $Tot(d) = light(d) + light(400 - d)$*, which is obviously a symmetric function with respect to the axis* $d = 200\,cm$*. Red curve: light piping via SR, with* $R = 98.5\%$*. Gray curve: light piping via TIR, with* $R = 99.4\%$*. Green curve: light piping via TIR if* $\theta > \theta_c$*, else via SR. Blue curve: photons missing TIR reflection for* $\theta > \theta_c$ *due to reflection inefficiency are recovered via SR (see Sec. 6.5).*
In the SR simulation a smaller cell cross section was chosen: $4.6\,cm \times 4.1\,cm \times (300 + 100)\,cm$*, to compare the performance with equal scintillating volume. In fact, in a design based on pure SR via VM2000 it is envisaged that the detector consists of a big tank with inserts of mirror foils to segment the total volume in a modular array. Therefore no other materials and/or dead volumes are present, compared to the* $\sim 2\,mm$ *walls and* $\sim 5\,mm$ *air gap necessary in a scintillation cell. The outermost segments at* $(0 - 50)\,cm$ *and* $(350 - 400)\,cm$ *are the cell buffers*

Thus the only open channels for light loss are piping and photoelectron conversion. The $5\,cm$ side dimension is chosen following the MC predictions of the full scale detector, which indicate that this size optimizes the signal-to-background ratio in the "hybrid" LENS design (Sec. 2.4.3 and ref. [Mey03]). The $3\,m$ cell length is a kind of upper limit in the range of considered reasonable geometries (longer dimensions are in principle desirable, but light losses in the cell would be to too severe).

This ideal case sets an important benchmark: no real cell can perform better, however good the optical transparency of the scintillator.

Results In Fig. 7.5 the MC predictions for the main light piping solutions are shown. The various simulation-specific assumptions are described in the caption of the same figure.

The simulated light attenuation curves can be fitted with a double exponential function (eq. 4.3 on page 82), as described in Sec. 4.5.2 and applied for the analysis of the light piping measurements. However, this procedure leads to results not completely meaningful in some of the fits. For this reason Table 7.6 reports the 2-exp fit parameters, in analogy with the analysis

Table 7.6: *Fit parameters for the curves in Fig. 7.5. The weights, $W_{1,2} = I_{1,2}/(I_1 + I_2)$, refer to $x_0 = 50\,cm$ (see Eq. 4.3 on page 82).*

Simulation	W_1	$(\mu_1 \pm \sigma)\,(cm)$	W_2	$(\mu_2 \pm \sigma)\,(cm)$	$\mu_{mean}\,(cm)$
TIR $R = 99.4\%$	0.036	69 ± 57	0.964	1191 ± 113	1061
SR $R = 98.5\%$	0.550	141 ± 2	0.450	1135 ± 50	323
TIR or SR	0.495	230 ± 5	0.505	$\sim \infty$	654
TIR and SR	0.157	117 ± 34	0.843	$\sim \infty$	1874

in Tables 4.1, 4.2, 4.3, 4.4, 4.5, together with a coarse mean attenuation length, derived from a global single exponential fit (the quality of the fit is in general not very good, except for the case of pure TIR light piping).

Discussion The MC calculations show that TIR alone with 99.4% efficiency is superior to SR alone with $R_{VM2000}(430\,nm) = 98.5\%$, not only for what concerns the attenuation length, but also in the absolute PY: the lower TIR collection at short distance is more than compensated by the higher amount of light detected by the other PMT. Only in a shorter cell ($l \lesssim 150\,cm$ + buffers) SR would be superior to TIR, however at the cost of a less uniform detector response. This would imply a stronger correlation between spatial and energy resolution: the uncertainty in the spatial reconstruction translates to an additional error in the energy reconstruction.

What is found is consistent with the expectations: SR guiding is advantageous over TIR at short distances, since no solid angle is lost, but TIR ensures more light collection at longer distances, because it has a superior reflection efficiency.

Obviously, the best absolute performance is offered by a mixed TIR-SR light piping, which combines the advantages of the two methods (see Sec. 6.5 for the definition of the TIR-SR mixed guiding used in the simulations). No direct light piping measurement has been carried out to estimate the efficiency of a TIR-SR pipe, i.e. to understand whether reality is closer to the "TIR or SR" model or to the "TIR and SR" one. Including this uncertainty, the conclusion is that a LENS optical module with the simulated geometry, built with the available technology, should exhibit a limit attenuation length due to light piping losses only:

$$6\,m \lesssim \mu_{limit} \lesssim 20\,m \tag{7.11}$$

This means that the goal of a total effective attenuation length in the range of the module dimension ($\gtrsim 3\,m$) can be met if the contribution due to absorption in the scintillator is of the order of $\sim 6\,m$. For the operation of a shorter cell this demand would be less stringent.

7.2.2 MC Study of a Benchmark Realistic Detector

Input Parameters of the MC In order to verify this conclusion, other MC simulations have been carried out, reconsidering the cases studied above with a realistic benchmark model:

- Rounded corners in the scintillator volume are implemented in all the simulations, except for the pure-SR case, where no physical containment cell is needed. The radius of curvature at the corners is set to $0.4\,cm$ (the same as in the LENS prototype quartz cells, to be described in the next chapter).

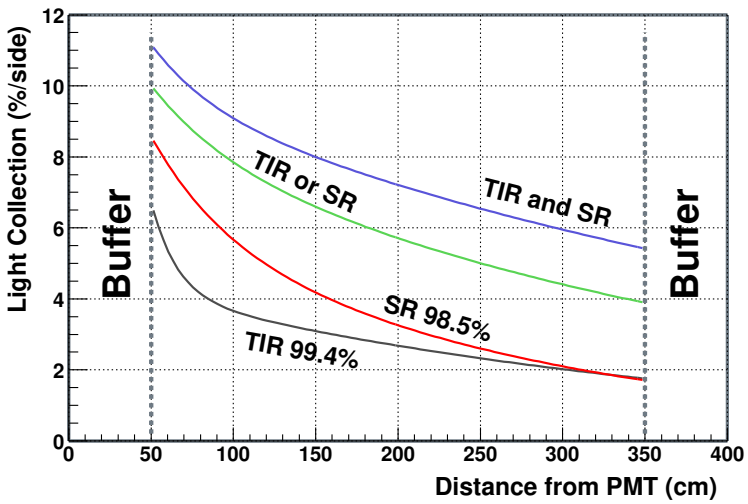

Figure 7.6: *MC predictions for some realistic high-transparency liquid scintillator cells (see text and Table 7.7 for a description of the simulated system). The definitions are the same as in Fig. 7.5.*

Table 7.7: *Attenuation lengths at various wavelengths for the scintillator simulated in Fig. 7.6. For increasing wavelengths, light attenuation is dominated by: BPO ($\lambda \lesssim 360\,nm$, mostly inelastic scattering), bis-MSB ($360\,nm \lesssim \lambda \lesssim 420\,nm$, mostly inelastic scattering), Anisole ($\lambda \gtrsim 420\,nm$, absorption).*

$\lambda(nm)$	380	400	410	420	430	440	450	500
$\mu(cm)$	0.31	2.6	35	260	577	779	909	2304

- Absorption has been switched on, corresponding to a scintillator mixture $Anisole + BPO(3\,g/l) + bis - MSB(20\,mg/l)$ and to a constant $\mu = 20\,m$ in the cell walls and buffers. Table 7.7 gives the attenuation lengths of the simulated scintillator mixture at various wavelengths. Attenuation with absorption and inelastic scattering is implemented as described in Sec. 6.4.

- The emission spectrum is the one of BPO, which is efficiently shifted by bis-MSB to an emission peaked at $\sim 420 - 440\,nm$ within few centimeters.

The other assumptions are the same as in the previous section.

The chosen simulated composition represents an example of an unloaded scintillator with good transparency. A metal-loaded scintillator can hardly be better, thus the predictions of these simulations give a benchmark of the best performance achievable in a realistic LENS module.

Results and Discussion The results of the simulations are reported in Fig. 7.6 and Table 7.8. We note that the implementation of the cell rounded corners has introduced a fast light

Table 7.8: *Fit parameters for the curves in Fig. 7.6. The last two rows report the fit parameters for the same simulations, carried out assuming a low-reflectance model:* $R_{TIR} = 99.2\%$ *and* $R_{SR} = 98.2\%$.

Simulation	W_1	$(\mu_1 \pm \sigma)\,(cm)$	W_2	$(\mu_2 \pm \sigma)\,(cm)$
TIR $R = 99.4\%$	0.393	16 ± 3	0.607	354 ± 25
SR $R = 98.5\%$	0.316	45 ± 2	0.684	242 ± 4
TIR or SR	0.178	45 ± 4	0.822	397 ± 8
TIR and SR	0.143	34 ± 5	0.857	520 ± 13
low-TIR or low-SR	0.188	41 ± 4	0.812	360 ± 7
low-TIR and low-SR	0.145	36 ± 6	0.855	521 ± 15

attenuation component in the TIR-based cell. TIR light piping is in this case inferior to SR over the entire detection volume. This result confirms the high sensitivity of TIR light piping to geometry, as observed in Secs. 4.6.3 and 6.5. The MC simulations predict that mixed piping ensures the highest response homogeneity and the best absolute performance, with a factor ~ 2 greater photo-collection in the central volume, compared to TIR or SR alone.

The PDP in Fig. 7.6 translates to $PY \sim 0.12\,Q \times LY$, where Q is an experimental "quality factor" ($Q < 1$), which includes losses due to partial PMT coverage and lower effective PMT QE. For $Q \sim 0.7$ and $LY \sim 6000\,phs/MeV$ (as assumed for the Yb simulations), $PY \sim 500\,pe/MeV$.

7.2.3 Conclusions

The results of the simulation of a limit ideal detector, where light is only lost due to piping inefficiency and photo-conversion at the PMTs, show that light guiding offered by commercially available materials in the geometry considered for LENS will not dominate the effective attenuation length and therefore does not represent a limiting factor for the Indium-LENS concept. This conclusion is confirmed by MC simulations of "realistic" benchmark scintillation cells, where light attenuation due to inelastic scattering and absorption is properly implemented. It is shown that an effective attenuation length $> 3\,m$ and an absolute photoelectron yield of $\sim 500\,pe/MeV$ are in principle feasible.

MC simulations of the full LENS detector performed at Saclay [Mey03] have shown that the In-BS background can be reduced to a level $S/N > 2$ with a hybrid design (see Sec. 2.4.3), where the In cells have the same geometry simulated here, effective attenuation length $\mu = 2.9\,m$ and $PY = 310\,pe/MeV$. The combination of this result with our analysis shows that *pp* neutrino detection is not limited by light transport to the PMTs and hence in principle feasible, provided that a stable In-loaded scintillator, with high LY and excellent transparency can be developed and that the absolute optical performance of a real cell is correctly predicted by the MC. The experimental test of these fundamental requirements is one of the primary goals of the LENS pilot phase.

This issue is addressed in the next chapter, where the results are reported of measurements of the optical performances of prototype cells filled with a benchmark liquid organic scintillator and with In-loaded scintillators synthesized and purified at MPIK.

Part III

LENS Prototypes

Chapter 8

Optical Performance of LENS Prototype Cells

8.1 Introduction

The preliminary LENS R&D has indicated that the observation of pp neutrinos with ^{115}In can be technically feasible if it is experimentally demonstrated that the performance of a LENS indium cell meets the quantitative demands specified in the previous chapter. The latter test is one of the primary goals of the pilot phase. MPIK has committed in this experimental program, leading the design and construction of a set of high purity quartz cells for use as LENS prototypes, of a dark room facility equipped with PMTs, NIM and digital VME electronics, and developing indium β-diketonate scintillators (In-acac) at a mass scale of several liters. This chapter reports on the experimental characterization of the optical performance of LENS prototype cells, with the following structure:

- In a preliminary phase the optimal parameter area for the In-acac scintillator formulation has been selected, both with MC studies and with the results of the measurement of "pre-prototype" cells. This studies are described in Sec. 8.2.
- A system has been set up in our dark room with the aim to measure the optical performance of prototype scintillator detectors. This is described in Sec. 8.3.
- The prototype cell has been first filled with a PXE-based scintillator, to measure the benchmark high-performance limit of the detector, in an experimental equivalent of the MC studies in Sec. 7.2. The results are reported in Sec. 8.4.
- This work has been finalized with the measurement of three different indium scintillator samples synthesized at MPIK. Results are presented in Sec. 8.5.

The results of all the prototype measurements are summarized and discussed in Sec. 8.6. The conclusions of this work are given in Sec. 8.7.

8.2 Preliminary Studies

MPIK has invented and developed a novel technique to dissolve metals in organic liquid scintillators, based on the chemistry of β-diketones. This approach has been successfully applied

to indium in the context of the LENS project (other applications are discussed in [Buc04]). The procedures for the synthesis of high purity $In(acac)_3$ to dissolve in organic solvents is published in [BHS03] and the optical properties of In-acac scintillators comprehensively studied in [MPI03, Buc04]. This system and the advantages of the β-diketonates approach have also been briefly described in Sec. 2.4.3.

We focus here on the problem of the optimization of the scintillator composition for application in a long module. The aim of this study is to select the formulation that provides the best light output in a LENS cell.

8.2.1 Optimization of the Scintillator Composition

The Problem The most critical problem of the In-acac scintillators is that the $In(acac)_3$ molecule has an absorption band that overlaps with the UV emission of anisole. Efficient luminescent systems are realized when the excitation energy of the solvent molecule is non-radiatively transferred to the fluor. The choice of the latter is tailored to maximize this energy transfer. In the In-acac system there is a competition between fluor and $In(acac)_3$ to catch the solvent excitation energy. $In(acac)_3$ gives no detectable fluorescence when excited at its absorption band, hence this molecule acts as quencher: it dissipates a part of the solvent excitation, which would be otherwise available for conversion into the final scintillation light.

The strategy to obtain good light yields (LY) is to enhance the "solvent $\rightarrow$ fluor" pathway relative to the quenching "solvent $\rightarrow$ $In(acac)_3$" dissipation. The choice of anisole as the base solvent and the concentration of $In(acac)_3$ are constrained by the demand of high metal loading. Therefore the only handle for controlling the energy transfer is the fluor choice and its concentration. It is found that the best performances are given by PPO and BPO and in both cases it is observed that, at high $In(acac)_3$ concentrations, the LY measured in a $20\,ml$ sample (by fluorimetry as well as by irradiation with γ sources) monotonically increases with the fluor concentration, up to the fluor solubility limit. The shape of the LY as a function of the fluor concentration is well explained by theoretical models of light quenching [Buc04]. An example of measured LY versus BPO concentration is shown in Fig. 8.1.

At the benchmark of 5% indium loading, light yields interesting for LENS are only obtained with fluor concentrations that are "unusual" in unloaded scintillators, where LY saturation, followed by the onset of self-quenching effects, is typically observed at few g/l. The addition of bis-MSB improves dramatically the LY in the PPO system, probably because the PPO primary emission still overlaps with the $In(acac)_3$ absorption band. The light output in BPO systems is found far less sensitive to the bis-MSB concentration, as a consequence of the more "right-shifted" emission spectrum (cf. Fig. 2.1 on page 40). In samples with 5% indium loading and BPO concentration of $100\,g/l$, $LY = 52 \pm 3\%$ relative to BC505 is measured. PPO-based samples reach $LY = 35 \pm 2\%$ for $200\,g/l$ PPO and $500\,mg/l$ bis-MSB.

The scintillator formulation has to maximize the PY in a cell, which is not necessarily the same as maximizing the absolute primary yield in a small sample. In fact, self-absorption in the scintillator is another parameter that enters the problem. In standard scintillators the fluors have a minor role in the long-range attenuation because of their low concentration. This is however not the case for the In-acac formulation. It is found that BPO has a much worse transparency in the visible region than PPO[1], however PPO gives useful LY only at very high

[1] Several attempts to purify BPO gave no significant improvement of the transparency in the visible range, see [Buc04].

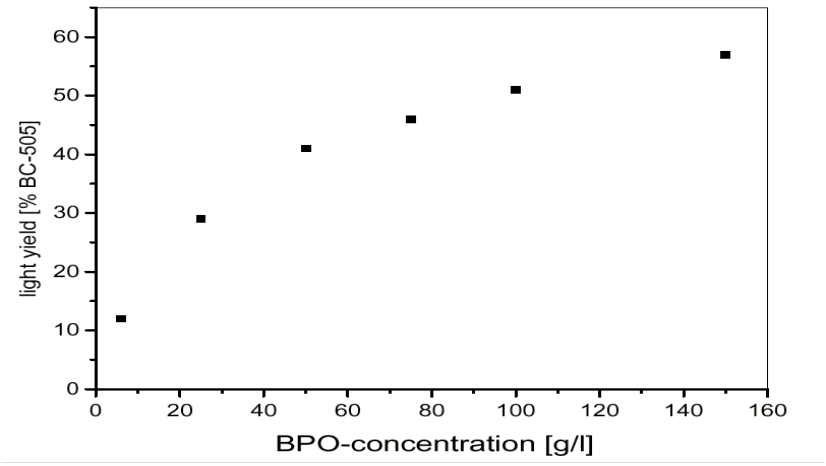

Figure 8.1: *Measured LY for In-acac scintillator samples (In 5% by weight) as a function of the BPO concentration. Figure from [Buc04].*

concentrations and with the addition of a large amount of bis-MSB, which also degrades the scintillator transparency.

The single attenuation contributions and the total attenuation length calculated for the system "anisole + $In(acac)_3$ (indium $50\,g/l$) + BPO($50\,g/l$) + bis-MSB ($100\,mg/l$)" are plotted in Fig. 8.2. At the reference wavelength of $430\,nm$ the attenuation length of this system is dominated by BPO: $\mu_{BPO} \sim 1.5\,m$. The optical purity of the $In(acac)_3$ material, obtained by sublimation of the raw synthesized crystal powder, is good: $\mu_{In(acac)_3} \sim 3\,m$. The other scintillator component give minor contributions $\mu_{anisole} \sim \mu_{bis-MSB} \sim 10\,m$. The resulting total attenuation length at $\lambda = 430\,nm$ is $\mu_{tot} \sim 0.85\,m$, which is in good agreement with the direct spectrophotometric measurement of this sample. At this stage, the conclusion is that reasonable light outputs and homogeneous detector response can be obtained either with a more indium-diluted scintillator (so that less fluor is needed), or with much shorter cells than initially envisaged. The decision for the LENS pilot phase was the latter and hence prototype quartz cells of $5\,cm \times 5\,cm \times 100\,cm$ have been built.

The purpose of this preliminary work is to find the parameter area where the best compromise between primary LY and efficient light transport over long distances is realized. This was achieved by MC simulation and by probing the multi-parameter space of the problem with a few tests in a small volume pre-prototype cell. The results presented in this section selected the scintillator composition for the implementation in the final LENS prototype.

Solution via MC Simulations The optimization of the scintillator composition requires a model of light transport that includes the best physics of emission, energy transfer and photon absorption. The experimental input data are the fluor emission spectra, the extinction coefficients of each single component of the system and the estimation of their fluorescence yields. Such a model has been described in Sec. 6.4 and already used in the MC simulations reported in the previous chapter (see e.g. Fig. 7.6). The MC simulations presented here assume:

- Cell geometry of $5\,cm \times 5\,cm \times 100\,cm$, square section with rounding at the corners

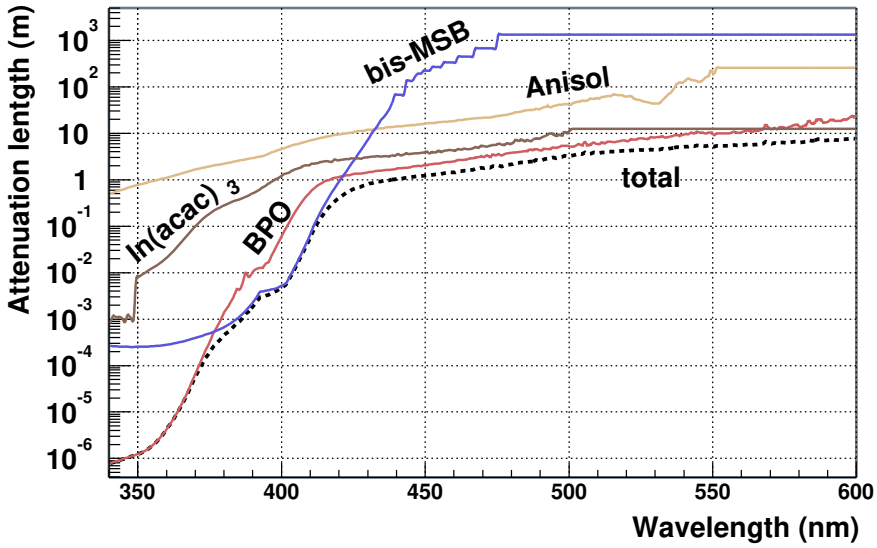

Figure 8.2: *Attenuation lengths, calculated from spectrophotometric extinction data, for a system: anisole + $In(acac)_3$ (indium $50\,g/l$) + $BPO(50\,g/l)$ + $bis-MSB(100\,mg/l)$. Details on the spectrophotometric measurements in ref. [Buc04].*

($4\,mm$ radius of curvature), $2\,mm$ wall thickness and $5\,mm$ air gap on top of the scintillator. No buffers.

- Scintillator based on anisole as solvent, $In(acac)_3$ as metallorganic compound, BPO as primary fluor, bis-MSB as WLS. The concentration of $In(acac)_3$ is fixed to the value corresponding to $50\,g/l$ In loading. The BPO concentrations is varied. The attenuation lengths are calculated from the concentrations and the extinction coefficients of each component, as in Fig. 8.2. The parameters in Table 6.1 are used for the relative probabilities of absorption and inelastic scattering.
- The emission spectrum of BPO is assumed as primary scintillation spectrum (Fig. 2.1 on page 40), because it is found that the energy transfer to bis-MSB is predominantly radiative [Buc04].
- LY as measured by us in $20\,ml$ samples [Buc04].
- Light piping via TIR and SR. The refractive index of scintillator, walls and PMT window is $n = 1.5$. The reflection coefficients are $R = 99.7\%$ for $\theta > \theta_c$ and $R = 98.5\%$ for $\theta < \theta_c$. This choice corresponds to an intermediate case between the limits "TIR or SR" and 'TIR and SR" defined and discussed in Sec. 6.5 and simulated in Sec. 7.2.
- The PMTs are coupled to the cell ends with flat photocathode, $\pi/4$ surface coverage. The "green-enhanced" QE is chosen (Fig. 5.1 on page 100). The optical model of the PMTs is implemented, as described in Sec. 6.6.

The results of the simulations are shown in Fig. 8.3. The effect of BPO self-absorption is

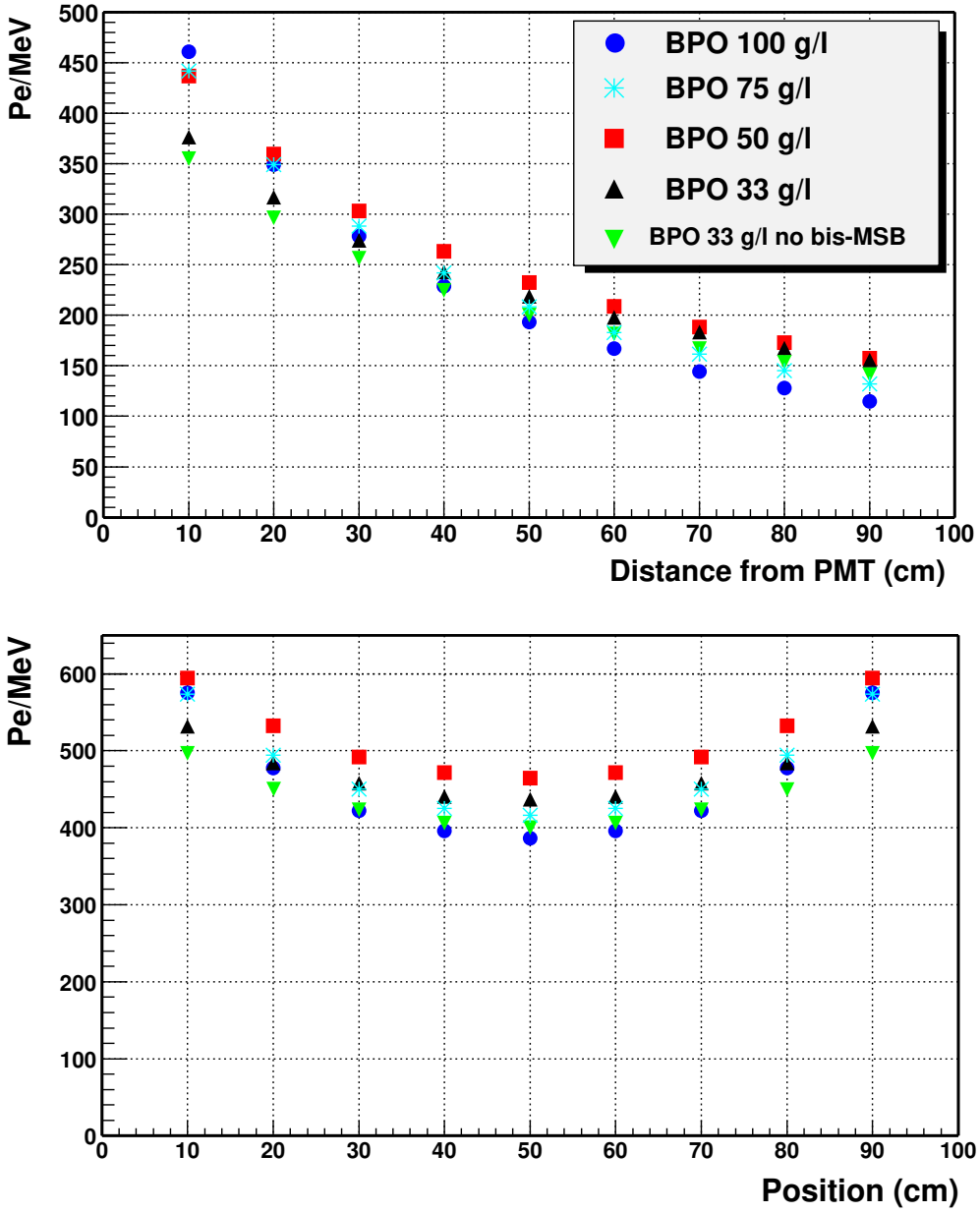

Figure 8.3: *Simulation of the PY in a In-loaded cell for different BPO concentrations. Top: attenuation curve for the light measured by one PMT. Bottom: sum charge at the two sides, as a function of the source position. Bis-MSB is included, at* $100\,mg/l$*, in all but one simulation (green-downward triangular markers), where bis-MSB is absent to check the effect of the* λ*-shifter in a BPO system. The PY is given in absolute* pe/MeV*, assuming that the reference BC505 has* $LY = 12000\,pe/MeV$*.*

Table 8.1: *The samples measured in the small prototype cell. Details about sample preparation and spectrophotometric measurements are found in [Buc04].*

Sample	Purpose
Anisole + BPO(3 g/l)	Benchmark
Anisole + BPO(50 g/l)	Absorption BPO
An + BPO(50 g/l) + $In(acac)_3$(In 5%)	Absorption In Material
An + BPO(50 g/l) + bis-MSB(100 mg/l)	Impact λ-shifter
An + BPO(50 g/l) + bis-MSB(250 mg/l)	Dependence bis-MSB Concentration
An + BPO(50 g/l) + bis-MSB(500 mg/l)	Effect High bis-MSB Concentration

clear to see: the scintillator with 100 g/l gives the highest light output in a small sample, however at the cell center the PY is predicted to be the lowest among the considered cases. The best compromise is expected at $\sim 50\,g/l$ BPO, which has 42% primary LY compared to the standard BC505. The model predicts that bis-MSB is useful, even if BPO emits already at long wavelengths.

The PPO system with the highest LY (PPO 200 $g/$l and bis-MSB 500 mg/l) has also been compared with BPO. Surprisingly, the simulations indicate that a higher PY at the cell center could be achieved. This happens because even at 200 g/l the PPO absorption is much less than the BPO absorption at 50 g/l. In fact, the attenuation in the PPO system at $430\,nm$ is dominated by bis-MSB, due to the high concentration. If the absorbed light is efficiently reemitted, this part of the attenuation length does not imply a real light loss. However, these conclusions are strongly model-dependent, because the simulations are very sensitive to the imposed fluorescence wavelength cut, i.e. to the efficiency and wavelength dependence of the bis-MSB reemission at $\lambda \sim 430\,nm$ (see Table 6.1 on page 131).

8.2.2 First Experimental Indications

A preliminary small-volume test system has been set up in our dark room with the aim of probing several samples during the process of scintillator optimization. Moreover, this work permitted to develop and test the experimental techniques to use in the subsequent optical characterization of the big prototype cell, to be described in the next section.

The cell used was the same quartz tube measured for light piping (Fig. 4.4 on page 80). The external dimensions are $1.5\,cm \times 1.5\,cm \times 110\,cm$ and the quartz thickness is $0.2\,cm$. The cell has been closed with welded windows on both sides and modified with the opening of a filling stub at one end. At the other end, a PMT has been coupled. No VM2000 have been used and hence light was piped by TIR only. The electronics and data-acquisition are similar to those of the light piping measurements and are a simplified version of the system set up for the final full-scale prototype cell, which will be described in the next section.

For each filling, the charge signal from the PMT has been measured as a function of the source distance. As source, an external collimated $380\,nm$ LED was used. This excites the scintillator fluors, which in turn reemit light isotropically inside the cell. The measured samples are listed in Table 8.1.

The main experimental output of these tests was the determination of the light intensity attenuation curve, as for the light piping measurements. The system has not been calibrated

Table 8.2: *Summary of the measurements in a* $1.5\,cm \times 1.5\,cm \times 110\,cm$ *cell. The relative PY is measured through the ADC-position of the* ^{137}Cs *Compton-edge at* $5\,cm$ *distance from the PMT. The estimated relative error is* $\sim \pm 5\%$. μ_{long} *and* W_{long} *are the longest attenuation length and its relative weight returned by a double exponential fit of the attenuation curve (same analysis as described in Sec. 4.5.2).*

Sample	Relative Yield	$\mu_{long}\,(cm)$	$W_{long}(5\,cm)$
Anisole + BPO(3 g/l)	not measured	218 ± 16	0.66
Anisole + BPO(50 g/l)	1	123 ± 5	0.74
An + BPO(50 g/l) + $In(acac)_3$(In 5%)	0.56	57 ± 2	0.70
An + BPO(50 g/l) + bis-MSB(100 mg/l)	0.59	81 ± 5	0.59
An + BPO(50 g/l) + bis-MSB(250 mg/l)	0.52	72 ± 10	0.69
An + BPO(50 g/l) + bis-MSB(500 mg/l)	0.49	91 ± 14	0.48

for absolute determinations, however a qualitative comparison of the samples relative light outputs was obtained by irradiating the cell with a ^{137}Cs source at the reference distance of $d = 5\,cm$, where the effects of self-absorption are only important for the energy transfer to bis-MSB. Table 8.2 reports a summary of the analysis of the measurements.

The results have given the following indications:

- The two anisole/BPO samples had performances consistent with the expectations (the agreement with the simulations is good). In particular, the long-range attenuation of the 3 g/l BPO sample is only slightly worse than what was found in the TIR piping measurements at $(\mu_{long}(430\,nm) = (259 \pm 5)\,cm$, see Sec. 4.6.2). The difference is consistent with the attenuation length of this sample, $\mu_{430} \simeq 4.3\,m$.

- The addition of $In(acac)_3$ to the base Anisole + BPO (50 g/l) determines a reduction of the light output at $5\,cm$ distance to $\sim 56\%$ of the unloaded scintillator. This is in good agreement with the independent LY measurements performed in a 1 cm vial, which give for the In-loaded and unloaded samples $LY \sim 42\%$ and $\sim 80\%$ respectively, relative to the standard BC505[2]. The observed drop of the attenuation length is not consistent with the expectations for the best measured $In(acac)_3$. It turned out that the $In(acac)_3$ crystals of the used batch did not have homogeneous optical purity and that the sample dissolved in the scintillator belonged to the least pure part. Later measurements at the spectrophotometer confirmed that the $In(acac)_3$ component used for this measurements had only $\sim 1\,m$ absorption length [Buc04]. This observation has allowed to improve the procedure for the preparation of the $In(acac)_3$ crystals for the later use in the prototype.

- The addition of bis-MSB at $100\,mg/l$ produces a slight increase in the PY, also observed in the LY measurements. The effective attenuation length is notably improved, as an effect of the wavelength shift.

- The increase of the bis-MSB concentration to $250\,mg/l$ determines a reduction of the light intensity measured at $5\,cm$ distance. The LY measurements show however that

[2]The limit LY measured for an unloaded anisole/BPO scintillator is $\sim 90\%$ of BC505 [Buc04]. At higher BPO concentrations self-quenching is observed.

the output from a small sample is nearly independent of the bis-MSB concentration. Therefore this effect is likely due to short-range photons interactions with bis-MSB.

With our set up it is not possible to disentangle unambiguously bis-MSB absorption from wavelength-shifting with characteristic scale length $\mu_{shift} \sim 1\,cm$ (the internal dimension of the quartz cell). In fact, after few reflections in the pipe, light has been selected by the TIR acceptance. If the wavelength shift is not realized in a very short range (i.e. before the first reflection), light is reemitted isotropically and $\sim 50\%$ gets lost at the next reflection. Wavelength shifting becomes again convenient when the path-length to the PMT is longer than the absorption length due to the other components.

At $250\,mg/l$, $\mu_{bis-MSB} \sim 1\,cm$ for $\lambda \sim 405 - 410\,nm$. In this range the total absorption length from the other components of the scintillator is $\sim 20\,cm$. In a bigger cell or in a cell wrapped with VM2000 foils, the bis-MSB attenuation might not result in a real loss.

- The increase of the bis-MSB concentration to $500\,mg/l$ reduces further the measured light intensity from $5\,cm$ distance. Moreover, even at longer distances light is attenuated faster, as can be seen by the lower weight of the long attenuation component. This means that the attenuation due to bis-MSB dominates even beyond the reference $5\,cm$ distance.

The conclusion of these measurements is that $\sim 100\,mg/l$ of bis-MSB in the base In-loaded scintillator improves the cell performance. Higher concentrations do not improve the long-range effective attenuation length and introduce short-range attenuation. With our system, it is difficult to say to which extent this short-range bis-MSB attenuation is a real absorption, or still a wavelength shift, however less efficient due to limited solid angle for TIR acceptance. In any case, a concentration in the range of $100\,mg/l$ seems the safest choice for the final LENS prototype.

8.3 Experimental Technique

The final prototype cell measured in our dark room is one of a set of 12 identical quartz modules built by MPIK for the LENS pilot phase. The raw profile tubes have been manufactured by the *Heraeus Quartz Glas GmbH* out of "synthetic quartz crystals". The *Helma* company has welded the two side windows and manufactured two openings and stoppers for the cell filling and emptying, one on each side. The cells have been finally annealed by Heraeus. The cell dimensions are $5\,cm \times 5\,cm \times 100\,cm$. Fig. 8.4 shows a drawing of the transversal section, as it appears during the measurements of the optical performance, to be described later.

The purpose of this campaign of measurements was to characterize the performance of a single LENS detector unit. The parameters to measure are:

1. Energy resolution
2. Spatial resolution
3. Absolute PY
4. Dependence of the cell response on the source position

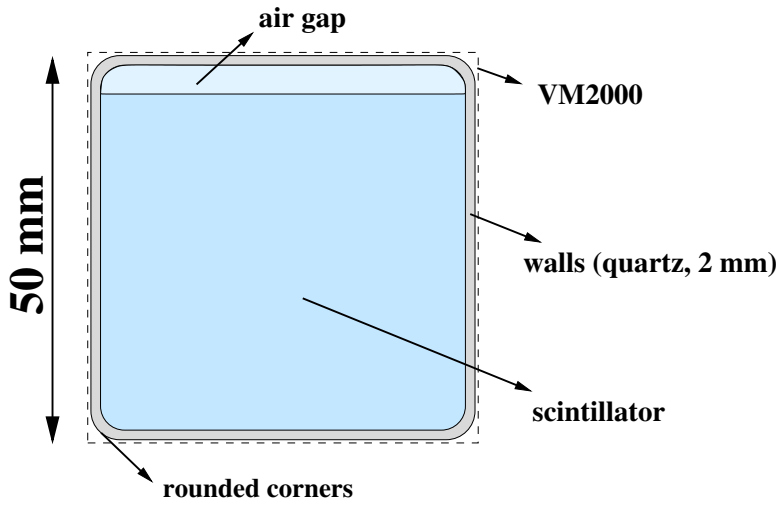

Figure 8.4: *Section of the prototype LENS cell. The side dimension is 50 mm, the quartz thickness 2 mm and normally a space of ∼ 5 mm on top of the liquid was left free to avoid that the scintillator touches the stoppers of the filling openings (not shown in the figure). All the features shown are implemented in the simulations reported in this chapter.*

A measuring system has been set up in our dark room to accomplish the above goals. Most useful is to test the detector response to the deposition of single known energies in the scintillator, so that the cell performance can be deduced directly, without deconvolving the primary energy spectrum. This concept has been implemented with the Compton-back-scattering (CBS) technique. Fig. 8.5 shows a drawing of the experimental set-up and the logic scheme of the front-end electronics and data-acquisition (DAQ).

Set-Up The cell is irradiated with a collimated γ source and the Compton-scattered electrons deposit a continuum energy spectrum in the scintillator. The resulting light pulses are measured in coincidence on both PMTs. An additional liquid scintillation unit is located on the back side of source and collimator, opposite to the cell. A three-fold coincidence can be set, which selects the events with simultaneous energy deposition in the cell and in the back-scattering box. These events are due to:

1. Random coincidences, in particular of a source event in the box and an uncorrelated background count in the cell

2. Coincidence of a source Compton scattering, where the γ is back-scattered by the scintillator in the box and then has an interaction in the cell

3. Coincidence of a source Compton scattering, where the γ is back-scattered by the cell and then has an interaction in the box

The events of case 3 deposit in the cell a nearly mono-energetic spectrum with the energy of the CBS peak:

$$E_{CBS} = E_\gamma \frac{2E_\gamma}{2E_\gamma + m_e} \tag{8.1}$$

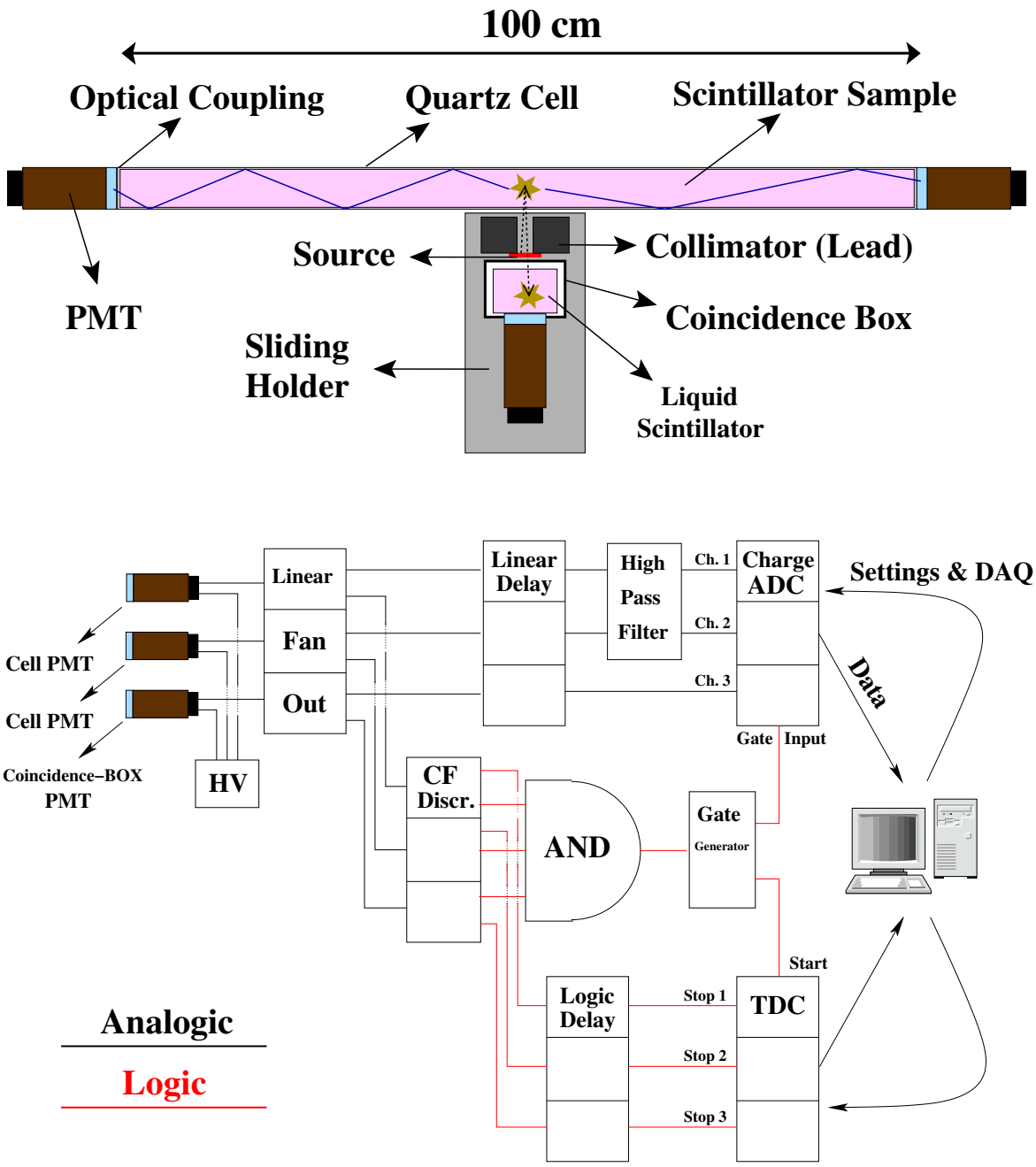

Figure 8.5: *Top: schematic view of the experimental set-up realized in our dark room for the optical measurement of the prototype cell. A collimated γ source is fixed on a sliding holder to irradiate the cell at any position. The collimator width is 12 mm. The scintillation light propagates in the cell and can be eventually detected by two PMTs optically coupled on both ends. An auxiliary liquid-scintillator device can be used to select events with a nearly mono-energetic deposition, by requiring the prompt coincidence of the Compton in the cell and the back-scattered γ in the box.*
Bottom: logic scheme of the front-end electronics and DAQ.

Table 8.3: *Specifications of the PMTs coupled to the prototype cell.*

type	diameter	active diameter	Photo-cathode	number dynodes	operating HV	rise time	jitter (fwhm)
ETL9954B	$52\,mm$	$46\,mm$	$RbCsSb$	12	$1.8-2.0\,kV$	$2\,ns$	$2.2\,ns$

where E_γ is the energy of the γ and m_e the mass of the electron, measured in the same unit as E_γ. The events of type 1 and 2 are the backgrounds for the analysis of the CBS peak.

Electronics and DAQ The signals from the PMTs are doubled by a linear fan-out. One output is sent to form the trigger condition and the logic *start-stop* signals for a Time-to-Digital-Converter (TDC). The other copy of each analogic signal is delayed of the time required for the system to trigger and then sent to an integrating charge-sensitive Analog-to-Digital-Converter (ADC).

The PMT signals are discriminated by a constant fraction discriminator (CF), which delivers two output signals per section. One is delayed and sent to the stop input of the TDC, the other to a coincidence unit for the formation of the trigger. The coincidence level can be set to 3 (CBS selection), or 2 (Compton spectrum). The AND logic output is shaped with a gate generator and sent to the *start* input of the TDC and to the gate input of the ADC.

For every event that satisfies the trigger condition, the ADC measures the total charge delivered by each PMT, which is proportional to the energy deposited in the scintillator. The TDC measures the time elapsed between the common *start* (the trigger signal) and the delayed outputs of the CF. The difference between these times gives the delay of one PMT relative the other, which relates to the position of the source in the cell, via photons time-of-flight.

The PMTs used are the low-background version of the ETL9954B. Their characteristics are listed in Table 8.3. The analogic and logic electronics is NIM, the digital part is VME. ADC and TDC are 12-bits (4096 channels) and are remotely controlled. The DAQ program to drive the VME electronics has been developed at MPIK and is documented in [Las02]. The ADC and TDC data are written in form of binary files and stored on a local disk.

A multi-purpose data-reading and data-analysis platform has been developed during this work. It is based on the *ROOT* toolkit from CERN. First the raw binary data are converted off-line into an *object-oriented* format and stored in *ROOT* files. Each event contains the digital VME outputs of all the active channels, hence three charges and three times. Data are then opened and analyzed with dedicated *macros*.

The Measurements In the next sections the results of the measurements are shown, first for a benchmark PXE cell, then for three In-acac samples. For each scintillator sample measured in the prototype cell the results will be reported as follows:

1. Measurement of the light intensity at one PMT as a function of the source distance. Results are given in arbitrary units and compared with the MC predictions. The curves are fitted with eq. 4.3 and the effective short and long-range attenuation lengths are calculated.

2. Determination of the detector energy resolution and spatial resolution at the energy of the CBS peak. Two pure γ emitters have been utilized: a ^{137}Cs and a ^{54}Mn source

Table 8.4: *Attenuation lengths at various wavelengths for the measured PXE + p-TP* $(2.0\,g/l)$*+bis-MSB* $(20\,mg/l)$ *scintillator. The attenuation at* $\lambda \lesssim 420\,nm$ *is dominated by bis-MSB, above by absorption in the solvent.*

$\lambda(nm)$	380	400	410	420	430	440	450	500
$\mu(cm)$	0.25	5.2	78	580	1300	1700	2300	9500

($E_\gamma = 662\,keV$ and $835\,keV$, respectively). The ^{137}Cs source have a much higher activity and hence most of the measurements refers to its CBS recoil electron energy: $E_{CBS}^{^{137}Cs} = 477\,keV$. This energy is particularly significant for LENS, because it is close to the energy of the γ_3 in the ν-tag and is representative of the hard-Bremsstrahlung range. The CBS of the ^{54}Mn source is also well suited to LENS: $E_{CBS}^{^{54}Mn} = 639\,keV$, which is similar to the sum energy deposited by the ν-tag (see level scheme in Fig. 2.5 on page 46). In fact, a crucial issue in LENS is how well the tag energy ($613\,keV$) can be resolved from the ^{115}In β end-point ($495\,keV$).

3. The PMT charge measured at point 2 is calibrated relative to the peak amplitude of the single-photoelectron charge distribution. The PY derived from this comparison is reported and compared with the data of the energy resolution.

The data analysis procedures will be described while reporting the PXE measurements.

8.4 Measurements of a Benchmark PXE Cell

The prototype cell has been filled with a PXE-based scintillator to study the detector performance in a benchmark case. The PXE comes from a batch measured by Borexino in CTF [Bor04]. The composition is PXE + p-TP $(2.0\,g/l)$ + bis-MSB $(20\,mg/l)$. The scintillator LY is $\sim 83\%$ relative to BC505, which translates to $\sim 10000\,ph/MeV$.

The original attenuation length was $2.7\,m$ at $430\,nm$. The scintillator used for these measurements has been further purified by us [Buc04] and the spectrophotometric attenuation lengths at various wavelengths are reported in Table 8.4.

In the wavelength range of the emission peak ($420 - 450\,nm$) the scintillator shows an attenuation length much longer than the module dimension. Therefore these measurements test the optical integrity of the quartz cell and the precision of the the piping reflection coefficients given in Chapter 4, through the comparison with the MC predictions.

After the cell filling, the PXE has been flushed with nitrogen for about one hour to sweep oxygen, which can decrease the scintillation yield (the same procedure is also adopted for the In-acac samples). Two sets of measurements have been performed:

- TIR light piping
- TIR plus VM2000 light piping

In the former case the cell is used "just so" and light is piped via total internal reflection at the quartz/air and scintillator/air boundaries. In the latter case a VM2000 profile has been wrapped around the cell (without optical coupling), as shown in Fig. 8.4. The VM2000 recovers the photons that are not TIR-trapped in the cell, as explained in Sec. 6.5.

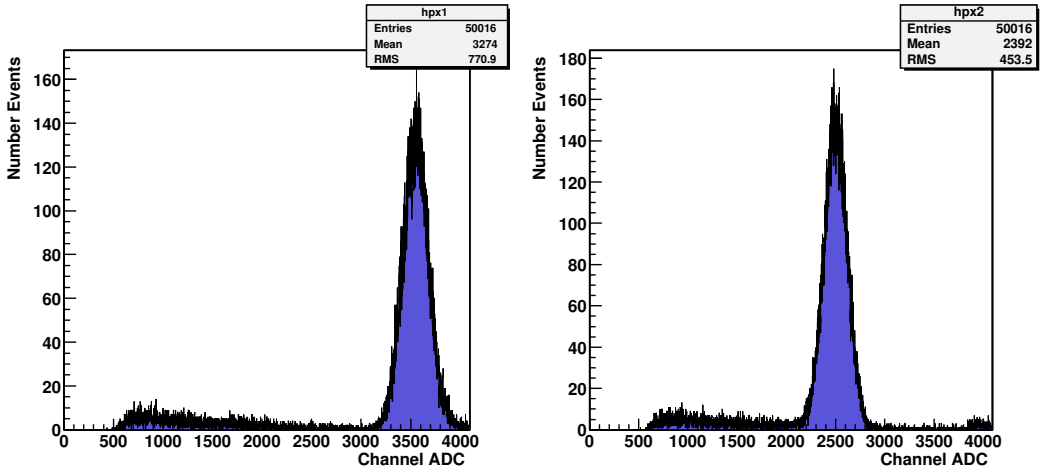

Figure 8.6: *Distribution at the two PMTs of the measured charge from 50000 LED pulses. The abscissa is the ADC channel, which is proportional to the charge delivered by the PMT (a "pedestal" offset of* $\sim 100 - 150$ *channels must be subtracted). The ordinate is the number of events per bin. In this measurement the LED is at* $5\,cm$ *distance from the "left" PMT and the gains are adjusted to equalize the charge amplitudes at the cell center. The distributions are gaussian around the peak. If it is assumed that the observed standard deviation is purely statistical, then the total collected charge is* $\sim 10^3\,pe$*. The statistical error of the peak channel is* $\pm 0.03\%$ *(the gaussian fit returns an error of* $\sim 1\,ch$*). However the real error during a LED scan is dominated by the drifts in the total gain of the system from one position to another. It has been evaluated from repeated measurements that this uncertainty is* $\sim 1\%$*.*

8.4.1 TIR Cell

Light Attenuation The light attenuation curve has been measured by scanning the cell response to a $380\,nm$ LED, as also described in Secs. 4.5 and 8.2.2. In these measurements the LED replaces the radioactive source on the sliding holder shown in Fig. 8.5. We remind that the LED is connected to an electric circuit triggered externally with a logic TTL signal. The LED delivers a fast (few ns width) light pulse at the leading edge of the TTL signal. This light is absorbed by the bis-MSB in the scintillator and reemitted isotropically inside the cell. The light intensity can be adjusted from a sub-Poisson photo-statistics to $> 10^3$ detected photons at the PMTs. High intensity is chosen, to decrease the photo-statistical fluctuations of the single light pulse.

For each position 50000 LED events are acquired. Fig. 8.6 shows an example of the charge distribution measured at the PMTs.

The light attenuation curves measured with an LED scan are shown in Fig. 8.7. For comparison, the graphics also reports the normalized data-points obtained with the CBS peak of the ^{137}Cs source (measurement to be described later). In this latter case, the scintillator is excited by the CBS recoil electron.

The normalized prediction of the full photon-tracing MC simulation of the system is also shown in the figure. This simulation assumes the geometry of the prototype (Figs. 8.4 and 8.5), the same physics included in the simulations described in Sec. 8.2.1, with the following

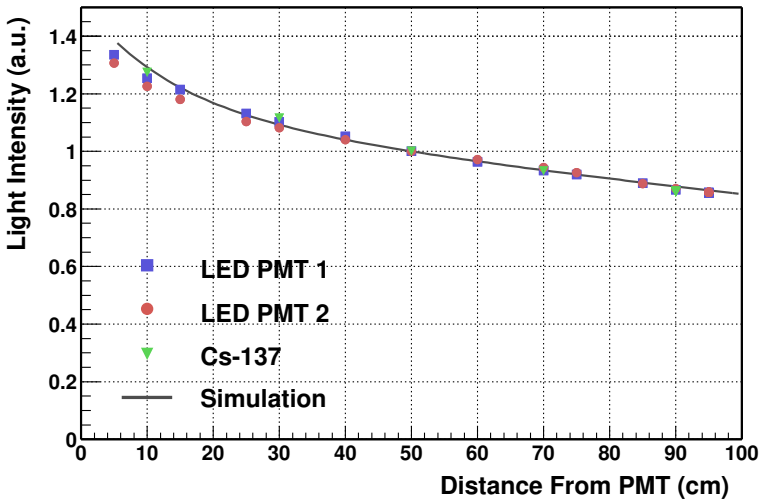

Figure 8.7: *Measured light intensity as a function of the source distance in the PXE cell, with TIR piping. The markers represent the data points, the solid line is a simulation of the system. The square and circular markers represent the mean PMT charge measured by the two PMTs under scintillator excitation with a 380 nm LED. The triangular markers are the results of the CBS runs with a ^{137}Cs source. Data and simulation are arbitrarily normalized to 1 at $d = 50\,cm$ (cell center).*

specific inputs:

- The PXE attenuation lengths are used (see Table 8.4)
- Light piping is realized by TIR, with $R_{TIR} = 99.4\%$
- The PMT coverage is reduced to the sensitive area specified by the manufacturer ($d = 46\,mm$)

No significant differences are observed in the light attenuation curves measured by the two PMTs, as expected. It can be seen that the CBS data points are consistent with the LED curves. A small departure between simulation and experiment is observed at short distances, where the simulation predicts a slightly faster attenuation[3]. However, in the rest of the curve MC and data are in very good agreement.

The results of the quantitative analysis of experimental and simulated curves are given in Table 8.5. About 90% of the light that can be piped by TIR propagates in the cell with an effective attenuation length of $\sim 3\,m$. The simulation is somewhat more "pessimistic" concerning the fraction of light with long effective attenuation (82%), however it predicts a similar asymptotic attenuation length. This means that the physics of light propagation in the cell is well understood and that no light loss mechanisms beside the known ones are present.

[3]It must be noted that the attenuation curves are not absolute. They are compared with each other upon an arbitrary normalization at the cell center. Therefore the fact that the simulation stays above the data at short distance does not mean that it predicts more light than really observed, but rather that a larger fraction of the primary light is expected to get lost in the first part of the curve.

Table 8.5: *Parameters returned by a double exponential fit to the experimental data and the simulation of Fig. 8.7.* μ_{short} *and* μ_{long} *are the effective short and long attenuation lengths of eq. 4.3.* W_{short} *and* W_{long} *the relative weight referenced to* $d = 5\,cm$*, i.e.* $W_{short,long}$ *is the fraction of the light detected from* $5\,cm$ *distance that decays with a* $\mu_{short,long}$ *attenuation length. "LED average" is the curve obtained by averaging for each distance the response of the two PMTs.*

	$\mu_{short}\,(cm)$	W_{short}	$\mu_{long}\,(cm)$	W_{long}
LED PMT 1 ("left")	15.3	0.130	297 ± 12	0.870
LED PMT 2 ("right")	8.9	0.103	289 ± 4	0.897
LED average	11.2	0.112	288 ± 5	0.888
Cs-137	24.6	0.151	305 ± 7	0.849
Simulation	13.6	0.181	330 ± 16	0.819

TDC Calibration The LED scan also allows to calibrate the TDC channel-to-distance scale with a high photoelectron-statistics source. Fig. 8.8 shows the TDC distributions for three source positions and the TDC calibration for the entire set of LED data.

The calibration points are fitted with a linear function. For this measurement, the mean conversion factor is $\sim 3.7\,ch/cm$. The linear fit to the data is not good: $\chi^2/d.o.f. \sim 5.5$, with 6 degrees of freedoms. This feature has been observed in all the measurements and is a hint for systematic non-linearities in the position-TDC scale. However this uncertainty is sufficiently small to allow the estimation of the cell spatial resolution with a $\sim 5\%$ error.

From the analysis of the TDC peaks and the calibration it is deduced that a single LED event can be reconstructed via time-of-flight difference with a spatial resolution of $\sim \pm 2\,cm\,(1\sigma)$.

CBS Measurements The raw data of a $\sim 3\,h$ ^{137}Cs CBS run with the source at the cell center are shown in Fig. 8.9. The CBS peak is visible in the ADC spectra, however the background in the region of interest is not negligible compared to the CBS signal. The same figure explains the origin of this background and thus helps to define suitable off-line cuts to improve the S/N ratio. The ADC charge distribution in the coincidence box shows a continuum Compton spectrum with a low energy peak. This means that many three-fold coincidence events deposit in the scintillation box an energy higher than the $185\,keV$ of a ^{137}Cs back-scattered γ. These events are a background and can be rejected on a event-by-event basis by demanding that the energy deposited in the coincidence box is lower than an upper cut. Furthermore, the TDC event distribution shows that many events are spatially reconstructed far from the source location. Therefore a further TDC cut can be applied, to reject the events that are not consistent with the source position. The effect of the cuts discussed is shown in Fig. 8.10.

The energy spectrum of the events surviving all cuts shows a nearly gaussian CBS peak, with a modest background contamination on the left side of the peak. The latter is sufficiently small to allow a precise determination of the energy resolution by fitting with a gaussian plus an asymmetric background, or a gaussian plus an exponential tail plus a constant background (called "pseudo-gaussian functions" hereafter). In both cases the fit is very good and the estimation of the standard deviation is nearly independent of the assumed low energy background

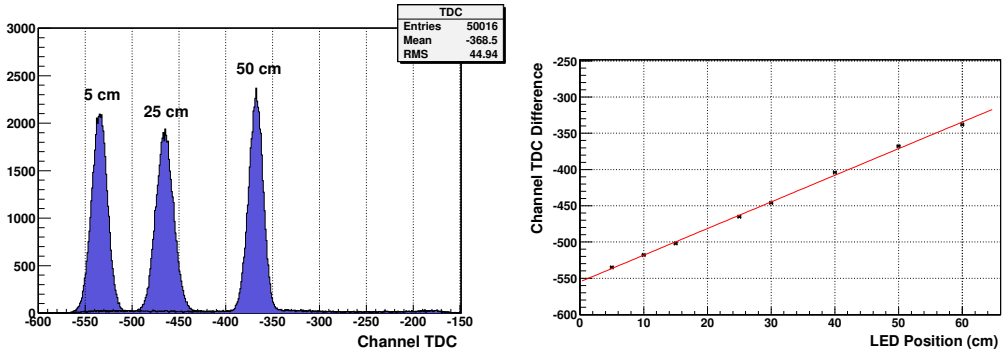

Figure 8.8: *Left: TDC distributions measured with the LED at 5 cm, 25 cm and 50 cm from one PMT. The abscissa is the difference between the TDC channels of the two PMTs. From the measured standard deviation it is deduced that the spatial resolution of a single LED event is* $\sim 1.9\,cm$*, with* $\sim 10^3$ *total detected pe (estimated from the width of the ADC distribution).*
Right: Calibration of the Position-to-TDC scale obtained with a LED scan. The markers represent the TDC peak channels for each probed distance (the estimated error bars are reported). The solid line is a linear fit. The slope is $\sim 3.7\,ch/cm$.

Table 8.6: *Analysis of the* ^{137}Cs*-CBS measurements with the PXE-TIR cell (*$E = 477\,keV$*). The relative* 1σ *error of the energy resolutions is* $\pm 2\%$*. For the spatial resolution it is* $\pm 1.5\%\,(stat) \pm 5\%\,(sys)$*, where the systematic error derives from the uncertainty in the channel-to-distance scale.*

Distance from PMT 1 (cm)	σ_E PMT 1 (%)	σ_E PMT 2 (%)	σ_E Sum (%)	σ_x (cm)
10	10.6	13.0	8.4	4.9
30	11.0	12.3	8.5	5.0
50	12.6	11.4	8.7	4.4
70	12.9	10.3	8.5	4.1

shape.

The figure also shows that the TDC spectrum obtained by selecting only the events in the CBS energy window has a sharp gaussian peak that corresponds to the source position.

Figs. 8.11 and 8.12 show how the single-PMT ADC spectra and the TDC spectrum change with varying source positions. The amplitude of the ADC peaks varies in agreement with the LED scan (these data-points have been reported in Fig. 8.7), and the shape is in all cases well fitted by a pseudo-gaussian function. The TDC data demonstrate the good spatial reconstruction capability of the time-of-flight technique for events depositing energies in a region of interest for LENS.

The results of the analysis of ADC and TDC CBS data are reported in Table 8.6. At $477\,keV$ an energy resolution of $(8.5 \pm 0.2)\%$ (1σ) is found, slightly dependent on the source location, as expected from the light attenuation curves. One PMT (the "right", or "2", in the convention of the previous figures) has a slightly better energy resolution. This can be due to a higher QE or to a better single-photoelectron (single-pe) spectrum. The spatial resolution

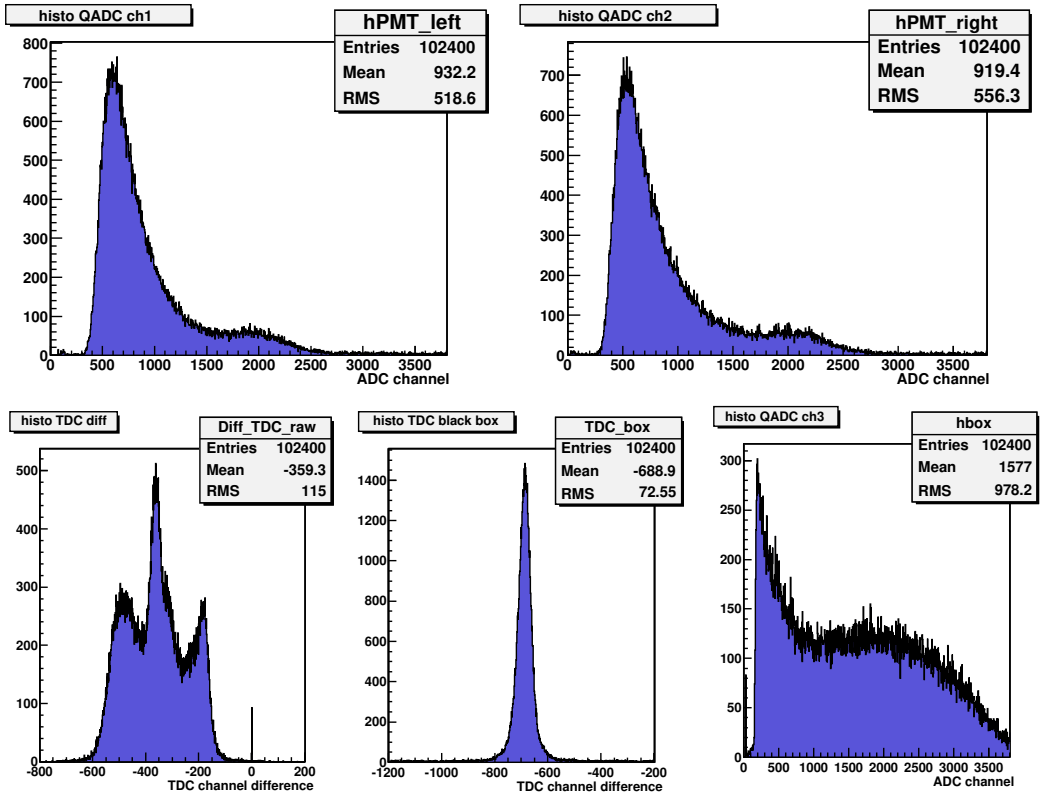

Figure 8.9: *Example of raw ADC-TDC data for a CBS run with source in the cell center. The CBS peak is visible on both distributions around channel 2000. The left side of the distribution is however shaded by the tail of the low energy background.*
Top: ADC spectra of the energy deposited in the cell, measured by the two PMTs.
Bottom left: TDC spectrum of the time difference between "left" and "right" PMT.
Bottom center: TDC spectrum of the time difference between the coincidence-box signal and the average time of the two PMTs of the cell.
Bottom right: ADC energy spectrum measured in the coincidence box. The PMT gain is tuned to have the ^{137}Cs Compton shoulder within the ADC dynamic range.

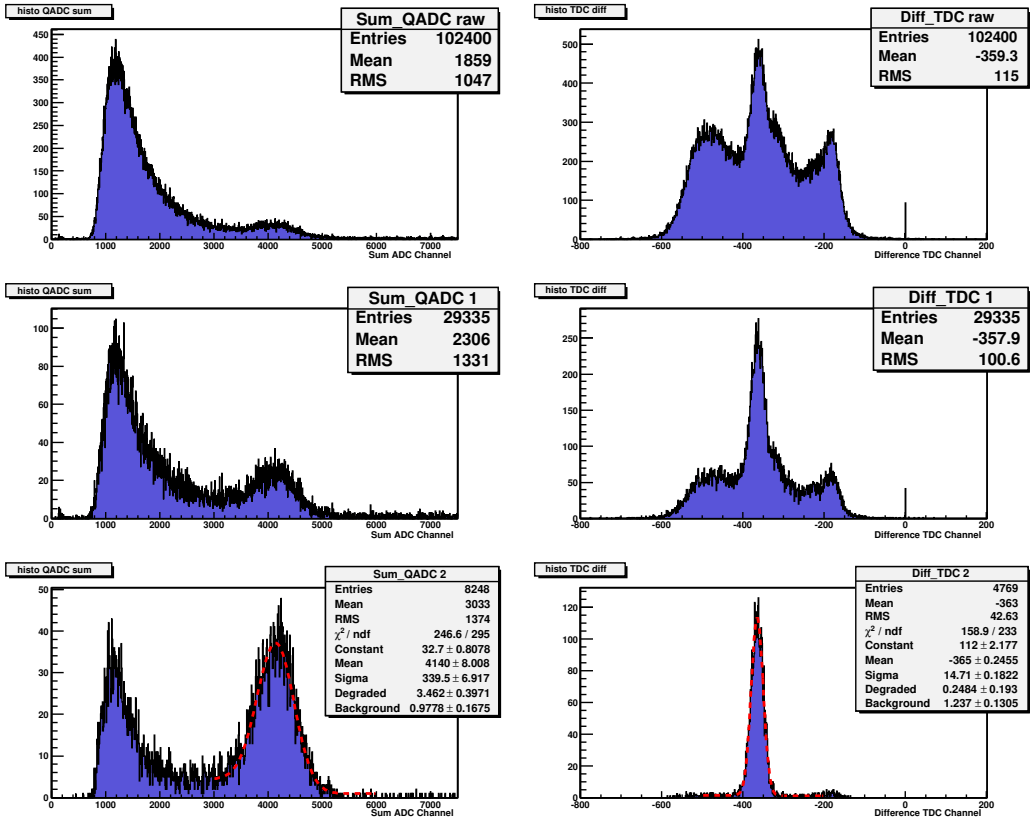

Figure 8.10: *Top left: raw CBS Sum-ADC spectrum. The plot is the distribution of the total charge measured for each acquired event, calculated by summing the ADC values of the two PMTs. The spectrum corresponds to the single PMT distribution shown on top of Fig. 8.9*
Top right: TDC spectrum. It is the same plot of the bottom-left pad of Fig. 8.9.
Middle left: Sum-ADC spectrum obtained after cutting all the events with an ADC charge in the coincidence box higher than channel 1000 (cut_1). The S/N for the CBS peak has significantly improved.
Middle right: TDC spectrum after cut_1. The events reconstructed far from the cell center have decreased.
Bottom left: Sum-ADC spectrum after imposing cut_1 plus a cut on the TDC corresponding to $\sim \pm 2\sigma$ of the source peak. The CBS peak is now clearly highlighted and can be fitted with a gaussian function that takes into account the small background on the left side of the peak.
Bottom right: TDC spectrum after imposing cut_1 plus a cut on the Sum-ADC charge, corresponding to $\sim^{+3\sigma}_{-2\sigma}$ of the CBS peak. The distribution is dominated by the 477 keV CBS events and can be fitted with a gaussian function plus a small constant background.

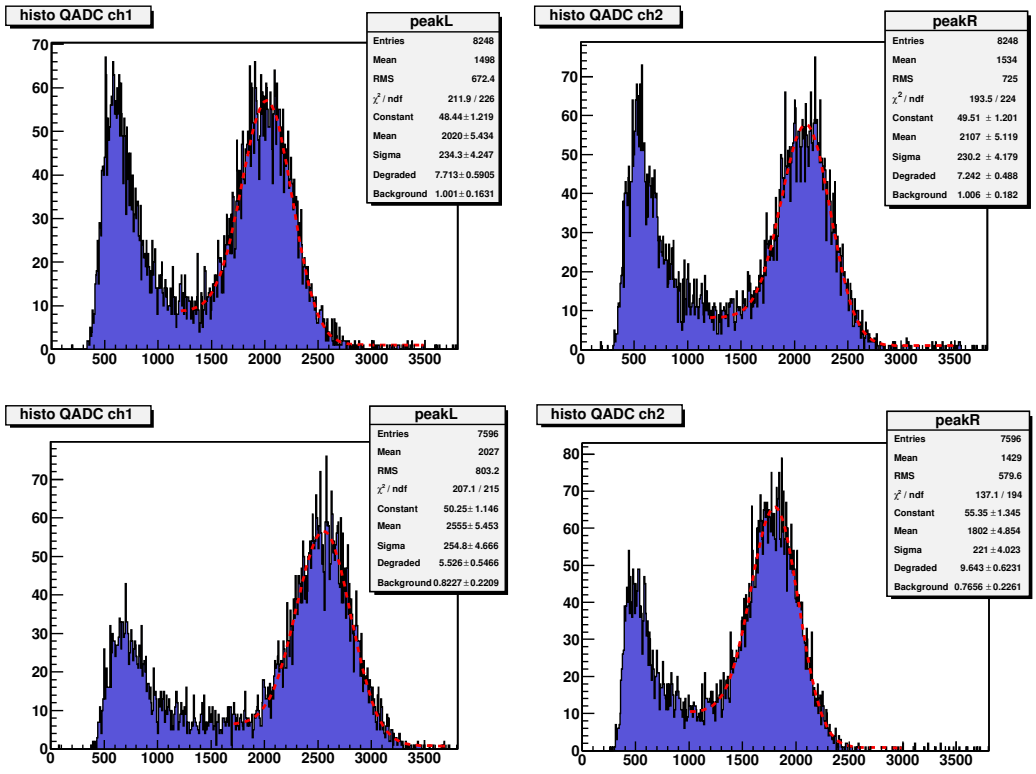

Figure 8.11: ^{137}Cs-*CBS charge spectra measured by each PMT after all cuts described in Fig. 8.10, for two source positions.*
Top: source at the cell center ($d = 50\,cm$ from both PMT).
Bottom: source at $d = 10\,cm$ from the "left" PMT.

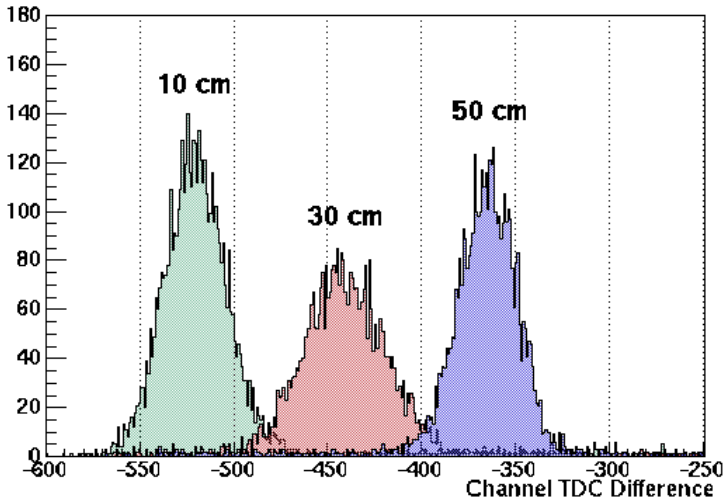

Figure 8.12: *Superposition of the ^{137}Cs-CBS TDC spectra measured at various source positions with the PXE-TIR cell, after all cuts are applied. The source was located at $d = 10\,cm$, $30\,cm$ and $50\,cm$ from the "left" PMT.*

via differential time-of-flight is $\sim 4.5\,cm$ (1σ) and seems to have a weak dependence on the source position.

Single-Photoelectron Calibration The detector energy resolution gives an indication of the PY. If it is assumed that the width of the CBS peak is dominated by the statistical fluctuations in the total number of *pe*, it is found that $\bar{N}_{pe} = 132 \pm 6$ at $477\,keV$. This would translate to $PY = (277 \pm 13)\,pe/MeV$. Repeating the calculation for each PMT leads to $\bar{N}_{pe}^{left} = 63 \pm 2$ and $\bar{N}_{pe}^{right} = 77 \pm 2$. The estimated number of *pe* per PMT is statistically compatible with the energy resolution of the sum spectrum. However the energy resolution of each PMT may contain additional contributions, beside the photoelectron statistics. In order to estimate independently the PY, the system has been calibrated by measuring the response to a single photoelectron. For this measurement the LED has been used.

The light intensity was tuned to a sub-Poisson statistics of *pe* (the mean number of *pe* per LED pulse is $\ll 1$), so that the probability to measure events with more than one *pe* is negligible. The acquisition shown in Fig. 8.5 had to be modified: the trigger for the ADC was synchronized with the external LED-TTL signal, so that the integration gate was opened in coincidence with each expected *pe*. The TDC was disabled, since most of the times the *start* was not followed by any correlated *stop*. The PMT gain set for the cell measurements was too low to permit to study the single-*pe* spectrum, therefore a low-noise $\times 50$ amplification stage has been introduced. The precision of the amplification factor was tested at a digital oscilloscope and was better than 3%. A *high-pass* passive circuit was necessary to filter out the $50\,Hz$ network noise.

The measured spectra are reported in Fig. 8.13. It is observed that the "left" PMT has a bad single-*pe* spectrum, while the "right" PMT exhibits a well-resolved peak. Various attempts to improve the "left" PMT response (by changing HV and connected electronics)

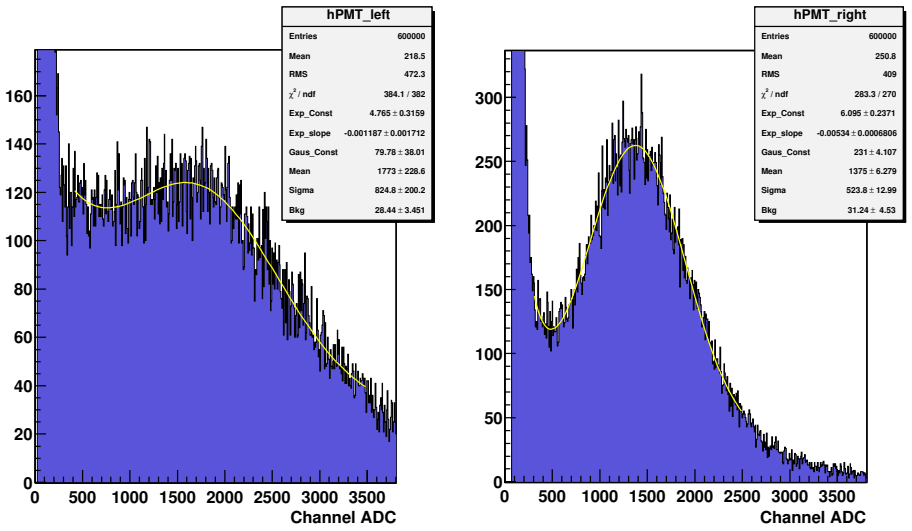

Figure 8.13: *Example of single-pe charge spectra for the two used PMTs. The spectra are fitted with the sum of an exponential plus a gaussian function. The precision of the peak determination is* $\sim 10\%$ *for the "left" PMT,* $\sim 1\%$ *for the right PMT. The signals are amplified of a factor 50 relative to the CBS spectra in Fig. 8.11.*

Table 8.7: *Estimations of the PY for the PXE-TIR cell. Source at the cell center. The column of the single-pe calibration reports the value estimated multiplying by 2 the average number of pe detected by the better calibrated "right" PMT. The MC estimation is the product of the predicted photon detection probability (7.5%) times the scintillator primary LY (*$\sim 10000\, phs/MeV$*).*

resolution (pe/MeV)	single-pe calibration (pe/MeV)	MC (pe/MeV)	Exp/MC
$\gtrsim 280$	~ 330	~ 750	~ 0.44

were unsuccessful. Therefore the precision of the single-pe charge estimation for the "left-side" PMT is poor. The comparison of the single-pe ADC peaks with the results of the CBS charge measurements gives a calibration of the PY at the PMTs: $N_{pe}^{left} = 63 \pm 7$ and $N_{pe}^{right} = 73 \pm 3$. These values are consistent with the evaluations based on the energy resolution. Therefore it can be concluded that at this energy the detector resolution is dominated by the statistical fluctuations of the number of photoelectrons.

Comparison between Experimental and MC PY Table 8.7 summarizes the analysis of the PY based on the CBS measurements and the single-pe calibration, and reports for comparison the predictions of the MC simulation. The disagreement between experimental data and simulation is huge: the MC predicts more than twice as much light than observed. This discrepancy must be understood, since the conclusions of the previous chapter on the feasibility of the LENS concept depend dramatically on the detector energy resolution.

With a rough calculation it can be verified that the MC predictions are reasonable. Let us

consider an event depositing $1\,MeV$ energy in the cell center. About 10000 primary photons are generated. The half is lost after few reflections due to the TIR angular acceptance. The experimental attenuation curve in Fig. 8.7 shows that about 70% of the photons should be able to reach the PMTs from a distance of $50\,cm$[4]. Here the geometrical photocathode coverage is 66%. The PMT QE is $\sim 27\%$ in air at normal incidence. However many effects should increase the effective PMT sensitivity: optical coupling, higher photocathode absorption above the critic angle (see Fig. 5.16), collection of the photons reflected from the opposite side. For simplicity, it can be assumed $QE = 30\%$.

It follows that the approximate number of expected photoelectrons is: $N_{pe} \sim 10000 \times 0.5 \times 0.7 \times 0.66 \times 0.3 \sim 700$, very close to the MC prediction.

This fundamental question will be addressed again in Sec. 8.6, after the results of all the other measurements will be presented.

8.4.2 TIR Cell with VM2000 Wrapping

After completion of the sets of measurements reported in the previous section, the cell has been wrapped in a VM2000 profile. The VM2000 comes from the same batch of the samples characterized in Chapter 4.

Light Attenuation The transparency of the VM2000 at $380\,nm$ is very poor, therefore the light attenuation curve could not be measured with the external LED. The cell has been irradiated with the ^{137}Cs source and the trigger coincidence level switched to 2. This condition selects all the events in the cell above threshold ($\sim 100\,keV$) and the rate is dominated by the source Compton spectrum. The ADC position of the Compton "edge" is used as an estimator of the relative light intensity. Some examples of ^{137}Cs Compton spectra acquired during the measurement of the light attenuation curve are shown in Fig. 8.14.

The precision achievable with the estimation of the light intensity from the Compton-edge position is lower than for the LED. However the detector has sufficiently good energy resolution to produce a clear peak around the Compton-edge, whose position is estimated with $\sim 1\%$ error through a fit with a pseudo-gaussian function. The light attenuation curves deduced from a Compton scan along the cell are shown in Fig. 8.15.

The measurements of the two PMTs are in slight disagreement in the initial part of the curves. A left-right asymmetry was not observed in the previous measurement and is not found with the indium samples, either (see later). It is possible that this disagreement is due to a slow drift of the gain of one PMT. The curves are however in good agreement for $d > 40\,cm$, which is the range that gives the asymptotic light attenuation in the cell.

The predictions of two MC simulations are also plotted in the figure. The simulations have the same assumptions and input parameters as in the previous section, except for light piping, which is now possible either via TIR and via SR. Two limit cases are shown in the figure, which are defined in Sec. *6.5* ("TIR or SR" and "TIR and SR").

The analysis of the curves is reported in Table 8.8. The experimental average asymptotic attenuation length is $(4.2 \pm 0.3)\,m$, significantly better than that measured with TIR alone.

[4]It must be noted that the fast decay at very short distances ($d < 5\,cm$) is dominated by the loss of the solid angle for direct illumination of the PMT. This fast decay component is not present when the source is at $50\,cm$ distance. The 0.70 transport efficiency is estimated from the ratio of the experimental attenuation curves at $5\,cm$ and $55\,cm$.

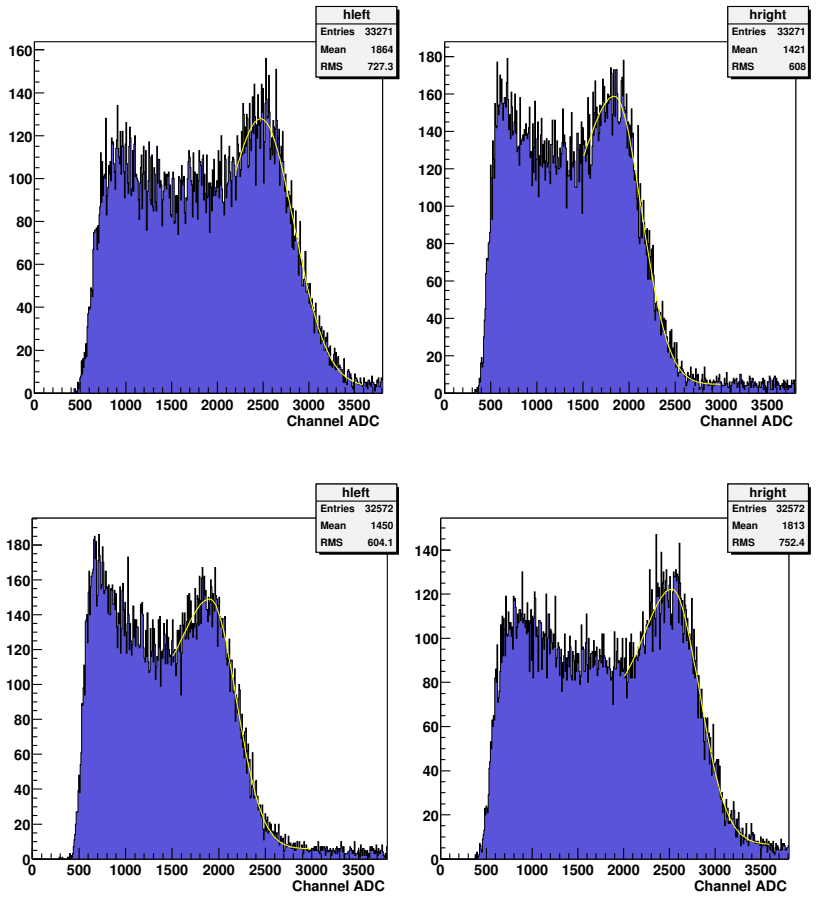

Figure 8.14: *Compton spectra from irradiation with a ^{137}Cs source in the PXE TIR+VM2000 cell. The background has been reduced with a $\pm 2\sigma$ cut on the TDC.*
Top: source at $d = 5.0\,cm$ from the "left" PMT.
Bottom: source at $d = 95.0\,cm$ from the "left" PMT.

Table 8.8: *Parameters returned by a double exponential fit to the experimental data and the simulation of Fig. 8.15.*

	$\mu_{short}\,(cm)$	W_{short}	$\mu_{long}\,(cm)$	W_{long}
LED "Left" PMT	13.2	0.075	417 ± 20	0.925
LED "Right" PMT	20.4	0.123	441 ± 68	0.877
LED Average	16.2	0.094	418 ± 29	0.906
^{137}Cs-CBS	/	/	386 ± 32	~ 1
Simulation "TIR or SR"	16.6	0.079	316 ± 7	0.921
Simulation "TIR and SR"	14.8	0.050	375 ± 13	0.950

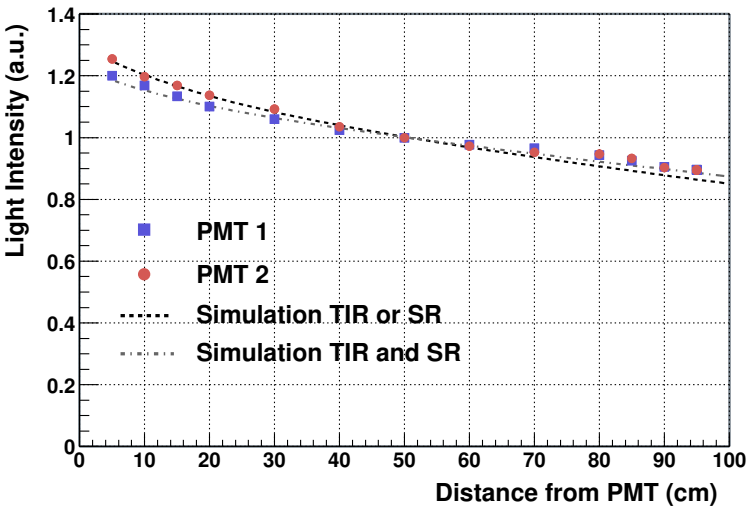

Figure 8.15: *Light attenuation curves for the PXE cell, TIR piping plus VM2000 wrapping. The markers represent the data points, the curves are simulations of the system for the two limit cases discussed in Sec. 6.5. Data and simulations are arbitrarily normalized to 1 at* $d = 50\,cm$ *(cell center). The data points have a statistical error from the estimation of the Compton-edge of* $\sim 1\%$.

This result disfavors the "TIR or SR" scenario, namely that light lost by TIR piping above the critic angle is not recovered by the VM2000. Intuitively, if this was the case, the effective attenuation length should not improve, because the VM2000 simply pipes light that would have been lost by TIR, however with a lower efficiency than TIR. This is confirmed by the MC, which predicts a similar μ_{long} as for TIR alone. Even the MC calculation for the limit case in which the effective reflectivity above the critic angle is 99.99% (the VM2000 recovers the 0.6% measured TIR inefficiency) gives a slightly worse performance than measured, though compatible within the errors. A significant underestimation of the TIR reflection coefficient or of the scintillator transparency seems to be excluded by the good agreement between data and MC in the TIR cell. A possibility is that the VM2000 reflectivity is slightly underestimated. For instance, a simulation with $\bar{R}_{VM2000} = 98.7\%$ and ideal "TIR and SR" predicts $\mu_{long} = (418 \pm 7)\,cm$.

CBS measurements The ^{137}Cs ADC and TDC CBS spectra after all cuts are displayed in Fig. 8.16, for the base case of source in the cell center.

The analysis of the ADC and TDC peaks is presented in Table 8.9. The last row reports the results of a ^{54}Mn run carried out with the source irradiating the cell center. The energy resolution is $(5.2 \pm 0.15)\%$ at $477\,keV$ and $(4.6 \pm 0.15)\%$ at $639\,keV$. The former corresponds to a limit $PY = (775 \pm 25)\,pe/MeV$, the latter to $PY = (740 \pm 25)\,pe/MeV$.

The TDC scale was calibrated with the Compton scan. The standard deviation of the TDC distribution for the ^{137}Cs CBS events translates to a spatial resolution of $(3.2 \pm 0.2)\,cm$ at the cell center. In the other positions the spatial resolution is slightly worse, as also observed in the TIR measurement. The spatial resolution measured with the ^{54}Mn should be better than the ^{137}Cs one, because more photoelectrons are detected. The opposite is observed and this

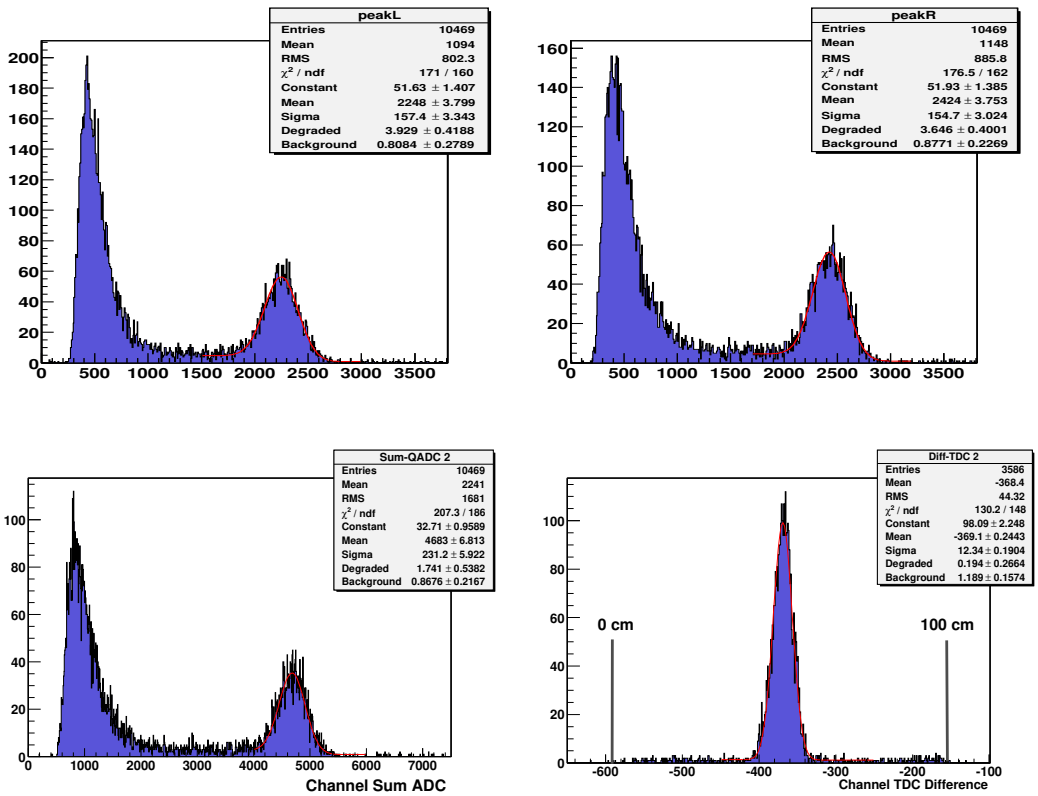

Figure 8.16: *CBS spectra for the PXE cell with VM2000, ^{137}Cs source at cell center.*
Top: final CBS ADC spectra measured for each PMT, after the off-line background cuts.
Bottom left: Corresponding Sum-ADC spectrum.
Bottom right: TDC spectrum for all the events in the CBS energy window. For comparison, the approximate TDC channels corresponding to the position of the ends of the cell are indicated by the two vertical segments.

Table 8.9: *Analysis of the CBS measurements with the TIR-VM2000 PXE cell. The relative $\pm 1\sigma$ error of the energy resolution is $\pm 2\%$ for the single PMT, $\pm 3\%$ for the sum. For the spatial resolution it is $\pm 1.5\%\,(stat) \pm 5\%\,(sys)$, where the systematic error derives from the uncertainty in the channel-to-distance scale.*

Energy (keV)	Distance from PMT 1 (cm)	σ_E PMT 1 (%)	σ_E PMT 2 (%)	σ_E Sum (%)	σ_x (cm)
477	10	7.0	7.2	5.4	4.1
477	30	7.3	6.9	5.2	4.0
477	50	7.5	6.7	5.2	3.2
639	50	6.6	5.5	4.6	3.6

Table 8.10: *Estimations of the PY for the PXE-TIR cell. Source at the cell center.*

resolution (pe/MeV)	single-*pe* calibration (pe/MeV)	MC "TIR or SR" (pe/MeV)	MC "TIR and SR" (pe/MeV)	Exp/MC
$\gtrsim 760$	~ 720	~ 1740	~ 1920	$\sim 0.40 - 0.44$

is an indication that the systematic uncertainty of σ_x might be worse than the estimated 5%.

The single-*pe* calibration of the ADC amplitude gives an average of $\sim (172 \pm 5)\, pe/PMT$ at $477\, keV$, translating to $PY = (720 \pm 20)\, pe/MeV$. Therefore energy resolution and single-*pe* calibration are also in this case in agreement with each other, within the errors. Table 8.10 summarizes the analysis of the PY. Also in this case the absolute output of the MC prediction is a factor > 2 higher than the experimental result.

It can be concluded that in the PXE benchmark case the prototype cell with VM2000 wrapping collects more than twice as much light as the same cell with no reflective foils. This is an experimental evidence that the VM2000 serves not only to pipe the light outside the TIR acceptance, but also compensates the non ideal performance of the quartz cell. If this was not the case, the ratio PY_{TIR+SR}/PY_{TIR} would have 2 as an upper limit, since in the ideal case about 1/2 of the total solid angle is covered by TIR. Also this effect is well understood with the MC: in an ideal geometry $PY_{TIR+SR}/PY_{TIR} < 2$ (cf. Fig. 7.5, where the simulations are calculated for an ideal square geometry), however in a real cell this ratio can be > 2, because of the recovering of the light lost at the cell rounded corners (see Fig. 7.6 and relevant discussion). In this specific case, the MC predicts $PY_{TIR+SR}/PY_{TIR} \sim 2.3 - 2.6$ (cf. Tables 8.7 and 8.10), depending on the chosen mixed-piping scenario. The experimental value is $PY_{TIR+SR}/PY_{TIR} \sim 2.3$, where for both measurements the highest estimation of the PY between energy resolution and photoelectron calibration was chosen.

8.5 Measurements of Indium-Loaded Prototype Cells

The measurements with PXE have shown that the prototype cell works properly and that the VM2000 wrapping increases the photoelectron efficiency of more than a factor 2, as also predicted by the simulations. Consequently this design was also chosen for the indium measurements.

8.5.1 Scintillator Samples

Several hundreds grams of $In(acac)_3$ crystals have been synthesized and purified by sublimation in our chemical laboratory at MPIK, for use in this optical measurements and for loading in the final LENS prototype at Gran Sasso. The base organic solvent, anisole, was also purified from an initial spectrophotometric attenuation length of $\sim 5\, m$ at $430\, nm$ to $\sim 9\, m$.

Three scintillator samples have been measured in the prototype cell. They have been prepared by subsequent additions of components to a common base:

1. Anisole + $In(acac)_3$ (Indium $20\, g/l$) + BPO ($27\, g/l$) + bis-MSB ($50\, mg/l$)
2. Anisole + $In(acac)_3$ (Indium $44\, g/l$) + BPO ($47\, g/l$) + bis-MSB ($50\, mg/l$)

Table 8.11: *Attenuation lengths at various wavelengths for the measured $In(acac)_3$ scintillator samples. The "Indium $44\,g/l$ - I" row refers to the $50\,mg/l$ bis-MSB sample, the "Indium $44\,g/l$ - II" to the $100\,mg/l$ sample.*

$\lambda(nm)$		380	400	410	420	430	440	450	500
	Indium $20\,g/l$	0.09	0.99	13	76	140	170	200	540
$\mu(cm)$	Indium $44\,g/l$ - I	0.08	0.93	12	55	88	110	130	340
	Indium $44\,g/l$ - II	0.05	0.50	6.6	43	83	110	130	340

3. Anisole + $In(acac)_3$ (Indium $44\,g/l$) + BPO ($47\,g/l$) + bis-MSB ($100\,mg/l$)

The measurement of the first sample aims at studying the cell performance in the lowest limit of the indium loading range that is considered interesting for a solar neutrino detector. Since less $In(acac)_3$ is dissolved, the quenching is reduced and hence the concentration of BPO can also be lowered, thus improving the scintillator transparency. This sample has a primary photon yield of $\sim (44 \pm 2)\%$ relative to BC505. The latter has an absolute LY of $\sim 12000\,ph/MeV$, hence our sample is estimated to have a primary light output of $\sim 5300\,ph/MeV$.

The samples 2 and 3 have the indium loading targeted by LENS and are the base case for the pilot phase. The BPO concentration was chosen as the best compromise between primary LY and final scintillator transparency, based on the results of the MC studies presented in Sec. 8.2. Two bis-MSB concentrations have been tested, to better understand the dependence of the detector performance on the WLS concentration, after the first indications from the small cell. The LY of both samples is $(42 \pm 2)\,\%$ of BC505, translating to $\sim 5000\,ph/MeV$.

Table 8.11 reports the attenuation lengths calculated from the spectrophotometric determinations of the extinction coefficients of each component of the mixture. The attenuation-length spectra for a specific case with similar composition as our sample 2 was shown in Fig. 8.2. The direct spectrophotometric measurement of the attenuation lengths in the final scintillation mixture are in good agreement with the values reported in the table. More details about the sample preparation, LY and spectrophotometric measurements are given in ref. [Buc04].

The simulations reported in this section are based on the same general assumptions discussed for PXE and use each time the attenuation lengths relevant to the specific sample. The optimistic "TIR and SR" light piping is assumed, because the PXE measurements have shown that this model gives the best effective description of the cell performance in the limit of very low attenuation in the scintillator.

8.5.2 20 g/l Indium Cell

Light Attenuation The estimation of the Compton edge position from the pseudo-gaussian fit used for the PXE cell is less easy with the indium cell, due to the lower energy resolution. The Compton edge smears into a shoulder and no clear peak can be distinguished. However, the position of the Compton shoulder is not a good absolute reference, because it depends on the energy resolution. When the source is distant from the PMT the energy resolution is worse and the shoulder appears further shifted to lower amplitudes.

The systematic error introduced by this smearing effect has been experimentally measured. The CBS peak position has been compared with an estimation of the Compton edge position,

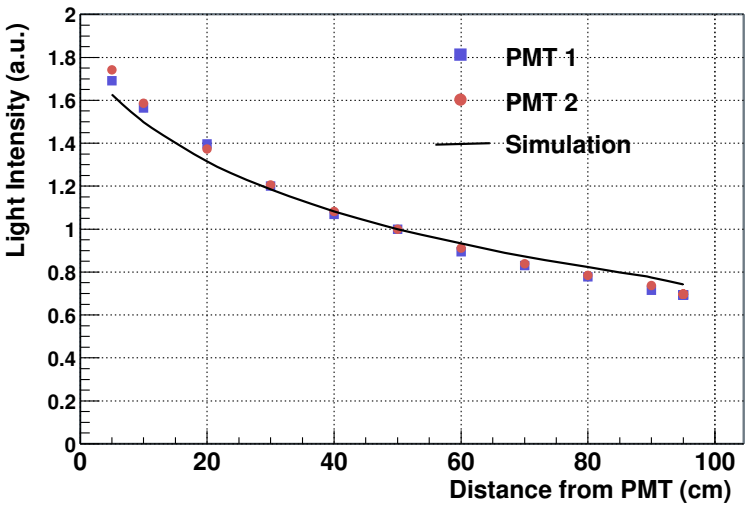

Figure 8.17: *Light attenuation curve for the Indium-loaded cell (In* $20\,g/l$*). The markers represent the data points, the solid line is a simulation of the system. Data and simulation are arbitrarily normalized to 1 at* $d = 50\,cm$ *(cell center). The data points have a statistical error of* $\sim \pm 0.01$ *in the arbitrary units of the graphics. The errors due to systematic drifts of the electronics gain during the measurement is estimated to be* $\sim \pm 2\%$.

obtained by fitting the shoulder of the spectrum with a pseudo-gaussian function (as done with PXE in Fig. 8.14). With the ^{137}Cs source at $5\,cm$ distance from the PMTs, the ratio of the amplitude of the Compton shoulder to the CBS-peak position is $ADC_{Sh}/ADC_{CBS} = 0.90 \pm 0.01$ for both PMTs. At $95\,cm$ it is $ADC_{Sh}/ADC_{CBS} = 0.78 \pm 0.02$ for the "left" PMT and 0.83 ± 0.02 for the "right" PMT. This shows that the Compton shoulder has a systematic "shift" with respect to the fixed CBS energy.

This problem can be solved by fitting the spectrum with a better function, for example with the convolution of the theoretical Compton spectrum with an energy resolution function. However it was believed that a simpler and safer solution was to perform the cell scan with a CBS measurement. The disadvantage of this method is that the trigger rate of events in the CBS window was only $3\,Hz$ with our set-up (the source activity was $\sim 2 \times 10^4\,Bq$). However, the CBS peak is nearly symmetric and hence the centroid of the distribution can be evaluated with good precision even with a limited statistics. About 20 minutes per position were necessary to determine the ADC and TDC peak positions with $\sim 1\%$ accuracy.

The results of the CBS scan are shown in Fig. 8.17, together with the MC-predicted light attenuation curve. The two PMTs are in good agreement with each other. The data are in reasonably good agreement with the simulation, however the differences seem larger than in the PXE measurements. In particular, the simulation predicts a less fast light attenuation either at short and at long distances, i.e. an overall slightly better performance.

This might be due to the fact that this cell was filled too much, up to the level of the stoppers. A little amount of anisole has come out of the cell, due to capillary forces, and has corroded part of the VM2000 foils. Unfortunately this accident was discovered only a few weeks after filling, when the cell was emptied and refilled with the next sample. It was

Table 8.12: *Parameters returned by a double exponential fit to the experimental data and the simulation of Fig. 8.17.*

	$\mu_{short}\,(cm)$	W_{short}	$\mu_{long}\,(cm)$	W_{long}
^{137}Cs-CBS average	23.1	0.282	154 ± 17	0.718
Simulation "TIR and SR"	16.5	0.202	161 ± 3	0.798

Table 8.13: *Analysis of the ^{137}Cs CBS measurements with the $20\,g/l$ Indium cell. The relative $\pm 1\sigma$ error of the energy resolution is $\pm 3\%$ for the single PMT, $\pm 2.5\%$ for the sum. For the spatial resolution it is $\pm 2\%\,(stat) \pm 5\%\,(sys)$, where the systematic error derives from the uncertainty in the channel-to-distance scale.*

Distance from PMT 1 (cm)	σ_E PMT 1 (%)	σ_E PMT 2 (%)	σ_E Sum (%)	σ_x (cm)
50	14.4	13.0	10.4	6.7
75	17.4	11.4	10.0	6.7

possible to reconstruct the degradation process of the VM2000 *a posteriori*, by analyzing the cell performance as a function of the time. The PY had a fast downward drift of $\sim 15\%$ in the first few days and then stabilized after one week. Concerning the light attenuation curve, two measurements have been carried out: a fast Compton scan immediately after the prototype connection, and the CBS scan reported in the figure after three days, when a clear gain drift had already occurred. The results of the first Compton light attenuation scan, though less precise, are consistent with the later CBS scan. However, it cannot be excluded that the original cell light attenuation was slightly better.

The results of the analysis of the experimental and simulated curves are given in Table 8.12.

CBS Measurements The energy and spatial resolutions measured with the ^{137}Cs CBS peak for two source positions are given in Table 8.13. Due to the problems discussed above, only the data acquired in the first day of measurements are presented.

The limit PY at the cell center corresponding to the measured energy resolution is $PY = (195 \pm 5)\,pe/MeV$. The single photo-electron calibration gives $PY = (230 \pm 10)\,pe/MeV$. These results and the MC prediction are summarized in Table 8.14.

The light at the cell center is less than 1/3 of PXE. The difference of LY gives a factor 1/2 and the lower scintillator transparency explains the rest. In fact, the MC predicts a similar ratio as observed.

8.5.3 44 g/l Indium Cell

The results of the two measured samples ($50\,mg/l$ and $100\,mg/l$ bis-MSB concentration) will be reported and commented together.

After the experience of the previous sample, it was payed particular attention not to fill the cell up to the stopper level. The ADC response to the ^{137}Cs CBS line was continuously

Table 8.14: *Estimations of the PY for the 20 g/l indium cell. Source at the cell center. The MC estimation is the product of the predicted photon detection probability ($\sim 11.2\,\%$) times the scintillator primary LY ($\sim 5300\,ph/MeV$).*

resolution (pe/MeV)	single-pe calibration (pe/MeV)	MC (pe/MeV)	Exp/MC
$\gtrsim 195$	~ 230	~ 590	~ 0.39

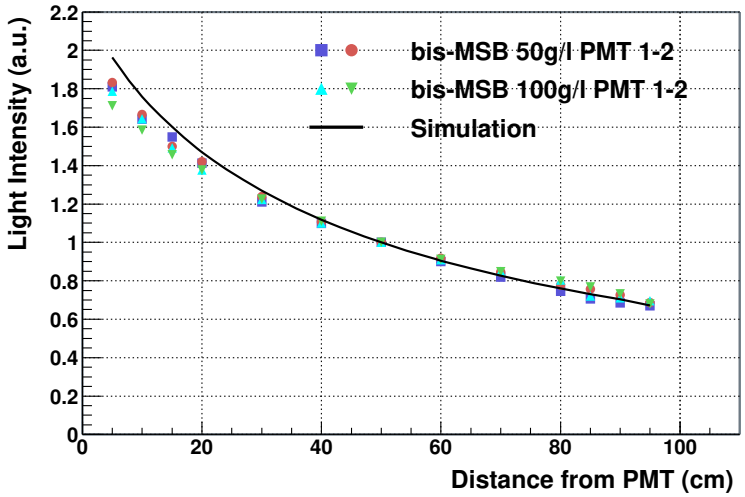

Figure 8.18: *Light attenuation curves for the 44 g/l indium cell, for both measured samples. The markers represent the data points, the solid line is a simulation of the system. For simplicity, only the simulation for one sample is shown, because the MC predicts no significant differences in the attenuation curves of the two samples. Data and simulation are arbitrarily normalized to 1 at $d = 50\,cm$ (cell center). The data points have a statistical error of $\sim \pm 0.01$ in the arbitrary units of the graphics. The drifts of the electronics contribute another $\sim \pm 2\%$ error.*

monitored on both samples for several days and no significant drifts were observed.

Light Attenuation Also in this case the light attenuation curves have been measured with CBS scans. Results are shown in Fig. 8.18.

No significant differences are observed in the attenuation of the two samples. The simulation reproduces very well the asymptotic behaviour of the experimental curves, whereas it predicts a slightly faster light attenuation at $d \lesssim 30\,cm$. This means that this prototype system performs better than expected at short distance, and as expected at long distance.

Table 8.15 reports the fit parameters of experimental and simulated attenuation curves.

The experimental finding that the two samples exhibit very similar attenuations is also predicted by the MC.

The higher μ_{long} of the simulations seems to contradict the visual comparison with data. The reason is that the two attenuation lengths considered are not very different and therefore

Table 8.15: *Parameters returned by a double exponential fit to the experimental data of Fig. 8.18 and the relevant simulations.*

	$\mu_{short}\,(cm)$	W_{short}	$\mu_{long}\,(cm)$	W_{long}
^{137}Cs-CBS average bis-MSB (50mg/l)	18.0	0.253	128 ± 3	0.747
^{137}Cs-CBS average bis-MSB (100mg/l)	15.7	0.203	128 ± 4	0.797
Simulation bis-MSB (50mg/l)	20.9	0.342	142 ± 3	0.658
Simulation bis-MSB (100mg/l)	20.0	0.327	139 ± 3	0.673

Table 8.16: *Analysis of the CBS measurements with the $44\,g/l$ indium cell. Measurement at the cell center. The relative $\pm 1\sigma$ error of the energy resolution for the ^{137}Cs (^{54}Mn) measurements is $\pm 1.5\%$ ($\pm 3\%$) for the single PMT, $\pm 1\%$ ($\pm 2.5\%$) for the sum. For the spatial resolution it is $\pm 1\%\,(stat) \pm 5\%\,(sys)$, where the systematic error derives from the uncertainty in the channel-to-distance scale.*

Bis-MSB (mg/l)	Energy (keV)	σ_E PMT 1 (%)	σ_E PMT 2 (%)	σ_E Sum (%)	σ_x (cm)
50	477	18.4	15.6	11.8	7.2
50	639	14.3	12.5	9.9	6.5
100	477	18.6	15.3	11.6	7.0

they are strongly correlated parameters in the fit. The fit to the simulations requires a larger weight for the short component to reproduce the first part of the curve. However μ_{short} is sufficiently long to give a significant tail at longer distances. Therefore the fit needs a slightly longer μ_{long} for the simulations than for data. It can be observed that the opposite happened in the analysis of the $20\,g/l$, where μ_{long} of data and simulation are similar, though the MC was visually superior.

This discussion shows that the analysis based on the double exponential fit is a useful tool, but can be misleading if a single fit parameter is used to describe the global performance of the system.

CBS Measurements The results of the analysis of the ^{137}Cs and ^{54}Mn CBS runs are reported in Table 8.16. There is a weak indication that the sample at higher bis-MSB concentration gives better energy and spatial resolutions. The results are however compatible within the errors.

Fig. 8.19 shows the ADC and TDC spectra of a high statistics run with the $100\,mg/l$ bis-MSB sample.

The estimations of the PY are given in Table 8.17. The values derived from the single-*pe* calibrations are in this case significantly higher than those based on the energy resolution. A similar indication is also observed in the $20\,g/l$ indium sample (Table 8.14). It is likely that for low absolute numbers of detected photoelectrons the departure of the energy resolution from the ideal $\frac{1}{\sqrt{N}}$ statistical limit becomes more important. For example, a contribution to the degradation of the energy resolution that certainly increases with decreasing number of

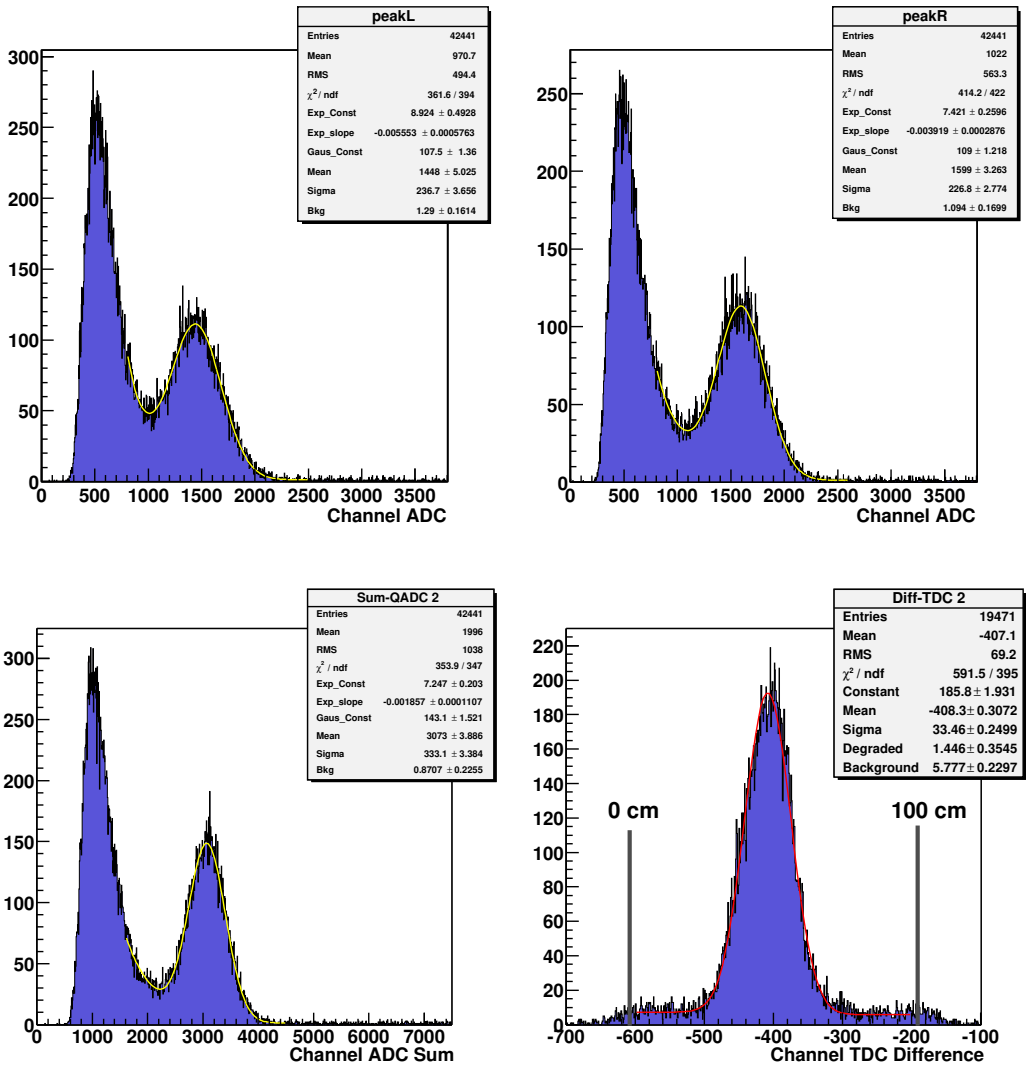

Figure 8.19: *CBS spectra for the 44 g/l indium cell (bis-MSB 100 mg/l), ^{137}Cs source at cell center.*
Top: CBS ADC spectra after cuts, measured for each PMT.
Bottom left: Corresponding Sum-ADC spectrum.
Bottom right: TDC spectrum for all the events in the CBS energy window. For comparison, the approximate TDC channels corresponding to the position of the ends of the cell are indicated by two vertical segments.

Table 8.17: *Estimations of the PY for the measurement of the two 44 g/l indium scintillators. Source at the cell center. The MC estimation is the product of the predicted photon detection probability (∼ 8.75 % and ∼ 8.90% for 50 mg/l and 100 mg/l bis-MSB, respectively) times the scintillator primary LY (∼ 5000 phs/MeV for both samples).*

Sample (bis-MSB mg/l)	resolution (pe/MeV)	single-pe calibration (pe/MeV)	MC (pe/MeV)	Exp/MC
50	$\gtrsim 150$	~ 190	~ 440	~ 0.43
100	$\gtrsim 155$	~ 200	~ 450	~ 0.44

photoelectrons is the width of the single-pe charge distribution (Fig. 8.13).

The measurements of the PY and of the light attenuation curve are brought together in Fig. 8.20, which shows the absolute detector performance as a function of the source position.

In Fig. 8.21 the CBS spectra of two runs of similar statistics are superimposed, one with the ^{137}Cs source, the other with ^{54}Mn (sample with $50\,mg/l$ bis-MSB). The figure gives an idea of how well the MPIK LENS prototype would energetically resolve a typical hard-Bremsstrahlung event (similar energy as the ^{137}Cs CBS recoil electron) from the delayed ν-tag ($E = 613\,keV$). The efficient resolution of these two events is the crucial parameter for the feasibility of the LENS experiment, as discussed in Sec. 2.4.3. With the results presented in this chapter for the MPIK high-indium-loading prototype, those two energies are $\sim 1.5\,\sigma$ apart.

8.6 Summary and Discussion

Summary In this chapter the results of experimental investigations of the optical performances of LENS prototype cells have been reported.

In Sec. 8.2 preliminary MC and experimental studies are discussed. This work has prepared the final prototype phase, by selecting the optimal area in the composition parameter space of In-acac scintillators developed at MPIK. In Sec. 8.3 the experimental set up and the methods employed for the measurements of prototype cells have been described. Our prototype system has been first characterized with a benchmark PXE-based scintillator. The experimental technique and the analysis procedures have been developed and tested with this sample. The results, reported in Sec. 8.4, have shown that notable photoelectron yields and light attenuation lengths are achievable with this prototype system. In Sec. 8.5 the results obtained with indium-loaded scintillators developed at MPIK have been given. Three samples have been measured, differing by indium loading and fluors concentration.

The main results of this chapter are summarized in Table 8.18. The prototype detector with indium loadings of interest for LENS has given energy resolutions of $10 - 12\%$ at $\sim 500\,keV$ and asymptotic attenuation lengths in the range of $1.3 - 1.5\,m$. The estimated PY was $\sim 190 - 230\,pe/MeV$.

In Fig. 8.22 all the measurements of spatial resolution have been displayed as a function of the number of photoelectrons. The spatial resolution can be parametrized by a function $\sigma_x \sim \frac{k}{\sqrt{N_{pe}}}$, where N_{pe} is the number of photoelectrons and k a constant. The fit gives $k \sim 65$.

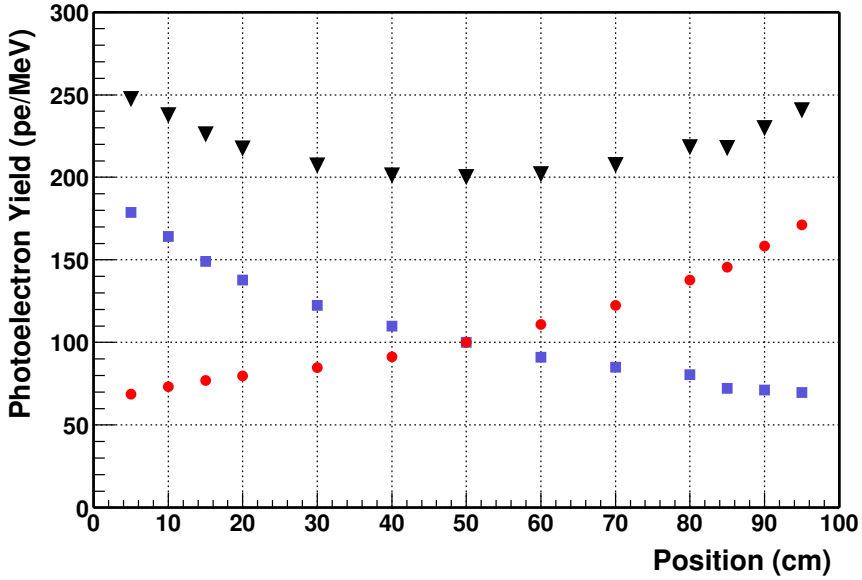

Figure 8.20: *PY as a function of the source position for the 44 g/l MPIK indium prototype cell. Ordinates are given in absolute number of photoelectrons per MeV of deposited energy. The attenuation curves for both PMTs (square and circular markers) and the sum of the charges (triangular markers) are shown. The conversion factor is assumed such that at the cell center* $PY \simeq 200\, pe/MeV$*, as calculated from the single-pe calibration (Table 8.17).*

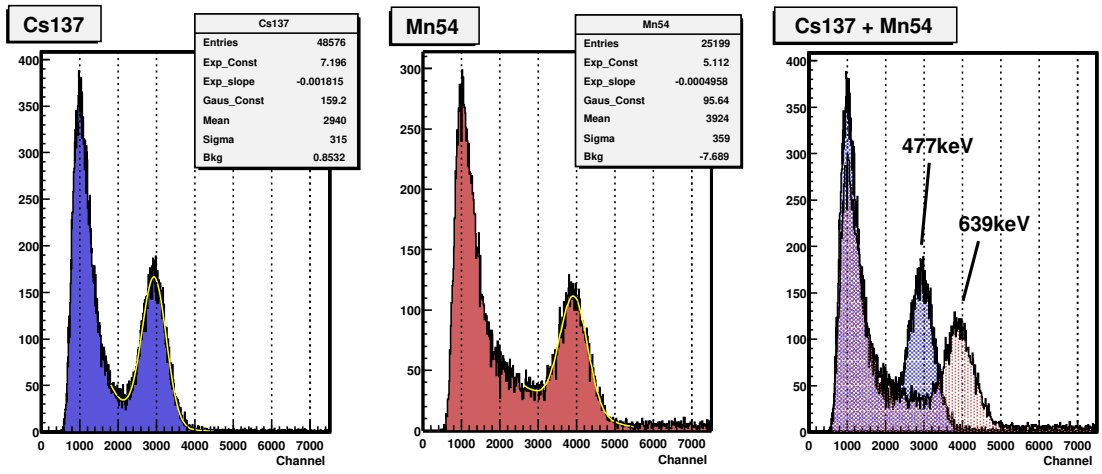

Figure 8.21: *Resolution of two spectral lines with the MPIK LENS prototype (indium 44 g/l).*

Table 8.18: *Summary of the main results of the optical measurements of LENS prototypes carried out at MPIK. The measured samples are described in Secs. 8.4 and 8.5.1. TIR means that light is piped via total internal reflection. "TIR+SR" describes a cell where light escaping TIR is recovered by external uncoupled mirror foils. W_l is the weight of the long-range attenuation component, μ_l, at $5\,cm$, for a double exponential fit of the light attenuation curve. μ_l^{MC} is the long attenuation length of the curve predicted by our photon-tracing simulation. $\sigma_E^{477\,keV}$ and $\sigma_x^{477\,keV}$ are energy and spatial resolutions measured at the energy of the ^{137}Cs CBS recoil electron. PY is the total photoelectron yield at the PMTs and $\frac{PY_{exp}}{PY_{MC}}$ the ratio of the experimental to the predicted yields. The errors of the parameters are evaluated in the relevant sections.*

Scintillator	Light Piping	W_l	μ_l (m)	μ_l^{MC} (m)	$\sigma_E^{477\,keV}$ $(\%)$	$\sigma_x^{477\,keV}$ (cm)	PY (pe/MeV)	$\frac{PY_{exp}}{PY_{MC}}$
PXE	TIR	0.89	2.9	3.3	8.7	4.4	330	0.44
PXE	TIR + SR	0.91	4.2	3.2 - 3.8	5.2	3.2	760	0.40 - 0.44
In $20\,g/l$	TIR + SR	0.72	1.5	1.6	10.4	6.7	230	0.39
In $44\,g/l$ -I	TIR + SR	0.75	1.3	1.4	11.8	7.2	190	0.43
In $44\,g/l$ -II	TIR + SR	0.80	1.3	1.4	11.6	7.0	200	0.44

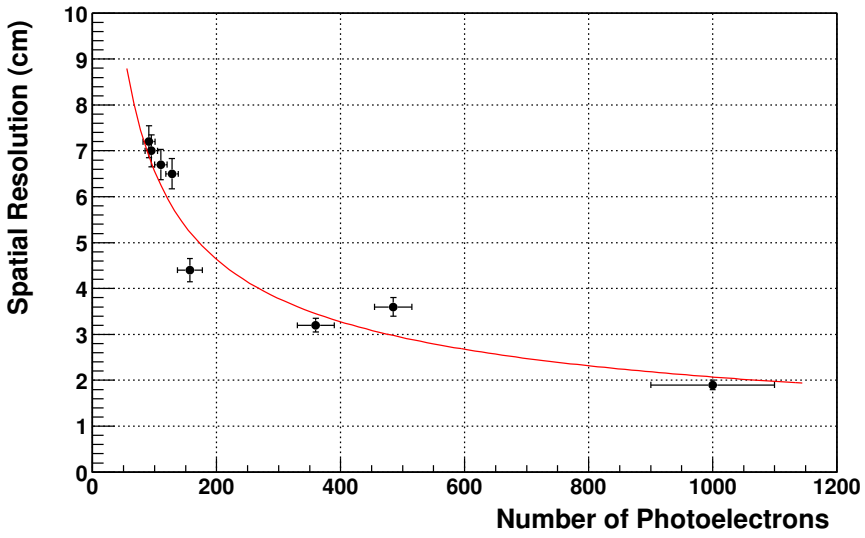

Figure 8.22: *Experimental spatial resolution as a function of the total number of detected photoelectrons. Each marker represents one of the measurements reported in this chapter. All the CBS data with ^{137}Cs and ^{54}Mn have been used. The last data point on the right side of the graphics is the LED measurement, where the number of photoelectrons has been tentatively deduced from the ADC peak width. The solid line is a fit with the function $f(N_{pe}) = \frac{65.5}{\sqrt{N_{pe}}}$.*

The scatter of the data with respect to the fit function is big, however the parametrization gives a useful "rule of thumb" to predict the time-of-flight energy resolution of a LENS cell for a wide range of cases, with better than 20% precision.

Comparison with Previous Measurements The results presented in this chapter can be compared with a previous experimental work published in 1990 [Suz90]. The authors have synthesized an In-loaded scintillator, filled a test cell and measured its optical performance.

The scintillator consisted of an emulsion of an In inorganic salt (indium trichloride tetrahydrate) in the organic scintillating solvent. About 30% of the mass consisted of a surfactant, which had the capability to mix the inorganic polar part with the non-polar organic scintillator. Loading of up to 7.5% were possible.

This scintillator has been loaded in a prototype cell and measured with a very similar technique as the one described in this chapter. The cell was a quartz cylindrical tube $1\,m$ long and $5\,cm$ in diameter. Two $2''$ PMTs were coupled to both ends. The CBS technique with a ^{137}Cs source was implemented to measure the attenuation length, the energy resolution and the spatial resolution of the prototype.

With 5% In loading by weight, the authors report:

- $LY \sim 52\%$ relative to the unloaded scintillator
- $\mu_{long} \sim 155\,cm$
- $\sigma_E(477\,keV) \sim 11.7\%$
- $\sigma_x(477\,keV) \sim 4.5\,cm$

The paper does not describe the details of the light piping, however it seems that TIR only was used.

In this work it was shown that a cylindrical cell operated with TIR piping is not the best choice to optimize the detector energy resolution (Fig. 6.1). Furthermore, it has been demonstrated by MC and as well experimentally that the use of reflective foils strongly enhance the light collection efficiency. On the other hand, a cylindrical cell has a volume-averaged better TIR acceptance than a square cell and the surface match with the PMTs is better. However, even taking the latter arguments into consideration, we believe that our prototype system gives better intrinsic optical performances. It is then difficult to explain why the energy resolutions in the two detectors are the same.

Discussion on the PY The last column of Table 8.18 reminds us that more than a factor 2 of light is missing, according to the MC predictions. In Sec. 8.4.1 it was shown with an approximate calculation that the MC cannot be wrong of a factor 2, unless some of the assumptions of the model that have not been verified experimentally are wrong. The fact that the simulations reproduce reasonably well the experimental light attenuation curves suggests that the discrepancy in the PY is not related to light losses "on the way" to the PMTs. This is corroborated by the observation that the experimental deficit relative to the MC is nearly constant, despite the measured samples are very different from each other.

Two possibilities are conceivable: that the estimated number of primary photons is wrong, or that the detection probability at the PMTs is overestimated (or a combination of both). It

should be considered that the absolute estimation of the scintillator LY relies on the assumption that our BC505 standard gives $LY \sim 12000\,pe/MeV$, which is a very uncertain value (see discussion in [Eli97] and in the footnote on page 145). Similarly, the absolute PMT QE is also a very uncertain coefficient. However, it seems unlikely that even a two-fold overestimation of both parameters can explain a ~ 0.4 reduction factor of the experimental response compared to the predictions.

A reasonable explanation is that the $2''$ PMTs utilized in the cell have an effective photocathode coverage smaller than the specification, or that the PMTs are less sensitive in a broad outer photocathode area, compared to the center. The mean light reduction factor is 0.42 ± 0.02, which would be consistent with an effective sensitive diameter ~ 0.65 of the specification.

Our LNGS-INR colleagues at Gran Sasso have measured an identical quartz prototype cell filled with an indium hydroxy-carboxylate scintillator [INR03]. They have used $3''$ PMTs, which cover completely the cell ends. They report $PY = (1100 \pm 50)\,pe/MeV$. This sample, the PXE standard and a $48\,g/l$ MPIK scintillator have been measured in the LENS prototype array at the LLBF (more details will be given in the next chapter). A relative comparison of the light outputs have given $PY_{LNGS}/PY_{PXE} \sim 0.7$ and $PY_{MPIK}/PY_{PXE} \sim 0.3$ at the prototype center. The latter ratio is consistent with our optical measurements. This means that the LNGS-INR scintillator would give a light output of $\sim 500\,pe/MeV$ in our set-up and $\sim 1200\,pe/MeV$ according to our MC. The error of this estimation is very large, however the combination of our optical measurements with a $2''$ PMT, the optical measurements at Gran Sasso with a $3''$ PMT, and the relative comparison of PXE and In-hydroxy-carboxylate scintillator at the LLBF seems to give a strong evidence that the disagreement between experimental and MC PY in our prototype is explained by a trivial lack of photocathode coverage at the cell ends.

The experimental test of this hypothesis is a fundamental task for the completion of the LENS pilot phase. The PMT that we have used are the same that have been installed in the LLBF prototype array at Gran Sasso (to be described in the next chapter). $2''$ is the proper dimension to pack the cells in a compact matrix. A bigger PMT would require more space between neighbouring cells and a more complicated design. Suitable light concentrators are also under investigation.

8.7 Conclusions

The results of this chapter cover the performance of a LENS prototype cell for a broad range of scintillator compositions. The measurements are consistent with each other and indicate that the In-acac scintillators with loading suitable for LENS, measured in our set-up, give a PY in the range of $200\,pe/MeV$ and an effective asymptotic attenuation length of $\sim 1.3\,m$.

At present, the prototype optical performance measured at MPIK do not meet the original LENS goals, which require better energy resolution ($> 300\,pe/MeV$), to suppress the Bremsstrahlung background, and better attenuation length ($\sim 3\,m$), to build long cells and hence minimize the costs.

The photon-tracing MC simulations developed during this work are found to give a good description of the experimental light attenuation curves. However the absolute predictions of the model are a factor > 2 higher than the measured PY.

In the previous section it has been argued that the "missing light" might be lost at the

PMTs, due to limited photocathode sensitive area. The cross-check of our results with the optical measurements performed at Gran Sasso gives a strong indication in that sense.

The energy resolution is the crucial parameter of the In-LENS concept, therefore the test of this hypothesis is the last experimental missing information to conclude the characterization of the detector optical performance. After this verification, we will be confident to have achieved a full understanding of the performance of a LENS module and to be able to predict reliably the detector response for any chosen geometry and scintillator.

Chapter 9

LLBF: LENS Low Background Facility

9.1 Introduction

The LENS pilot phase aims at testing whether the proposed novel concept for the spectroscopy of low energy solar neutrinos can be implemented in a practical experiment. The goal is to understand whether a detector can be built with sufficient performances to allow a clear identification of the solar signal. At this regard, it is fundamental to investigate experimentally the most critical backgrounds.

The backgrounds for the ^{176}Yb and ^{115}In targets have been investigated during the LENS R&D through MC simulations that assumed various designs and benchmark levels of radiopurity and optical performances. These studies have been carried out at Saclay [Cri01, Mal01, Mey01, Mey02, Mey03], MPIK [Sch00] and as well in this work (Sec. 7.1). However, the final goal of the LENS pilot phase is to measure the most critical backgrounds in a prototype detector, under the most similar conditions as those of the envisaged final experiment.

For this purpose, the MPIK has led the design, construction and installation of the LENS Low Background Facility (LLBF) at the *Laboratori Nazionali del Gran Sasso* (LNGS), in Italy.

9.2 LLBF (LENS Low Background Facility)

9.2.1 Motivations

The LLBF has been conceived as a multi-purpose system with sufficient shielding and enough shielded volume to be usable as a test facility for various ultra-low background applications.

The primary objective of the LLBF was to house a sufficiently large prototype system to simulate a segment of the LENS detector. This implies providing effective shielding from cosmic rays and environmental radioactivity, so that the intrinsic backgrounds of the LENS experiment can be realistically estimated.

For ^{115}In as a ν-target, the crucial issues to address in a ultra-low background environment are:

- Measurement of the ^{115}In β-spectrum, particularly near the $(499 \pm 4)\,keV$ end-point
- Measurement of the ^{115}In β-Bremsstrahlung spectrum in a LENS-like modular detector
- Measurement of the attainable single background rate above the ^{115}In activity

- Simulation of the ν-tag and evaluation of the correlated backgrounds

9.2.2 Design

Requirements The suppression of the cosmic ray flux and related direct and induced backgrounds imposes the choice of an underground location. The LNGS rock overburden ensures a $\sim 10^6$ reduction of the cosmic muons (residual flux: $1.1\,\mu/h/m^2$ [MAC99]).

The LLBF design strategy was to build a passive shielding to provide:

1. a factor $\gtrsim 10^6$ reduction against the external $2615\,keV$ ^{208}Tl gamma[1].
2. a strong shielding against ambient neutrons
3. a tight sealing to prevent the diffusion of radioactive noble gases (in particular ^{222}Rn) from the ambient air, and a N_2 flushing system to continually purge the inner volume

The shielding materials are also sources of background, therefore they need to be carefully selected upon screening of their contamination in natural radioactive isotopes.

The shielded volume must be large enough to house an array of prototypes and possibly a surrounding calorimetric and anti-coincidence system.

Implementation The final LLBF facility is shown in Fig. 9.1. It is a three-layer passive shielding with $190\,cm \times 190\,cm \times 520\,cm$ external dimensions and a shielded volume of $70\,cm \times 70\,cm \times 400\,cm$ ($\sim 2m^3$). The total mass is $80\,t$. The shielding consists of (from outside to inside):

1. $20\,cm$ polyethylene
2. $23\,cm$ carbon steel
3. $15\,cm$ electrolytic copper

The polyethylene acts as a neutron absorber. Its structure is multilayer, so that, optionally, additional boron sheets or cadmium foils can be "sandwiched" between polyethylene plates.

Steel is a "low-cost" efficient γ absorber. It is preferred to lead because the latter might bend under its own weight in such a massive structure. The intrinsic contamination of steel varies strongly, depending on the row material and the past treatment of the melting furnace. The steel used for the LLBF has been selected from a high quality batch screened with High-Purity Germanium spectroscopy (HP-Ge) at the MPIK underground laboratory.

Electrolytic copper is intrinsically much purer than steel (however also more expensive), and for this reason it is used as the last shielding layer around the detector. At see-level copper is activated by the cosmic radiation, which gives rise to the production of the long-lived radioactive isotopes ^{54}Mn, ^{57}Co, ^{58}Co, ^{60}Co, with an equilibrium activity at the mBq/kg level [Heu93]. Therefore, the shielding copper has been transported and stored underground immediately after production. Table 9.1 shows the results of a HP-Ge measurement of a sample of the LLBF copper, carried out in Gran Sasso.

The calculated LLBF performance for the shielding of the $2.615\,MeV$ ^{208}Tl line are reported in Table 9.2.

[1] This is the highest energy among the most intense naturally-occurring γ sources.

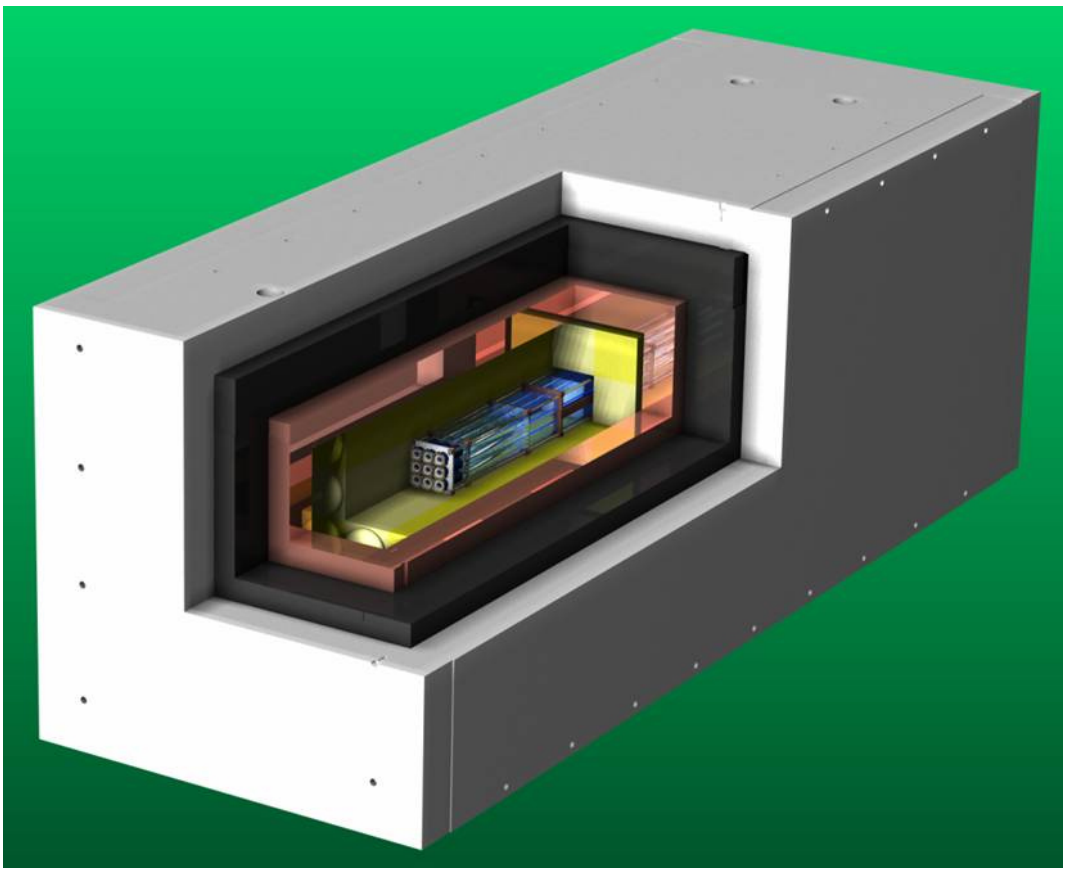

Figure 9.1: *Photo-realistic rendering of the complete LLBF shielding, which houses the LENS prototype array in its core (to be described later).*

Table 9.1: *Trace radioactive contaminants in the electrolytic copper used for the LLBF shielding, from a HP-Ge measurement at LNGS (sample mass:* $124.7\,kg$*, live time:* $70.45\,d$*). In all cases the activity were below the detection sensitivity and only upper limits could be derived. For the case of* ^{60}Co*, the measurement shows that no significant cosmogenic activation as occurred. Analysis from [Ned02].*

^{238}U (g/g)	^{232}Th (g/g)	^{nat}K (g/g)	^{60}Co $(\mu Bq/kg)$
$< 2 \times 10^{-12}$	$< 7 \times 10^{-12}$	$< 4 \times 10^{-9}$	< 11

Table 9.2: *Calculated LLBF performance for the shielding of the* $2.615\,MeV$ ^{208}Tl *line.* L_{att} *is the attenuation length, defined as the distance at which the radiation intensity drops of a factor* $1/e$. L_{shield} *is the thickness of the considered layer and* T *the calculated transmission probability. Data from [Sch01].*

	$L_{att}(cm)$	$L_{shield}(cm)$	T
Polyethylene	23.4	20	0.42
Steel	3.34	23	1.03×10^{-3}
Copper	2.96	15	6.36×10^{-3}
Total LLBF			2.76×10^{-6}

The shielding is hermetically sealed and a pipeline flushes nitrogen inside the LLBF to remove radon and other radioactive gases. The nitrogen flux is monitored at inlet and outlet.

The opening and closing of the shielding is facilitated by a modular macro-bricks structure on both short sides. Disassembling or assembling the LLBF front side requires the work of two persons for about two hours. To move detectors in and out of the LLBF, a "drawer" has been designed, consisting of a copper table sitting on the bottom surface of the inner volume, which slides on a pneumatic rail-system. The loading capacity of the drawer (and hence of the LLBF) is $2\,t$.

The LLBF facility is housed in a barracks that also includes: a control room, with electronics, PCs and network connection; a fire extinguishing system; and a ventilation system with temperature and humidity control.

9.2.3 Experimental Program

The construction of the LLBF was financed by the *Max Planck Gesellshaft* in 2000. The final In-LENS prototype has been installed in October 2003 and the background measurements are currently ongoing. The chronology of the LLBF design, construction, characterization and experimental program are summarized in Table 9.3.

After the completion of the LLBF installation in 2001, the experimental program has started with the preliminary characterization of the shielding performance. This work is reported in the next section. Upon the results of the first phase of the R&D, in 2002 the LENS collaboration has decided to focus on indium for the final pilot phase. During this year, the LLBF prototype program has been prepared at MPIK with the finalization of:

- Design and construction of the quartz optical modules and of the support frame
- PMTs and electronics procurement
- DAQ and data-reading/analysis software

The experimental program for the LENS pilot phase at LLBF has considered two phases:

1. Bench-marking with the measurement of the prototype array filled with PXE
2. Measurement of the prototype array with four In-loaded cells

Table 9.3: *Chronology of the LENS prototype program at LLBF.*

Summer 2000	First concept
Autumn 2000	Design shielding and housing barracks. Material selection
Nov-Dec 2000	Order of the parts
Mar 2001	Completion material procurement Underground storage of Cu at Gran Sasso
Jul-Sept 2001	Assembly of the shield
Nov 2001	First start-up
Dec 2001	Test radon removal system HP-Ge background measurement outside the shielding
Jan-Feb 2002	HP-Ge background measurement inside the shielding
2002	Decision to finalize the prototype design for indium Design and construction of the prototype cells and support frame Order of PMTs and electronics Development of DAQ and data-reading/analysis software
Mar-Jun 2003	Installation of a PXE prototype array Electronics, cabling and test runs
Jun-Aug 2003	First background run with the PXE prototype array
Aug 2003	Completion of the electronics, start second PXE run
Oct 2003	Installation of 4 In-cells and start data-taking

Preliminary results of the phase 1 are presented in Sec. 9.4. First results of the ongoing measurements of the final LENS prototype are given in Sec. 9.5.

9.2.4 Preliminary Measurements of the LLBF Performance

Radon Removal System For the test of the radon removal system the outlet of the nitrogen purging line has been connected to a Rn-monitor. The LLBF has been flushed with a nitrogen flux of $0.3\,m^3/h$ and the activity in the radon monitor has decayed exponentially with the expected $\sim 6\,h$ time constant (one volume exchange) from a value of $\sim 100\,Bq/m^3$ (the average ambient level in the experimental area) to the detection sensitivity (a few Bq/m^3) in $\sim 24\,h$.

High-Purity Germanium Background Measurement Inside the Shielding Before installing any prototype in the LLBF it was necessary to measure the residual external background. For this purpose a HP-Ge detector has been installed inside the LLBF and let counting for 525 hours. The Ge crystal was shielded from its own dewar by an additional temporary wall was erected using low-background lead and copper bricks. The dewar was periodically filled from outside by mean of a liquid nitrogen line.

The results of this background measurement are shown in Fig. 9.2, which also compares the background inside the LLBF with the one measured outside the shielding. The background rates for the main γ-lines from primordial and cosmogenic radioactivity are listed in Table 9.4.

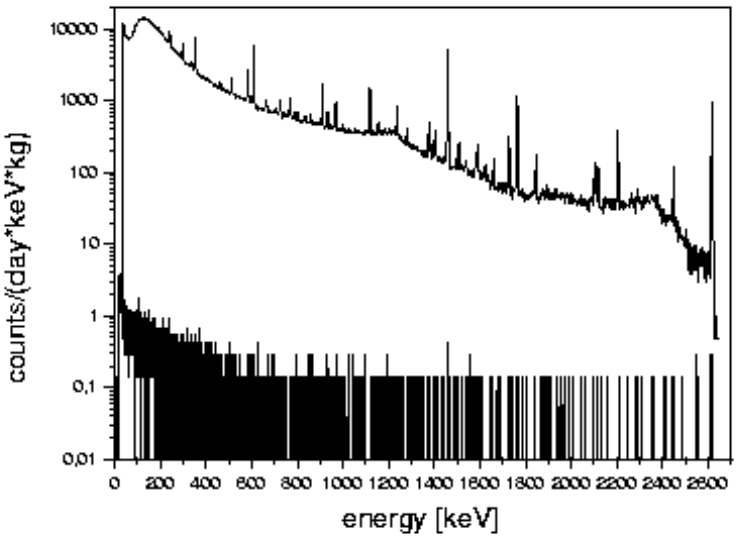

Figure 9.2: *Results of the HP-Ge background measurements in the LLBF. The graphics shows the superposition of the spectra measured outside (top) and inside the shielding (bottom,* $525\,h$ *counting time).*

Table 9.4: *Background rates for the main* γ*-lines from primordial and cosmogenic radioactivity. The detector background (fourth column) is the measurement of the* $\beta\beta$*-Heidelberg-Moscow experiment with this Ge detector alone, inside a low-background shielding[HM02]. The Ge crystal has a mass of* $0.9\,kg$.

Source	Energy (keV)	LLBF (c/d)	Ge background (c/d)
^{214}Pb	352	1.1 ± 0.2	0.55 ± 0.09
$e^- - e^+$	511	0.28 ± 0.11	0.74 ± 0.10
^{214}Bi	609	0.21 ± 0.11	0.35 ± 0.07
^{137}Cs	662	0.32 ± 0.12	0.50 ± 0.09
^{228}Ac	911	0.18 ± 0.09	0.27 ± 0.06
^{60}Co	1173	< 0.15	1.32 ± 0.11
^{60}Co	1333	< 0.10	1.36 ± 0.12
^{40}K	1461	0.64 ± 0.17	0.14 ± 0.05
^{208}Tl	2616	0.32 ± 0.12	0.19 ± 0.05
integral	100-400	69 ± 2	49
integral	400-2700	26 ± 1	46

Table 9.5: *Radioactive contaminations in the PMTs used for the LENS prototype. All the activities are given in mBq/PMT. Data and analysis from [Lau03].*

^{226}Ra	$^{234}Pa-m$	^{235}U	^{232}Th	^{40}K	^{137}Cs	^{60}Co
176 ± 5	156 ± 74	10 ± 2	35 ± 2	136 ± 14	< 1	1.8 ± 0.5

No prominent lines are found, neither from primordial, nor from cosmogenic radioactive nuclides. The background level measured in the LLBF is at all energies of the same order of magnitude of the previous estimation of the HP-Ge detector background [HM02].

The conclusion of this measurement is that the LLBF offers an ultra-low-background environment of comparable level with that of the best $\beta\beta$-decay experiments. These are the ideal conditions to study the intrinsic backgrounds of the LENS experiment.

9.3 LENS Prototype Detector at LLBF

9.3.1 Design

Structure The LENS prototype detector is a 3×3 matrix of quartz optical modules, each identical to the one characterized in our dark room (see previous chapter and Figs. 8.4 on page 167 and 8.5 on page 168). In addition, two $5\,cm \times 5\,cm \times 50\,cm$ acrylic bars are optically coupled to the ends of each cell, to provide shielding against the PMT radioactivity. Each cell is wrapped with VM2000 foils, to enhance light piping and reduce light-cross talk between neighbouring cells. Except for the acrylic buffers, the cells are used as in the optical measurements reported in Sec. 8.4.2. The cell optical performances are expected to be accordingly similar to those measured at MPIK.

The array of cells is mechanically supported by a frame made of copper and acrylic. All parts have been carefully selected after background screening in the MPIK underground laboratory.

Fig. 9.1 is a photo-realistic rendering of the LLBF shielding with the prototype detector in its core. The figure sketches also the optional *outer-array*. This is a system of 8 $20\,cm \times 20\,cm \times 300\,cm$ scintillation cells that might be implemented in a later phase of the LLBF experimental program.

PMTs The PMTs are an ultra-low background version of the same type used for the optical measurements reported in the previous chapter (specifications in Table 8.3 on page 169). The results of a HP-Ge background measurement at LNGS are reported in Table 9.5. The voltage dividers are also low-background and have been designed in collaboration with ETL.

Calibration Sources Several encapsulated calibration γ-sources are mounted on the end of wires, which are introduced in the LLBF through four Teflon hoses. The hoses run along the support frame, one at each corner of the central cell of the matrix. During the background measurements the calibration hoses are closed with silicon stoppers to prevent the diffusion of radon inside the shielding. The most utilized sources are: ^{137}Cs, for the calibration of the low energies, and ^{228}Th for the high energies (through the daughter nuclide ^{208}Tl).

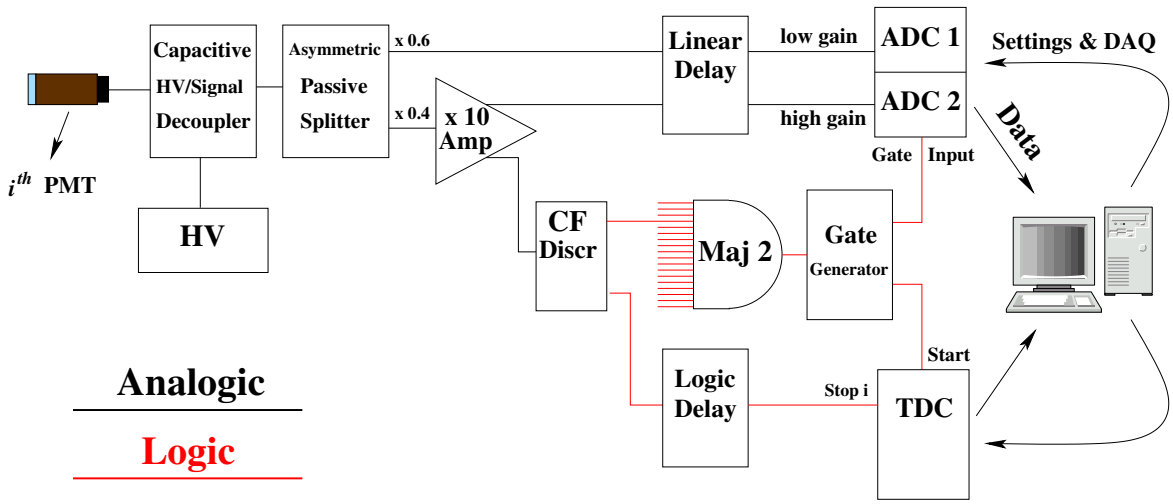

Figure 9.3: *Simplified scheme of the final LLBF electronics and DAQ. One channel of the total 18 is shown.*

9.3.2 Electronics & DAQ

The set-up developed for the dark room and documented in the previous chapter (see Fig. 8.5 on page 168) has been taken as a test for the project of the electronics and DAQ of the LLBF. Important differences between the dark-room set-up and the LLBF read-out system are:

- Implementation of 18 analogic channels (2 PMTs $\times$ 9 cells)
- Dynamic coverage of a broader energy range (0, $\sim 4\,MeV$)

Fig. 9.3 shows how the LLBF electronics has been implemented. In order to minimize the number of cables to feed through the shielding, high voltage (HV) and PMT signal are driven by the same cable (a standard coaxial RG-58) and the decoupling is realized by a passive capacitive circuit. The PMT analogic signal is then split by an asymmetric passive splitter (a simple resistive circuit with $50\,\Omega$ impedance match), which gives two outputs with amplitudes of ~ 0.6 and ~ 0.4 relative to the input signal. The $\times 0.6$ analogic line is directly delayed and digitized by a charge-sensitive ADC, while the $\times 0.4$ signal is sent to a $\times 10$ NIM amplifier. The latter has two outputs: one is used to form the trigger, the other is delayed and digitized by a second ADC.

Compared to the system of Fig. 8.5, here the trigger condition is based on the *majority* logic. The majority level is set to 2, which means that a trigger is produced whenever two of the 18 PMTs get over the CF threshold.

The two analogic channels come to the ADCs in the final amplitude ratio of $\sim 0.6/4 \sim 1/7$. The PMT HV is set such to have the dynamic range of the "high-gain" ADC covering the energy interval [0, $\sim 600\,keV$]. Consequently, the ADC digitizing the "low-gain" channel covers the range [0, $\sim 4\,MeV$][2].

The design of the passive splitter and the choice of the PMT HV settings have been optimized to avoid saturation effects at very high energies in the low-gain channel. These

[2]The dynamic range of the ADCs is fixed by the manufacturer to an integral charge of $400\,pC$.

can be introduced either by the PMTs, if they are operated at a too high HV, and by the electronics. For example, our $\times 10$ amplifier are non-linear for input signals having $> 300\,mV$ peak-amplitude.

The HV-signal decoupler, the asymmetric splitters and the linear delays have been constructed by the electronic department of MPIK. The nuclear electronics is NIM-standard and, for the digital part, VME-standard.

Variant trigger logics are sometimes used:

1. Trigger built by the low-gain line, realized by simply swapping the cabling shown in Fig. 9.3. This solution allows to set a higher hardware energy threshold and is used to have the system triggering above the ^{115}In β -spectrum.

2. Majority level set to 4. This condition is the hardware requirement that two cells are in coincidence and is used to investigate the In-Bremsstrahlung events from a more compact set of data (single β-decays are hardware-cut).

DAQ The DAQ software to drive the digital electronics has been developed at MPIK and is documented in [Las02]. For each event the following digital measurements are written on file:

1. ADC integral charge of the low-gain signal

2. ADC integral charge of the high gain signal

3. TDC elapsed time between a common start and the delayed output of the CF-discriminators

The above structure is repeated for each of the 18 channels of the LLBF electronics.

The two ADC channels provide an event energy reconstruction, with the high-gain channel giving improved resolution for $E < 600\,keV$. The TDC information is used for the event spatial reconstruction, as described in the previous chapter.

Data-Reading and Data-Analysis Software A multi-purpose data-reading and data-analysis software has been developed during this work (brief description in Sec. 8.3). This software has been used to open the VME raw binary files and convert their content into an object-oriented format suitable for analysis within the *ROOT* environment. ROOT [BR96] is a data-analysis toolkit of the CERN libraries and is intended as an extension of the predecessor *PAW*. ROOT implements a wide spectrum of graphics applications and data-analysis utilities in the modern object-oriented programming philosophy. Most of the graphics shown in this thesis and the relevant data-analysis have been carried out using ROOT.

9.4 Preliminary Results of the PXE Run

9.4.1 Measurements

All 9 cells of the LENS prototype array have been filled with a PXE scintillator from the same batch measured in our dark room. Composition, preparation and optical properties are the same reported in the previous chapter.

After a first phase of test and debugging of the electronics, two long background runs have been carried out with this system:

1. In the run-1 the prototype was read by a simplified version of the electronics. Only one analogic channel per PMT was implemented and no TDC. The signals from the decoupling station were sent to a fan-out and two outputs used for the trigger and for the ADC charge measurement.

2. Before run-2 the system has been upgraded to the final logic of Fig. 9.3, with the introduction of a second ADC and the implementation of the time-of-flight measurement using the TDC.

During the tests prior to the start of the run-1 it was realized that the measured background rate was sufficiently low to enable a measurement of the ^{14}C content of the PXE scintillator. Therefore the gain of the PMTs was tuned to obtain the dynamic range specified in the previous section: $[0, \sim 600\,keV]$. In this range the ^{14}C β-spectrum can be resolved with good precision and the energy scale can be approximatively determined by use of the ^{137}Cs Compton-edge.

For the PXE run-2, the primary goal was to investigate with spectral information the high energy natural radioactivity and the muon events, still keeping good sensitivity at low energies with the implementation of the double ADC reading described in the previous section.

Some preliminary results of the analysis of the PXE run-1 will be presented. The analysis of the run-2 is in progress.

9.4.2 Calibration and Monitoring

Energy Calibration Fig. 9.4 shows the energy spectra of two ^{137}Cs calibrations, one performed short after the start of the run, and the other 20 days later, at the end of the measurement.

The stability of the system was very good. As an example, the fit of the Compton-edge of the central cell gives $(6121 \pm 36)\,chs$ for the former calibration and $(6128 \pm 54)\,chs$ for the latter.

The energy is preliminarily estimated with the only two available calibration points:

1. the ADC pedestal charge acquired when the signal baseline is digitized

2. the ^{137}Cs Compton-edge

The pedestal channel is assumed as $E = 0$ and the Compton-edge peak channel as $E \sim 450\,keV$. The latter assumption follows from the experimental determination of the charge ratio of the Compton-edge (CE) to the Compton back-scattering peak (CBS, $E = 477\,keV$) in the optical measurements of the PXE cell wrapped with VM2000:

$$Q_{CE}/Q_{CBS} = 0.94 \pm 0.01 \tag{9.1}$$

The ADC-to-energy scale is then interpolated by a linear function.

Event Display A program has been written to display each event. This allows to reconstruct the topology and energy distribution of the events and to monitor anomalies, noise, etc. Fig. 9.5 shows some examples of ^{137}Cs events. Fig. 9.6 displays an event acquired during the background run and interpreted as due to a high-energy cosmic muon crossing the detector.

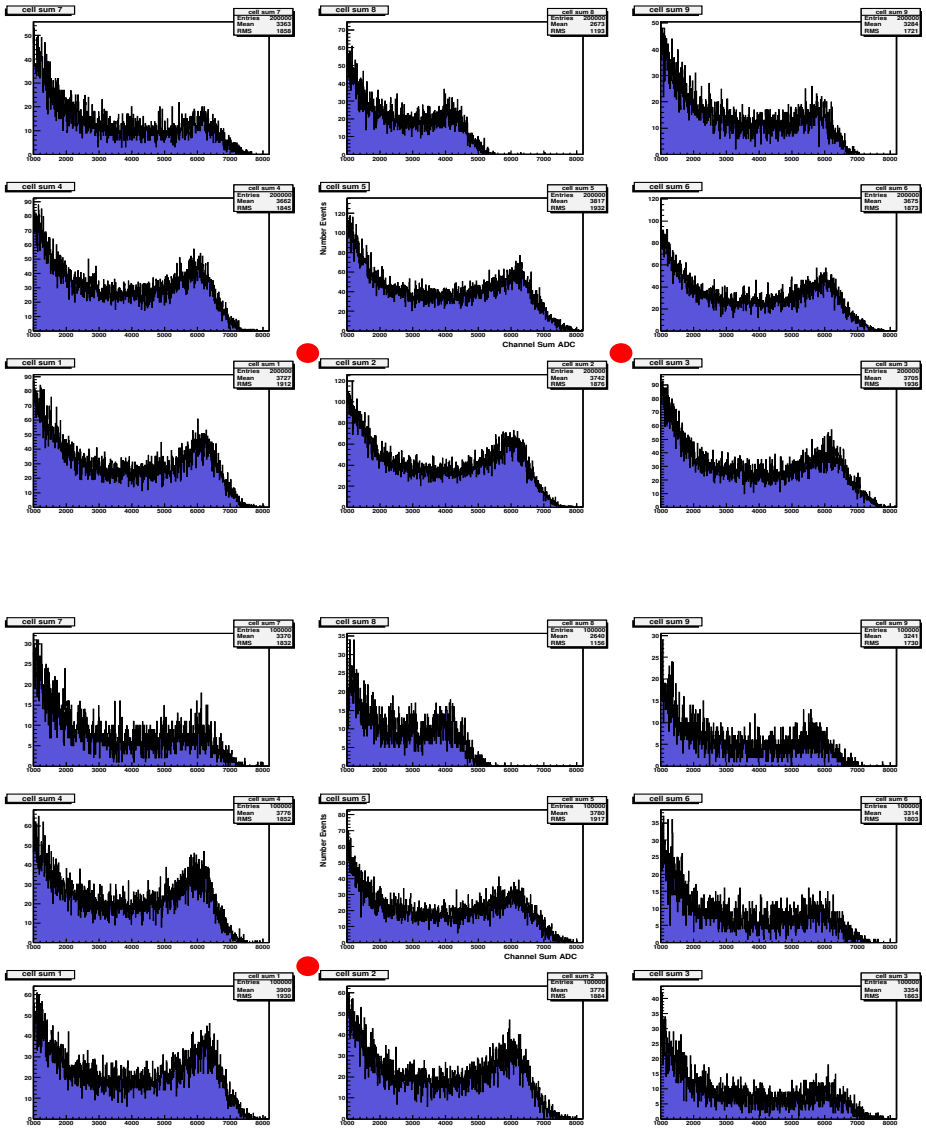

Figure 9.4: *Top:* ^{137}Cs *calibration performed on June 12 2003, 3 days after the start of the first PXE run. The red markers indicate the positions probed with the source.*
Bottom: calibration performed on July 2 2003, when the run was stopped. In this calibration less statistics was acquired and the source was only located at the bottom left corner of the central cell, thus irradiating with higher efficiency the four cells around this point.
Each pad displays the sum ADC spectra, for the pair of PMTs belonging to the same cell ($ADC_{PMT1} + ADC_{PMT2}$)*, with the first 1000 channels omitted. The* 3×3 *graphical matrix reproduces the arrangement of the prototype array, as seen from the counting room. The cells have been conventionally labeled with progressive numbers from 1 to 9, proceeding from left to right and bottom to top.*
One of the PMTs of the cell "8" had gain problems and this explains the lower sum-ADC values. In both calibrations the source was equidistant from the PMTs.

Figure 9.5: *Examples of events from the ^{137}Cs calibration.*
Top: single Compton scattering with deposition of an energy around the Compton-edge.
Bottom: multi-hit Compton with total deposited energy corresponding to $\sim 450\,keV$.
In all the pads the green ("back" label) and red ("front" label) bars represent the ADC charge of the single PMTs. The blue bar ("total" label) is the sum charge. The vertical scale is expressed in ADC channels and the pedestal offset ($\sim 180\,chs/PMT$) is subtracted.

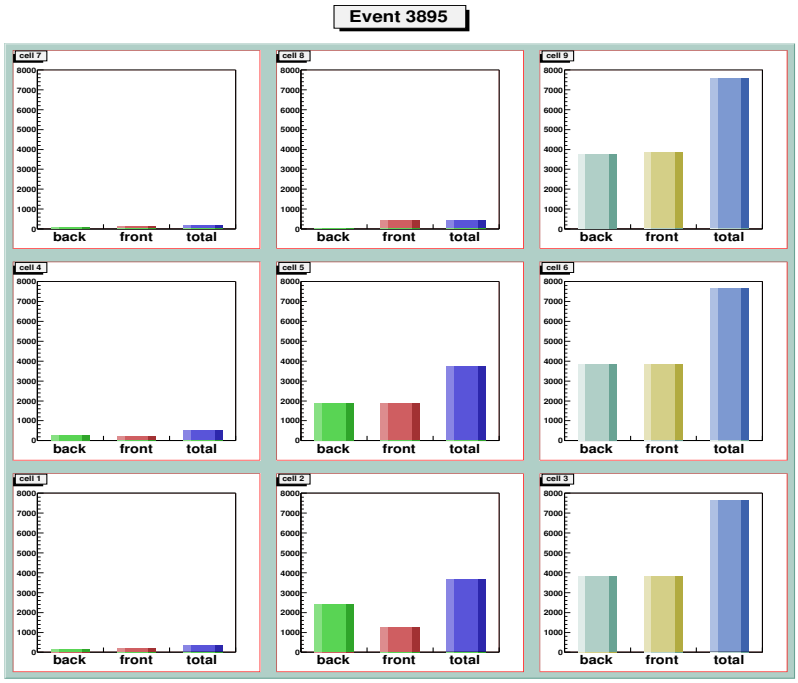

Figure 9.6: *Example of muon crossing the detector. The light colors indicate an overflow ($E > 600\,keV$, corresponding to $\sim 3800\,ch/PMT$). The vertical muon track is clearly visible. Muons deposit a huge energy in the scintillator and give rise to overflows. The charge measured in the neighbouring cells is probably due to electronic or light cross talk.*

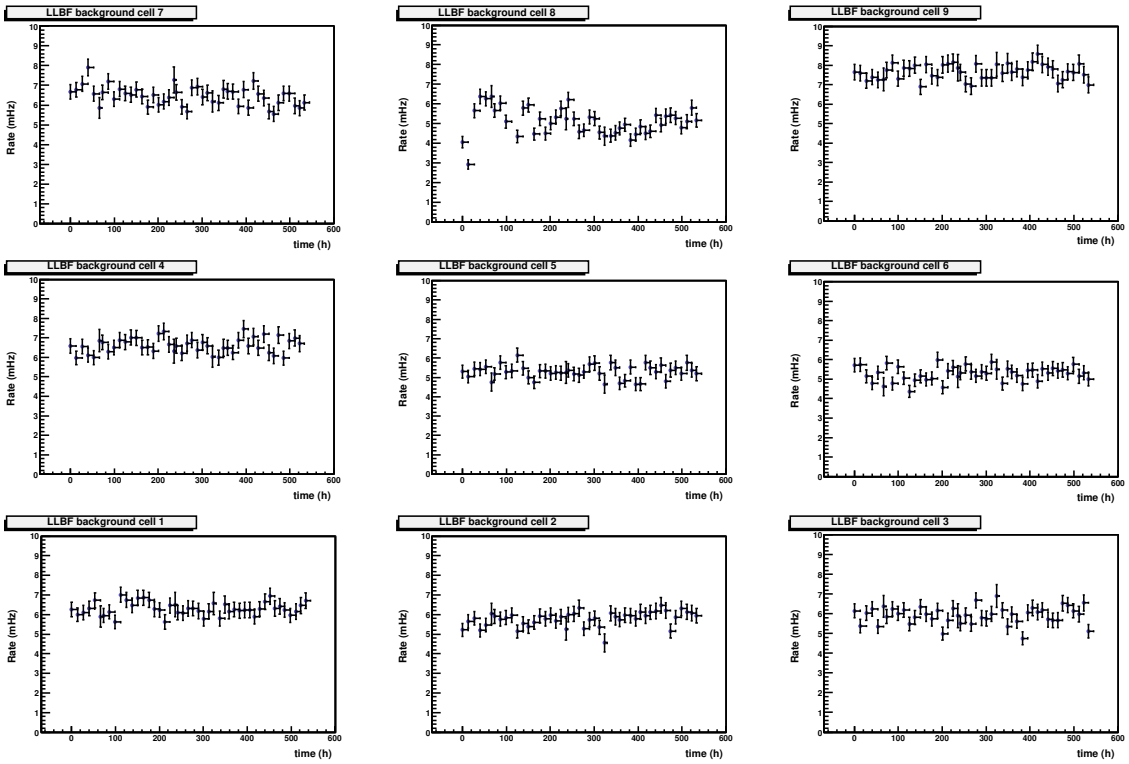

Figure 9.7: *Count rate for single-cell events above a* $\sim 35\,keV$ *software threshold. Data are grouped in* ~ 12 *hours bins and the background rate is given in* $mHz/cell$*. The measurement live time selected for the analysis is* $535.3\,h$*. The event selection for the cell 8 is not reliable, due to gain problems of one PMT.*

Event Rate Fig. 9.7 shows the integral background rates in all the 9 cells as a function of the time, for the following off-line software event selection:

1. both PMTs of a cell above the baseline noise level
2. sum charge delivered by the two PMTs over a software energy threshold of $\sim 35\,keV$
3. none of the other 8 cells satisfying the conditions 1 and 2 (single-cell events)

The background rate during the ~ 23 days counting time was stable. Sporadic bursts of noise events have been observed, mostly coming from the cell "9". In the analysis, the few hours in which the hardware trigger rate was dominated by noise have been considered dead time. With this selection, the measurement live time is 535.3 hours.

The average counting rate of single-cell events above the considered $\sim 35\,keV$ threshold is $5 - 7\,mHz/cell$. Each cell contains a PXE mass of $\simeq 1850\,g$, hence the measured integral background rate translates to:

$$B(E > 35\,keV) \sim 3 \times 10^{-3} s^{-1} kg^{-1} \tag{9.2}$$

It will be shown in the next section that this rate is dominated by the intrinsic ^{14}C contamination of the PXE.

9.4.3 Preliminary ^{14}C Analysis

The energy spectra of the single-cell events acquired in the PXE-run1 are plotted in Fig. 9.8.

In all the cells the spectra show a very prominent contribution from a low energy source with cut-off at $\sim 150\,keV$. End-point and spectral shape are consistent with the expected ^{14}C contamination in the scintillator (see [Bor98, Res00]).

A preliminary analysis based on the observed rates will be presented. For simplicity, only the central cell is considered, because it has the best signal-to-background ratio, due the more effective anti-coincidence shielding from the other cells. For this cell, Fig. 9.8 shows that the software threshold can be pushed down to $\sim 20\,keV$ without observing spectral distortions due to electronic noise and hardware threshold.

The ^{14}C activity in each cell is given by:

$$A = \frac{16 m N_A}{\tau M} R = (0.325 \pm 0.005) \times 10^{18}\, R\,(mBq/cell) \tag{9.3}$$

where $m = (1850 \pm 30)\,g$ is the PXE mass in the cell, N_A the Avogadro number, τ the lifetime of ^{14}C, M the molar weight of PXE ($210\,g/mol$) and R the $^{14}C/^{12}C$ isotopic ratio (^{14}C atoms per ^{12}C atom). The factor 16 is the number of carbon atoms per PXE molecule ($C_{16}H_{18}$).

In the energy interval [$20\,keV$, $200\,keV$] the measured background rate is:

$$B = (4.92 \pm 0.07)\, mHz \tag{9.4}$$

where the uncertainty is statistical only.

The underlaying non-^{14}C background rate in the same energy window is extrapolated from the background at $E > 200\,keV$, assuming for simplicity that it is a linear function of the energy:

$$b \sim 0.80 \pm 0.08(stat)\, mHz \tag{9.5}$$

Therefore the estimation of the ^{14}C activity in the cell is:

$$A = B - b \sim 4.1 \pm 0.1(stat)\, mHz \tag{9.6}$$

where the efficiency for the ^{14}C detection above the threshold has been neglected (i.e. it is set to 1).

Introducing eq. 9.6 in eq. 9.3 and solving for R it is found:

$$R \sim [12.6 \pm 0.4(stat)] \times 10^{-18} \tag{9.7}$$

The value measured by Borexino in CTF for this sample is $R = [11.74 \pm 0.28(syst.) \pm 0.03(stat.)] \times 10^{-18}$ [Res00]. Considering the approximation of our calculation, the agreement is remarkably good.

The background rates and energy spectra of the other cells are very similar to the one of the central cell and this is consistent with a constant ^{14}C contamination. Work is in progress to implement the more precise ^{14}C analysis used in Borexino, which is based on the fit of the spectrum with a theoretical function.

One of the primary goals of the $4\,t$ CTF prototype detector was the measurement of the ^{14}C level in organic liquid scintillators to use in Borexino [Bor98]. It has been shown that the $^{14}C/^{12}C$ ratio of a PXE sample can be determined in the LLBF with a reasonable precision, in a $1.85\,kg$ sample and a measurement live time of a few weeks. From eq. 9.7 and Fig. 9.8 it can be estimated that the limit sensitivity of this detector is of a few 10^{-18}.

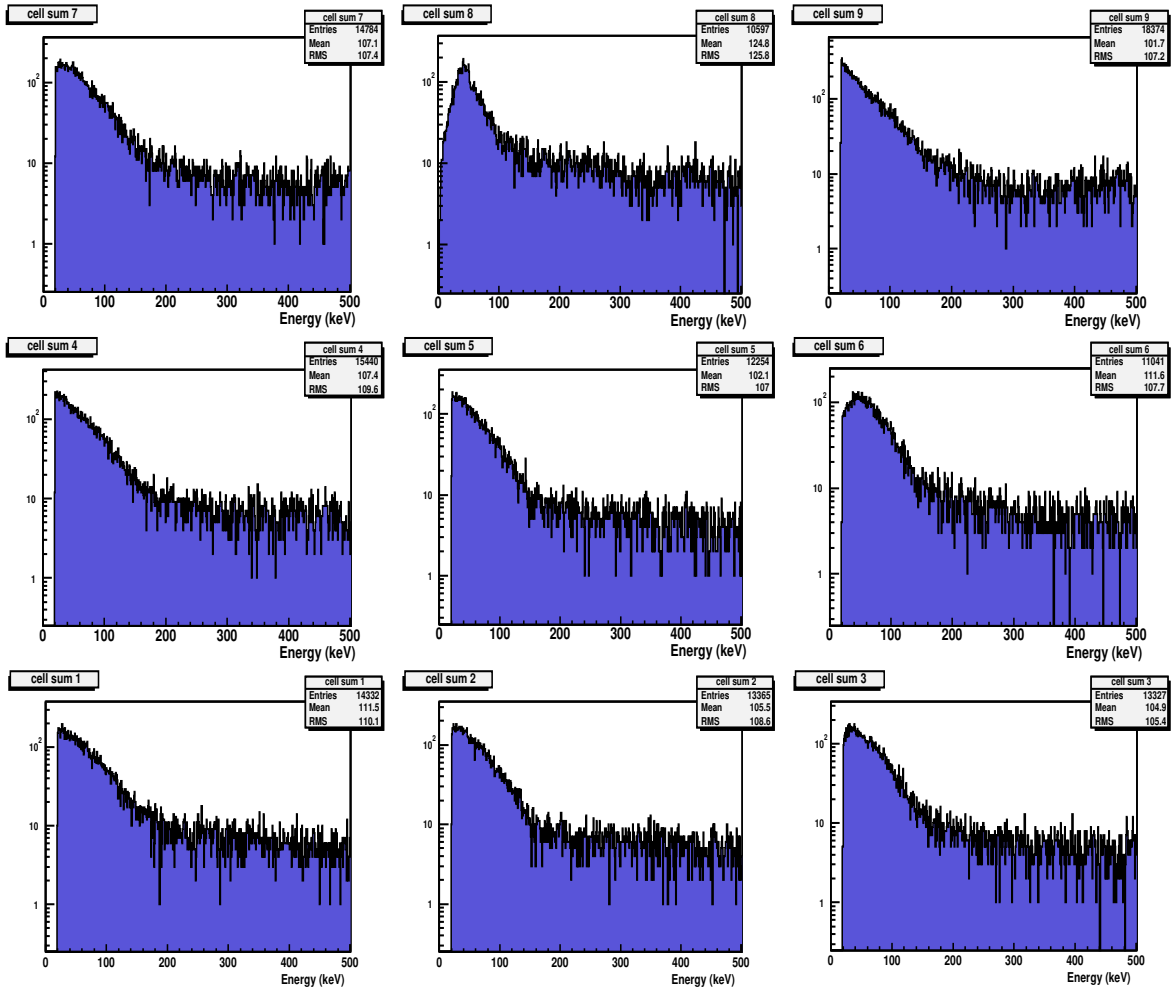

Figure 9.8: *Sum ADC spectra of the 535.3 hours PXE run-1 for single-cell events (one cell only above threshold). The matrix shows the results of each cell of the prototype array. In all the graphics the abscissa is the sum of the ADC channels converted to the equivalent energy. The ordinate is the total number of events per keV and the units are in logarithmic scale. A software cut of 20 keV is imposed. All the cell clearly show the ^{14}C β-spectrum (end-point at 156 keV). The cell 8 (top-center) had gain problems, the 9 (top-right) a high rate of spurious noise counts.*

Table 9.6: *In-loaded scintillator samples in the LLBF prototype. "Cell" is the detector label number, following the conventions of the PXE runs. LY is the light yield measured in a small vial, relative to BC505 for the In-acac samples, to a PC/BPO mixture for the In-CHO samples [Cat03]. The latter standard is measured to be ∼ 105% of BC505 [Buc04]. More details about the chemistry of the scintillators are found in Sec. 2.4.3 and refs. [BHS03, Buc04, INR03].*

Cell	In-Complex	In concentration (g/l)	Mass (kg)	LY (%)
2	$In(acac)_3$	47	1.80	42 ± 2
4	$In(acac)_3$	1	~ 1.8	~ 80
6	$InA_{0.6}OH_{2.4}$	54	1.67	78 ± 5
8	$InA_{0.6}OH_{2.4}$	51	1.63	73 ± 5

9.5 First Results of the Final LENS Prototype

In October 2003 the prototype has been dismounted, four PXE cells removed, emptied and filled with In-loaded scintillators produced in Heidelberg (In-acac) and Gran Sasso (In-CHO). The detector has been then remounted and data taking is still ongoing.

In this section some first results from the indium measurements will be given. All the analysis presented are still at a very preliminary stage.

9.5.1 Samples

Some properties of the scintillator samples being measured in the LLBF are reported in Table 9.6. The In-acac sample in the cell "2" contains $50\,g/l$ BPO and $100\,mg/l$ bis-MSB. It is therefore very similar to the last sample optically characterized in the previous chapter. The second In-acac sample is a low indium loading version containing a mixture of PXE and anisole, $4\,g/l$ BPO, $2\,g/l$ p-TP and $25\,mg/l$ bis-MSB. The purpose is to make a comparative estimation of the background contributions from fluor and In material and to test the performance of a β-diketonate scintillator for low metal concentrations [3]. The other two samples have been synthesized at Gran Sasso [INR03]. Their better LY compared to the high-loading MPIK scintillator is due to the combination of two factors:

1. The In-CHO formulation uses PC as base solvent. Unloaded PC scintillators are ∼ 15% better than anisole-based scintillators

2. $50\,g/l$ BPO in the In-acac sample is the best compromise between LY and transparency (Sec. 8.2.1). However, at this fluor concentration the $In(acac)_3$ quenching is still very strong (Fig. 8.1 on page 161).

[3] Metal concentrations in this range are of interest also for other applications. For example, $1\,g/l$ is the Gd concentration required to improve the neutron detection efficiency in reactor anti-neutrino detectors (See [Buc04]).

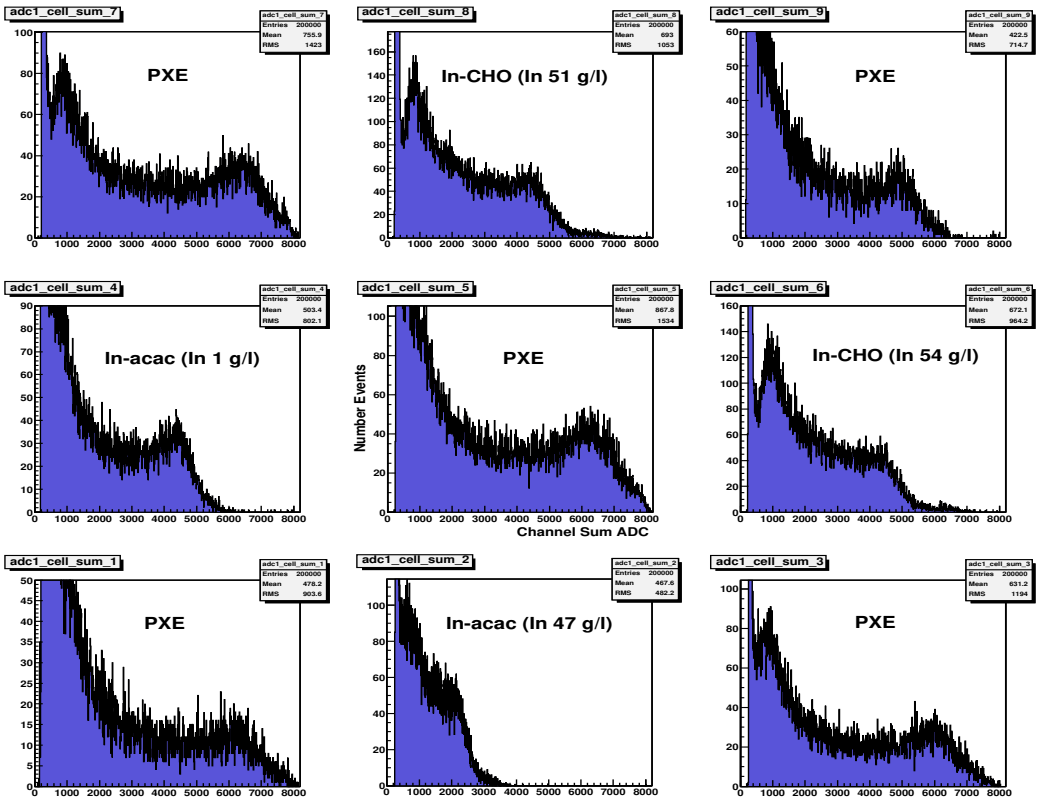

Figure 9.9: ^{137}Cs *calibration performed with the same HV settings used for the previous PXE run. In the latter the gain of the PMTs had been tuned to have the Compton edge at channel 6000 (sum of the ADC channels for the two PMTs). The plot shows that, after disassembling and reassembling the prototype array to install the indium cells, the light output of the PXE cells has remained the same, within* $\sim 3\%$ *(one of the PMTs of the cell 9 was replaced, therefore the correct setting was not known and this explains the lower gain).*

9.5.2 Optical Performances

Relative PY Fig. 9.9 shows the results of the first ^{137}Cs energy calibration carried out after closing the LLBF. The source was located at the center of the cells. The HV settings for the PMTs were the same employed in the previous PXE run. In the PXE cells the ADC amplitudes measured after dismounting and remounting the array are the same as before within $\sim 3\%$. Therefore, it is possible to compare the PY of the In-loaded cells with the PXE output, by calculating the ratio of the Compton-edge with respect to the average position in the PXE cells. The results of this estimation are given in Table 9.7.

The $47\,g/l$ In-acac cell is found to give $\sim 29\%$ of the PXE light output at the cell center. This is consistent with the results of the optical measurements reported in the previous chapter.

The In-CHO samples have a more than a factor two higher PY. Assuming that the light guides do not determine significant light losses, this would imply that the absolute PY of these cells is $\sim 500\,pe/MeV$.

Table 9.7: *Estimation of the PY of the In-loaded cells, relative to PXE.*

Cell	2	4	6	8
PY (% PXE)	29 ± 1	68 ± 3	68 ± 3	69 ± 3

Table 9.8: *Attenuation lengths measured in the LLBF. Analysis from [Vac03].*

Cell	2	4	6	8	5 (PXE)
$\mu\ (cm)$	95 ± 10	260 ± 40	165 ± 15	110 ± 15	255 ± 35

Light Attenuation The light attenuation curves have been estimated by moving the calibration source in $10\,cm$ steps and fitting the measured Compton-edge. The results are given in Table 9.8.

The value found for the $47\,g/l$ In-acac cell is lower than the result of the optical measurements in Heidelberg. This might be due to the systematic drift of the Compton-edge to lower energies, as the energy resolution worsens. This effect has been discussed and experimentally quantified in Sec. 8.4.2.

A more precise optical measurement of an In-CHO sample, performed by scanning the cell with several γ sources outside the LLBF, has given $\mu \sim 140\,cm$ [Cat03].

9.5.3 Stability

The prototype array is periodically calibrated to monitor the stability of the In-loaded cells. The amplitude of the ^{137}Cs Compton-edge is considered, as well as the light attenuation curve.

So far, all the In cells are stable within the errors [Vac03].

9.5.4 In-115 Beta-Spectrum

In Fig. 9.10 the "high-gain" spectra for a 1-day live-time measurement are shown. In all the In-cells the ^{115}In β-spectrum is clearly observed. The experimental shape of the spectrum near the end-point is an important input for the calculation of the In-Bremsstrahlung background.

9.5.5 Background Spectra

The "low-gain" energy spectra acquired in a $105\,h$ run are shown in Fig. 9.11. No event selection is applied. It is reminded that the low-gain channel provides spectral information in the energy interval $[0, \sim 4\,MeV]$.

The background rate of the high-loading MPIK cells above the ^{115}In β end-point is lower than the one of the In-CHO cells and only slightly worse than that measured in PXE, which seems to be dominated by ^{40}K ($E = 1.46\,MeV$). The $1\,g/l$ In-acac scintillator is not significantly different than the PXE cells.

A good radiopurity is expected for the β-diketonate scintillators, at least for what concerns the In material, because in the sublimation process any non-volatile impurity is efficiently separated. The higher background rates of the In-CHO scintillators was also expected, because the chemical steps of the synthesis are not yet optimized for radiopurity.

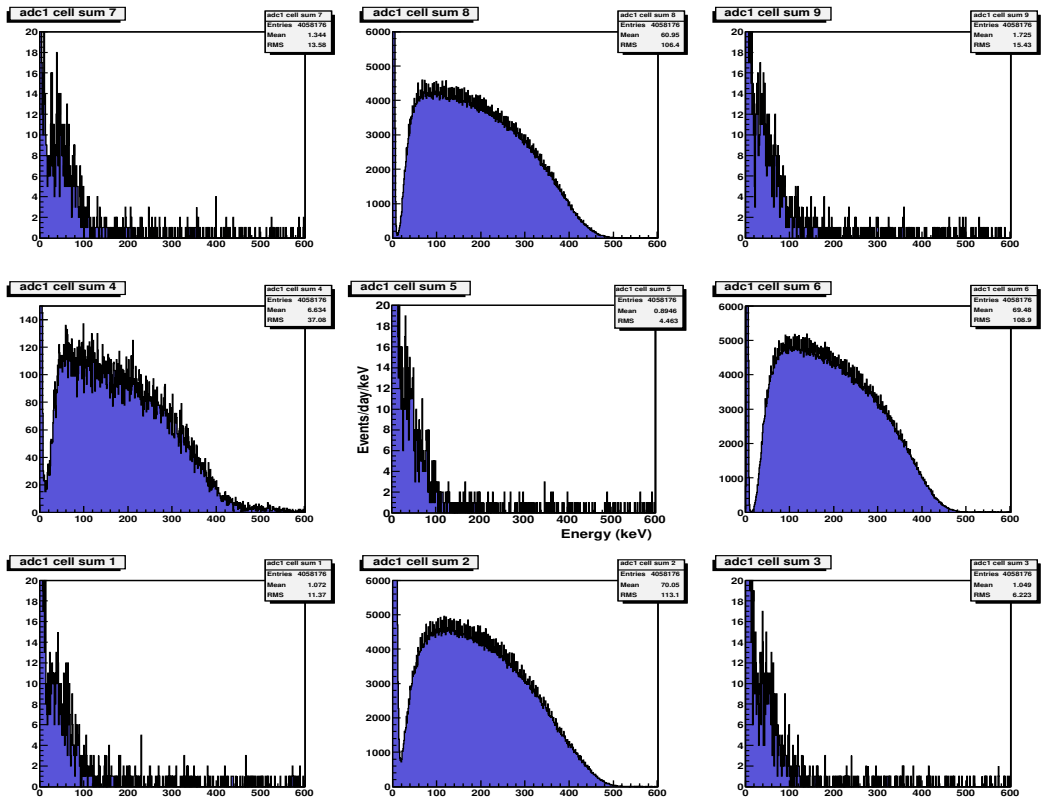

Figure 9.10: *Energy spectra with low threshold and a counting time of* $\simeq 1$ *day. The energy scale is preliminarily estimated from the* ^{137}Cs *calibration and the measurement of the ADC pedestal charge.*

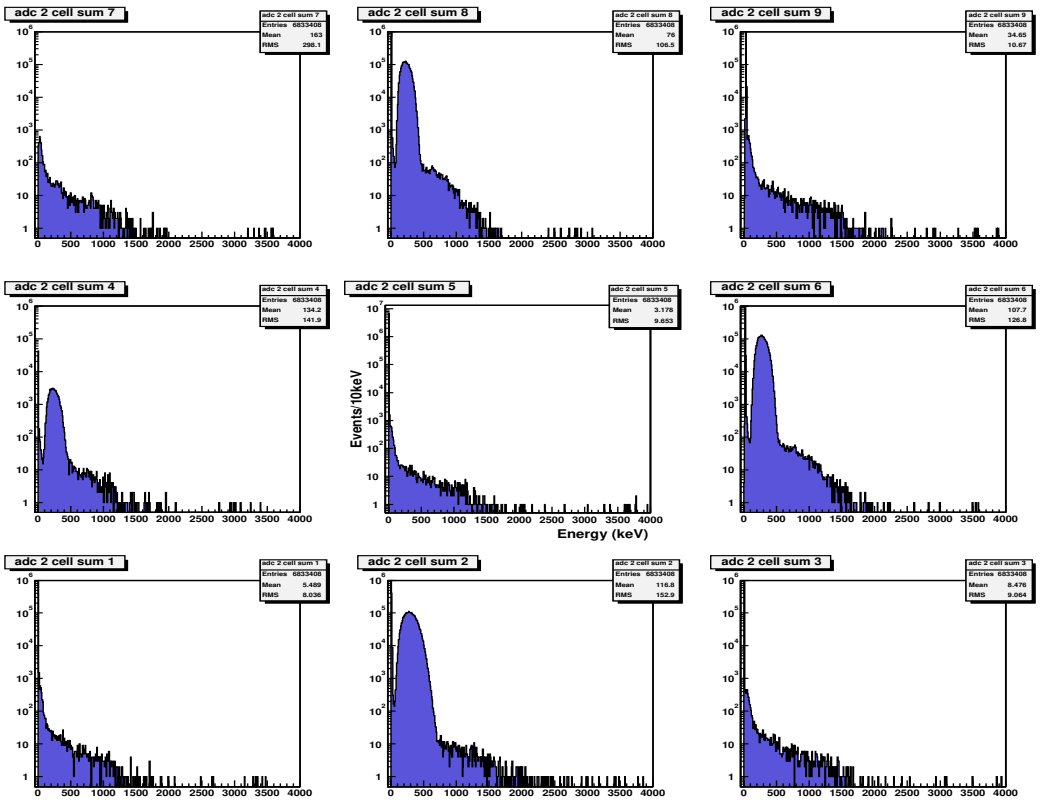

Figure 9.11: *Energy spectra with* $\sim 200\,keV$ *hardware threshold and a counting time of* $\simeq 105\,h$. *The energy scale is approximative. No event selection is applied.*

The internal radiopurity of the scintillator is a question of relevance, because high energy γ-rays in random coincidence with an In β-decay can produce fake tags (Sec. 2.4.3).

9.6 Summary and Outlook

The experimental study of the intrinsic detector backgrounds is one of the fundamental tasks of the LENS pilot phase. This program can be only pursued in an ultra-low background environment with characteristics as close as possible to those of the full-scale experiment. The LLBF (LENS Low Background Facility) has been installed at the Gran Sasso underground laboratory with the aim to operate a prototype array and investigate the LENS critical backgrounds.

The LLBF has been designed following strict low-background criteria and selecting all the materials after careful screening of their radioactivity. The final test of the LLBF performance with a HP-Ge measurement has shown that the LLBF has fully met its design goals.

A prototype detector has been built and installed in the LLBF. The electronics, the DAQ and the tools for data-reading and data-analysis have been developed and tested.

During the first experimental phase, the 9 prototype cells have been filled with a benchmark PXE scintillator. The PXE background runs have demonstrated the proper functioning of the system and the achievement of notable low-background levels. It has been found that the detector integral background rate is dominated by the intrinsic ^{14}C contamination of the PXE. A preliminary analysis of the first PXE run has been presented, which has shown that the ^{14}C content of a $\sim 1.85\,kg$ PXE sample is measured in the LLBF with a precision comparable to the one of the $4\,t$ CTF detector. The limit sensitivity of the LLBF detector is $^{14}C/^{12}C \sim 10^{-18}$.

LENS is now completing its pilot-phase program at the LLBF, with the ongoing measurement of a prototype containing four cells filled with In-loaded scintillators, three with $\sim 50\,g/l$ indium (one β-diketonate and two hydroxy-carboxylates), one with $1\,g/l$ (β-diketonate). Since the start of data-taking (a few months), all the In-loaded scintillator samples measured in the LLBF are stable.

The MPIK β-diketone scintillator with $\sim 50\,g/l$ indium loading gives a light output of $\sim 30\,\%$ relative to PXE (at the cell center) and an attenuation length of $\sim 1\,m$. This is consistent with the more precise optical measurements of a similar sample carried out at MPIK (Chapter 8). The sample with $1\,g/l$ indium has a light output of $\sim 70\,\%$ of PXE and an attenuation length similar to PXE. There are preliminary indications that the radiopurity of the β-diketone scintillator formulation is good.

The indium hydroxy-carboxylates scintillators developed at Gran Sasso give a photoelectron yield of $\sim 70\%$ relative to PXE and an attenuation length of $\sim 1.5\,m$. The light output of these samples is the best ever measured in an In-loaded scintillator at such high metal loadings. However, the hydroxy-carboxylate systems are expected to be chemically weaker than the β-diketones and the stability must be confirmed on a longer time scale. Moreover, the radioactive contamination of these samples must me evaluated and possibly improved.

The stability of the indium-loaded scintillators will be monitored for a time scale of the order of one year. The completion of the background measurements and the release of an official analysis are scheduled for the end of 2004.

Chapter 10

Conclusions of the LENS Pilot Phase

10.1 Summary

In Chapter 1 the field of solar neutrino physics has been reviewed. Particular emphasis has been given to the description of how our understanding of the sun and of the fundamental neutrino properties has changed from the first pioneering measurements to the most recent developments. The solar neutrino detectors have given the first strong indication that neutrinos are not massless, as the Standard Model postulates, and have opened a new era. Meanwhile this indication has become an evidence.

Low energy ($< 1\,MeV$) solar neutrinos occupy a special position in this context, because they connect the fundamentals of particle physics and astrophysics. So far, only the radiochemical gallium experiments GALLEX-GNO and SAGE have observed the *pp* neutrinos, which are produced in the nuclear reactions founding the energy generation in the sun. However, these experiments provide only an integral rate and cannot disentangle the single neutrino fluxes.

LENS is a project aiming at the real-time spectroscopy of low energy solar neutrinos. The LENS detection principle is based on the neutrino-induced inverse-EC reaction on suitable target nuclei. It is required that the neutrino-capture leads to a transition to an isomeric state. The coincidence of the prompt electron from the neutrino-capture and the delayed de-excitation of the product nuclide gives a powerful tool for the suppression of the background.

The LENS project has focused on two target candidates: ^{176}Yb and ^{115}In. The experimental concept and the target-specific challenges are described in Chapter 2.

For both isotopes, the rejection of the background requires the detector to be highly segmented. Therefore the understanding of the overall detector performance largely depends on the characterization of a single unit. The aim of the first phase of this work was to develop a model to predict and understand the performances of a LENS cell. This model has been used to address specific questions of the two proposed targets and the results of these studies have contributed to determine the strategy to follow in the pilot phase.

A crucial technical challenge of the ytterbium concept is the short delay ($\tau = 50\,ns$) and the low energy ($E_\gamma = 72\,keV$) of the neutrino-tag. The major concern is that, due to statistical fluctuations, single background events can originate signals which are falsely identified as neutrino captures. The probability for such a fluctuation depends on the mean pulse-shape of a single event, in particular on the fraction of the signal charge that is detected in the tag time-window. Various effects contribute to determine the "late" charge of a signal. First of

all, organic scintillators are known to emit light with a time distribution that contains slow components. The question is whether in a metal-loaded scintillator, due to the presence of the additional chemical species, those slow components are enhanced.

This problem has been addressed in Chapter 3. The fluorescence decay-time of several samples has been measured, including standard fast unloaded scintillators of common use in nuclear physics, and as well an Yb-loaded and an In-loaded scintillator sample. No significant differences were found between benchmark and metal-loaded scintillators. However, the fraction of light typically emitted with $\sim 20\,ns$ or longer time constants was $5 - 10\%$, hence certainly non-negligible.

After emission, photons propagate in the cell and another contribution to the signal late-charge is due to the photons that travel a longer path than the average. Light trapping due to reflections at the cell ends is particularly dangerous. In Chapter 5 the optical properties in the visible range of the most used photocathodes have been experimentally investigated in two sample PMTs. The photocathode reflectance was measured and the polarization change of the reflected beam analyzed. These experimental inputs have been combined with a theoretical model of the optics of the photocathode, to determine its complex refractive index and its thickness. The result of this work is a model able to predict the fraction of the light impinging on a PMT that is reflected, absorbed or transmitted, as a function of wavelength and angle.

The scintillator decay-time and the PMT reflections have been implemented in the optical model of a LENS cell and the mean pulse-shape of a single event was predicted via MC simulations (Chapter 7). This information was combined with the MC prediction of the detector photoelectron yield to estimate the "self-correlation" probability, namely the probability that a single event mimics a neutrino capture. The latter translates to a self-correlated background rate by considering the rate of single events expected in a ytterbium detector.

The conclusion of this analysis was that a minimum delay cut of $\sim 40\,ns$ and $\sim 60\,ns$ has to be imposed to assure an adequate signal-to-background ratio, for pp and ^7Be neutrinos, respectively. The resulting efficiency for the detection of solar neutrinos was calculated to be ~ 0.22 and ~ 0.16. These results have contributed to disfavor the ytterbium option and consequently to shift the focus of the LENS R&D to indium.

Due to the β-instability of the ^{115}In target, the In detector needs a very high segmentation and a good energy resolution to discriminate the solar signal from the background. The demand of "granularity" implies a cell transversal dimension of $\sim 5\,cm$. The goal length is $\sim 300\,cm$. With this geometry, the light produced by an event inside the cell needs on average $\gtrsim 30$ reflections to be piped to the PMTs. A major question is whether light piping in LENS cells can be realized with sufficient efficiency to meet the detector demand of energy resolution.

This problem has been studied in Chapter 4. The two mechanisms for light piping, total internal reflection (TIR) and specular reflection (SR), have been experimentally investigated. A system has been set up to measure the reflection coefficients of TIR on finished quartz surfaces and SR by multi-layer birefringent dielectric foils (VM2000 from 3M). The result was $R = 99.4\%$ for TIR and $R = 98.5\%$ for SR by VM2000. Both were measured at $\lambda = 430\,nm$, the typical wavelength of the emission peak in the LENS scintillators.

The implications of these results for the LENS concept have been analyzed by MC simulations in Chapter 7. It was demonstrated that, given the measured reflection coefficients, the light attenuation in a $5\,cm \times 5\,cm \times 400\,cm$ cell would not be dominated by light piping and that the goal of an attenuation length of $\sim 3\,m$ would mostly depend on the transparency of the scintillator. This result was decisive to advance the In-LENS project from the R&D to the prototype phase.

With LENS fully entering the pilot phase, it was necessary to complete the work on the detector modeling with the implementation of a more precise physics of light interaction in the scintillator. This required the interaction processes of light with each of the scintillator components to be measured and implemented in the photon-tracing simulation of the detector. This topic is discussed in Chapter 6, which also describes how all the experimental inputs measured during this work have been implemented in the full optical model of a LENS cell. In Chapter 8 it is described how this model was used to prepare the final prototype measurements, by selecting the optimal formulation for the In-β-diketonate scintillator developed at MPIK.

After this phase of detector design, the project has entered the last experimental phase, with the measurement of prototype detectors. The crucial issues to address in the LENS pilot phase are of two different kinds: related to the detector optical performances and to the intrinsic backgrounds.

The former topic has been covered in Chapter 8. A prototype quartz cell of dimensions $5\,cm \times 5\,cm \times 100\,cm$ has been set up in our dark room and first filled with a standard PXE-based scintillator. The excellent transparency and high light yield of this sample have provided an ideal benchmark of the limit performances of the detector. The cell has been measured with TIR light piping and then wrapped with a VM2000 profile to guide the light escaping TIR via SR. In each case, the light attenuation length, the energy resolution, the spatial resolution and the absolute photoelectron yield have been measured. The cell with VM2000 wrapping has provided more than twice as much light as the TIR cell, and also a better attenuation length. The benchmark performances for this case were: $\mu = 4.2\,m$, $\sigma_E(477\,keV) = 5.2\,\%$, $\sigma_x = 3.2\,cm$, $PY = 750\,pe/MeV$.

Three In-loaded samples synthesized at MPIK have been measured in the same prototype cell. One had $20\,g/l$ indium loading, the others $44\,g/l$, differing from each other for the wavelength-shifter concentration. For the high-loading samples, the measured parameters were: $\mu = 1.3\,m$, $\sigma_E(477\,keV) = 11.6\,\%$, $\sigma_x = 7.0\,cm$, $PY = 200\,pe/MeV$. The attenuation length and the PY relative to the PXE cell are correctly predicted by the MC simulations. However, these predict a factor > 2 higher absolute PY. The reason of this disagreement is under investigation. An explanation is that the effective sensitive area of our PMTs is lower than what is assumed. The cross-check with other experimental data supports this hypothesis.

In order to study the fundamental issues related to the backgrounds, the LENS Low Background Facility (LLBF) has been installed at Gran Sasso. It consists of a $80\,t$ passive shielding and provides a shielded volume of $\sim 2m^3$. The design and the performance of the LLBF are described in Chapter 9.

Recently a prototype detector made of a 3×3 matrix of quartz cells, all identical to the one measured in Heidelberg, has been installed and operated. The benchmark performances of the system have been tested with the 9 cells filled with PXE. It has been shown that the background of this prototype is dominated by the ^{14}C contamination of the scintillator and a preliminary analysis has determined a $^{14}C/^{12}C$ ratio which is in very good agreement with the measurement of the same scintillator in the $4\,t$ CTF detector of Borexino.

The LLBF program has entered the last phase, with the installation of four In-loaded cells in the prototype array. Some preliminary results have been presented, which show that the system is fully operative and works as expected. In particular, the optical performances of the In-prototype cells are stable in time and consistent with the results of the dark-room optical characterization. The LLBF measurements are ongoing and the data analysis is in progress.

10.2 LENS Feasibility: at Which Cost?

When the LENS collaboration formed the primary goal of the project was to develop an experiment with the potential to give the ultimate proof that solar neutrino flavor-oscillate and to pin-down the oscillation solution realized by nature among the several scenarios still allowed at that time (Sec. 2.1.1).

After the recent developments in the field (Sec. 1.4.6), the target of a real-time spectroscopic sub-MeV solar neutrino detector must shift from discovery to confirmation, precise parameters determination and precision astrophysical test. To compete with the constraints provided by past, present and upcoming experiments and give a significant scientific output, a new pp and ^7Be detector has to measure the neutrino interaction rate with a very high precision, at least 3% (Sec. 1.5.1).

In the next sections we will try to draw some conclusions from the results of the LENS R&D and prototype phase. We will distinguish the "technical feasibility" from the "practical feasibility". The former concerns the question whether the technology has been developed to build a reliable detector, with the capability to measure the solar neutrino signal with an acceptable signal-to-background ratio. The "practical feasibility" addresses the question whether a "technically feasible" experiment can achieve the aforementioned precision at a reasonable cost.

10.2.1 LENS-Ytterbium

The LENS R&D has not proven the "technical" feasibility of an ytterbium experiment. A stable Yb-loaded scintillator has been synthesized, however major issues concerning the ^{235}U and ^{169}Yb backgrounds have remained unsolved (Sec. 2.3.3).

Even if the experiment was technically feasible, this work has demonstrated that the cut of the self-correlated background would imply a large loss of efficiency for solar neutrinos. It was shown that, after imposing the minimum delay cut necessary to reject the self-correlations, the detector efficiency would be ~ 0.16 for ^7Be and ~ 0.22 for pp neutrinos. These estimations are only upper limits of the real achievable efficiency, because they consider only the probabilities that the neutrino-signature is realized after the minimum delay cut and that the coincidence is tagged by a suitable algorithm (Sec. 7.1). We assume that in a real detector the total efficiency would be ~ 0.15 for both ^7Be and pp neutrinos and with this input we try to estimate which mass is necessary for an Yb-LENS experiment.

Let us assume that a calibration of all the Yb-LENS systematics to the level of 2% is possible (only as an exercise). Then the statistical error of the flux measurement must be $\sim 2\%$ to ensure that the total error is $\sim 3\%$, the threshold that makes a real time low energy solar neutrino experiment scientifically interesting (Sec. 1.5.1).

Assuming no other statistical uncertainties, 2% precision corresponds to 2500 observed events. The interaction rate in natural ytterbium is $\sim 6\, y^{-1}t^{-1}$ for both ^7Be and pp, which includes the ν_e survival probability given by the LMA solution ($P_{ee} \sim 0.65$). This gives an observable $\sim 0.9\, y^{-1}t^{-1}$, due to the detection inefficiency. The required ~ 2500 events would be observed with a target exposure of $\sim 2800\, ty$. For an experimental live-time of 5 years, the detector must contain $\sim 560\, t$ of natural Yb. At a benchmark loading of 5% by weight, this translates to a $\sim 11\, kt$ detector. A high granularity is required to reject random ^{14}C coincidences (Sec. 2.3.2) and each module would contain $\sim 100\, kg$. Therefore $\sim 10^5$ cells are needed and at least 2×10^5 PMTs.

These arguments, together with the severe technical problems related to the ^{235}U and ^{169}Yb backgrounds, have convinced the LENS collaboration that the Yb-LENS concept is not viable.

10.2.2 LENS-Indium

Detection of *pp*-Neutrinos The experimental work carried out at MPIK and LNGS has led to the comprehensive optical characterization of the performances of a single detector unit. This information is complementary to the MC studies carried out at Saclay [Mey01, Mey02, Mey03], which use the performances of a single cell as an input parameter to predict the background rate and the ν-detection efficiency of the full scale LENS experiment.

We remind (see Secs. 2.4.3 and 7.2.3) that those simulations have shown that the detection of *pp* neutrinos with an acceptable S/N is technically feasible if:

- the "hybrid" detector design is chosen
- the energy resolution corresponds to $\geq 300\,pe/MeV$
- the effective attenuation length is $\mu \geq 3\,m$
- the spatial resolution is $\geq 15\,cm$ (1σ) at $100\,keV$

We will refer to these results as a benchmark for the required performance of a single LENS cell.

With the detector parameters measured in this work, a LENS experiment based on In-β-diketonates, (In-acac), seems technically feasible only with a more indium-diluted scintillator and with a module length much shorter than the R&D goal of $3\,m$. In Sec. 8.6 it was pointed out that with a better light collection at the PMTs the photoelectron yield of the detector might be improved of up to a factor 2. This must be proven, however even in this case, the goal of $\mu \sim 3\,m$ would remain very far, as the experimental results and the MC simulations of the $20\,g/l$ indium cell have demonstrated.

A design based on the In-acac scintillator would consider in the best realistic case a cell length of $\sim 1.5\,m$ and a limit photoelectron yield of $\sim 300\,pe/MeV$. The extrapolation at low energies of the spatial resolution measured in our samples at $477\,keV$ and $639\,keV$ suggests that $\sigma_x \sim 15\,cm$ at $100\,keV$ should be feasible. Therefore a *pp* indium experiment with an In-β-diketonate scintillator at $\sim 45\,g/l$ might be technically feasible provided that:

- The length of the detector basic unit is decreased from the design goal to $\lesssim 1.5\,m$
- It is experimentally demonstrated that the photoelectron yield can be improved from the present $\sim 200\,pe/MeV$ to $\sim 300\,pe/MeV$ with an efficient light concentrator or a larger PMT

We have seen that the In-hydroxy-carboxylate scintillators (In-CHO) developed at Gran Sasso give a significantly higher PY than the In-acac formulation. With the In-CHO systems the goal energy resolution is already at hand, even without an improvement of the present prototype design. However, also these scintillators have given attenuation lengths in the $\sim 1.5\,m$ range. Furthermore, highly hydrolyzed In-complexes are believed to be more fragile systems than the β-diketonates (Sec. 2.4.3). Fundamental questions about the long-term stability and the

chemical robustness of this formulation will have to be answered in the LLBF. Furthermore, it has to be evaluated whether the background rate above the In β-decay spectrum measured in the LLBF is sufficiently low, or otherwise how this level can be improved.

At the start of the R&D on the LENS project, the initial concept envisaged a homogeneous-segmented detector (only In-loaded cells), with indium loading at $\sim 100\,g/l$, cells $3\,m$ in length, and high ν detection efficiency. At the closing of the pilot phase the following facts have been established:

- Two scintillator formulations have been successfully tested in prototypes, which could ensure the technical viability of the concept, however with $\sim 50\,g/l$ indium-loading and a $\sim 1.5\,m$ cell length.
- MC studies have shown that the soft Bremsstrahlung background can be suppressed, however at the cost of "diluting" the detector by surrounding each In-cell by unloaded modules ("hybrid" design, schematic view in Fig. 2.8 on page 51). The resulting ν detection efficiency after all cuts is ~ 0.25, provided that two indium cells are separated by at least $15\,cm$ of an indium-free scintillator.

We use the above inputs to carry out a similar estimation to the one reported in the previous section for ytterbium. The interaction rate in natural indium is $\sim 65\,y^{-1}t^{-1}$ (LMA oscillation scenario), which gives an observable $\sim 16\,y^{-1}t^{-1}$. Therefore, the required statistical precision implies $\sim 150\,ty$ indium exposure, for example a $30\,t$detector for 5 years live time. With the viable cell geometry and In-loading, each indium cell would contain $\sim 150\,g$ indium and the detector would need $\sim 2 \times 10^5$ loaded cells, plus the unloaded part. Including the latter, the total scintillator mass would be in the range of $15\,kton$. About 10^6 PMTs and the relevant electronics would be required.

This means that an In detector for *pp*-neutrinos based on the LENS concept might be technically feasible, but it is not practically viable.

The arguments about the technical feasibility discussed above have only considered the statistical precision of the experiment. However, it seems very challenging to reduce the systematic error to 2%. In such a large and diluted detector a viable source calibration cannot achieve this level of precision. For comparison, the two exposures of GALLEX to a $\sim 2\,MCi$ ^{51}Cr source (the strongest artificial ν sources ever produced) have provided a calibration of the reaction rate with an error of $\sim$ 10%. A dedicated calibration experiment with a more compact detector would be probably necessary.

Detection of ^7Be-Neutrinos The challenge of $pp-\nu$ detection in In-LENS resides in the irremovable low energy internal background due to the ^{115}In β-decay. This affects only marginally the detection of higher energy neutrinos. The possibility to measure the $^7Be-\nu$ flux with an indium experiment has been considered in the past and even more recently (e.g [DN85, Suz90, HS01]). The design and operation of such a detector would be easier and more affordable:

- No In-free volume is necessary
- A lower granularity is sufficient and hence the cell cross-section can be made larger
- The conditions for the tag can be relaxed, thus increasing the detection efficiency

MC simulations carried out at Saclay have considered a detector consisting of In-cells only, with the same benchmark performances assumed for the *pp* analysis [Mey02]. The results indicate that for a $S/N \sim 10$ the cell cross section can be $10\,cm \times 10\,cm$ and the detection efficiency would be $\varepsilon \gtrsim 50\%$. In this case, a 2% statistical precision would require $\sim 70\,t$ of indium and a live time of 5 years (assuming again the LMA oscillation scenario). With a length of $1.5\,m$, each cell would contain $\sim 700\,g$ of indium, therefore $\sim 10^5$ cells would be needed and twice as much PMTs and electronic channels.

This would still be a very expensive experiment, however a lower mass version might be an interesting "back-up" solution if Borexino would fail its challenging experimental program.

10.3 Outlook

LENS is now completing its pilot phase, with the background measurement of the prototype detectors in the LLBF. The stability of the scintillator will be monitored for a long time and the data analysis completed. However, on the base of the experimental results of the pilot phase, of the indications of MC analysis and of the new scientific context, the European groups of the LENS collaboration do not intend to issue a proposal for the construction of the LENS experiment.

Glossary

ADC: Analog to Digital Converter

bis-MSB: 1,4-bis(2-MethylStyryl)Benzene

BPO: 2-(4-Bi-Phenyl)-5-phenylOxazole

BS: BremsStrahlung

CBS: Compton Back Scattering

CC: Charge Current

CF: Constant Fraction (discriminator)

CNO: Carbon-Nitrogen-Oxygen fusion cycle

CTF: Counting Test Facility (Borexino)

DAQ: Data AcQuisition

EC: Electron Capture reaction

ES: Elastic Scattering

HP-Ge: High Purity Germanium

HV: High Voltage

i.a.: isotopic abundance

In-acac: Indium acetyl-acetonate

In-CHO: Indium hydroxy-carboxylate

LED: Light Emitting Diode

LENS: Low Energy Neutrino Spectroscopy

LLBF: LENS Low Background Facility

LMA: Large Mixing Angle (MSW oscillation solution)

LY: Light Yield

MC: Monte Carlo (simulation)

MCA: Multi-Channel Analyzer

MSW: Mikheyev-Smirnov-Wolfenstein matter-enhanced oscillations

mwe: meters of water equivalent

NC: Neutral Current

NIM: Nuclear Instrumentation Modules

PC: Pseudo-Cumene, (1,2,4-Trimethylbenzol)

PMT: PhotoMultiplier Tube

PY: Photoelectron Yield

***pe*:** photoelectron

***pep*:** proton-electron-proton fusion reaction

PDF: Probability Density Function

PDP: Photon Detection Probability

***pp*:** proton-proton fusion reaction

PPO: 2,5-diphenyloxazole

p-TP: para-TerPhenyl (1,4-diphenyl-benzol)

PXE: Phenyl-ortho-XylylEthane

QE: Quantum Efficiency

SC: Self-Correlated, Self-Correlation

SM: Standard Model of elementary particles and interactions

SNP: Solar Neutrino Problem

SR: Specular Reflection

SSM: Standard Solar Model

TDC: Time to Digital Converter

TIR: Total Internal Reflection

TPHC: Time to Pulse Height Converter

TTL: Transistor-Transistor Logic

VME: VersaModule Eurocard

WLS: WaveLength Shifter

Thanks

At the end of a long and exciting way, which closes a phase of my life, I would like to thank all those who have contributed to the success of this work.

Innanzitutto ringrazio i miei genitori, Rosario e Mirella, per avermi trasmesso l'amore per il sapere e per avermi comunicato, con il loro stesso esempio, l'importanza di perseguire nella vita, con passione e determinazione, ciò che davvero si ama.

I express my sincere gratitude to Prof. Dr. Till Kirsten, for bringing this exciting subject to my attention, for advertising me and supporting my application at MPIK and... also for introducing me in the Heidelberg chess club!

I am in debt with Dr. Stefan Schönert for his inestimable contribution. He has supported this work and continuously encouraged and stimulated my scientific growth. I hope he will soon resolve to habilitate, so that more and more students will benefit from his experience!

This work has been supported by the MPIK. I particularly appreciated the assistance I received from the institute and the solicitous help in various situations.

The work described in this thesis is the result of a fruitful collaboration with all the other colleagues of the *Nachwuchsgruppe* led by Dr. S. Schönert. I would like to thank all the members of this "dream-team": Christian Buck, Dr. Frank X. Hartmann, Ute Schwan and Dr. Thierry Lasserre. It has been a pleasure to work together with Christian, because of his effectiveness and healthy pragmatism. I also thank him for sharing a pleasant time in Heidelberg and Gran Sasso. I address a special thank to Frank, for teaching me a lot about chemistry and physics (especially symmetries!) in the most funny way. I also learnt from him how to distinguish in some cases the real science from good-looking fakes. Ute has been for me the brightest example of organization and reliability. Allerdings möchte ich mich bei ihr insbesondere dafür bedanken, weil Sie immer mir gegenüber sooooo lieb gewesen ist! I thank very much Thierry for the very pleasant time we shared inside and outside of the MPIK, working fruitfully for a long time side by side and often enjoying our free time together. He has been a sort of "big brother" and his enthusiasm for physics and life was often inspiring to me (in both two fields!).

This work has benefited from the technical help of several persons. I thank the staff of the mechanical workshop of the MPIK, and especially Frank Kleinbongardt, who has constructed most of the mechanical parts used for the dark-room measurements. I thank Dr. Gerd Heusser for help and useful discussions in matter of radioactivity and low-background, Erhard "Ebu" Burkert and Dr. Jurgen Kiko for very instructive discussions about electronics, Norbert Bulian and Klaus Jänner for the construction of the LED boards used for the light piping measurements and of some electronic modules used in the LLBF. I also thank Peter Mögel and Erich Borger for the transformation of many raw quartz tubes in real prototype cells, and Dr. Josepha Oehm for the help with the clean-room.

I cannot forget the beautiful time spent in Gran Sasso and I would like to express my

gratitude to all the persons from the LNGS who have collaborated to the realization of the LLBF experimental program: Dr. Carla Cattadori, Dr. Olivier Besida, Assunta di Vacri, Dr. Igor Barabanov and Dr. Nicola Ferrari.

I thank all the members of the international LENS collaboration, for inspiration, encouragement and many stimulating discussions.

I have received help and suggestions from many physicists external to our project. I remind here Dr. Thimo Bastuck for the precious assistance in the ellipsometric measurements of the PMT photocathodes, and Prof. Dr. Eckart Lorenz for introducing us to the wonderful properties of the VM2000 super-reflective foils.

A part of my work at MPIK has been devoted to GNO. I thank Prof. Dr. Wolfang Hampel and Florian Kaether for the fruitful collaboration in the activities related to this experiment.

Many persons have contributed to improve substantially the quality of this thesis. At the first place, I would like to express my gratitude to Dr. Ferenc Dalnoki-Veress, who has carefully read and corrected several chapters of this work and has managed to "clean" my poor English, at least as much as needed (and possible!). I also thank him for many helpful advices and last for his lovely attitude. I appreciated very much the help of Dr. Elisa Resconi, who has opened my mind to clarity, logic and conciseness (unfortunately very late!), thus notably improving the readability of some chapters. Besides, I thank her for sincere listening to all my heart problems during our lunch-breaks in the last three years. Last, I thank Dr. Georg Rugel for correcting one of my last chapters when I was in desperate *Zeitnot* and for helping me to translate the abstract in German.

I thank all the friends of the MPIK with whom I shared a very pleasant time, and in particular Davide Franco, who has brought new enthusiasm in my life in the last few months; Dr. Burkhard Freudiger, a person one can absolutely trust, in the work as well as in life; Peter Peiffer, for many coffees and as many funny stories about women; and Dr. Hardy Simgen, for interesting discussions about physics and chess.

Ich bedanke mich ganz herzlich bei Isabel, die mich während meines Schreibens geduldig und liebevoll gepflegt hat und dadurch vermieden hat, dass ich in den letzten paar Wochen vor dem Abgabetermin völlig in einen unmenschlischen Lebenszustand gerutscht bin.

Last, I would like to thank my *Gutachter,* Prof. Dr. Till Kirsten and Prof. Dr. Karl-Tasso Knöpfle, for careful and patient reading of this thesis.

Bibliography

[AH29] R.d'E. Atkinson, F.G Houtermans, *Z. Phys.*, **54** (1929), 656

[AWT03] G.Audi, A.H.Wapstra and C.Thibault, *Nucl. Phys. A*, **729** (2003), 337

[Bah89] J.N. Bahcall, *Neutrino Astrophysics*, Cambridge University Press, 1989

[Bah97] J.N. Bahcall, M.H. Pinsonneault, S. Basu, J. Christensen-Dalsgaard, *Phys. Rev. Lett.*, **78** (1997), 171 and J.N. Bahcall, S. Basu, M.H. Pinsonneault, *Phys. Lett. B*, **433** (1998), 1

[BD64] J.N. Bahcall, *Phys. Rev. Lett.*, **12** (1964), 300 and R. Davis, *Phys. Rev. Lett.*, **12** (1964), 303

[Bet39] H.A. Bethe, *Phys. Rev.*, **55** (1939), 434

[BGP02] J.N. Bahcall, M.C. Gonzalez-Garcia, C. Peña-Garay, *J. High Energy Phys.*, **07** (2002), 0054

[BHS03] C. Buck, F.X. Hartmann, S. Schönert, U. Schwan, *J. Radioan. Nucl. Chem.*, **258** (2003), 255

[Bir64] J.B.Birks, *The Theory and Practice of Scintillation Counting*, Pergamon, 1964

[Bir68] J.B. Birks, *J. Phys. B*, **1** (1968), 946

[BKS99] J.N. Bahcall, P.I. Krastev, A. Y. Smirnov, *Phys. Rev. D*, **58** (1999), 096016-1

[Bog01] G. Bogaert for the GLAST collaboration, *proceedings of the 7th International Conference on Advanced Technology and Particle Physics*, (Villa Olmo, Como 15-19 October 2001)

[Bor98] Borexino collaboration (G. Alimonti et al.), *Astrop. Phys.*, **8**, 141 (1998); Borexino collaboration (G. Alimonti et al.), *Nucl. Instr. Meth. A*, **406** (1998), 411 and Borexino collaboration (G. Alimonti et al.), *Phys. Lett. B*, **422** (1998), 349

[Bor02] Borexino collaboration (C. Arpesella et al.), *Astrop. Phys.*, **18** (2002), 1

[Bor04] Borexino collaboration, prepared for submission to *Nucl. Instr. Meth. A*, 2004

[BP03] J.N. Bahcall, C. Peña-Garay, hep-ph/0305159 (2003)

[BPB01] J.N. Bahcall, M.H. Pinsonneault, S. Basu, *Astrophys. J.*, **555** (2001), 990

[BR96] R. Brun, F. Rademakers, *ROOT - An Object Oriented Data Analysis Framework*, Proc. AIHENP'96 Workshop, Lausanne, Sep. 1996, Nucl. Inst. & Meth. in Phys. Res. A 389 (1997) 81-86. See also http://root.cern.ch/.

[Bro01] C. Broggini for the MUNU collaboration, *Nucl. Phys. B (Proc. Suppl.)*, **91** (2001) 105

[Buc04] C. Buck, *Development of Metal-Loaded Liquid Scintillators for Future Detectors to Investigate Neutrino Properties*, "Dissertation", Universität Heidelberg, 2004

[BV92] F. Boehm, P. Vogel, *Physics of Massive Neutrinos*, Cambridge University Press, 1992

[BW64] M. Born, E. Wolf, *Principle of optics*, Pergamon Pres, 1964

[Cas85] V. Castellani, *Astrofisica Stellare*, Zanichelli, 1985

[Cas97] V. Castellani, S. Degl'Innocenti, G. Fiorentini, M. Lissia, B. Ricci, *Phys. Rept.*, **281** (1997), 309

[Cat03] C.M. Cattadori et al., LENS internal communication, 2003

[Cat04] C.M. Cattadori et al., in preparation for submission to *Nucl. Instr. Meth. A*, 2004

[CHO99] CHOOZ collaboration (M. Apollonio et al.), *Phys. Lett. B*, **466** (1999), 415

[CHRV86] M. Cribier, W. Hampel, J. Rich, D. Vignaud, *Phys. Lett. B*, **182** (1986), 89

[Cla83] D.D. Clayton, *Principle of Stellar Evolution and Nucleosynthesis (2nd edition)*, The University Chicago Press, 1983

[Cri84] M. Cribier et al., *DAPNIA/Saclay report*, 1984

[Cri01] M. Cribier, LENS internal note, 2001

[Dav68] R. Davis et al., *Phys. Rev. Lett.,* **14** (1968), 20

[DN85] A.K. Drukier, R. Nest, *Nucl. Instr. Meth. A*, **239** (1985), 605

[Edd20] S.A. Eddington, *Observatory*, **43** (1920), 341

[Eli97] F. Elisei et al., *Nucl. Instr. Meth. A*, **400** (1997), 53

[Eji00] H. Ejiri et al., *Phys. Rev. Lett.*, **85** (2000), 2917

[FB00] M. Fujiwara et al., *Phys. Rev. Lett.*, **85** (2000), 4442 and M. Bhattacharya et al., *Phys. Rev. Lett.*, **85** (2000), 4446

[FMB02] G. Fogli et al., *Phys. Rev. D*, **67** (2003), 073002; M. Maltoni, T. Schwetz, J. Valle, *Phys. Rev. D*, **67** (2003), 093003; J.N. Bahcall, M.C. Gonzalez-Garcia, C. Peña-Garay, *J. High Energy Phys.*, **02** (2003), 009

[Fog02] G.L. Fogli, E. Lisi, A. Marrone, D. Montanino, A. Pallazzo, *Phys. Rev. D*, **66** (2002), 053010

[GAL92] GALLEX collaboration (P. Anselmann et al.), *Phys. Lett. B*, **285** (1992), 376

[GAL98] GALLEX collaboration (W. Hampel et al.), *Phys Lett. B*, **420** (1998), 114 and GALLEX collaboration (W. Hampel et al.), *Phys Lett. B*, **436** (1998), 158

[GAL99] GALLEX collaboration (W. Hampel et. al), *Phys. Lett. B*, **447** (1999), 127

[Gam38] G. Gamow, *Phys. Rev.*, **53** (1938), 595

[GFM00] A. de Gouvea, A. Friedland, H. Murayama, *Phys. Lett. B*, **490** (2000), 125

[GK01] V.M. Gelis, E.A. Kozlitin et al., LENS internal note, 2001 and V.M. Gelis, E.A. Kozlitin, U. Schwan, LENS internal note 2001

[GNO00] GNO collaboration (M. Altmann et al.), *Phys. Lett. B*, **490** (2000), 16

[GNO03] E. Bellotti for the GNO collaboration, proceedings of the TAUP2003 conference (in press)

[GP69] V. Gribov, B. Pontecorvo, *Phys. Lett. B*, **28** (1969), 49

[Gro00] D.E. Groom at al., *Eur. Phys. J. C*, **15** (2000), 1

[Har04] F.X. Hartmann et al., prepared for submission to *Nucl. Instr. Meth. A*, 2004

[Hea91] O.S.Heavens, *Optical Properties of Thin Solid Films*, Dover Publication, 1991

[HES03] H.E.S.S. collaboration, Collected H.E.S.S. Contributions to the 28th ICRC, Tsukuba, 2003

[Heu93] G. Heusser, Proc. 3rd Int. Summer School on Low-Level Measurememnts of Radioactivity in the Environment: Technique and Applications, Huelva, Spain, 1993

[Heu95] G. Heusser, *Ann. Rev. Nucl. Part. Sci.*, **45** (1995), 543

[HM02] $\beta\beta$-Heidelberg-Moscow collaboration, private communication, 2002

[Hom98] B.T. Cleveland et al., *Astrophys. J.*, **496** (1998), 505

[HS01] F.X. Hartmann, S. Schönert, presented by F. von Feilitzsch, in V. Berezinsky, F. Vissani (Eds.), Proc. Fifth International Top. Workshop at LNGS on Solar Neutrinos, INFN, Gran Sasso, 2001, p. 388

[INR01] LNGS-INR-RAS LENS group, LENS internal note, 2001

[INR03] LNGS-INR-RAS LENS group (C.M. Cattadori et al.), submitted to *J. Rad. Phys. Chem.*, 2003 and LNGS-INR-RAS LENS group (C.M. Cattadori et al.), LENS internal communication, 2003

[Kam96] Kamiokande collaboration (Y. Fukuda et al.), *Phys Rev. Lett.*, **77** (1996), 1683

[Kam03] KamLAND collaboration (K. Eguchi at al.), *Phys. Rev. Lett.*, **90** (2003), 021802

[Kir99] T. Kirsten, *Rev. Mod. Phys.*, **71** (1999), 1213

[Kno89] G.F.Knoll, *Radiation Detection and Measurement*, 2nd edition, John Wiley & Sons, 1989

[Lan93] T.Lang, *Photocathode characterisation*, Thorn EMI research report X.2818/1A (1993)

[Las02] T. Lasserre, *A multi-purpose Data Acquisition System for the LENS pilot phase*, LENS internal note, 2002

[Lau03] M. Laubenstein, private communication, 2003

[LENS99] LENS collaboration, *Letter of Intent*, Laboratori Nazionali del Gran Sasso, 1999

[Lor02] E. Lorenz, private communication, 2002

[LSND01] LSND collaboration (A. Aguilar et al.), *Phys. Rev. D*, **64** (2001), 112007

[MAC99] MACRO collaboration (M. Ambrosio et al.), *Astr. Part. Phys.*, **10** (1999), 11

[Mal01] J. Mallet, LENS internal note, 2001

[Mey01] J-P. Meyer, LENS internal note, 2001

[Mey02] J-P. Meyer, LENS internal note, 2002

[Mey03] J-P. Meyer, LENS internal note, 2003

[MNS62] Z. Maki, M. Nakagawa, S. Sakata, *Prog. Theor. Phys.*, **28** (1962), 870

[Mot03] D. Motta et al., *Nucl. Phys. B (Proc. Suppl.)*, **118** (2003), 451

[MPI03] C. Buck, F.X. Hartmann, T. Lasserre, D. Motta, S. Schönert, U. Schwan, *J. Luminesc.*, **106** (2004), 57

[MS86] S.P. Mikheyev, A.Y. Smirnov, *Nuovo Cim. C*, **9** (1986), 17

[MS04] D. Motta, S. Schönert, in preparation for submission to *Nucl. Instr. Meth. A,* 2004

[MT92] M.E. Moorhead, *Reflectors in Cherenkov Detectors*, PhD thesis, University of Oxford (1992) and M.E.Moorhead and N.W.Tanner, *Nucl. Instr. and Meth. A*, **378** (1996), 162

[Ned02] H. Neder, *Kupfer-Probe für LENS - "CuHD", Auswertung der ersten Messperiode*, memo, 2002

[Pei03] P.Peiffer, *Optimierung des Äusseren Myon-Vetos am Borexino Experiment*, Diplomarbeit, Universität Heidelberg, 2003

[Pho94] Philips-Photonics, *Photomultiplier tubes principle & application*, Philips Export B.V., 1994

[Pon46] B. Pontecorvo, Chalk River Report PD205 (1946), reprinted in *B. Pontecorvo - Selected Scientific Works*, Società Italiana di Fisica, 21, 1997

[Rag76] R.S. Raghavan, *Phys. Rev. Lett.*, **37** (1976), 259

[Rag97] R.S. Raghavan, *Phys. Rev. Lett.*, **78** (1997), 3618

[Rag01a] R.S. Raghavan, LENS internal communication, 2001

[Rag01b] R.S. Raghavan, *hep-ex/0106054* (2001), submitted to *Phys. Rev. Lett.* and R.S. Raghavan, LENS internal note, 2002

[Ran94] G.Ranucci et al., *Nucl. Instr. Meth. A*, **350** (1994), 338

[Rap85] J. Rappaport et al., *Phys. Rev. Lett.*, **54** (1985), 2325

[RC56] C.L. Cowan, Jr., F. Reines, F.B. Harrison, H.W. Kruse, A.D. McGuire, *Science* **124** (1956), 103 and C.L. Cowan, Jr., F. Reines, *Phys. Rev.*, **113** (1959), 273

[Res00] E. Resconi, *Measurements with the Upgraded Counting Test Facility (CTF-2) of the Solar Neutrino Experiment Borexino,* Dissertazione del Dottorato di Ricerca, Università di Genova, Italy (2000)

[RGL98] G.Ranucci, A. Goretti, P. Lombardi, *Nucl. Instr. Meth. A*, **412** (1998), 374

[RWH64] M.L.Roush, M.A.Wilson, W.F.Hornyak, *Nucl. Instr. Meth.*, **31** (1964), 112

[Sac] Dapnia CEA/Saclay LENS group (M. Cribier et al.), LENS internal report

[SAG91] SAGE collaboration (A.I. Abazov et al.), *Phys. Rev. Lett.*, **67** (1991), 3332-3335

[SAG99a] SAGE collaboration (J.N. Abdurashitov et al.), *Phys. Rev. C*, **59** (1999), 2246

[SAG99b] SAGE collaboration (J.N. Abdurashitov et al.), *Phys. Rev. C,* **60** (1999), 055801

[SAG02] SAGE collaboration (D.N. Abdurashitov et al.), J. Exp. Theor. Phys., **95** (2002), 181 and V.N. Gavrin for the SAGE collaboration, proceedings of the TAUP2003 conference (in press)

[Sch00] S. Schönert, LENS internal note, 2000

[Sch01] S. Schönert, LENS internal note, 2001

[Sch02] S. Schönert, *Nucl. Phys. B (proc. Suppl.)*, **118** (2003), 62

[Shi03] J. Shirai for the KamLAND collaboration, *Nucl. Phys. B (proc. Suppl.)*, **118** (2003), 15

[SK98] SK collaboration (Y. Fukuda et al.), *Phys. Rev. Lett.*, **81** (1998), 1562

[SK99] SK collaboration (M. Nakahata et al.), *Nucl. Instr. Meth. A*, **421** (1999), 113

[SK02] SK collaboration (S. Fukuda et al.), *Phys. Lett. B*, **539** (2002), 179 and M.B. Smy for the SK collaboration, *Nucl. Phys. B (proc. Suppl.)*, **118** (2003), 25

[SLO03] S. Schönert, T. Lasserre, L. Oberauer, *Astrop. Phys.*, **18** (2003), 565

[SNO00] SNO collaboration (J. Boger et al.), *Nucl. Instr. Meth. A*, **449** (2000), 72

[SNO02] SNO collaboration (Q.R. Ahmad et al.), *Phys. Rev. Lett.*, **89**, 011301 (2002) and SNO collaboration (Q.R. Ahmad et al.), *Phys. Rev. Lett.*, **89** (2002), 011302

[SNO03] SNO collaboration (Q.R. Ahmad et al.), nucl-ex/0309004 (2003), submitted to *Phys. Rev. Lett.*

[Ste02] F. Steinbuegl et al., submitted to *World Scientific*, 2002 and F. Steinbuegl, *Diplomarbeit*, TUM-Munich, 2002

[Suz90] Y. Suzuki, K. Inoue, Y. Nagashima, S. Hashimoto, T. Inagaki, *Nucl. Instr. Meth. A*, **293** (1990), 615

[Tim76] H.Timan, *Revue Technique Thomson-CSF*, **8** (1976)

[TMG99] H.G.Tompkins and W.A.McGahan, *Spectroscopic Ellipsometry and Reflectometry, a user guide*, John Wiley & Sons, 1999

[Tur01] S. Turk-Chièze et al., *Ap. J. Lett.*, **555** (2001), L69

[Vac03] A. di Vacri, LENS internal note, 2003

[Web00] M.F. Weber et al., Science Vol., **287** (2000), 2451

[Wei37] C.F. von Weizsäcker, *Phys. Z.*, **38** (1937) 76 and C.F. von Weizsäcker, *Phys. Z.*, **39** (1938) 633

[Win93] R. Wink et al., *Nucl. Instr. Meth. A*, **329** (1993), 541

[Wol78] L. Wolfenstein, *Phys. Rev. D*, **17** (1978), 2369